Springer Proceedings in Materials

Saluru Baba Krupanidhi
Anjali Sharma
Anjani Kumar Singh
Vinita Tuli *Editors*

Recent Advances in Functional Materials and Devices

Select Proceedings of AFMD 2023

Springer

Springer Proceedings in Materials

Volume 37

Springer Proceedings in Materials publishes the latest research in Materials Science and Engineering presented at high standard academic conferences and scientific meetings. It provides a platform for researchers, professionals and students to present their scientific findings and stay up-to-date with the development in Materials Science and Engineering. The scope is multidisciplinary and ranges from fundamental to applied research, including, but not limited to:

- Structural Materials
- Metallic Materials
- Magnetic, Optical and Electronic Materials
- Ceramics, Glass, Composites, Natural Materials
- Biomaterials
- Nanotechnology
- Characterization and Evaluation of Materials
- Energy Materials
- Materials Processing

To submit a proposal or request further information, please contact one of our Springer Publishing Editors according to your affiliation:

European countries: **Mayra Castro** (mayra.castro@springer.com)
India, South Asia and Middle East: **Priya Vyas** (priya.vyas@springer.com)
South Korea: **Smith Chae** (smith.chae@springer.com)
Southeast Asia, Australia and New Zealand: **Ramesh Nath Premnath** (ramesh.premnath@springer.com)
The Americas: **Michael Luby** (michael.luby@springer.com)
China and all the other countries or regions: **Mengchu Huang** (mengchu.huang@springer.com)

This book series is indexed in **SCOPUS** database.

Saluru Baba Krupanidhi · Anjali Sharma ·
Anjani Kumar Singh · Vinita Tuli
Editors

Recent Advances in Functional Materials and Devices

Select Proceedings of AFMD 2023

Springer

Editors
Saluru Baba Krupanidhi
Indian Institute of Science
Bangalore, India

Anjani Kumar Singh
Department of Physics
Atma Ram Sanatan Dharma College
University of Delhi
Delhi, India

Anjali Sharma
Department of Physics
Atma Ram Sanatan Dharma College
University of Delhi
Delhi, India

Vinita Tuli
Department of Physics
Atma Ram Sanatan Dharma College
University of Delhi
Delhi, India

ISSN 2662-3161 ISSN 2662-317X (electronic)
Springer Proceedings in Materials
ISBN 978-981-99-6765-0 ISBN 978-981-99-6766-7 (eBook)
https://doi.org/10.1007/978-981-99-6766-7

This Springer imprint is published by the registered company Springer Nature Singapore Pte Ltd.
The registered company address is: 152 Beach Road, #21-01/04 Gateway East, Singapore 189721, Singapore

Paper in this product is recyclable.

Organizers

Chief Patron

Shri Pawan Jaggi, Chairman, ARSD College

Patron

Prof. Gyantosh Kumar Jha, Principal, ARSD College

Conference Chair

Prof. Vinita Tuli, Coordinator, IQAC

International Advisory Board

Dr. Seema Vinayak, Director, SSPL-DRDO
Dr. N. Kalaiselvi, Director General, CSIR
Prof. Amar Bhalla, UTSA, USA
Prof. Ruyan Guo, UTSA, USA
Dr. Shiv Kumar, ER&IPR-DRDO
Prof. S. B. Krupanidhi, IISC, Bangalore
Prof. S. Annapoorni, Univ. Of Delhi
Dr. Manoj Sharma, SSPL-DRDO
Prof. Mohd. Ajmal Khan, Jamia Milia Islamia
Dr. D. Kanjilal, IUAC, New Delhi

Dr. Ravi Kant Mishra, Univ. of Manchester, UK
Dr. R. K. Podila, Clemson University, USA
Dr. R. K. Kotnala, Chairman NABL, India
Dr. David Kocman, SLOVENIA

National Advisory Board

Dr. O. P. Thakur, NSUT, Delhi
Prof. S. C. Kaushik, IIT Delhi
Prof. Monika Tomar, Miranda House, DU
Prof. A. S. Rao, DTU, Delhi
Dr. Ajay Agarwal, IIT-Jodhpur
Prof. Ranjana Jha, NSUT, Delhi
Dr. Ashok Kumar, NPL, Delhi
Dr. Renu Sharma, SSPL-DRDO
Prof. S. S. Islam, Jamia Millia Islamia
Prof. Arijit Chowhdhuri, ANDC, University of Delhi
Dr. Isha Yadav, SSPL-DRDO
Dr. Shibu Saha, NPL, Delhi
Dr. Rahul Prajesh, CEERI-Pilani
Dr. Javid Ali, Jamia Milia Islamia

Convener and Program Chairs

Dr. Shankar Subramanian
Dr. Anjali Sharma

Conference Secretaries

Dr. Anjani kumar Singh
Dr. Raghvendra Pandey
Mr. Mohd. Sadiq
Dr. Manisha
Dr. Amit K. Vishwakarma
Dr. Abid Hussain

Finance Committee

Ms. Swati
Dr. Rakesh Malik
Dr. Rita Singh

Publication Committee

Dr. Ashutosh VishwaBandhu
Dr. Arvind Kumar
Mr. Lalit Kumar

Oral Session Committee

Dr. Manish
Dr. Yogesh Kumar
Dr. Rajveer Singh

Technical Program Committee

Dr. Avanish Pratap Singh
Mr. Bhupender Singh
Mr. Ashok

Poster Session Committee

Dr. Devender Rana
Dr. B. L. Prashant

Local Organizing Committee

Dr. Pinky Dureja
Dr. Nutan Mishra
Dr. Geeta Sanon
Dr. Pankaj Narang
Mr. Pravata Kumar Behera

Foreword

I am delighted to announce that the Department of Physics has been successful in organizing 2nd International Conference on *Advanced Functional Materials and Devices (AFMD-2023)* under the aegis of Internal Quality Assurance Cell of ARSD after the grand success of AFMD-2021.

Atma Ram Sanatan Dharma College has gained a reputation in recent years for its commitment to equality and excellence. Founded in 1959, the college has undergone significant changes and transformations in the post-independence period. However, its strong foundation along with the importance of leadership while adapting to a new environment have contributed to the College's success. The College is accredited by the NAAC with an A++ rating with a score of 3.77, the highest among all Delhi university colleges. Also, the college got all over India 6th position in NIRF by the Ministry of Education, GOI. ARSD college is rapidly evolving to become the best place for research. The Department of Physics, Chemistry, Biology and Mathematics has received funding for the Department of Biotechnology from the Government of India through the Star Faculty Program which highlights the quality of research in the college. In addition, ARSD's commitment to research and innovation is also reflected in the establishment of the central instrument facility and Centre for Innovation and Entrepreneurial Leadership (CIEL) collaboration with M/o MSME. The faculty has also received many prestigious grants and the college has become a renowned research centre. The main purpose of ARSD college is to develop talents in its ecosystem and enable them to reach their potential through ethical practices. I extend my best wishes to the college and hope it continues to pave the way for the advancement of knowledge in society.

The AFMD 2023 conference was a remarkable event that featured 29 Invited Lectures delivered by renowned researchers. It also received an overwhelming response with 196 abstracts submitted for oral and poster presentations from all around the world. The conference commenced with an inaugural ceremony led by the esteemed Chief Guest, Shri Pawan Jaggi, Chairman of ARSD College, followed by a plenary talk by Prof. Hoe Tan from the Australian National University, Australia. I extend my sincere appreciation to all the invited speakers and participants who

shared their valuable knowledge and research findings during this event. The conference theme was highly relevant to the advancements in technology that we witness in the present day. Researchers from various corners of the globe have been diligently working toward the progress of technology for the betterment of society. Their dedication and efficiency have been commendable, and their contributions are instrumental in shaping the future of technological innovation for the benefit of all.

I am delighted to announce that the publication of this proceeding book marks the culmination of the research papers presented at AFMD 2023. I extend my heartfelt congratulations to all the authors whose papers have been selected for inclusion in this publication after rigorous review procedure. I would also like to express my sincere gratitude to the esteemed reviewers and editors for their dedicated efforts and time in reviewing and refining the papers. The Editorial Board, under the leadership of renowned researcher Prof. S. B. Krupanidhi (Emeritus Scientist, IISc, Bangalore), played a crucial role in overseeing the publication process, and I am grateful to him for his valuable cooperation. I would like to acknowledge the hard work and dedication of the other editors, Prof. Vinita Tuli, Dr. Anjali Sharma Kaushik, and Dr. Anjani Kumar Singh, who have contributed immensely to shaping this book. Their expertise and commitment have been instrumental in giving form and structure to the content within. Furthermore, I would like to express my appreciation to the conference convener, Dr. S. Shankar Subramanian, and the entire organizing team for their exceptional efforts in ensuring the resounding success of AFMD-2023. Their meticulous planning and execution have contributed to the conference's grand success and the publication of this esteemed proceeding book.

I extend my best wishes to the convener, the organizing team, and all involved for their future endeavors. May they continue to achieve remarkable accomplishments, adding numerous feathers of success to their hats.

Unity marks the start. Cohesion propels us forward. Collaboration brings triumph.

July 2023

Prof. Gyantosh Kumar Jha
Principal
Atma Ram Sanatan Dharma College
University of Delhi
Delhi, India

Preface

The book titled "Recent Advances in Functional Materials and Devices" unveils the carefully curated proceedings from the 2nd International Conference on "Advanced Functional Materials and Devices" (AFMD-2023). The conference, AFMD-2023, was held online from 13–15 March 2023 and was organized by the Department of Physics and Internal Quality Assurance Cell of Atma Ram Sanatan Dharma College, University of Delhi, New Delhi, India. This publication showcases papers that highlight the remarkable progress made in the field of functional materials, encompassing electronic, magnetic, optical, adaptive, and dielectric materials, among others. These materials are crucial in developing new functionalities and enhancing performance in the current technological era. The book explores a wide range of topics, including materials for energy harvesting, biomedical applications, environmental monitoring, photonics and optoelectronic devices, strategic applications, and high-energy physics.

With its comprehensive coverage, this book provides a valuable reference for beginners, researchers, and academicians interested in the latest functional materials for device applications. The conference comprised invited and technical sessions, facilitating discussions with respected speakers who shared their expertise in various subjects such as multifunctional materials, biomaterials, materials for environmental studies, Theoretical simulations based on density functional theory and solar simulation of materials, 2D materials, perovskite and double perovskite materials, smart materials, materials for energy conversion and storage, advanced functional materials, polymeric materials, composites, materials for sustainable development, nanomaterials and thin films, smart devices, quantum dots synthesis techniques, and characterization tools for smart devices.

During the conference, one plenary speaker, four keynote speakers, and twenty four invited speakers delivered exceptional research presentations spanning various fields of material science. Additionally, 101 oral presentations and approximately 95 poster presentations provided a gracious opportunity for participants to share their recent research work with one another. The conference received a total of 196 abstract submissions from around the globe, including countries such as Australia, USA, Mexico, Malaysia, United Kingdom, South Korea, and Japan. Out of these

submissions, 28 full papers were accepted after rigorous review by two experts in the field. The publication of this proceeding book centers on the scope of Material Science, thanks to the efforts of peer reviewers who provided constructive critical comments, suggestions for improvements, and corrections, thereby enhancing the quality of the selected papers. We express our sincere gratitude to all the authors who submitted their papers, as their contributions were instrumental in the conference's success.

We firmly believe that the papers published in this proceeding book will not only expand readers' knowledge but also provide a new platform for research growth. Lastly, we extend our heartfelt thanks to the esteemed editors, International/National Advisory committees, session chairs, program committee members, and external reviewers who dedicated their time and effort to ensuring the scientific excellence of the program. We would also like to express our appreciation to Springer Nature for their unwavering support, which served as both strength and inspiration for the organizers throughout this remarkable journey of success.

Bangalore, India — Prof. Saluru Baba Krupanidhi
Delhi, India — Dr. Anjali Sharma
Delhi, India — Dr. Anjani Kumar Singh
Delhi, India — Prof. Vinita Tuli

Acknowledgments

I would like to take this opportunity to express my deepest gratitude to Prof. Gyantosh Kumar Jha, Principal of ARSD College for continuous support and encouragement for this edited book. The culmination of our collective efforts has resulted in a work that I am truly proud of, and it would not have been possible without the invaluable support and assistance from many individuals.

First and foremost, I extend my heartfelt thanks to the authors who entrusted their work to this book. Your insightful contributions, dedication, and expertise have enriched the content and made this publication truly exceptional. Your willingness to share your knowledge and perspectives has undoubtedly made a significant impact on our readers and the academic community.

I would also like to extend my gratitude to Priya Vyas, Associate Editor at Springer Nature for their unwavering commitment and hard work throughout the entire process. Your meticulous attention to detail, thoughtful suggestions, and tireless efforts in reviewing, refining, and organizing the chapters have been instrumental in shaping the book into its final form. Your expertise and professionalism have ensured the highest quality standards and a seamless publishing experience.

Furthermore, I would like to acknowledge the support and guidance provided by the production team and their staff. Their dedication, professionalism, and commitment to excellence have been vital in bringing this book to fruition. Their expertise in navigating the publishing process, from initial discussions to the final publication, has been invaluable, and I am grateful for their unwavering support.

I am also indebted to the peer reviewers who generously shared their time and expertise to provide constructive feedback and suggestions for improvement. Your rigorous evaluation and insightful comments have undoubtedly strengthened the quality and credibility of this book.

Last but not least, I would like to express my heartfelt appreciation to my family, friends, and colleagues who have provided me with unwavering support, encouragement, and understanding throughout this journey. Your belief in me and your constant words of encouragement have been a source of inspiration and motivation.

To everyone involved, whether directly or indirectly, in the creation and publication of this edited book, please accept my sincerest gratitude. Your contributions,

support, and dedication have made this endeavor a truly rewarding and fulfilling experience. It is with great pleasure that I acknowledge and recognize the significant role each one of you has played in the success of this book.

Thank you all for your invaluable contributions, and I hope that this book will make a positive impact on its readers and the academic community.

Dr. Anjani Kumar Singh
Corresponding Editor

Contents

Synthesis and Characterizations of Hexagonal Perovskite-Related Oxide for Solid Electrolyte Application 1
Paras Saini, Hera Tarique, Hemant Kumar, Anjani Kumar Singh, Raghvendra Pandey, and Prabhakar Singh

Evidence of Ferromagnetic Short-Range Correlations in Sol–gel Synthesized $La_{1.88}$ $Sr_{0.12}CoMnO_6$ Nanoparticles 15
Swati Jharwal and Arvind Kumar

Studies on Electrical Properties of Thin Film-Based Layered FeFET Devices 29
Akshay Panchasara, Urjitsinh Rathod, Savan Katba, Mahesh Jivani, and Ashish Ravalia

Investigation of Structural and Electrical Properties of Ternary System LCMO-CFO-BT 35
Manurbhav Arya, Chitralekha, S. Gaurav, and S. Shankar

Investigations of Atomic Disorder and Grain Growth Kinetics in Polycrystalline $Gd_2Ti_2O_7$ Pyrochlore 45
Ankita, Umang Berwal, Vinod Singh, Yogendra Singh, and Satyendra Singh

Graphical User Interface (GUI): Characterization Technique for Photonic and Plasmonic Structures 57
Pushpa Bindal and Ayasha Malik

Effect of Synthesis Conditions on the Photoluminescent Properties of Eu Doped Gadolinium Oxide Phosphors 69
Kajal Kaushik, Ruby Priya, Harmanpreet Kaur, Kulwinder Singh, and O. P. Pandey

Extraction of Carbon from Biomass-Based Bamboo and Coconut Husk for Enhancement of High-Performance Supercapacitor 77
Giriraj Dandekar, Gauresh Godkar, Omkar Salvi, Brijeshkumar Yadav, Mahadev Sonavane, and Rounak Atram

Biopolymer-Based Biosensors: Fabrication and Properties 89
Rakhi Pandey and Garima Mathur

Synthesis Cum Structural, Mechanical, Optical and Piezoelectric Studies of L(+)-Tartaric Acid Crystals Adulterated with Malachite Green and Trypan Blue Dyes 99
Preetika Dhawan, Karan Grover, and Harsh Yadav

Investigating the Morphological Evolution, Electron Paramagnetic Resonance, & Electrical Properties of Barium Titanate with Sn-Incorporation 113
Sachin Kumar, Anurag Pritam, Vaibhav Shrivastava, O. P. Thakur, and Vandna Luthra

Photoluminescence and Optical Studies of a Temperature Sustainable Dy^{3+} Doped Silicate Phosphor for Photonic Applications 127
Vibha Sharma, Shreya Maurya, and A. S. Rao

Exploration of Molybdenum Disulfide Nanostructures Through Raman Mode Detection 137
A. P. Sunitha and K. Nayana

Electronic and Optical Properties of Transparent Conducting Perovskite $SrNbO_3$: Ab Initio Study 155
Rakesh Kumar, Patel Maneshwar Rai, Nitesh K. Chourasia, Manish Kumar, Arun Kumar Singh, Aavishkar Katti, and Ritesh Kumar Chourasia

Tribology of Spray Formed Aluminium-Based Materials 173
N. Raja, G. Gautam, S. K. Maurya, A. Sharma, S. Singh, A. K. Singh, and R. Pandey

Enhanced Structural and Optical Properties of Pr^{3+}Substituted Gadolinium Garnet Ferrite for Optical Devices Application 183
Anjori Sharma and Dipesh

Investigation on Structural, Dielectric and Ferromagnetic Properties of Yttrium Doped Nickel Ferrites ($NiY_{0.05}Fe_{1.95}O_4$) Prepared by Modified Sol–gel Route 193
Nisha Yadav, Prachi Jain, and O. P. Thakur

Thermoelectric and Optical Properties of Half–Heusler Compounds RbYX (X = Si, Ge): a First Principle Study 199
Dinesh Kumar and Prakash Chand

Gap Solitons Supported by Cosine Apodized Optical Lattices in Centrosymmetric Photorefractive Crystals 215
Draupath Umesh, Ritesh Kumar Chourasia, and Aavishkar Katti

Characterization of Nanocrystalline ZnS Thin Film on *p*–Si by Chemical Bath Deposition Method 227
Ajeet Gupta, Arun Kumar, Mudit Prakash Srivastava, Vijay Singh Meena, Sandeep Kumar, and Devendra Kumar Rana

Investigation of Dielectric and Electrical Behaviour of $Y_2Ti_2O_7$ Pyrochlore 235
Saurabh Singh, Raghvendra Pandey, Gaurav Gautam, Anjani Kumar Singh, Bheeshma Pratap Singh, Asha Dhaiya, and Prabhakar Singh

Preparation and Structural Investigation of Olivine Structured $LiFePO_4$ 245
Veronica Thongam, Hera Tarique, Radheshyam, and Raghvendra Pandey

$Tm^{3+}/Dy^{3+}/Tb^{3+}$ Doped Barium Zinc Phosphate Glasses for Multicolor Emission 257
Kusum Rawat, Amit K. Vishwakarma, Kaushal Jha, and Vinita Tuli

Structural and Optical Properties of Chalcogenide WS_2 Thin Film 267
Avneesh Kumar, Sandeep Kumar, Mudit Prakash Srivastava, Prachi Yadav, Surbhi, and Devendra Kumar Rana

Investigating Efficiency of Glucose-Derived Graphene Quantum Dots in Photocatalysis 275
Anshu Gangwar and Mohan Singh Mehata

Structural, Electrical and Hydroelectric Cell Investigation in Environment Friendly LSMO:BT Composite 289
Chitralekha, S. Shankar, and Aman Pal Singh

Origin of Gap Solitons in Gaussian Apodized Centro-Symmetrical Non-linear KLTN Lattices 297
Draupath Umesh, Ritesh Kumar Chourasia, Aavishkar Katti, and Bajrang Lal Prashant

About the Editors

Prof. Saluru Baba Krupanidhi is a Materials Scientist who integrates in an exemplary manner fundamental science with engineering of materials and devices. He has worked as Professor at Indian Institute of Science, Bangalore, for more than 22 years. At present, he is serving as Emeritus Professor at IISc. He is internationally recognized in the areas of integrated ferroelectrics and compound semiconductor technology as evidenced by invited lectures at international meetings and memberships of editorial boards. Professor Krupanidhi's research is focused on developing epitaxial thin films of complex oxides for electro-optic, ferroelectric, and high permittivity dielectric applications and heteroepitaxial compound semiconductors for optoelectronic applications. His major contributions in the area of complex perovskites include ECR plasma-assisted development of low-temperature epitaxy, rapid thermal processing, modeling of crystallization in perovskite thin films under strong thermal gradients, and engineered properties in the superlattices of ferroelectric perovskites.

Dr. Anjali Sharma received her B.Sc., M.Sc., and Ph.D. degrees in Physics in the years 2006, 2008, and 2013, respectively, from University of Delhi. At present, she is serving as Assistant Professor at Atma Ram Sanatan Dharma College, University of Delhi. He is also working as Fellow of Institute of Eminence, University of Delhi. Her research interests are in gas sensor systems that include sensor characterization and development of metal oxide films for sensor coatings. She is working toward the fabrication of MEMS-based electronic nose for gas sensing applications. Her area of interest also includes metal oxide-based thermoelectric energy harvesters and fabrication of 2D materials like MoS2 for sensing applications. She has published more than 60 papers in journals of high repute with h-index of 22 and has been granted two Indian patents.

Dr. Anjani Kumar Singh is Assistant Professor in the Department of Physics, Atma Ram Sanatan Dharma College, University of Delhi. He completed his M.Sc. from U P Autonomous College, Varanasi and Ph.D. from Delhi University in the year 2010. He worked as Teaching cum Research Fellow at N.S.I.T., New Delhi.

During his Ph.D. work and afterward, he has published thirty research papers in peer-reviewed international journals and international conferences. He is Life Member of The Materials Research Society of India (MRSI). His major research interests are electrostriction-based dielectric materials and fuel cells and supercapacitors. He has edited a book with Springer Nature.

Prof. Vinita Tuli received her B.Sc., M.Sc., and Ph.D. degrees in Physics in the years 1993, 1995, and 2004, respectively, from University of Delhi. At present, she is serving as a Professor at Atma Ram Sanatan Dharma College, University of Delhi. Her research area is multiferroic material for solar cell. She has published more than 15 research papers in international journals. She has completed two national projects and also actively involved in many students and administrative activities of the institute. Currently she is serving as Co-ordinator of IQAC, ARSD College.

Synthesis and Characterizations of Hexagonal Perovskite-Related Oxide for Solid Electrolyte Application

Paras Saini, Hera Tarique, Hemant Kumar, Anjani Kumar Singh, Raghvendra Pandey, and Prabhakar Singh

1 Introduction

Nowadays, clean energy storing and conversion technologies such as fuel cells, solar cells, super-capacitors, and batteries have emerged as viable options for addressing the world's growing energy needs. While each of these technologies offers unique advantages out of these fuel cells currently being used to generate green and clean energy, which offers promising alternative to traditional power generation [1]. Fuel cells are the devices that convert energy from chemical reactions into electrical energy [1–3]. The fuel cell was first demonstrated by RW Grove in 1838 but it was not commercialized at that time [3–6]. Among various types of fuel cells, SOFCs have gained significant attention due to their ability to function at intermediate to high temperatures, resulting in higher energy conversion efficiency compared to other fuel cell types. This makes them a promising alternative for power generation applications. In Solid oxide fuel cells (SOFCs), as air flows along the cathode, the oxygen molecules acquire electrons and split into oxide ions at the cathode-electrolyte interface [6–9]. Yttrium-stabilized-zirconia (YSZ) is highly effective electrolyte material in SOFCs, however due to its high operating temperature, it faces substantial challenges such as high manufacturing cost, low lifetime, and reduced chemical stability [10–12]. These issues limit the widespread use of SOFCs. Bismuth oxide-based

P. Saini
Department of Physics, Amity Institute of Applied Sciences, Amity University, Noida 201303, India

H. Tarique
Department of Physics, Jamia Millia Islamia (Central University), New Delhi 110025, India

H. Tarique · A. K. Singh · R. Pandey (✉)
Department of Physics, ARSD College, University of Delhi, New Delhi 110021, India
e-mail: raghvendra@arsd.du.ac.in

H. Kumar · P. Singh
Department of Physics, Indian Institute of Technology (BHU) Varanasi, Varanasi 221005, India

S. B. Krupanidhi et al. (eds.), *Recent Advances in Functional Materials and Devices*,
Springer Proceedings in Materials 37, https://doi.org/10.1007/978-981-99-6766-7_1

electrolyte is another option for SOFCs, but it has a limited temperature range of stability, (around 700–820 °C). When the oxygen pressure is low, this electrolyte can be reduced to bismuth metal [10–12]. Efforts are being made to find new electrolyte materials for SOFCs that can reduce operating temperatures, provide longer lifetimes, increase chemical and structural stability, and have lower manufacturing costs. Hexagonal perovskite materials show immense potential as an electrolyte in Intermediate temperature SOFCs [12, 13]. These structures consist of hexagonal AX_3 layers that are closely packed together, or a combination of cubic and hexagonal AX_3 layers in close proximity [14]. Hexagonal perovskites may prove advantageous in creating new ionic conductors for various energy-related technologies. Several crystal structures are associated with hexagonal perovskite oxides. However, it is challenging to find oxide ion conductors that have hexagonal perovskite-like structures. Sacha Fop et al. and M. Yashima et al. have reported hexagonal perovskites with high oxide ion conductivity at intermediate temperatures at broad range of oxygen partial pressure [14–16]. Bezdorozhev et al. have reported the characteristics and phase composition of hexagonal perovskite are influenced by the amount of strontium present [17]. Sakuda et al. have reported the effect of doping Cr^{6+} on conductivity enhancement in $Ba_7Nb_4MoO_{20}$ hexagonal perovskite [18]. The properties of the H-perovskite-based electrolytes $Ba_3NbMoO_{8.5}$ and $Ba_7Nb_4MoO_{20}$ have been reported by Nakayama [19]. Recently, Yasui et al. have published their work on hidden chemical order in $Ba_7Nb_4MoO_{20}$ by using XRD and NMR. [20, 21] Therefore, in worldwide a lot of work is going on this special hexagonal oxide. As for structure concern, $Ba_7Nb_4MoO_{20}$ crystallizes in the three-dimensional trigonal structure having space group $P\bar{3}m1$. The crystal structure $Ba_7Nb_4MoO_{20}$ is shown in Fig. 1. This structure comprises seven inequivalent Ba^{2+} sites in which first and second Ba^{2+} site Ba^{2+} is separately bonded to ten O^{2-} atoms in a 10-coordinate geometry with varying Ba–O bond distances in these two inequivalent sites. In 3rd Ba^{2+} site, Ba^{2+} is bonded to six O^{2-} atoms in a 6-coordinate geometry. There are three shorter and three longer Ba–O bond lengths. Ba^{2+} forms BaO_{12} cuboctahedra at the fourth Ba^{2+} site by bonding with twelve O^{2-} atoms, which share corners with nine other BaO_{12} cuboctahedra, faces with six other BaO_{12} cuboctahedra, and faces with seven NbO_6 octahedra. Ba^{2+} forms BaO_{12} cuboctahedra at the fifth Ba^{2+} site by bonding with twelve O^{2-} atoms, which share corners with nine other BaO_{12} cuboctahedra, faces with six other BaO_{12} cuboctahedra, and faces with seven other NbO_6 octahedra. Ba^{2+} is bound to twelve O^{2-} atoms in the sixth Ba^{2+} site to create the BaO_{12} cuboctahedra, which also include nine equivalent BaO_{12} cuboctahedra, three equivalent MoO_4 tetrahedra, three equivalent BaO_{12} cuboctahedra on their faces, and four equivalent NbO_6 octahedra on their faces. Ba^{2+} forms BaO_{12} cuboctahedra at the seventh Ba^{2+} site by bonding with twelve O^{2-} atoms. These cuboctahedra share faces with four NbO_6 octahedra, three comparable NbO_4 tetrahedra, and corners with nine other cuboctahedra. A detailed crystal structure of $Ba_7Nb_4MoO_{20}$ was reported in the literature [1, 14–20, 22].

In this work, we synthesized the $Ba_7Nb_4MoO_{20}$ (BNMO) hexagonal perovskite by using the solid-state reaction technique and investigated the phase formation of the material via XRD analysis and pattern was indexed with standard ICSD

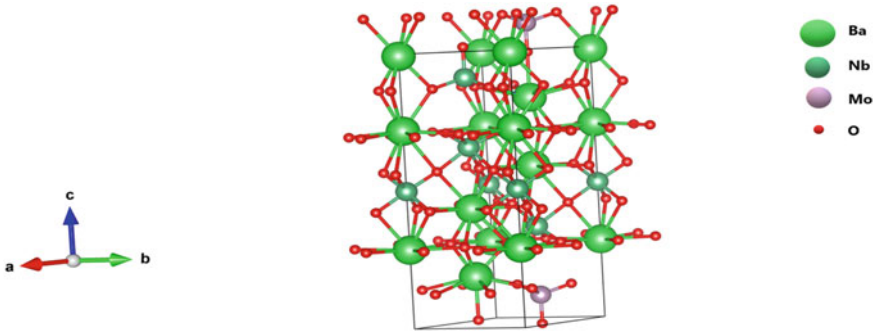

Fig. 1 Crystal structure of $Ba_7Nb_4MoO_{20}$

database. Compositional concentration and its microstructure were examined using SEM–EDX technique. The sample's chemical composition and molecular structure were analyzed and identified through Raman spectroscopy. Additionally, FT-IR was conducted to explore the molecular structure and examine the vibrations and rotations of chemical bonds. The band-gap energy was calculated by Ultraviolet–Visible (UV–Vis) spectroscopy via Tauc's plot. Electrochemical Impedance spectroscopy measurement was carried out in order to check the conductive behavior of the sample.

2 Experimental

2.1 Synthesis

In this paper, we prepared the $Ba_7Nb_4MoO_{20}$ sample by solid-state reaction method. Barium carbonate ($BaCO_3$, 99.99%), Niobium pentoxide (Nb_2O_5, 99.99%), and Molybdenum trioxide (MoO_3, 99.99%) were used as the starting materials [1, 15]. The powders of these materials were mixed in stoichiometric ratio as described below:

$$7(BaCO_3) + 2(Nb_2O_5) + (MoO_3) \rightarrow Ba_7Nb_4MoO_{20} + CO_2 \uparrow \quad (1)$$

The molecular weights of the precursor components are as follows:

$$BaCO_3 - 197.35, Nb_2O_5 - 265.81, \text{ and } MoO_3 - 143.94.$$

It is important to ensure that the stoichiometric ratio of the precursor powders was thoroughly mixed by using an agate mortar and pestle for 2 h, and ball milled for 2 h in order to obtain a homogeneous mixture. The precursor sample powder is then calcined in a muffle furnace, maintaining the heating rate of 5°/min, at a

temperature of 1050 °C for 48 h in static air [1]. The calcined sample was then ground thoroughly for 2 h using an agate-mortar and pestle. And hence obtained calcined sample was pelletized by using hydraulic press. The average thickness and diameter of the samples were 1.89 mm and 9.49 mm, respectively. The pelletized samples were sintered in a furnace, maintaining a heating rate of 5°/min, at 1200 °C for 5 h [1]. Then, further characterizations were done from the calcined powders and sintered pellets of the sample.

2.2 Characterizations

2.2.1 XRD Analysis

The XRD study has been performed to evaluate phase purity and stability of the samples by using Rigaku Miniflex desktop diffractometer at room temperature. While XRD analysis the Cu-Kα_1 radiation was used, and the resulting XRD patterns were collected with a step size of 0.02° in the range of 20°–80°, using a wavelength (λ) of 1.5415 Å [16, 20, 21].

2.2.2 SEM-EDX Analysis

The Scanning Electron Microscope (SEM) micrograph was recorded at room temperature for the surfaces of BNMO (JEOL Japan SEM, JSM 6610LV) and the image was taken at resolution of 2 μm.

2.2.3 RAMAN Analysis

The sample's chemical composition and molecular structure were analyzed and identified through Renishaw Invia II Raman microscopy at room temperature in the range of 200–1000 cm^{-1}.

2.2.4 FTIR analysis

FT-IR analysis was conducted at room temperature to explore the molecular structure and to examine the vibrations and rotations of chemical bonds by using Nicolet iS50 FTIR Tri-detector. The spectra of the sample were obtained in the range of 400–4000 cm^{-1}.

2.2.5 UV-Vis's Spectroscopy Analysis

UV–Vis's spectroscopy analysis of the sample was conducted by using JASCO V 670 Spectrometer. The spectrum was recorded in absorption mode within the wavelength range of 200–2000 nm (with 400 nm/min scan speed). Data from the absorbance spectra were used to determine the sample's band gap energy.

2.2.6 Impedance Spectroscopy Analysis

Electrical impedance spectroscopy for the synthesized system was carried out in the temperature range of 573–923 K using 6500 P Wayne Kerr Impedance analyzer. The pellets were coated with a layer of Platinum paint and dried for 30 min in a muffle furnace at 1000 ˚C. The measurements were then performed within the frequency range 20 Hz to 1 MHz and temperature range of 573–923 K with an interval of 50 K.

3 Results and Discussion

3.1 XRD Study

In order to determine the physical properties of the calcined sample for the composition, X-ray diffraction (XRD) was conducted (by using Rigaku Miniflex desktop) at room temperature. [6] While XRD analysis the Cu-Kα_1 radiation was used, and the resulting XRD patterns were collected with a step size of 0.02° in the range of 20°–80°, using a wavelength (λ) of 1.5415 Å [16, 20, 21]. The XRD pattern of the $Ba_7Nb_4MoO_{20}$ sample is shown in Fig. 2 and unit cell parameters are given in Table 1. The obtained diffractogram was analyzed to confirm that the samples whether in a pure phase or not, and their compositions were identified with the space group $P\bar{3}m1$ [1, 15]. Crystal structure of the composition has 7H polytype hexagonal phase. The peaks observed are very sharp in all samples of XRD pattern which suggests that the samples prepared are highly crystalline. The peaks with maximum intensity are observed at 27.91° and 30.61°. A few minor peaks marked as * are also observed revealing some impurity phases (Such as $Ba_5Nb_4O_{15}$) present in the sample.

3.2 SEM and EDAX Analysis

The Scanning Electron Microscope (SEM) micrograph was recorded at room temperature for the surfaces of BNMO (JEOL Japan SEM, JSM 6610LV). Before the SEM investigations, the pellets were coated with a gold Palladium alloy to prevent charging of the surface (This coating provides a uniform surface of the pellets for analysis and

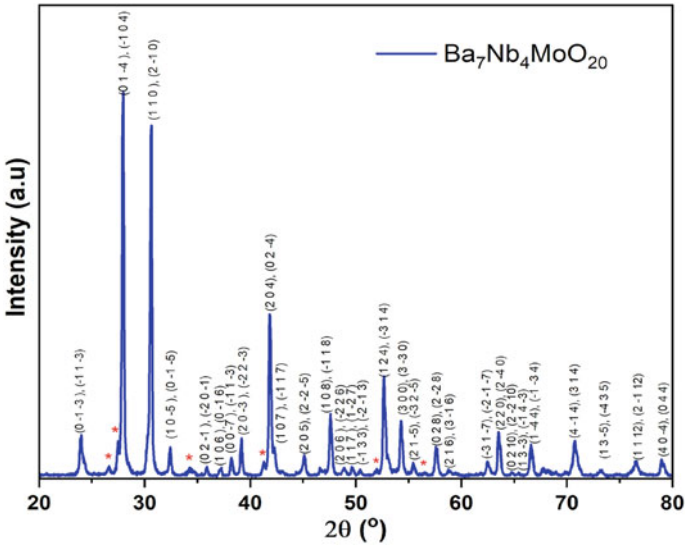

Fig. 2 XRD pattern of calcined BNMO sample at room temperature

Table 1 The unit cell parameters with space group *P* $\underline{3}$ *m1*

a	B	c	α	β	γ
5.8644 Å	5.8644 Å	16.52719 Å	90°	90°	120°

helps to increase the secondary electron emission). Figure 3 shows the SEM image of the surface of dense $Ba_7Nb_4MoO_{20}$ pellet sample.

From the SEM micrographs, it is observed that primary phase formation has taken place. The grains show cored morphology with good contact, which implies that the pellet is dense. The typical grain size of the sample was measured using Image-J software [6]. The results show that the average grain size for $Ba_7Nb_4MoO_{20}$ ranges from 0.4 to 3.0 μm. Archimedes' density of the composition was found to be around 95% to theoretical one.

To verify the presence of all constituent elements in the sample of $Ba_7Nb_4MoO_{20}$, we conducted an EDS mapping of a dense sample surface (Fig. 4). The resulting EDS analysis data is presented in Table 2, which shows the atomic% and weight% of elements present in the composition for the $Ba_7Nb_4MoO_{20}$ sample. 5–10% variation was seen in the theoretical and experimental data of elemental concentration.

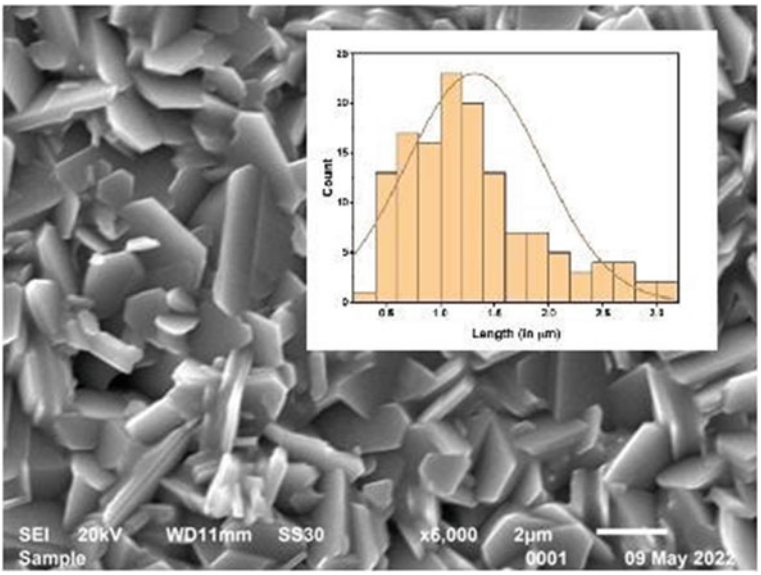

Fig. 3 The SEM micrographs of the surface of the dense $Ba_7Nb_4MoO_{20}$ sample at 2 µm scale

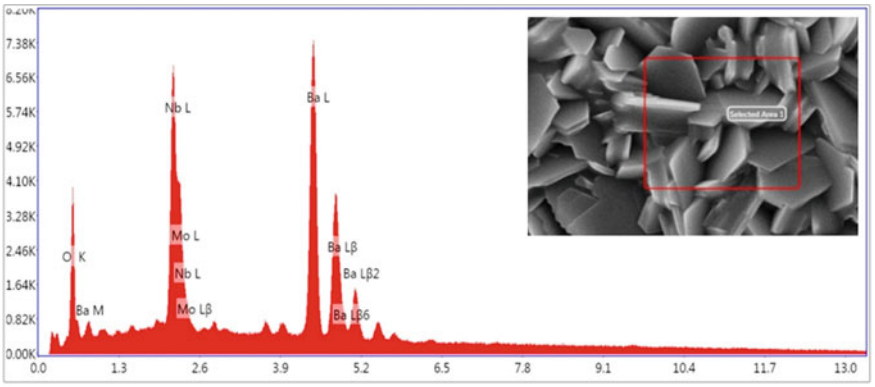

Fig. 4 EDS scan for the BNMO sample

Table 2 EDS analysis summary of BNMO sample

Elements	Theoretical atomic %	Atomic %	Weight %
Ba	21.875	28.430	59.450
Nb	12.500	15.340	21.700
Mo	3.125	4.230	6.180
O	62.500	51.990	12.660

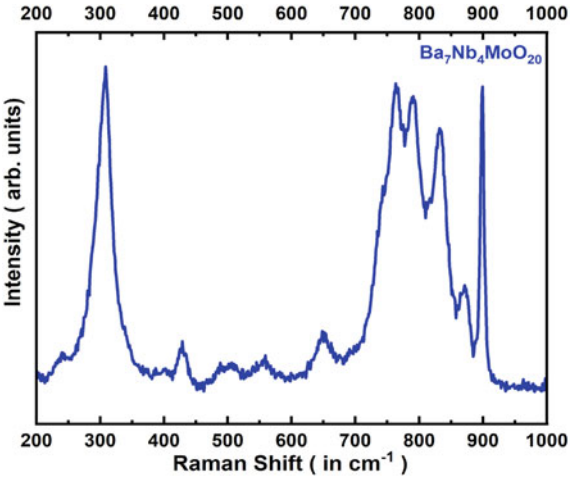

Fig. 5 Raman spectra of BNMO sample at room temperature

3.3 Raman Analysis

The Raman scattering spectra of the $Ba_7Nb_4MoO_{20}$ sample were obtained at room temperature in the range of 200–1000 cm^{-1}, as shown in Fig. 5. $Ba_7Nb_4MoO_{20}$ sample belongs to the D_{3_d} crystallographic point group with a $P\bar{3}m1$ space group [23]. The intense peak is observed at 300 cm^{-1}. Observations from the Raman spectra indicate that Mo exhibits a tetrahedral $[MoO_4]^{2-}$ mode at around 900 cm^{-1} [23].

The low-intensity peaks between 400 and 700 cm^{-1} at 420, 500, 550, and 650 cm^{-1} provide evidence for octahedrally coordinated Nb or Mo sites [19]. The modes between 400 and 700 cm^{-1} are attributed to NbO_6 or MoO_6 in several different compounds. The peak splitting occurs at 750 to 900 cm^{-1} because the stretching vibration mode has various frequencies. Two bands at approximately 300 and 800 cm^{-1} correspond to $[NbO_4]$ or $[MoO_4]$ tetrahedral groups [23]. Minor changes in the spectra could be attributed to the unique structural properties of various compounds, such as the presence of face-sharing octahedra in the structure.

3.4 FTIR Analysis

FTIR spectra of the $Ba_7Nb_4MoO_{20}$ was (Nicolet iS50 FTIR Tri-detector) obtained in the range of 400–4000 cm^{-1} at room temperature as shown in Fig. 6. In IR plot analysis, the peak near 820 cm^{-1} is attributed to the [Mo–O] stretching vibration mode of the tetrahedral group of $[MoO_4]^{2-}$ [24]. In the range of 440–460 cm^{-1}, weak infrared absorption bands are observed, this can be caused by vibration modes associated to bending in the medium frequency range [24].

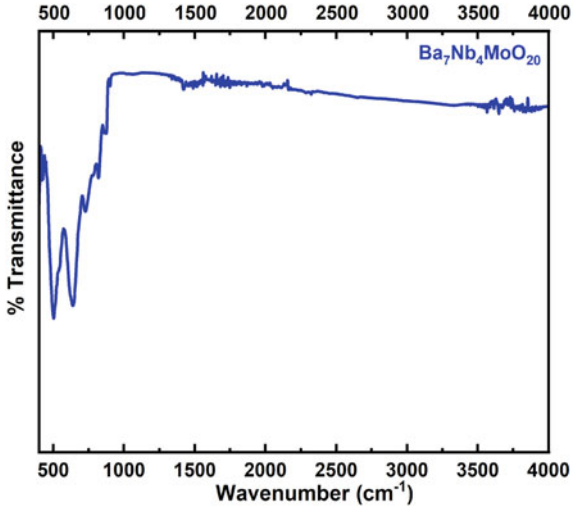

Fig. 6 FT-IR spectra of $Ba_7Nb_4MoO_{20}$ sample is obtained at room temperature

3.5 UV–Vis' Spectroscopy Analysis

In Fig. 7a UV–visible spectra of the sample $Ba_7Nb_4MoO_{20}$ is plotted. The spectrum was recorded between 200 and 2000 nm wavelength range. Data from the absorbance spectra were used to determine the sample's band gap energy. Tauc's plot for BNMO sample is shown in Fig. 7b. The Tauc's equation was used to calculate the value of Band gap [25, 26]. The Tauc's equation is:

$$\alpha hv = A\left(hv - E_g\right)^n \tag{2}$$

In order to calculate the optical band-gap energy of the $Ba_7Nb_4MoO_{20}$ sample, a plot of "$(\alpha hv)^{\frac{1}{n}} Vshv$" was formed using the above relation, "A" is a constant that is independent of energy, "α" is the incident light's absorption coefficient and "hv" represents the energy of the light. Depending on the kind of electron transition, the value of "n" is assumed to be either 2 or 1/2 for indirect or direct inter-band transitions respectively. The linear portion of the plot was extrapolated to zero, and the resulting value for the energy band gap was determined to be 3.3870 eV. In contrast, the $Ba_7Nb_4MoO_{20}$ sample from the Materials Project website exhibits an energy band gap of 2.64 eV [28]. A little bit higher energy gap was obtained for the investigated sample possibly due to the presence of some impurity phases in the sample.

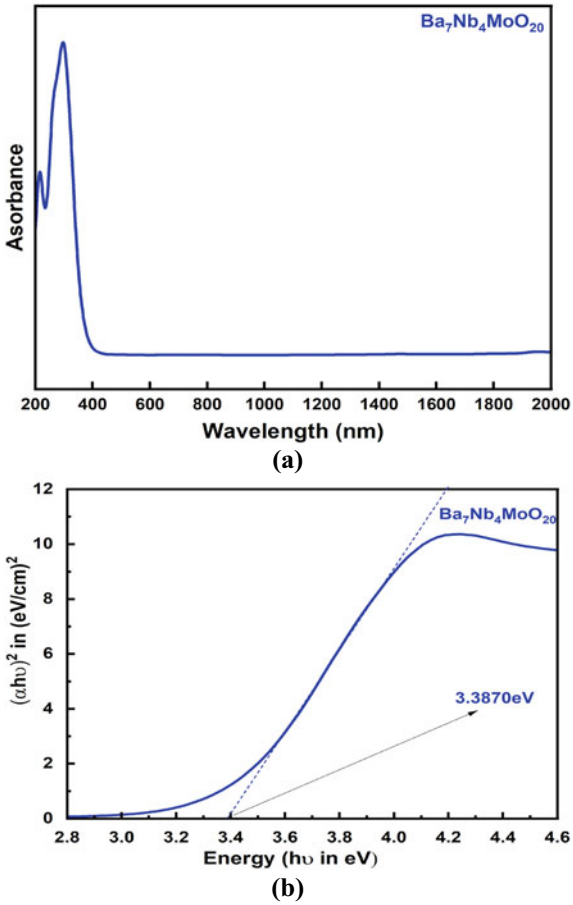

Fig. 7 **a** UV–Visible spectra of the sample BNMO and **b** Energy band gap was determined by Tauc's plot of BNMO sample

3.6 Impedance Spectroscopy Analysis

Electrical spectroscopy for the synthesized system was carried out in the temperature range of 573–923 K using 6500 P Wayne Kerr Impedance analyzer. Figure 8a shows the Arrhenius plot for the BNMO sample. The conductivity values at different temperature were calculated using $\sigma = \frac{L}{RA}$ relation where "σ" is the conductivity and "R" is the resistance, "A" is the area and "L" denotes the length. The resistance "R" is calculated using the fitted Cole–Cole plot [1, 15, 27].

From plot (a), it has been found that as the temperature rises, the conductivity of the sample increases, which may be explained by an increase in charge carrier concentration. The values of conductivity exhibited by the sample at different intermediate temperature ranges are shown in Table 3. The Arrhenius graphic clearly shows that conductivity is significantly influenced by temperature. At 510 °C, the BNMO sample's conductivity was found to be 3.54 $mScm^{-1}$. Putting this beside the

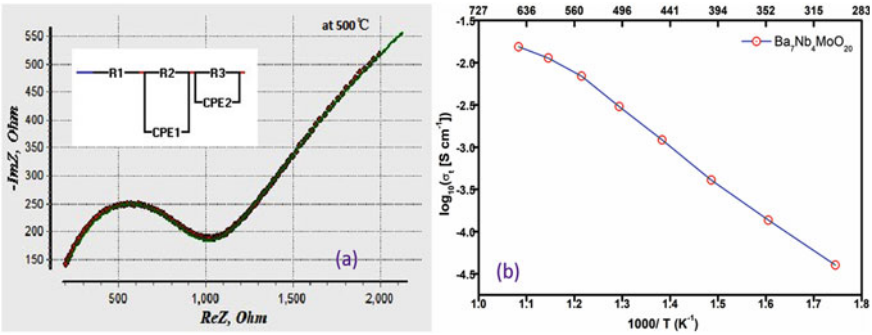

Fig. 8 **a** Representative complex impedance spectra of the BNMO sample at 500 °C. **b** Arrhenius plot for the BNMO sample

conductivity reading provided by Sacha Fop et al., which is approximately equivalent to 4.0 $mScm^{-1}$ [1, 16]. The maximum conductivity for the BNMO sample comes out to be at 650 ˚C with a value of 0.01547 Scm^{-1}. This value of electrical conductivity can be considered decent for electrolytes of intermediate temperature solid oxide fuel cells and for the other electrochemical devices.

4 Conclusions

In this investigation, $Ba_7Nb_4MoO_{20}$ sample was prepared via solid-state reaction method. The prepared sample's XRD patterns are indexed with the MATCH program. The obtained diffractograms identify the structure of the sample belonging to the space group $P\bar{3}m1$. By using SEM technique, it is observed that highly dense sample formation has taken place. To analyze the phase formation, FT-IR analysis was performed, and it additionally verified the hexagonal structure. UV–visible spectra wavelengths were obtained for $Ba_7Nb_4MoO_{20}$ in the range of 200–2000 nm. UV–visible method was used to calculate the optical band-gap energy, and the result was 3.3870 eV. Electrical conductivity of $Ba_7Nb_4MoO_{20}$ sample was measured by using impedance spectroscopy. The Arrhenius plot clearly shows that conductivity is significantly influenced by temperature. The maximum conductivity for the $Ba_7Nb_4MoO_{20}$ sample was found to be 0.0154 $S.cm^{-1}$ at 650 °C. Based on the investigation, it can be concluded that the hexagonal perovskite-based $Ba_7Nb_4MoO_{20}$ system may be considered as a potential candidate solid electrolyte for electrochemical devices such as SOFCs.

Table 3 Electrical conductivity variation of BNMO sample with temperature

Compound	Conductivity (Scm^{-1})							
	300 °C	350 °C	400 °C	450 °C	500 °C	550 °C	600 °C	650 °C
$Ba_7Nb_4MoO_{20}$ (BNMO)	4.01052×10^{-5}	1.367×10^{-4}	4.0794×10^{-4}	1.219×10^{-3}	3.0223×10^{-3}	7.044×10^{-3}	1.1135×10^{-2}	1.547×10^{-2}

Acknowledgements Authors acknowledge the support of USIC, and DU for providing the experimental facilities. Authors are also appreciative to SERB for providing the funding support through the ECR project [ECR/2016/001152].

References

1. O'Hayre R, Cha SW, Colella W, Prinz FB (2016) Fuel cell fundamentals. Wiley. https://doi.org/10.1002/9781119191766
2. Dicks AL, Rand DAJ (2018) Fuel cell systems explained. Wiley. https://doi.org/10.1002/9781118706992
3. Barbir F (2013) PEM fuel cells. Theory and practice. Academic Press
4. Grove WRXXIV (1839) On voltaic series and the combination of gases by platinum. London Edinburgh Dublin Philos Mag J Sci 14(86–87):127–130. https://doi.org/10.1080/14786443908649684
5. Tarique H, Shahid R, Singh P et al (2022) Effect of potassium substitution at Sr-site on the structural, morphological and electrical properties in Sr3 − 3x K3x Si3O9 ($0.0 \leq x \leq 0.2$) trimer strontium meta-silicate. J Mater Sci: Mater Electron 33:14961–14971. https://doi.org/10.1007/s10854-022-08413-47
6. Saravanan R (2018) Solid oxide fuel cell (SOFC) materials. Mater Res Found 23:182. https://doi.org/10.21741/9781945291517
7. Ormerod RM (2003) Solid oxide fuel cells. Chem Soc Rev 32(1):17–28. https://doi.org/10.1039/b105764m
8. Singhal S (2000) Advances in solid oxide fuel cell technology. Solid State Ionics 135(1–4):305–313. https://doi.org/10.1016/S0167-2738(00)00452-5
9. Kilner JA, Burriel M (2014) Materials for intermediate-temperature solid-oxide fuel cells. Annu Rev Mater Res 44(1):365–393. https://doi.org/10.1146/annurev-matsci-070813-113426
10. Hussain S, Yangping L (2020) Review of solid oxide fuel cell materials: cathode, anode, and electrolyte. Energy Transitions 4(2):113–126. https://doi.org/10.1007/s41825-020-00029-8
11. Minh NQ (1993) Ceramic fuel-cells. J Am Ceram Soc 76(3):563–588. https://doi.org/10.1111/j.1151-2916.1993.tb03645.x
12. Skinner SJ (2001) Recent advances in Perovskite-type materials for solid oxide fuel cell cathodes. Int J Inorg Mater 3(2):113–121. https://doi.org/10.1016/S1466-6049(01)00004-6
13. Fop S, McCombie KS, Wildman EJ et al (2020) High oxide ion and proton conductivity in a disordered hexagonal perovskite. Nat Mater 19(7):752–757. https://doi.org/10.1038/s41563-020-0629-4
14. Fop S, McCombie KS, Wildman EJ, Skakle JMS, Mclaughlin AC (2019) Hexagonal perovskite derivatives: a new direction in the design of oxide ion conducting materials. Chem Commun 55(15):2127–2137. https://doi.org/10.1039/C8CC09534E
15. Yashima M, Tsujiguchi T, Sakuda Y, et al (2021) High oxide-ion conductivity through the interstitial oxygen site in Ba7Nb4MoO20-based hexagonal perovskite related oxides. Nat Commun 12(1). https://doi.org/10.1038/s41467-020-20859-w
16. Coduri M, Karlsson M, Malavasi L (2022) Structure-property correlation in oxide-ion and proton conductors for clean energy applications: recent experimental and computational advancements. J Mater Chem A Mater 10(10):5052–5110. https://doi.org/10.1039/d1ta10326a
17. Bezdorozhev O, Solodkyi I, Ostroverkh A, Morozov I, Ostroverkh Y, Solonin Y (2022) Synthesis and characterization of (Ba1-xSrx)7Nb4MoO20 powders for proton-conducting solid oxide fuel cells. Ukr Chem J 88(4):63–78. https://doi.org/10.33609/2708-129x.88.04.2022.63-78
18. Sakuda Y, Hester JR, Yashima M Improved oxide-ion and lower proton conduction of hexagonal perovskite-related oxides based on Ba 7 Nb 4 MoO 20 by Cr 6+ doping. https://doi.org/10.2109/jcersj2

19. Nakayama S (2022) Characteristics of electrolyte-supported SOFC single cells using hexagonal perovskite Ba3MoNbO8.5 and Ba7Nb4MoO20 ceramics. Results in Mater 16. https://doi.org/10.1016/j.rinma.2022.100318
20. Yasui Y, Tansho M, Fujii K et al (2023) Hidden chemical order in disordered Ba7Nb4MoO20 revealed by resonant X-ray diffraction and solid-state NMR. Nat Commun 14(1):2337. https://doi.org/10.1038/s41467-023-37802-4
21. Chauhan A (2014) Powder XRD technique and its applications in science and technology. J Anal Bioanal Tech 5(6). https://doi.org/10.4172/2155-9872.1000212
22. Kumar A, Sharma SK, Grover V, Singh Y, Kumar V, Shukla VK, Kulriya PK (2022) Probing the short-range ordering of ion irradiated Gd2Ti2-yZryO7 ($0.0 \leq y \leq 2.0$) pyrochlore under electronic stopping regime. J Nucl Mater 564:153682. https://doi.org/10.1016/j.jnucmat.2022.153682
23. Brown Holden AA, Reedyk M, García-González E, Parras M, González-Calbet JM (2000) Raman scattering study of cation-deficient Ba(n)(MoNb)(n-δ)O(3n–x) and related perovskite-like oxides. Chem Mater 12(8):2287–2291. https://doi.org/10.1021/cm000037i
24. Jena P, Nallamuthu N, Hari Prasad K, Venkateswarlu M, Satyanarayana N (2014) Structural characterization and electrical conductivity studies of BaMoO4 nanofibers prepared by sol–gel and electrospinning techniques. J Sol-Gel Sci Technol 72(3):480–489. https://doi.org/10.1007/s10971-014-3460-z
25. García-González E, Parras M, González-Calbet JM (1999) Crystal structure of an unusual polytype: 7H-Ba7Nb4MoO20. Chem Mater 11(2):433–437. https://doi.org/10.1021/cm981011i
26. Redinger A, Siebentritt S (2015) Loss mechanisms in Kesterite solar cells. In Copper zinc tin sulfide-based thin-film solar cells. Wiley :363–386. https://doi.org/10.1002/9781118437865.ch16
27. Lvovich VF (2012) Impedance spectroscopy. Wiley. https://doi.org/10.1002/9781118164075
28. Materials Data on Ba7Nb4MoO20 by Materials Project. https://doi.org/10.17188/1704365

Evidence of Ferromagnetic Short-Range Correlations in Sol–gel Synthesized $La_{1.88}$ $Sr_{0.12}CoMnO_6$ Nanoparticles

Swati Jharwal and Arvind Kumar

1 Introduction

Oxide-based double perovskite compounds with crystal formula, $A_2BB'O_6$ have attracted the attention of researchers in the last two decades due to multifunctional properties exhibited by these compounds [1]. Double perovskite compounds were found to display interesting magnetic properties such as near room temperature ferromagnetism, colossal magneto-resistance, magneto-dielectric, etc., which have potential applications for the spintronic devices [2]. In comparison to oxide-based single perovskites of ABO_3 type, the double perovskites have another element at B-site (B′) [3]. This structural modification, i.e., different orders of ions at B-site produce multiple exchange interactions resulting from different oxidation states of B-site ions exhibited in different crystal symmetry and lattice distortions give rise to many of the functional properties for the compound [4, 5]. In the recent past lead-free inorganic perovskite structures are widely studied due to the need of clean and green technological advancements [3–9].

Among the various studied double perovskite materials, La-based double perovskites La_2CoMnO_6 (LCMO) and La_2NiMnO_6 (LNMO) are widely studied by researchers due to the magnetodielectric, magnetoresistance, and magnetocapacitance properties for possible application in spintronic devices [6]. They exhibit interesting magnetic properties owing to their multiple oxidation state in B/Mn ordering [7]. LNMO is a ferromagnetic semiconductor with paramagnetic to ferromagnetic transition near room temperature ~275 K [8]. La_2CoMnO_6 (LCMO) is known to be a ferromagnetic insulator which in its ordered state shows a ferromagnetic transition

S. Jharwal · A. Kumar (✉)
Materials Science Research Lab (Theory and Experimental, Department of Physics, ARSD College, University of Delhi, New Delhi 110021, India
e-mail: bhuarvind2512@gmail.com; arvindkumar@arsd.du.ac.in; arvind@jnu.ac.in

A. Kumar
School of Physical Sciences, Jawaharlal Nehru University, New Delhi 110067, India

S. B. Krupanidhi et al. (eds.), *Recent Advances in Functional Materials and Devices*, Springer Proceedings in Materials 37, https://doi.org/10.1007/978-981-99-6766-7_2

about 240 K due to the super-exchange interaction of Co^{2+}–O^{2-}–Mn^{4+} ions where Mn appears in its high spin state [9]. In its disordered state Co and Mn also appear in +3 charge state due to which the ferromagnetic transition is around 150 K [9]. When the A site of the compound $A_2BB'O_6$ is doped with holes, i.e., when Sr^{2+} replaces La^{3+} in LCMO, it is interesting to study the effect of anti-site disorder created in an otherwise ordered perovskite on the magnetic properties of the system [10]. In addition to the chemical disorder created by the doping, the manganite's structural disorder is also there because of Jahn Teller distortions and octahedral tilt [11]. Due to structural distortion, the interaction among the magnetic ions (B-Site ion) at the centre of the octahedra is also affected because the distortion of the structure leads to a change in the degree of overlap of the t_{2g} and e_g orbitals of the transition metal ion. As a result of which the occupying electrons take the type of magnetic configuration which saves maximum energy [12]. The exhibited magnetic properties as a result of interplay of structural and chemical disorder are worth studying. Aga Shahee et al has reported the existence of ferromagnetic correlations above the anti-ferromagnetic ordering temperatures at ~368 K for cubic perovskite manganite's [11]. Such ferromagnetic correlations are important from the point of view of application in the field of spintronics.

In this paper we have studied the magnetic interactions in LCMO and Sr doped LCMO nanoparticles synthesized by sol–gel method through temperature-dependent magnetization study and have observed the ferromagnetic short-range correlations in LSCMO nanoparticles formed in rhombohedral phase.

2 Experimental Details

2.1 Synthesis Details

Pure, La_2CoMnO_6 (LCMO) and Sr doped $La_{2-x}Sr_xCoMnO_6$ (LSCMO: x = 0.12) nanoparticles were synthesized by the sol–gel method. In the preparation of nanoparticles, nitrate precursors $La(NO_3)_3 \cdot Co(NO_3)_2 \cdot 6H_2O$, $Sr(NO_3)_2$ and $Mn(NO_3)_2$ were taken in stoichiometric ratio and dissolved in 100 ml of deionized water. Citric acid was added in the solution as the capping agent. The solution was further stirred continuously on a magnetic stirrer by maintaining a constant temperature of 70 °C till a viscous gel is obtained. The obtained gel was dried in a hot air oven at 150 °C for about 6 h to obtain a dry fluffy powder. The powder was ground in an agate mortar to obtain a very fine powder. This powder was kept for calcination in a muffle furnace at 600 °C for 4 h. The obtained black powder was ground and collected for further investigation of the physical properties via different experimental techniques. Figure 1 shows schematically the different steps in the synthesis of Sr doped LCMO nanoparticles by sol–gel method. The corresponding chemical reaction is as follows;

$$2La(NO_3)_3 + Co(NO_3)_2.6H_2O + Mn(NO_3)_2 + xSr(NO_3)_2 + \text{citric acid}$$

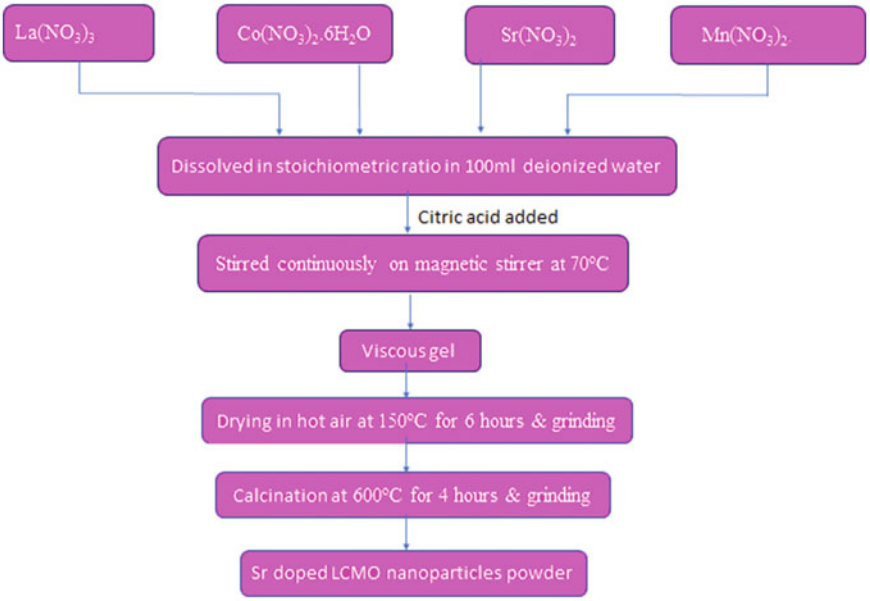

Fig. 1 Schematic representation of steps of synthesis by sol–gel method to prepare LCMO and LSCMO nanoparticles

$$La_{2-x}Sr_xCoMnO_6 + \text{gaseous products} \quad (1)$$

2.2 Characterization Techniques

X-ray diffraction spectra was recorded from Bruker D8 X-ray diffractometer using Cu-Kα source ($\lambda = 1.54060$ Å) to analyze the structural properties of the prepared nanoparticles of LCMO and LSCMO. To study the structural phase formation and bonding nature, Fourier transform infrared (FTIR) with attenuated total reflectance (ATR-FTIR, Bruker Tech.) and Raman spectroscopy were used. Raman Spectra was recorded with an excitation source of wavelength 514 nm of air-cooled Argon ion laser. Laser power at the sample was ~4 mW and typical spectral acquisition time was ~50 s with the spectral resolution of 1 cm^{-1}. To investigate the detailed magnetic properties, M–H curve at different temperature was recorded using the Quantum Design SQUID-VSM (VSM, Versa Lab) from 60 to 300 K.

3 Results and Discussion

3.1 Structural Study and Strain Calculation

Figure 2 shows the XRD pattern of LCMO and LSCMO nanoparticles. The peaks of XRD are indexed (JCPDS file no #53–1211) with proper (hkl) planes and confirm the formation of the desired nanoparticles. The peak positions in XRD pattern of LSCMO nanoparticles are slightly shifted toward the higher angle side compared to peak positions of LCMO nanoparticles. From Table 1 we can observe widening and shifting of the diffraction peaks with Sr doping indicating the replacement of the La ions with Sr ions in the LCMO host lattice. The crystallite size has also been estimated from Scherrer formula [13] and found to be in the range of 6–18 nm as tabulated in Table 1. It has also been observed that along with the widening and shifting of the diffraction peaks the synthesized materials are within the nanometer range. XRD pattern of the LSCMO shows that the full width at half-maximum (FWHM) of most of the peaks increases with a doping percentage of Sr which can be attributed to a decrease in crystallite size (Table 3).

To collect more information regarding the structural phase formed and other lattice parameters, the Rietveld refinement of X-ray diffraction pattern using FullProf software was carried out. Figure 3 shows the Rietveld refinement plots of LCMO and LSCMO nanoparticles. For the refinement procedure, initial input parameters (such as unit cell lattice parameters, space group and atom coordinates) are taken from matching reference patterns [14]. The pseudo-voigt function has been chosen in the present study for peak shapes in the refinement purpose. It has been found from Fig. 3 that observed and calculated patterns are in good agreement to each other. The X-ray diffraction pattern after refinement corresponds to rhombohedral structure (space group R3c (161)). Table 2 lists the Wycoff positions, lattice parameters and bond distances obtained from refinement. The value of parameters for LSCMO

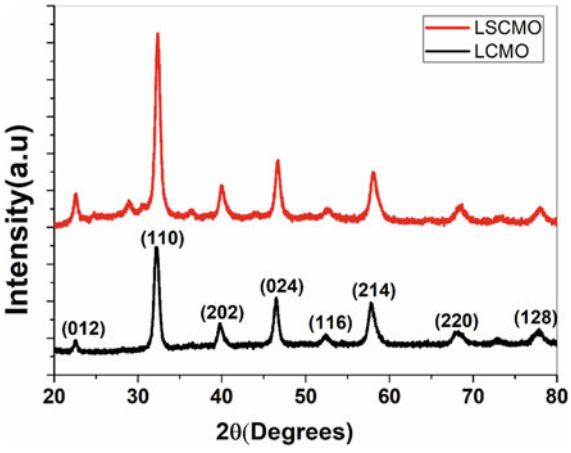

Fig. 2 X-ray diffraction pattern of the synthesized LCMO and LSCMO for nanoparticles

Table 1 Comparison of 2θ position and FWHM values of XRD peaks of XRD of LCMO and LSCMO nanoparticles

2θ positions of XRD peaks		FWHM (degrees)		Crystallite size (Scherrer formula)	
LCMO	LSCMO	LCMO	LSCMO	LCMO	LSCMO
22.54	22.57	0.46	0.50	17.66	16.13
32.23	32.36	0.73	0.76	11.30	10.89
39.84	40.04	0.75	0.79	11.18	10.73
46.49	46.68	0.71	0.73	12.08	11.81
57.90	58.15	1.07	1.10	8.51	8.24
68.18	68.42	1.50	1.24	6.39	7.73
77.77	77.93	1.26	1.06	8.09	9.67

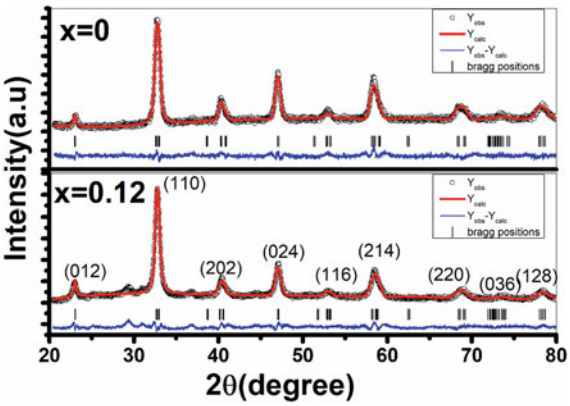

Fig. 3 Rietveld refinement of X-ray diffraction pattern of pure and Sr doped La_2CoMnO_6 nanoparticles. Observed (black dots), calculated (red solid line), and difference (blue line at the bottom) profiles. The black tick marks indicate the positions of the allowed Bragg reflections

varies slightly from LCMO which could be attributed to different ionic radii of Sr (1.13 Å) and La (1.06 Å) [14].

Induced strain (ε) in the prepared LCMO and LSCMO nanoparticles due to some distortions is estimated by plotting Williamson–Hall (W–H) plots as shown in Fig. 4a, b. The values of estimated crystallite size and strain are tabulated in Table 3. The crystallite size obtained from W–H plots is larger compared to values obtained by Debye Scherrer formula as the effect of broadening of peaks due to strain is not considered in it. It has been observed that the value of estimated strain in LSCMO sample is less as compared to the pure LCMO sample and the difference in the crystallite size measurement from Debye Scherrer formula and W–H plots is smaller in this case.

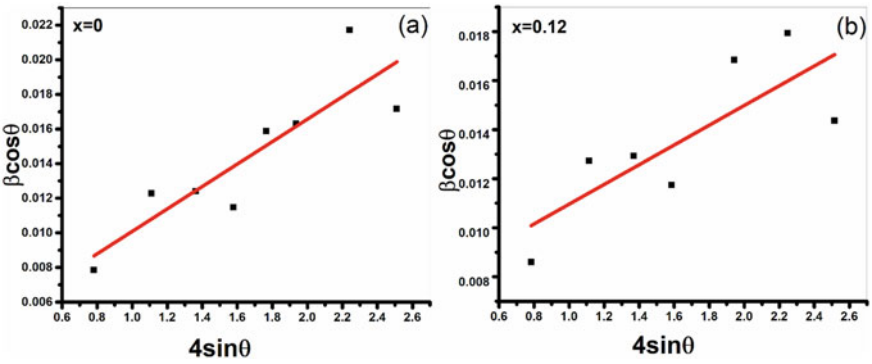

Fig. 4 **a**, **b** Williamson Hall (W–H) plots for the pure and Sr doped LCMO nanoparticles

Table 2 Structural parameters obtained from Rietveld analysis of LCMO and LSCMO nanoparticles

Parameters	x = 0	x = 0.12
Atomic positions	La:6a(0,0,0.250)	La:6a(0,0, 0.24961)
	Co/Mn:6a(0,0,0)	Co/Mn:6a(0,0, 0.0147)
	O:18b(0.457,0,0.252)	O:18b(0.5405,0,0.741)
Lattice parameters		
a	5.48 Å	5.44
b	5.48 Å	5.44
c	13.25 Å	13.47
d_{110}	2.74Å	2.72
La/Sr–O(Å)	2.73	2.73
Co/Mn–O(Å)	1.94	1.96
$\chi 2$	1.7	3.12

Table 3 Crystallite size and strain obtained from W–H plots for LCMO and Sr doped LCMO compound

Doping concentration (x)	Crystallite size (nm) (By Scherrer formula)	Crystallite size(nm) (W–H Plots)	Strain (calculated from W–H plots)
0	11.30	38.4	6.48×10^{-3}
0.12	10.89	19.97	4.02×10^{-3}

3.2 FTIR Spectroscopy Analysis

FTIR spectra of the material give insights about the attached functional groups and impurities present [15]. Figure 5 shows the absorbance spectra obtained for LCMO

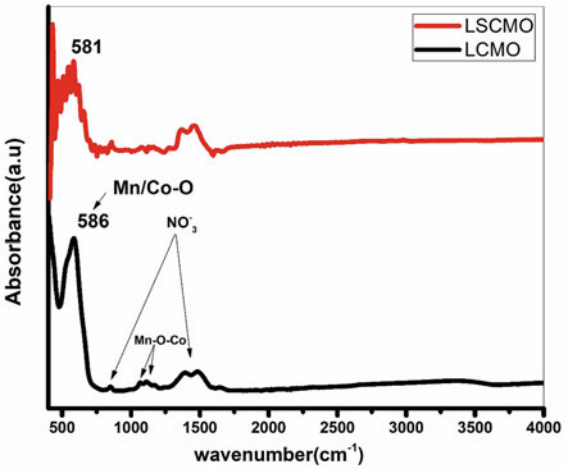

Fig. 5 FTIR spectra of LCMO and LSCMO nanoparticles in absorbance mode

and LSCMO nanoparticles in the wavenumber range of 400–4000 cm^{-1} recorded at room temperature (RT) [16]. A strong band at 586 cm^{-1} for the LCMO nanoparticles is obtained which is due to Co–O/Mn–O vibrations in LCMO nanoparticles. Some weak bands are also obtained around 1073 cm^{-1} and 1145 cm^{-1} which could be due to Mn–O–Co vibration in MnO_6 octahedra. Weak bands are also obtained at 1393 cm^{-1} and about 855 cm^{-1} which corresponds to vibration of nitrate ions [17]. The bands obtained at 1483 cm^{-1} could be due to vibration of N–O from the nitrate precursors taken [18]. In the LSCMO nanoparticles a strong band is observed at 581 cm^{-1}, i.e., the bands are shifted to lower wave number side with the doping of Sr in the LCMO lattice.

3.3 Raman Spectroscopy Study

Raman spectra of the material is an efficient way of detecting the phases present. The peaks in the spectrum at different wavelengths are corresponding to specific vibration of molecular bonds and lattices [15]. In double perovskite compounds ($A_2BB'O_6$) structure, the vibrational modes are due to BO_6 and $B'O_6$ octahedra and A-O bonds [19]. Figure 6 shows the Raman spectra of LCMO and LSCMO nanoparticles recorded at RT at an excitation wavelength of 514 nm. The spectra show a peak at ~662 cm^{-1} for LCMO and with a slight shifting in case of LSCMO which is due to the incorporation of Sr^{+2} ions in host LCMO. The observed peak in the spectra is due to A_{1g} symmetric stretching vibration mode of oxygen octahedra around cations [20, 21].

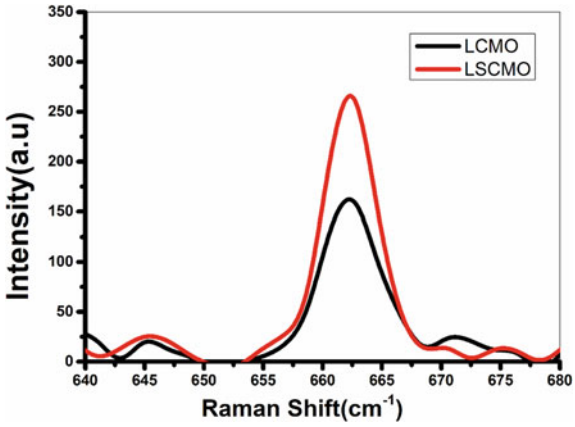

Fig. 6 Raman spectra of LCMO and LSCMO nanoparticles

3.4 Magnetic Measurements

Figure 7 plots magnetization as a function of magnetic field for LCMO and LSCMO nanoparticles at RT by varying magnetic field from −30,000 Oe to +30,000 Oe. The inset of Fig. 7 shows the M-H curve in low magnetic field region from −2700 Oe to +2700 Oe. The nature of M-H curves of LCMO and LSCMO nanoparticles indicate dominant paramagnetic nature of the double perovskites at room temperature. The magnetic parameters: maximum magnetization (M_s), coercivity (H_c) and retentivity (M_r) obtained from M-H data (Fig. 7) are tabulated in Table 4. The value of M_s and M_r for LSCMO was found to be increased whereas the value of H_c decreased for the LSCMO nanoparticles as compared to LCMO nanoparticles.

Figure 8a shows M–H curves recorded at various temperatures for LCMO and LSCMO nanoparticles. This also indicates an increase in maximum magnetization and coercivity at low temperature with Sr doping in LCMO host lattice. From Fig. 8a we can see that the LCMO and LSCMO nanoparticles undergo a transition to ferromagnetic behavior below room temperature from paramagnetic behavior shown at room temperature. Figure 8b represents the Zero field cooled (ZFC: black color) and field cooled (FC: red color) magnetization curve of LCMO and LSCMO nanoparticles in the temperature range 60–400 K. To know exactly the transition temperature, the first derivative of the ZFC magnetization as a function of temperature (inset of Fig. 8b), i.e., dM/dT Vs T graph for LCMO nanoparticles was plotted which indicates two transition temperatures at ~220 and ~175 K. Anomaly was observed at further lower temperatures around 100-115 K, which could be attributed to the glassy behavior indicated as T_g [24]. The observed transition at ~220 K and at ~175 K could be due to Co^{2+}–O^{2-}–Mn^{4+} ferromagnetic super exchange interactions and Co^{3+}–O^{2-}–Mn^{4+} ferromagnetic super exchange interactions, respectively [22, 23]. The ZFC–FC and dM/dT versus T graph (inset of Fig. 8b) plots for LSCMO(x = 0.12) nanoparticles indicate one prominent transition temperature at 175 K and a small minimum is obtained around ~360 K. This implies that with the doping of Sr

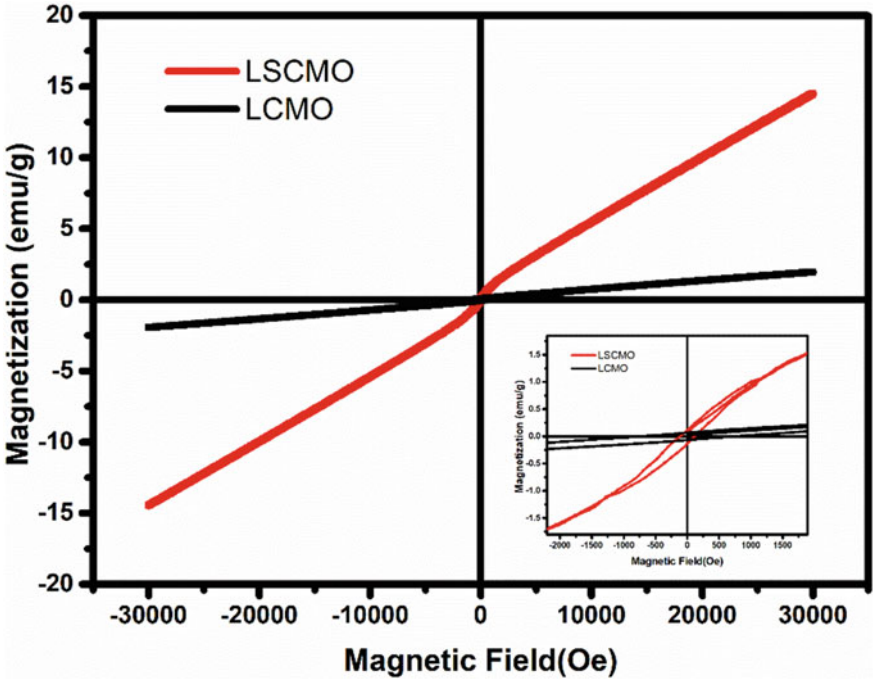

Fig. 7 Room temperature magnetization (M–H) curve of LCMO and LSCMO nanoparticles

Table 4 Magnetic parameters obtained from the M-H experimental curve

Composition	Remnant magnetization (M_r) (emu/g)	Maximum magnetization (M_s) (emu/g)	Coercivity values (H_c) (Oe)
La_2CoMnO_6	0.07	1.96	737.94
$La_{1.88}\ Sr_{0.12}CoMnO_6$	0.12	14.50	112.58

in LCMO nanoparticles the effect of ferromagnetic ordering due to Co^{2+}–O^{2-}–Mn^{4+} super exchange interaction is reduced and due to Co^{3+}–O^{2-}–Mn^{4+} ferromagnetic super exchange interactions are enhanced [10]. The existence of lower transition temperature in case of LSCMO indicates that Co^{3+} and Mn^{3+} exist whereas ideally only Co^{2+} and Mn^{4+} ions are expected in LCMO system [9].

In order to get more insight about the magnetic transition temperature of the compounds inverse of susceptibility was plotted as a function of temperature (Fig. 9). On extrapolating the linear portion of the inverse susceptibility for LCMO nanoparticles it intersects x-axis at about ~220 K. The linear portion of the graph beyond this temperature indicates paramagnetic nature in accordance with Curie–Weiss law [12]. For LSCMO (x = 0.12) nanoparticles the inverse susceptibility graph has two linear regions which on extrapolating intersect the x-axis at 350 K and ~175 K.

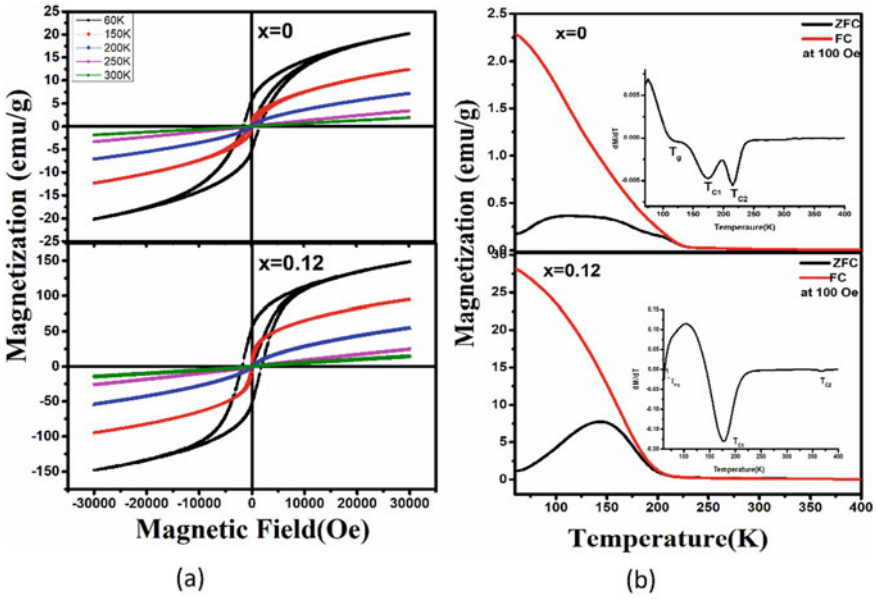

Fig. 8 **a** Magnetization curve of LCMO and LSCMO nanoparticles at 60, 150, 200, 250 and 300 K. **b** ZFC and FC curve at 100 Oe in temperature range 60–400 K. The inset shows the first derivative of ZFC magnetization values plotted as a function of temperature

The anomaly observed at ~360 K for Sr doped LCMO could be understood in terms of the effect of hole doping by Sr^{2+} at A site. Due to hole doping at A site, the valence of the B site ions i.e., Co/Mn can be affected [25]. As reported by Lan and coworkers [26] in their theoretical work that holes introduced by Sr doping in LCMO mainly go to oxygen sites and hence Mn^{3+} ions are introduced which disrupts the long-range ordering of Co and Mn [10]. Mn^{3+} ions with valence configuration $3d^4$, due to Jahn Teller effect spontaneously distorts the octahedron as it is energetically favorable, the increment in elastic energy due to distortion of octahedron is balanced by the energy saved due to lowering of e_g orbitals [12]. Mn^{3+} can interact ferromagnetically with the neighboring cation via double exchange mechanism. The transfer of electrons from Mn^{3+} to neighboring ion saves kinetic energy and is allowed only if both are ferromagnetically aligned [12]. Many researchers have reported the existence of ferromagnetic correlations above the curie temperature for Sr doped manganites [1, 25]. The inverse susceptibility plots and the $d\chi^{-1}/dT$ curves for LSCMO ($x = 0.12$) (inset of Fig. 9) indicate that above the ferromagnetic to paramagnetic transition temperature the behavior is not purely paramagnetic but ferromagnetic correlations exist and we obtain two peaks in $d\chi^{-1}/dT$ versus T graph namely at 368 and 385 K which could be due to varying stoichiometry of oxygen in the compound [26]. The existence of ferromagnetic correlations is evidence of the existence of Griffith like phase [1, 10, 25]

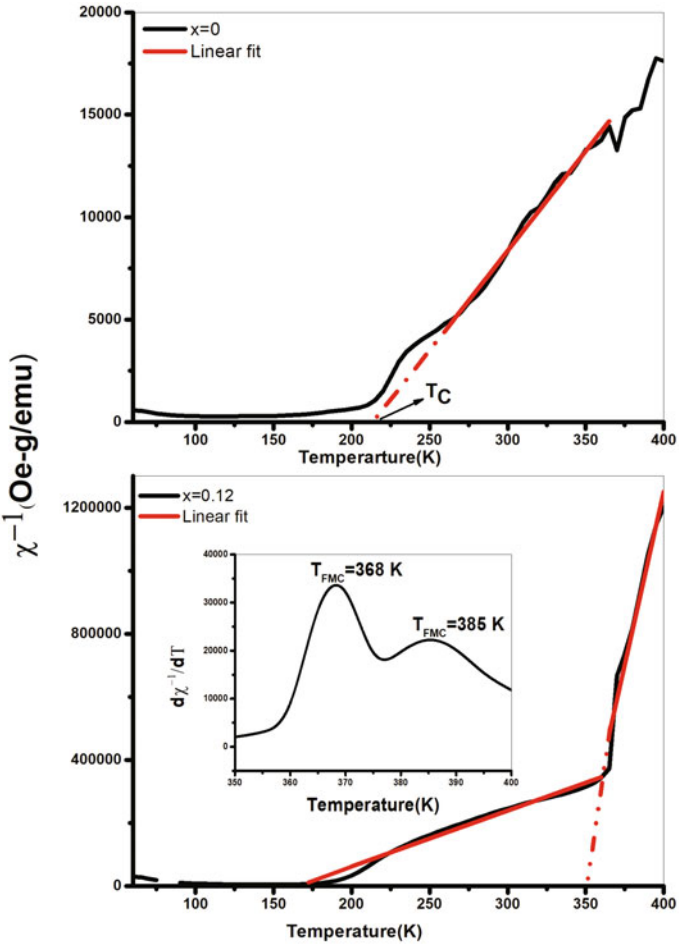

Fig. 9 **a** Inverse susceptibility versus T plot for LCMO nanoparticles, red line indicates linear fit according to Curie Weiss law. **b** Inverse susceptibility versus T plot for LSCMO nanoparticles, red line indicates linear fit according to Curie Weiss law, inset plots derivative of inverse of susceptibility with respect to temperature

4 Conclusion

Double perovskites La_2CoMnO_6 (LCMO) and $La_{1.88}$ $Sr_{0.12}CoMnO_6$ (LSCMO) have been synthesized successfully using the wet chemical synthesis method of sol–gel. The crystallite size estimated from the peaks of X-ray diffraction pattern using Debye Scherrer formula is around 6–18 nm. Rietveld refinement of X-ray diffraction pattern indicates formation of rhombohedral phase (S.G. No. R3c; 161). The Williamson Hall plots indicate that the strain reduces on doping with Sr in LSCMO nanoparticles. The FTIR and Raman spectra show characteristic bands corresponding to

Co/MnO_6 octahedra further confirming the formation of double perovskite structure. The magnetization study at room temperature shows paramagnetic nature of prepared compounds. From the temperature-dependent magnetization studies, we conclude that multiple interactions between the different oxidation states of B site ions exist. For LSCMO nanoparticles a Griffith like phase above curie temperature exists at 368 K which is useful for spintronics applications.

Acknowledgements The financial support received from the UGC in the form of UGC-BSR research start up grant (F.30-374/2017(BSR)), New Delhi, India is acknowledged. The authors are thankful to the Department of Physics, Banasthali Vidyapeeth and IIT Patna for characterization facilities provided.

References

1. Palakkal JP et al (2015) Observation of high-temperature magnetic transition and existence of ferromagnetic short-range correlations above transition in double perovskite La_2FeMnO_6. RSC advances 5(128):105531–105536
2. Kobayashi K-I et al (1998) Room-temperature magnetoresistance in an oxide material with an ordered double-perovskite structure. Nature 395(6703):677–680
3. Baettig P, Ederer C, Spaldin NA (2005) First principles study of the multiferroics $BiFeO_3$, Bi_2FeCrO_6, and $BiCrO_3$: structure, polarization, and magnetic ordering temperature. Phys Rev B 72(21):214105
4. Anderson MT, Greenwood KB, Taylor GA, Poeppelmeier KR (1993) B-cation arrangements in double perovskites. J Solid State Chem 22:197–233
5. Balcells Ll, Navarro J, Bibes M, Roig A, Martínez B, Fontcuberta J (2001) Appl Phys Lett 78:781
6. Balcells Ll et al (2001) Cationic ordering control of magnetization in Sr_2FeMoO_6 double perovskite. Appl Phys Lett 78(6):781–783
7. Murthy JK et al (2016) Antisite disorder driven spontaneous exchange bias effect in $La_{2-x}Sr_xCoMnO_6$($0 \leqslant x \leqslant 1$). J Phys: Conden Matter 28(8):086003
8. Mao Y, Parsons J, McCloy JS (2013) Magnetic properties of double perovskite La_2BMnO_6 (B= Ni or Co) nanoparticles. Nanoscale 5(11):4720–4728
9. Barrozo P, Albino Aguiar J (2013) Ferromagnetism in Mn half-doped $LaCrO_3$ perovskite. J Appl Phys 113(17):17E309
10. Khan A et al (2018) Effect of Sr-doping on electronic and magnetic properties of La2–$_xSr_xCoMnO_6$. In: AIP conference proceedings 1942. No. 1. AIP Publishing LLC
11. Mandal PR, Nath TK (2015) Evolution of griffith phase in hole doped double perovskite $La_{2-x}Sr_xCoMnO_6$ (x= 0.0, 0.5, and 1.0). Mater Res Express 2(6):066101
12. Shahee Aga, et al (2015) Evidence of ferromagnetic short-range correlations in cubic $La_{1-x}Sr_xMnO_{3-\delta}$ (x= 0.80, 0.85) above antiferromagnetic ordering. Phys Status Solidi (b) 252(8):1832–1838
13. Blundell S (2003) Magnetism in condensed matter 94–95
14. Patterson AL (1939) The Scherrer formula for X-ray particle size determination. Phys Rev 56(10):978
15. Kumar M, Prajapati B, Singh A (2020) B-site ordering effect on structural and magnetic properties of 'Y'-modified double perovskite La_2NiMnO_6 nanoparticles. J Mater Sci: Mater Electron 31(10):8099–8105
16. https://www.taylorfrancis.com/chapters/edit/, https://doi.org/10.1201/9781003197492-13/nanoscale-characterization-arvind-kumar-swati-manish-kumar-neelabh-srivastava-anadi-krishna-atul

17. Sadhu S, Chowdhury PS, Patra A (2008) Synthesis and time- resolved photoluminescence spectroscopy of capped CdS nanocrystals. J Lumin 128(7):1235–1240
18. Saberi A et al (2008) Chemical synthesis of nanocrystalline magnesium aluminate spinel via nitrate–citrate combustion route. J Alloy Compd 462(1–2):142–146
19. Dass RI, Yan J-Q, Goodenough JB (2003) Oxygen stoichiometry, ferromagnetism, and transport properties of La_{2-x} $NiMnO_{6+\delta}$. Phys Rev B 68(6):064415
20. Harbi A et al (2021) Tailoring the Griffiths-like cluster formation in the insulator ferromagnet spin-glass $Gd_2Ni_xCo_{1-x}MnO_6$ double perovskite. Phys Rev B 104(5):054404
21. Kumar D, Sathe VG (2015) Raman spectroscopic study of structural transformation in ordered double perovskites La_2CoMnO_6 bulk and epitaxial film. Solid State Commun 224:10–14
22. Magray MA, Ikram M (2019) Dielectric and Raman spectroscopy study of structural phase transformation of Sr-doped La_2CoMnO_6 double perovskite. J Mater Sci: Mater Electron 30(9):8655–8666
23. Truong KD et al (2007) Impact of Co/ Mn cation ordering on phonon anomalies in La_2Co MnO_6 double perovskites: Raman spectroscopy. Phys Rev B 76(13):132413
24. Dass RI, Goodenough JB (2003) Multiple magnetic phases of $La_2CoMnO_{6-\delta}$ (0<~ δ<~ 0. 0 5). Phys Rev B 67(1):014401
25. Eglitis RI (2014) Ab initio calculations of $SrTiO_3$, $BaTiO_3$, $PbTiO_3$, $CaTiO_3$, $SrZrO_3$, $PbZrO_3$ and $BaZrO_3$ (001), (011) and (111) surfaces as well as F centers, polarons, KTN solid solutions and Nb impurities therein. Int J Mod Phys B 28(17):1430009
26. Lan X, Kong S, Zhang WY (2011) Theoretical study on the electronic and magnetic properties of double perovskite $La_{2-x}Sr_xMnCoO_6$ (x= 0, 1, 2). Eur Phys J B 84:357–364

Studies on Electrical Properties of Thin Film-Based Layered FeFET Devices

Akshay Panchasara, Urjitsinh Rathod, Savan Katba, Mahesh Jivani, and Ashish Ravalia

1 Introduction

The demand for non-volatile memory devices with high storage capacity and low power consumption has increased exponentially in recent years. Resistive switching devices, which use resistance changes to store data, are a promising technology for future memory devices [1]. Among various resistive switching devices, FeFETs are attractive because of their simple structure and compatibility with standard complementary metal–oxide–semiconductor (CMOS) technology [2]. FeFETs consist of a ferroelectric gate oxide layer and a semiconductor channel, with a source, drain, and gate electrode [3]. The polarization of the ferroelectric layer can be used to modulate the channel conductivity, allowing for resistive switching [4]. The combination of ferroelectric materials and resistive switching in FeFETs has shown promise for use in non-volatile memory devices [4]. Ferroelectric Field Effect Transistor, is a type of transistor that uses ferroelectric materials to control its properties. Resistive switching is a phenomenon in which the resistance of a material can be switched between two states by applying an external voltage [5]. FeFETs are promising candidates for future electronic devices due to their nonvolatile memory capabilities and low power consumption. The use of ferroelectric materials in the transistor allows for data retention even when the power is turned off, which is important for

A. Panchasara · M. Jivani
Department of Electronics, Saurashtra University, Rajkot 360005, India

U. Rathod · A. Ravalia (✉)
Department Of Nanoscience and Advanced Materials, Saurashtra University, Rajkot 360005, India
e-mail: ashishravalia@gmail.com

A. Panchasara
Department of Computer Engineering, AI and Big Data, Marwadi University, Rajkot 360003, India

S. Katba
Department of Physics, School of Science, RK University, Rajkot 360020, India

S. B. Krupanidhi et al. (eds.), *Recent Advances in Functional Materials and Devices*,
Springer Proceedings in Materials 37, https://doi.org/10.1007/978-981-99-6766-7_3

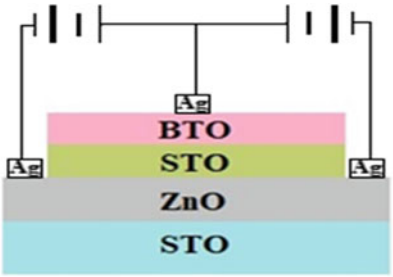

Fig. 1 FeFET device geometry

memory applications [6, 7]. In the present study, thin film-based layered FeFET has been investigated using an Ag (metal)/$BaTiO_3$ (Ferroelectric)/$SrTiO_3$ (Insulator)/ ZnO (Semiconductor) materials on $SrTiO_3$ *(100)* single crystalline substrate.

2 Experimental

Pulsed lase deposition (PLD) techniques are used to fabricate the thin film layer of $BaTiO_3$, $SrTiO_3$ and ZnO materials on $SrTiO_3$ *(100)* single crystalline substrate for layered FeFET geometry (Fig. 1.). First, ZnO layer was fabricated using 248 nm KrF laser having energy ~2 J/cm^2 at 4 Hz repetition rate and 500 °C. While $SrTiO_3$ was fabricated using ~2.5 J/cm^2 energy at 5 Hz repetition rate and 600 °C. Lastly, top layer of $BaTiO_3$ was fabricated using ~1 J/cm^2 energy at 5 Hz repetition rate and 720 °C. Structure of the FeFET was confirmed using X-ray diffraction (XRD) techniques. Surface morphological measurements were carried out using atomic force microscopy (AFM) measurement. I–V and channel resistance measurements were performed using Agilent 2612A source meter.

3 Results and Discussion

3.1 Structural

XRD data of BTO/STO/ZnO layer grown on STO (100) single crystalline substrate for FeFET is shown in Fig. 2. It can be clearly seen from the XRD data, that, BTO, STO and ZnO layer peak is observed.

BTO peak is observed along with the substrate peak suggesting the oriented growth with the substrate while ZnO peak is observed at different angel may be due to its different structure compared with the BTO and STO. BTO, STO and ZnO layers grown in single phasic nature without any detectable impurity.

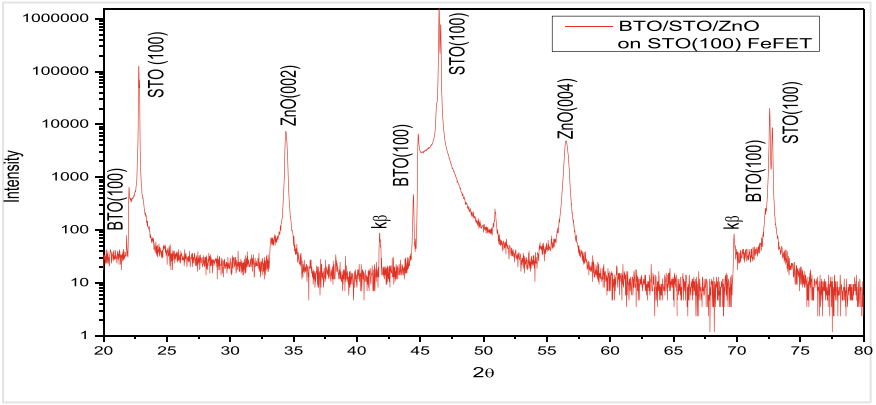

Fig. 2 XRD data of BTO/STO/ZnO layer grown on STO (100) single crystalline substrate for FeFET

3.2 Microstructural

Figure 3a and c shows the 2D micrographs and Fig. 3b and d shows the 3D micrographs of BTO and ZnO layer respectively. It can be clearly seen from the micrograph, that, both the layers show the homogenous spherical/oblate grain growth having the less rms roughness value. BTO possesses the average height in micron size whereas the ZnO layer shows the average height in nano size.

3.3 I–V Characteristic and Channel Resistance

To understand the charge-transport properties and channel resistance across the semiconductor ZnO layer, I–V measurements have been carried out by applying −5V—0V— +5V—0V——5V cycle. Figure 4 shows the I–V and channel resistance characteristics of BTO-based FeFET. It is observed that by applying cyclic voltages, forward bias doesn't show same behavior of current (0V—+ 5V—0V), whereas, in reverse bias, marginal gap is observed in current (0V—+ 5V—0V) in I–V and channel resistance graph. This behavior suggests that the leakage current plays a role in resistance switching in reverse bias.

This change in the resistance state in reverse bias may be due to leakage current formation across BTO and ZnO layer due to charge carrier of oxygen vacancies which released in first cycle (0 V to −5 V) and create the channels which get enhanced in the second cycle (−5 V to 0 V) due to already creating a path in first cycle and more charges released. The channel resistance is measured by applying the same cycle of I–V measurement. Figure 4b depicts the channel resistance data which shows the channel resistance change in the hysteresis of negative bias region due to the polarization of charges of BTO layer.

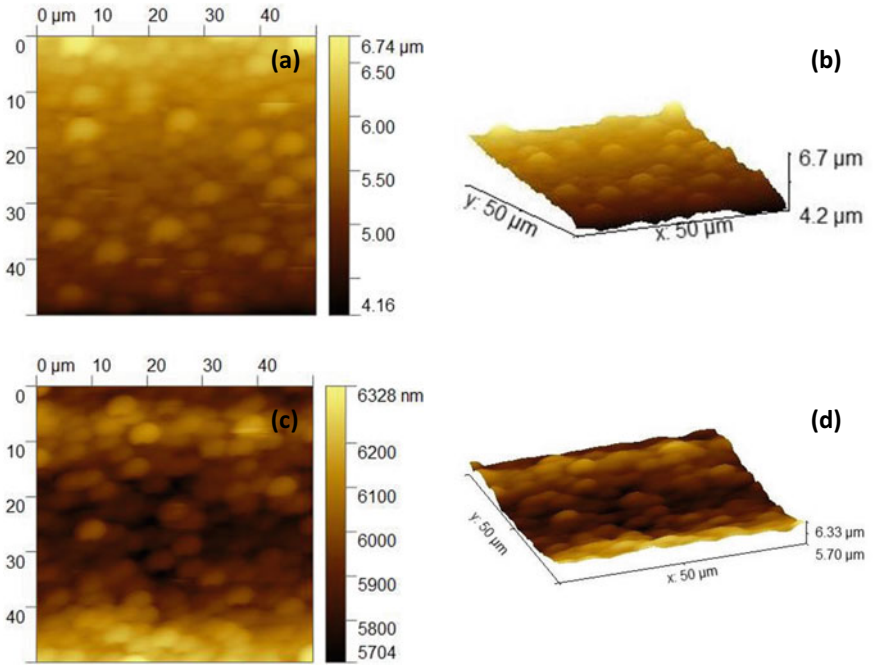

Fig. 3 2D and 3D AFM micrograph of BTO and ZnO layer of FeFET

3.4 Conclusion

We have studied the role of semiconductor channel in the I–V characteristics and channel resistance of PLD grown BTO/STO/ZnO layer on STO *(100)* based FeFET device. XRD studies confirm the single phasic nature of all layers of FeFET, while, AFM analysis shows the homogenous grain growth of BTO and ZnO layers. I–V and channel resistance data indicating the resistive switching in negative voltage bias region due to the formation of charge carrier across the BTO and ZnO layer and ferroelectric polarization of BTO charges affect the movement of free charge carriers. This information is important for understanding the transport properties of the layered FeFET device and optimizing its performance.

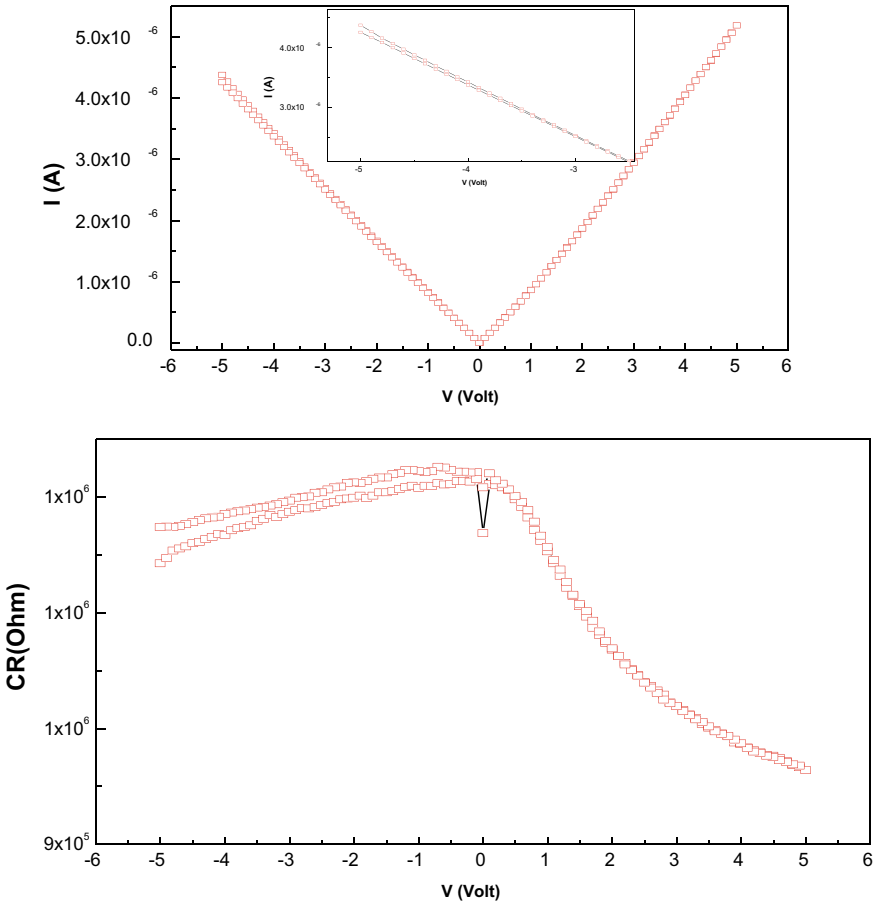

Fig. 4 **a** I–V characteristics (Inset: enlarge view of reverse bias region) and **b** channel resistance of FeFET

Acknowledgements Authors are thankful to Dr. B. R. Kataria, Head, Department of Nanoscience and Advanced Materials for providing PLD facility. We also thank Prof. Utpal Joshi, Department of Physics, Electronics and Space Science, Gujarat University for providing AFM and I–V measurement facility. ABR is thankful to IUAC, New Delhi for UFR-72317 and UGC DAE-CSR, Indore for CRS-ISUM/64A/CRS-347A projects funding. Authors are thankful to Prof. D. G. Kuberkar for their motivation and encouragement.

References

1. Waser R, Aono M (2012) Resistive switching memory: materials, devices, and applications. Mater Today 15(11):562–568. https://doi.org/10.1016/S1369-7021(13)70126-0
2. Funakubo H, Ishiwara H (2015) IEEE Trans Ultrason, Ferroelectr, Freq Control 62(10):1746–1761. https://doi.org/10.1109/TUFFC.2015.007070
3. Kuo S-Y, Cheng C-L, Hsu H-C, He J-H (2013) Ferroelectric field-effect transistor nonvolatile memory based on solution-processed ZnO films. IEEE Trans Electron Devices 60(11):3791–3796. https://doi.org/10.1109/TED.2013.2281426
4. Uchida K, Kawai T (2005) Ferroelectric-gate field-effect transistors: physics and technology. J Appl Phys 98(4):041101. https://doi.org/10.1063/1.2006229LNCS
5. Kim TH, Byun SJ, Kim KM, Kim HJ (2021) Recent advances in ferroelectric-gate field-effect transistors for nonvolatile memory applications. Nanomaterials 11(3):657. https://doi.org/10.3390/nano11030657
6. Kumar Singh M, Kumar S, Radhakrishnan MK (2020) Ferroelectric field-effect transistors for non-volatile memory applications: a review. J Mater Sci: Mater Electron 31(9):6532–6551. https://doi.org/10.1007/s10854-020-03109-3
7. Vagadia M, Ravalia A, Solanki PS, Pandey P, Asokan K, Kuberkar DG (2014) Electrical properties of BaTiO3 based – MFIS heterostructure: role of semiconductor channel carrier concentration. AIP Adv 4:057131. https://doi.org/10.1063/1.4880496

Investigation of Structural and Electrical Properties of Ternary System LCMO-CFO-BT

Manurbhav Arya, Chitralekha, S. Gaurav, and S. Shankar

1 Introduction

In the recent two decades, there has been an upsurge in research and development of multiferroics. Now, multiferroic materials are at forefront of materials research and technological innovations. The presence of more than 2 ferroic orders in these materials allows strong cross-coupling between electrical, magnetic, and mechanical properties. Ferroic orders are ferroelectricity, ferromagnetism, ferroelasticity, and ferrotoroidicity [1]. Cross couplings allow for electric field control of magnetization, magnetic field control of electric polarization, mechanical strain control by electric field, electric polarization control by applied mechanical stress, mechanical strain control by magnetization, and Magnetization control by applied mechanical stress [2]. This renders them to be utilized for a variety of applications, such as in magnetic data storage devices, energy storage devices, vibration energy harvesting devices, magnetic gradiometers, high voltage amplifiers, magneto-electric resonators, spintronics, quantum electromagnets, etc. [3].

Hitherto, it has been fairly well established in the literature on multiferroics that single-phase multiferroics exhibit weak magneto-electric coupling compared to

S. Gaurav has equally contributed as corresponding author in this work.

M. Arya · Chitralekha · S. Shankar (✉)
Functional Materials Research Laboratory, Department of Physics, ARSD College, University of Delhi, Delhi 110021, India
e-mail: sssubramaniam@arsd.du.ac.in; shankar3274@gmai.com

Chitralekha
Department of Physics, Multanimal Modi College, Ch. Charan Singh University, Meerut, U.P, India

M. Arya · S. Gaurav
Department of Applied Physics, Amity Institute of Applied Sciences, Amity University, U.P, Noida UP, India
e-mail: gsharma6@amity.edu

S. B. Krupanidhi et al. (eds.), *Recent Advances in Functional Materials and Devices*, Springer Proceedings in Materials 37, https://doi.org/10.1007/978-981-99-6766-7_4

multi-phase multiferroics. This has led researchers to focus on composite systems, such that, the strengthened magneto-electric coupling can be obtained at nano and bulk scales [4].

In literature, investigations have been carried out on the composite Co_2FeO_4-$BaTiO_3$ (CFO-BT). This composite has been shown to exhibit interesting magneto-electric properties. Co_2FeO_4 (CFO) is a spinel hard ferrite, that has an inverse spinel structure with *Fd3m* space group and face-centered cubic unit cell. Spinel ferrite corresponds to the General formula AB_2O_4, A denotes divalent metal ions at tetrahedral interstitial sites, whereas B denotes trivalent metal ions at octahedral interstitial sites. In CFO, cobalt ion occupies 8 out of 64 tetrahedral sites, whereas iron ion occupies 16 out of 32 octahedral sites, unique cationic distribution between tetrahedral and octahedral interstitial sites of lattice led to magnetic properties of CFO. It exhibits good physical stability, chemical stability, high saturation magnetization, high coercivity, and robust anisotropy and has applications in actuators, sensors, and magneto-optical recording media [5–8].

$BaTiO_3$ (BT) is a single perovskite, having *P4mm* space group with the chemical formula ABO_3. A denotes the atom at the corner of the unit cell, B denotes the atom at the center of the unit cell, and O denotes the atom at faces of the unit cell. The unit cell of BT is face-centered cubic, crystal structure of BT varies with temperature, five possible phases of BT are: rhombohedral, orthorhombic, tetragonal, cubic, and hexagonal [9]. BT shows exceptional ferroelectricity, piezoelectricity, pyroelectricity, and dielectric properties and has applications in sensors, high-density optical data storage, micro-capacitors, multi-layer ceramic capacitors, photoelectrodes, varistors, electro-optic devices, optical computing, and optical imaging [4, 6].

A class of materials called rare earth manganites has been studied extensively for their exciting properties, such as the existence of multi-ferroic orders, colossal magnetoresistance, and magnetic orderings [9]. Rare earth manganites have perovskite structures, and doping of rare earth elements led to the change in the valency state of manganese which has a significant impact on the transport properties of these materials [10]. La, Pr, Nd based manganites possess orthorhombic crystal structures with *pnma* space group. There have been interesting explorations on the multiferroic properties of these manganites, magnetoelectric properties shown by them can be described by different mechanisms, two major proposed mechanisms for their magnetoelectric effect are tilting of Polyhedra and frustrated magnetism [11]. These manganites have applications in magnetic storage devices, magnetic sensors, spintronics, and ferro-electromagnets.

$LaCaMnO_3$ (LCMO) is a lanthanum-based rare earth manganite, that has a perovskite structure. LCMO has an orthorhombic unit cell but transforms into a tetragonal unit cell as the doping of Ca is increased. In accordance with the chemical formula ABO_3 of perovskites, La and Ca ions occupy the A sites, Mn ions occupy the B site and the rest by oxygen ions at the faces of the unit cell [12]. MnO_6 Octahedra is found to be symmetrical, but they are titled at 20° compared to the ideal perovskite structure [13]. LCMO exhibits long-duration stability, good conductivity,

and magnetoresistance and has applications in information storage devices and solid oxide fuel cells.

An investigation into the synthesis of multiferroic composite by conjoining rare-earth manganite with CFO-BT composite has not been carried out yet. Taking into account the multiferroic effects shown by rare-earth manganites, their addition to single-phase or multi-phase multiferroic composites can lead to improved magneto-electric coupling at room temperature. In this view, the present investigation enumerates the synthesis of LCMO-CFO-BT composites and the study of their structural, and electrical properties.

2 Experimental Section

The "(1 - x) LCMO + x (0.7CFO-0.3BT)"(x = 0, 0.1 and 1) ternary system was synthesized using a conventional solid-state reaction route. Ferric oxide (Fe_2O_3, 95%, SQ- Fisher Scientific), Cobalt Oxide (Co_3O_4, 99%, AR-CDH), Lanthanum Oxide (La_2O_3, 99%, AR-Spectrochem), Calcium Oxide (CaO, 90%, LOBA Chemie), Manganese dioxide (MnO_2, 85%, Thomas Baker), Titanium dioxide (TiO_2, 99%, SQ-Fisher scientific), Barium Carbonate ($BaCO_3$, 99%, AR-SRL) were used as starting materials. Using the weight proportion method, appropriate quantities of Co_3O_4, and Fe_2O_3 were mixed to obtain $CoFe_2O_4$ (Cobalt ferrite, CFO) and $BaCO_3$, TiO_2 powders to obtain $BaTiO_3$ (barium titanate, BT). 70% of CFO and 30% of BT were taken and both were mixed to obtain a 0.7CFO-0.3BT composite. La_2O_3, CaO, and MnO_2 were mixed to obtain LCMO. The weights of powders were measured using the digital weighing machine. Both, the 0.7CFO-0.3BT mixture and LCMO were grinded separately with help of mortar and pestle for 6 h. Using a hot furnace, 0.7CFO-0.3BT was then calcined for 6 h at 1100 °C and LCMO was calcined for 6 h at 900 °C. The calcined powders were then mixed stoichiometrically, for x = 0.1, 0.5 g of 0.7CFO-0.3BT was taken and 4.5 g of LCMO, for x = 0, 5 g LCMO was taken, for x = 1, 5 g 0.7CFO-0.3BT was taken. Then, for all compositions (x = 0, 1, 0.1) grinding was done for 3 h. From each composition, Pellets were made, PVA (Polyvinyl alcohol) was used as a binder, a pelletizer kit and hydraulic press (at pressure 5 kg/cm^2) were used, and pellets obtained were disk and rectangular shaped. 0.7CFO-0.3BT, LCMO, 0.9LCMO-0.1(0.7CFO-0.3BT) compounds were sintered at 1150°, 950°, 1000 °C respectively in the furnace. Sintered materials were obtained and characterized using different techniques.

3 Results and Discussions

3.1 Structural Studies

Figure 1 shows powder X-ray diffraction patterns of pure LCMO, 0.7CFO-0.3BT, and 0.9LCMO-0.1(0.7CFO-0.3BT) ternary system. Each peak has been indexed using standard JCPDS file for pure LCMO, 0.7CFO-0.3BT. For the 0.7CFO-0.3BT composite, peaks of both pure CFO and pure BT are obtained in the diffraction pattern [5, 6]. XRD pattern reveals the formation of ternary phase purity, therefore, composite formation 0.9LCMO-0.1(0.7CFO-0.3 BT) is confirmed. This pattern shows both peaks of 0.7CFO-0.3BT composite and pure LCMO, therefore, a structural transformation has happened. Sharp peaks obtained imply the crystalline nature of composites. Crystallite Size (D) was obtained using Debye Scherrer Formula, $D = K\lambda/\beta COS\theta$, where K is shape factor (0.9), λ is Wavelength, β is full width at half maxima of the peak corresponding to miller indices (h k l) of a plane, θ is Bragg's Diffraction angle. Computed values of D are shown in Table 1. Addition of 0.7CFO-0.3 BT in LCMO led to increased crystallite size compared to pure LCMO, due to atomic rearrangements and lattice distortions produced.

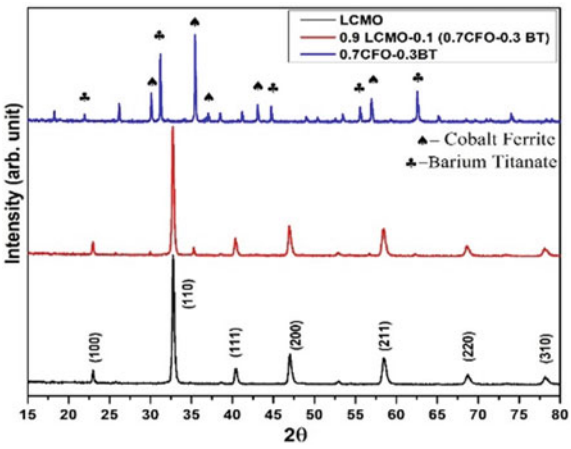

Fig. 1 XRD patterns of Composites

Table 1 Avg. crystallite size of composites

Material	Avg. Crystallite size (nm)
LCMO	189
0.7CFO-0.3BT	49
0.9LCMO-0.1(0.7CFO-0.3BT)	222

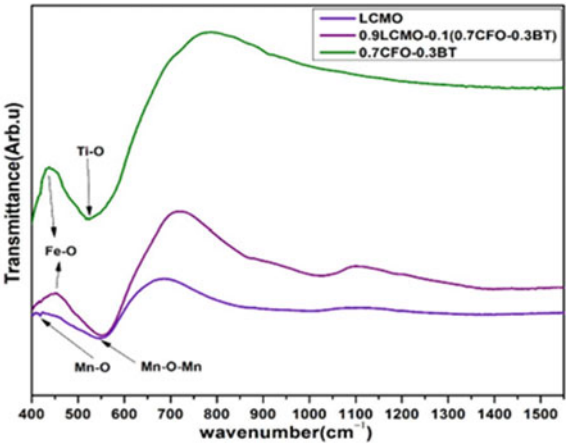

Fig. 2 FT-IR spectra of composites

3.2 FT-IR Spectroscopy

Fourier transform infrared spectroscopy for Pure CFO-BT, 0.9 LCMO-0.1(0.7 CFO-0.3 BT), and pure LCMO is shown in Fig. 2. Barium titanate shows a strong absorption peak near 539 cm^{-1}, this peak corresponds to the vibration of the Ti–O octahedron [14]. Characteristic Peaks for cobalt ferrite appear at 600 cm^{-1} and 450 cm^{-1} and these peaks correspond to octahedral, and tetrahedral structures, corroborating the existence of Fe–O stretching vibrations in Cobalt ferrite [6]. LCMO shows absorption bands nearby 600 cm^{-1} and 400 cm^{-1}. The band around 600 cm^{-1} is correlated with the stretching mode of Mn–O-Mn and Mn–O bonds, while the band near 400 cm^{-1} is correlated with the bending mode which is the result of variation in Mn–O-Mn bond angle [15]. Figure 2. shows that the addition of 0.7CFO-0.3BT in LCMO resulted in peak shifting and broadening around 700 cm^{-1}, a similar observation of peak shifting toward higher wavenumber is noticed for the peak around 500 cm^{-1}.

3.3 Dielectric Studies

The frequency dependence of the dielectric constant at an ambient temperature for Pure LCMO, 0.7CFO-0.3BT, and 0.9LCMO-0.1(0.7CFO-0.3BT) composites is shown in the Fig. 3. Dielectric response of any material is usually associated with the orientation of dipoles composed of bound charges. It has been figured out, that, hopping electronic or ionic charges can also lead to polarization processes [16]. Decrease in dielectric permittivity with frequency suggests a canonical dielectric relaxation process, hence, following Maxwell–Wagner polarization [7]. Figure 3 reveals that LCMO exhibits much higher values of dielectric constant compared to 0.7CFO-0.3BT for all values of frequencies, further the observed decrease in the

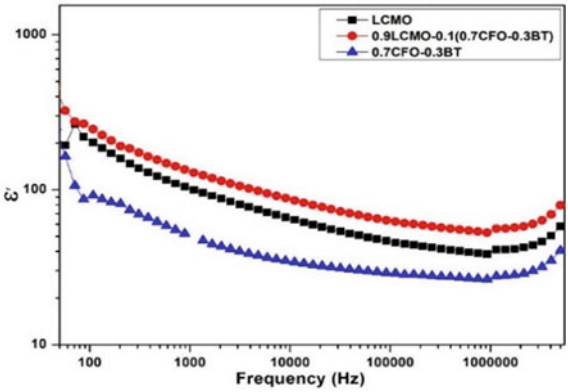

Fig. 3 ε′ versus frequency

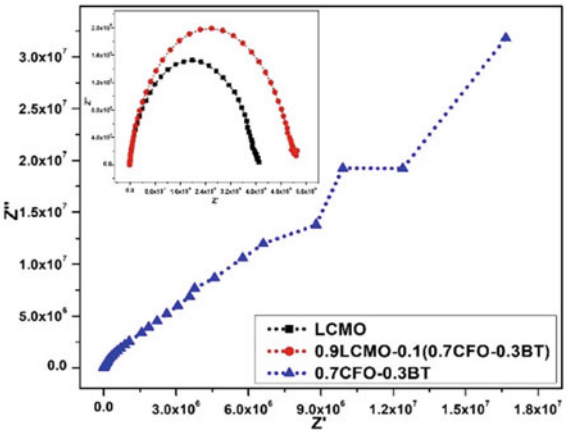

Fig. 4 Plot of Z′ versus Z″

values of the dielectric constant is due to the inability of electric dipoles to tune with the change in the frequency of the applied electric field [7]. Incorporating 0.7CFO-0.3BT in LCMO led to an improvement in dielectric behavior.

3.4 Impedance Spectroscopy

Impedance spectroscopy analysis at room temperature, the plot between Z′ and Z″ (Nyquist plot) is shown in Fig. 4. All semicircular curves begin from the origin and the center of semicircular curves lies below the real axis. Former reveals that the resistance of samples is predominantly due to grain boundary contributions. While the latter reveals the non-Debye-type behavior of synthesized composites [7]. No semicircular shape plot is obtained for 0.7CFO-0.3BT in intervals for Z′ and Z″ shown in the plot. The larger radius of 0.9LCMO-0.1(0.7CFO-0.3BT) plot

suggests it exhibits more resistive behavior compared to pure LCMO. LCMO is a good conductor, hence the contribution toward the total impedance of composite is far lower from LCMO compared to the much greater contribution of CFO-BT.

3.5 Impedance Dependence on Frequency

Figures 5 and 6 show the variation of the real and complex part of impedance with applied frequency for pure LCMO, 0.7CFO-0.3BT, and 0.9LCMO-0.1(0.7CFO-0.3BT) composites. Observing the evolution of complex Z″ is a crucial aspect in determining the impedance phase of composites [7]. In Fig. 6. Maximas are observable for LCMO and 0.9LCMO-0.1(0.7CFO-0.3BT) composite, there is a slight shift of maxima as the content of 0.7CFO-0.3BT is added to LCMO. Figure 5. shows Z′ almost remains constant for both pure LCMO and synthesized ternary composite up to a certain frequency, after a cut-off frequency is reached, Z′ is found to be decreasing, while for 0.7CFO-0.3BT there is a linear decrement.

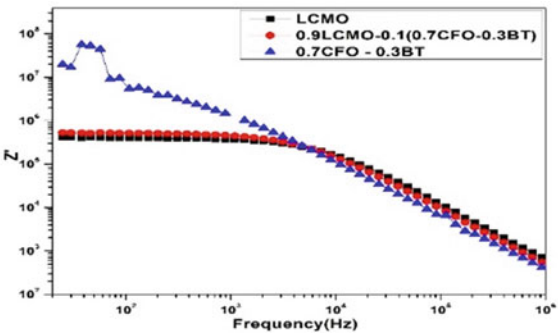

Fig. 5 Plot of Z′ versus frequency

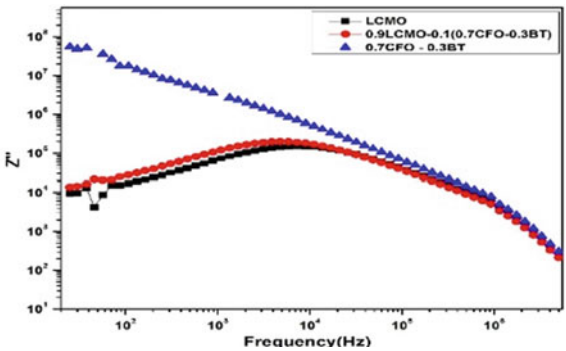

Fig. 6 Plot of Z″ versus Frequency

4 Conclusions

The ternary system 0.9LCMO-0.1(0.7CFO-0.3BT), Pure LCMO, and 0.7CFO-0.3BT were synthesized via the conventional solid state reaction method. Their structural, and electrical properties have been investigated. The X-ray diffraction pattern obtained confirms the presence of pure ternary phases in the synthesized ternary system, formation of 0.7CFO-0.3BT and pure LCMO were also confirmed. FTIR spectroscopy suggests that the 0.9LCMO-0.1(0.7CFO-0.3BT) composite showed a shift toward a higher wavenumber and broadening of the peak compared to pure LCMO. Variation of dielectric constant with frequency implies the presence of non-Debye type relaxation processes. Z' and Z'' versus frequency shows the variation of the real and complex part of impedance with frequency. The Nyquist plot (Z' vs Z'') shows the non-Debye-type behavior of the ternary composite, further addition of 0.7CFO-0.3BT composite to LCMO led to increased resistive behavior.

References

1. Shankar S, Thakur OP, Jayasimhadri M (2021) Significant improvement in dielectric, impedance, multiferroic and magnetoelectric properties of (1-X) $CO_{0.5}Ni_{0.5}Fe_2O_4$-$XBaTio_3$ bulk composites (X=0.1,0.10 and 0.20). J Mater Sci: Mater Electron
2. Palstra TTM, Blake GR (2006) Encyclopedia of materials. Elsevier
3. Vopson. MM (2015) Fundamentals of multiferroic materials and their possible applications. Critical Rev Solid State Mater Sci 223–250
4. Shankar S, Thakur OP, Jayasimhadri M (2020) Structural multiferroic and magnetoelectric properties of (1-x) $Bi_{0.5}La_{0.15}FeO_3$-$XBaTiO_3$ composite ceramics. J Mater Sci: Mater Electron
5. Dabas S, Chaudhary P, Kumar M, Shankar S, Thakur OP (2018) Structural, microstructural and multiferroic properties of $BiFeO_3$-$CoFe_2O_4$ composites. J Mater Sci: Mater Electron
6. Shankar S, Kumar M, Tuli V, Thakur OP, Jayasimhadri M (2018) Energy storage and magnetoelectric coupling in ferroelectric ferrite composites, J Mater Sci: Mater Electron
7. Shankar S, Thakur OP, Jayasimhadri M (2018) Impedance spectroscopy and conduction behavior in $CoFe_2O_4$-$BaTiO_3$ composites. J Electron Mater
8. Kamilla SK, Kumar A (2021) Cobalt ferrite: a review. In: International virtual conference on sustainable materials (IVCSM-2k20), Elsevier
9. Vijatović MM, Bobić JD, Stojanović BD (2008) History and challenges of barium titanate: part-1. Sci Sinter 155–165
10. Shankar S, Thakur OP, Jayasimhadri M (2021) Strong enhancement in structural, dielectric, impedance and magnetoelectric properties of $NdMnO_3$-$BaTiO_3$ multiferroic composites. Mater Chem Phys
11. Xia W, Pei Z, Leng K, Zhu X (2020) Research progress in Rare earth doped Perovskite Manganite oxide nanostructures. Nanoscale Res Lett
12. Serrao CR, Sundaresan A, Rao CNR (2008) Multiferroic nature of charge-ordered rare earth manganites. J Phys: Condens Matter
13. Abdel-Latif IA (2012) Rare earth manganites and their applications. J Phys 15–31
14. Faaland S, Knudsen KD, Einarsrud M-A, RØrmark L, HØier R, Grande T (1998) Structure, stoichiometry, phase purity of calcium substituted Lanthanum manganite powders. J Solid State Chem 320–330
15. Sun D, Jin X, Liu H, Zhu J, Zhu Y, Zhu Y (2011) Investigation on FTIR spectrum of barium titanate ceramics doped with alkali Ions. Ferroelectrics

16. Arabi A, Fazli M, Ehsani MH (2018) Synthesis and characterization of calcium doped Lanthanum nanowires as a photocatalyst for degradation of methylene blue solution under visible light irradiation. Bull Mater Sci 41–77
17. Delgado A, García-Sánchez MF, M'Peko JC, Ruiz-Salvador AR, Rodríguez-Gattorno G, Echevarría Y (2003) An elementary picture of dielectric spectroscopy in solids: physical basis. J Chem Educ

Investigations of Atomic Disorder and Grain Growth Kinetics in Polycrystalline $Gd_2Ti_2O_7$ Pyrochlore

Ankita, Umang Berwal, Vinod Singh, Yogendra Singh, and Satyendra Singh

1 Introduction

The wide range of physical, chemical, and structural properties of gadolinium titanium oxide, $Gd_2Ti_2O_7$ makes it a technologically crucial material. It is an excellent choice for many applications due to its special qualities, including coatings for high-temperature thermal barriers, rapid ion conductors, and catalysts [1]. The high radiation resistance of some compositions, such as $Gd_2Ti_2O_7$, pyrochlores are regarded as an inert fuel matrix for actinide transmutation [2, 3]. The kinetics of grain formation and microstructural evolution will have a substantial impact on the materials' structure, phase, and physical characteristics, as well as any potential applications.

Pyrochlore materials have the chemical formula $A_2B_2O_7$, in which A(cation) represents trivalent ion (rare-earth) and cation B is 3d, 4d, or 5d element with 1/8th of the oxygen vacant positions [4]. Pyrochlores are ceramics with a cubic structure of the fluorite type [5, 6]. The pyrochlore structure undergoes an order/disorder transformation because of disordering in the cation and anion vacancies [7–9].

Researching the atomic ordering or disordering in pyrochlore oxide, as well as the physical and chemical characteristics of pyrochlores, is particularly important for fully comprehending innovative materials and researching grain-growth dynamics [10]. Controlling grain growth is also highly helpful in pyrochlore engineering as it is a critical parameter in determining how transformable structural characteristics are [11, 12]. It's interesting to note that structural order/disorder has a substantial impact on physical and chemical characteristics of pyrochlore [13, 14]. Catalytic activities, ionic conductivity and the capacity to confine radionuclides are physicochemical features that are influenced by atomic ordering/disordering and grain

Ankita · U. Berwal · V. Singh (✉)
Department of Applied Physics, Delhi Technological University, New Delhi 110042, India
e-mail: vinodsingh@dtu.ac.in

Y. Singh · S. Singh
Special Centre for Nano Sciences, Jawaharlal Nehru University, New Delhi, India

S. B. Krupanidhi et al. (eds.), *Recent Advances in Functional Materials and Devices*,
Springer Proceedings in Materials 37, https://doi.org/10.1007/978-981-99-6766-7_5

size [15]. There are two types of grain growth processes: abnormal grain growth and regular grain growth [3, 16]. In general, the usual grain-growth process was preferred by micro-crystalline materials [17]. Curvature during regular grain growth is the reason behind the rotation and grain boundary migration/diffusion. However, when a few energetically favorable grains develop rapidly inside a framework of fine grains, anomalous grain growth results in a bimodal grain size distribution [18, 19]. Some grains develop abnormally quickly in comparison to the other grains because of greater atomic mobility near the grain boundaries [1, 20]. This influence is usually noticeable because impurity atoms or defects are present at the point of contact [21]. Lattice parameter and grain boundary velocity are inversely related [14]. The disorder-order transition phenomena that influence grain development of sample happens during annealing process [12, 22]. Increasing the annealing temperature results in a greater degree of cation order [23, 24]. The $A_2B_2O_7$ pyrochlore structure undergoes an order–disorder transformation which results from the disordering in cations and anion vacancies in the A and B-sites [16]. As annealing temperature and time are increased, atomic order/disorder and grain size also grow [25]. According to experimental findings, the sample spends more time in the pyrochlore phase at higher annealing temperatures [26, 27]. Disorder on the anion sublattice serves to enhance the quantity of mobile oxygen vacancies by forming Frenkel defects [2, 28]. Recent modeling results show that cation disorder increases ionic conductivity by increasing the concentration of mobile charge carriers and individual mobility [29, 30].

Two subsets of patterns make up XRD patterns. The fault fluorite structure, which is present in all materials regardless of order, gives rise to the first set [30, 31]. The pyrochlore superstructure is responsible for the second subset [32]. At low and intermediate temperatures, defect and boundary scattering controls heat transfer; at high temperatures, the phonon–phonon scattering takes control [33]. Because nanocrystalline materials have lower thermal conductivity and have more grain boundaries than comparable single crystal materials and these grain boundaries are considered to act as a barrier to the flow of heat [15, 34].

There aren't many published research that discuss how binary oxides, and semiconductors' thermal conductivity varies with grain size [26, 35]. However, it is reported that in pyrochlore, the thermal conductivity is affected by the substitution and cationic mass at very low temperatures [8]. As a result, it is necessary to better understand the thermal characteristics of pyrochlore-structured ceramic at room temperature as well as the impact of various scattering mechanisms [2, 36]. This study basically used a solid-state reaction method to create $Gd_2Ti_2O_7$ and studying its atomic ordering/disordering and grain growth dynamics [37]. Designing novel materials regarding technological purposes may benefit from knowledge of the atomic ordering/disordering and grain-growth dynamics [38].

2 Materials and Methodology

2.1 Materials

Gadolinium (III) oxide (CAS No.: 12064-62-9, 99.9% purity) and Titanium (IV) oxide (CAS No.:1306–38-3, 99.9% purity). Without further purification, all chemicals were used.

2.2 Methodology

Grinding a stoichiometric mixture of high-purity Gd_2O_3 and TiO_2 using a solid-state reaction route yielded pure phase $Gd_2Ti_2O_7$ samples. The majority of lanthanide sesqui-oxides are extremely sensitive to H_2O and CO_2 in the atmosphere. To assure the retention of intended stoichiometry, the starting chemicals, i.e., the existing hydroxides and carbonates were eliminated by mixing Gd_2O_3 and TiO_2 for an hour at 700 °C. Following that, a 6 g batch of the precursors (Gd_2O_3 and TiO_2) was mixed and grinded for about 7 h to ensure uniformity and homogeneity in our sample. Using a steel die set and 6t pressure, pellets of 10 mm diameter were formed. At varying heating temperatures ((a) 1100, (b) 1200, and (c) 1300 °C) prepared pellets were annealed in air for 24 h and 43 h. Figure 1 illustrates each step of this process in detail.

2.3 Characterization

Using the X-ray diffraction, structural analysis of the sintered pellets at various temperatures (1100, 1200, and 1300 °C) for different annealing time (24 and 43 h) was examined at JNU, Special Centre for Nano Sciences, New Delhi. On an XRD machine, Rigaku Diffractometer (Mini flex 600, Japan) the XRD structures of the pellets were captured with at 1°/min in 10°–80° range having Cu diode with Kα radiation of $\lambda = 1.5406A°$. At 532 nm excitation wavelength the Raman spectra for each pellet using a Raman analyzer (Enspectr R 532) at JNU, New Delhi was recorded. Scanning electron microscopy (SEM-JSM-IT 200, JEOL), at JNU, New Delhi, was used to examine each and every final sintered pellet.

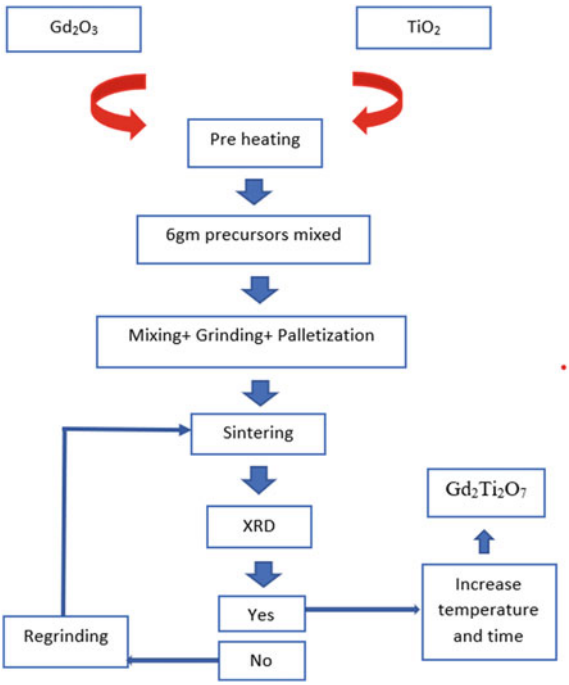

Fig. 1 Schematic diagram exhibiting solid-state reaction to yield $Gd_2Ti_2O_7$ pyrochlore

3 Results and Discussion

3.1 X-Ray Diffraction (XRD) Analysis

Figure 2 displays (a) XRD pattern for the entire series of $Gd_2Ti_2O_7$ milled for approximately 7 h using a mortar pestle. W–H Plot of $Gd_2Ti_2O_7$ at various temperatures for different annealing time- (b) 1100 (24 h) (c) 1100 (43 h) (d) 1200 (24 h) (e) 1200 (43 h) (f) 1300 (24 h) (g) 1300 (43 h). The milled powder is amorphous in nature, according to the nanopowders XRD pattern. The ball-milled nanopowders showed no impurity peaks from residual chemical compounds, proving that all of the reagents were evenly combined. Crystallite size, strain, and lattice constant of the samples annealed for various time interval (24 h and 43 h) is depicted in Table 1. XRD study has been carried out to investigate grain development and its effects on the structural characteristics of polycrystalline $Gd_2Ti_2O_7$. The sample exhibits unit cell parameter as 9.937598 A° which is calculated and demonstrated in Table 1 using XRD data. Because pyrochlore superstructure peaks are seen due to additional allowed reflection conditions, the intensity of these peaks was very low in accordance with the results presented (JCPDS No.23-0259) [39].

There is a rise in peak intensity and alteration in diffraction peak intensity toward high angles is seen due to increase in the temperature. The XRD peaks' full width at half maximum (FWHM) significantly decreased, indicating grain growth brought on

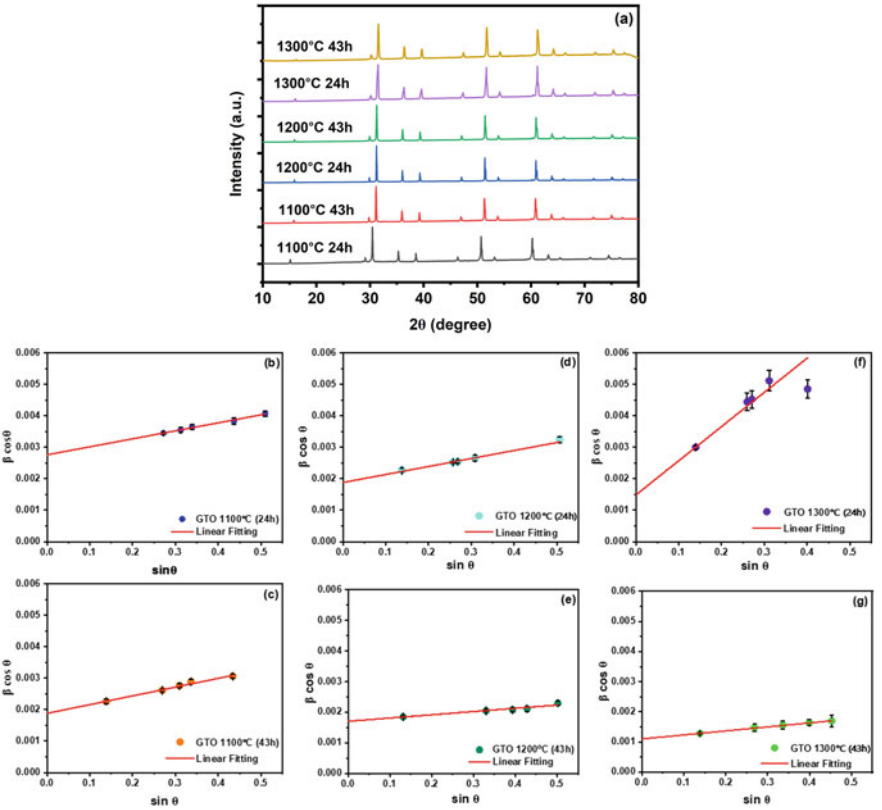

Fig. 2 **a** XRD pattern for entire series of $Gd_2Ti_2O_7$, W–H Plot of $Gd_2Ti_2O_7$ at various temperatures for different annealing time, **b** 1100 (24 h), **c** 1100 (43 h), **d** 1200 (24 h), **e** 1200 (43 h), **f** 1300 (24 h) and **g** 1300 (43 h)

Table 1 Structural variables calculated for $Gd_2Ti_2O_7$ at various temperatures for different time intervals using XRD results

Temperature (°C)	Time (h)	Intercept	Slope	Crystallite size	Strain	Lattice constant
1100	24	0.00276	0.00254	524.6834783	0.000265	10.16468798
	43	0.00188	0.00279	770.28	0.002715	9.950875689
1200	24	0.00182	0.00280	810.37	0.0003325	9.927795625
	43	0.00171	0.00368	846.8575439	0.000475	9.913683901
1300	24	0.00149	0.01086	971.8969128	0.000635	9.852264018
	43	0.0011	0.01178	1316.478545	0.0006975	9.816281546

by high-temperature annealing. Williamson-Hall analysis was used for determining the crystallite size and micro-strain of annealed samples. Computed crystallite size for samples that were heated at 1100, 1200, and 1300 °C for various time intervals is shown in Table 1. During annealing, temperature-induced grain growth caused an increase in crystallite size.

3.2 Raman Spectroscopy Analysis

To determine the impact of temperature for different time intervals on the sample, the Raman spectra for samples with temperature ranges for annealing, i.e., (a) 1100, (b) 1200, and (c) 1300 °C at different time intervals (24 h and 43 h) were compared. The entire series of $Gd_2Ti_2O_7$ sample's Raman spectra, which were recorded in the 150–750 cm^{-1} wavenumber range, are consistent with the earlier findings. It illustrates that with the increase in annealing time the position of Raman active modes remains unchanged. As a result, XRD and Raman spectroscopy indicates that the system's long-range order is affected by the grain growth primarily through micro-strain relaxation and crystallite size expansion, whereas its effects on structural ordering, particularly on anion lattice, did not seem to be particularly significant. Raman spectroscopy, which we employed to further our research, showed structural alterations brought on by a shift in oxygen's location in the anion sublattice. Theoretically, the $Gd_2Ti_2O_7$ pyrochlore exhibits six Raman active mode of vibration as a result of oxygen vibrations at the 48f and 8a sites. O-Gd-O bond bending causes the two most noticeable Raman bands, i.e., T_{2g} (310 cm^{-1}) and E_g, to appear. Another strong band which is A_{1g} (520 cm^{-1}) attributed to Gd-O stretch through the vibration in 48f (O) which is over < 100 > cubic axes has been given the oxygen position parameter (x). The intensities of the other four bands are weaker. 3 of the other 4 weak bands- at 212, 545 and 680 cm^{-1} were discernible. Raman active modes associated with Ti–O stretching are frequently not seen at lower wavenumbers because of Ti–O bond's short bond length. The Raman spectra can be used to estimate the blue shift in the pyrochlore, as shown in Fig. 3. In Fig. 3, Raman spectra for materials that were annealed for 24 and 43 h at temperatures of 1100, 1200 and 1300 °C are compared. In as-sintered sample, O-Gd-O bond bending caused four T_{2g} modes to appear at wavenumbers- 200, 308, 320 and 450 cm^{-1}, while the Gd-O stretch caused 1 A_{1g} mode to appear at wavenumber- 516 cm^{-1}. The existence of theoretically predicted modes lends additional support to the XRD findings that the as-sintered sample of $Gd_2Ti_2O_7$ formed an ordered pyrochlore structure. These peaks might contribute to Raman active modes of Ti–O because of the tight Ti–O length (1.8 A°), which was expected to occur at an elevated frequency range. The position of the Raman active modes during high-temperature annealing remained constant as the annealing temperature changed. This demonstrates that during heating, Gd_2Ti_2O7 does not change into a defective fluorite structure. The effect of annealing temperature was better understood through examination of the ratio of intensity (T_{2g}/A_{1g}) of the major peaks. The T_{2g}/A_{1g} ratio scarcely changes with annealing temperature, proving that

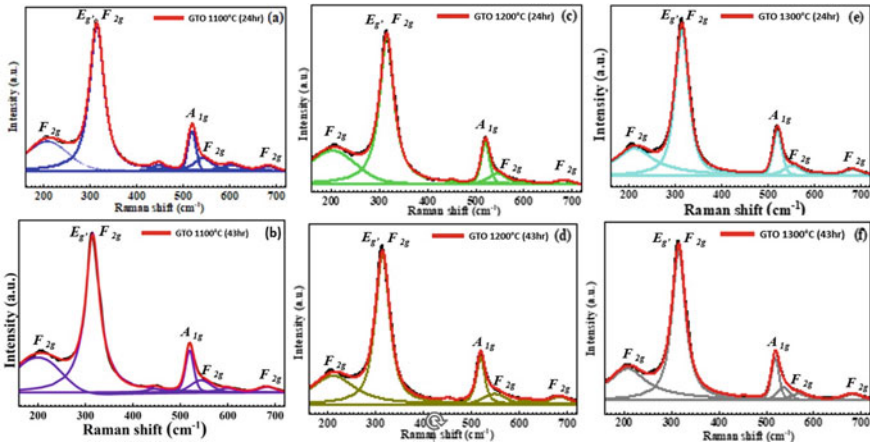

Fig. 3 **a–f** Raman spectra for entire series of $Gd_2Ti_2O_7$ at various temperature for different annealing time

the oxygen position is unaffected by rising annealing time intervals for specific value of heated temperature. In order to examine the impact of heating duration, Raman spectra for materials that undergo annealing at temperatures of (a) 1100, (b) 1200, and (c) 1300 °C for varying periods (24 h and 43 h) were analyzed. Figure 3 displays the results for comparison. It illustrates that when the annealing time increases, the positioning of Raman active modes stays unchanged. The illustration of intensity ratio (T_{2g}/A_{1g}) further exemplifies how negligible the annealing period affects the end result. As a consequence, grain expansion impacts the system's long-range order through an increase in crystallite size and a decrease in micro-strain, but has no discernible effect on the structural ordering, especially on the anion lattice which is supported by XRD and Raman spectroscopy.

3.3 Scanning Electron Microscopy

SEM images of milled samples show another characteristic of hand milling of micro-sized particles which contains nano-sized granules. Figure 3 shows the systematic SEM micrographs of $Gd_2Ti_2O_7$ at various temperatures for different annealing times, i.e., (a) 1100 (24 h), (b) 1100 (43 h), (c) 1200 (24 h), (d) 1200 (43 h), (e) 1300 (24 h) and (f) 1300 °C (43 h). The manual millined powder containing micron-size particles including nano-sized granules results in another characteristic of pyrochlores, as seen in SEM images of milled samples. According to SEM data, the average grain sizes were 400–1000 nm, greater than the samples made from milled powder, indicating that grain growth occurred during the sintering process. As heating temperature rose to 1100–1300 °C, microstructures were made up of homogenous grains and the average grain size increased which was determined using SEM data. It was found

that heating at 1100 °C produced a large number of evenly distributed pores along with an increment in grain size.

Micron sized porosity was produced at grain boundary and triple crossing due to sintering of the pellets synthesized initially, which contains accumulated crystals having wide size variation. When heating temperature raised about 1200 °C, then the grain size rose, while density of pores of micron sized reduced. Pore aggregation results in an increase in pore size. Dense granules have been produced as a result of raising the annealing temperature to 1300 °C. Figure 4 depicts micrographs of nc-$Gd_2Ti_2O_7$ specimens that have been annealed at 1100, 1200 and 1300 °C respectively at 24 and 43 h, to examine the effect of different time intervals on grain development. As anticipated, grain size is enhanced as heating time increases. This further highlights how temperature effects can be felt even for different heating times. To further understand how heating time and temperature affect grain growth, grain size was measured using SEM micrographs of each sample. It should be noticed that the SEM observed grain size is larger than the XRD estimated crystallite size. This is because grains are made up of multiple crystallites (Fig. 5).

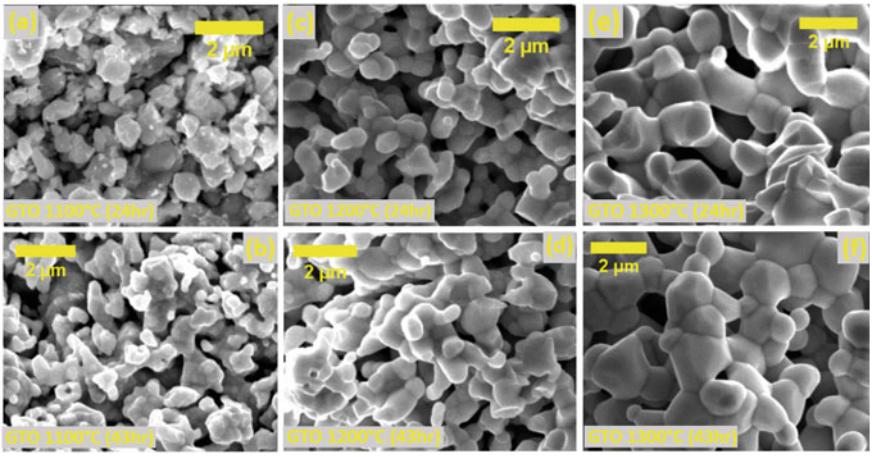

Fig. 4 Systematic SEM micrograph of $Gd_2Ti_2O_7$ at various temperature for different annealing time

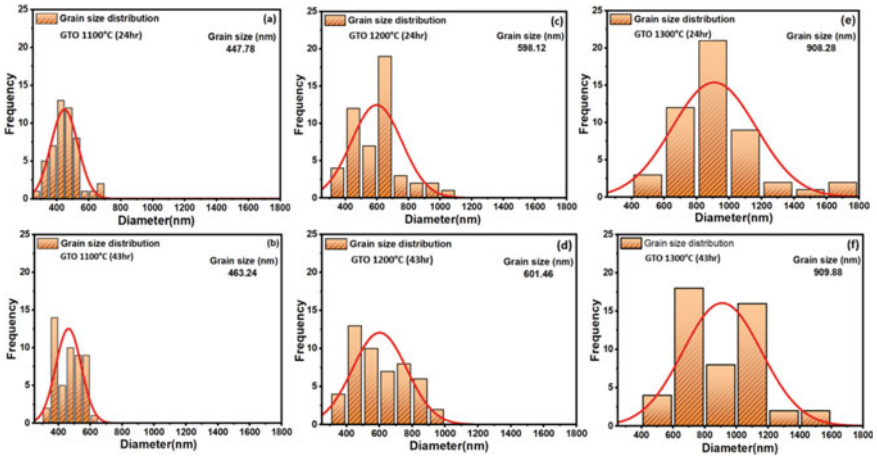

Fig. 5 **a**–**f** Gaussian fitting size distribution histogram from analyzed data of SEM for whole series of $Gd_2Ti_2O_7$ at various temperature for different annealing time [40]

4 Conclusion

Series of $Gd_2Ti_2O_7$ pyrochlore oxides were formed using solid-state route. SEM micrographs are used to confirm that almost spherical particles that have agglomerated are present. XRD and Raman spectroscopy results show that a single-phase pyrochlore structure has formed. $Gd_2Ti_2O_7$ shows enhancement in cation–anion order with the increase in annealing time at different annealing temperatures. XRD analysis shows an increase in crystallite size and strain with increasing annealing temperature and time. There is a decrease in lattice constant with the enhancement in temperature and annealing time which is calculated using XRD data. As the annealing temperature and time are increased, the $Gd_2Ti_2O_7$ grains gradually expand. The estimated grain size for the grain growth of $Gd_2Ti_2O_7$ has been anticipated using SEM data.

Acknowledgements We are thankful to DTU for the financial support and obliged to DTU family for encouraging us to carry out the research smoothly.

References

1. Lian J et al (2003) The order–disorder transition in ion-irradiated pyrochlore. Acta Mater 51(5):1493–1502
2. Janković B, Marinović-Cincović M, Dramićanin M (2015) Kinetic study of isothermal crystallization process of $Gd_2Ti_2O_7$ precursor's powder prepared through the Pechini synthetic approach. J Phys Chem Solids 85:160–172

3. Antić Ž, Prashanthi K, Ćulubrk S, Vuković K, Dramićanin MD, Thundat T (2016) Effect of annealing conditions on structural and luminescencent properties of Eu3+-doped $Gd_2Ti_2O_7$ thin films. Appl Surf Sci 364:273–279
4. Bonville P et al (2003) Low temperature magnetic properties of geometrically frustrated $Gd_2Sn_2O_7$ and $Gd_2Ti_2O_7$. J Phys: Condens Matter 15(45):7777
5. Ghanshyam P, Puchala B, Uberuaga BP (2019) Distortion-stabilized ordered structures in $A_2BB'O_7$ mixed pyrochlores. NPJ Comput Mater 5(1)
6. Berwal U, Singh V, Sharma R (2022) Key role of Tb3+ doping on structural and photoluminescence properties of $Gd_2Ti_2O_7$ pyrochlore oxide. Ceram Int 48(15):22307–22316
7. Panghal A, Kulriya PK, Kumar Y, Singh F, Singh NL (2019) Investigations of atomic disorder and grain growth kinetics in polycrystalline $La_2Zr_2O_7$. Appl Phys A 125:1–11
8. Fuentes AF, Montemayor SM, Maczka M, Lang M, Ewing RC, Amador U (2018) A critical review of existing criteria for the prediction of pyrochlore formation and stability. Inorg Chem 57(19):12093–12105
9. Berwal U, Singh V, Sharma R (2023) Structural and optical studies on Dy3+ doped $Gd_2Ti_2O_7$ pyrochlore as white light emission. Ceram Int 49(6):8897–8906
10. Guo Y et al (2022) High-entropy titanate pyrochlore as newly low-thermal conductivity ceramics. J Eur Ceram Soc 42(14):6614–6623
11. Tuller HL, Button DP, Uhlmann DR (1980) Fast ion transport in oxide glasses. J Non Cryst Solids 40(1–3):93–118
12. Berwal U, Singh V, Sharma R (2023) Effect of Ce4+→ Ce3+ conversion on the structural and luminescence properties of Ce4+ doped $Gd_2Ti_2O_7$ pyrochlore oxide. J Lumin 119687
13. Upmanyu M, Smith RW, Srolovitz DJ (1998) Atomistic simulation of curvature driven grain boundary migration. Interf Sci 6:41–58
14. Singh V et al (2022) Hydrogen induced structural modifications in size selected Pd-Carbon core-shell NPs: effect of carbon shell thickness, size and pressure. Int J Hydrogen Energy 47(25):12642–12652
15. Taylor CA (2016) Helium diffusion and accumulation in $Gd_2Ti_2O_7$ and $Gd_2Zr_2O_7$
16. Singh V, Sharma R (2022) Structural properties of TiS2/MWCNTs hybrid nanostructures. In: Proceedings of the international conference on atomic, molecular, optical and nano physics with applications: CAMNP 2019, pp 155–165
17. Zhang M et al (2020) Analysis of abnormal grain growth behavior during hot-press sintering of boron carbide. Ceram Int 46(10):16345–16353
18. Panghal A, Kumar Y, Kulriya PK, Shirage PM, Singh NL (2021) Atomic order-disorder engineering in the $La_2Zr_2O_7$ pyrochlore under low energy ion irradiation. Ceram Int 47(14):20248–20259
19. Jamkhande PG, Ghule NW, Bamer AH, Kalaskar MG (2019) Metal nanoparticles synthesis: an overview on methods of preparation, advantages and disadvantages, and applications. J Drug Deliv Sci Technol 53:101174
20. Stefanovsky SV, Yudintsev SV (2016) Titanates, zirconates, aluminates and ferrites as waste forms for actinide immobilization. Russ Chem Rev 85(9):962
21. Raison PE, Haire RG, Sato T, Ogawa T (1999) Fundamental and technological aspects of actinide oxide pyrochlores: relevance for immobilization matrices. MRS Online Proceedings Library (OPL) 556:3
22. Umang VS, Sharma R (2022) Structural hybrid nanostructures properties of TiS2/MWCNTs. In: Proceedings of the international conference on atomic, molecular, optical and nano physics with applications: CAMNP 2019, p 155
23. Zhang FX et al (2010) Increased stability of nanocrystals of Gd2 (Ti0. 65Zr0. 35) $2O_7$ pyrochlore at high pressure. J Alloys Compd 494(1–2):34–39
24. Park S et al (2015) Response of $Gd_2Ti_2O_7$ and $La_2Ti_2O_7$ to swift-heavy ion irradiation and annealing. Acta Mater 93:1–11
25. Xie D, Zhang K, Li W, Luo B, Guo H (2021) Self-propagating high-temperature synthesis of Sm and Zr Co-doped $Gd_2Ti_2O_7$ pyrochlore ceramics as nuclear waste forms. J Wuhan Univ Technol-Mater Sci Ed 36(2):196–202

26. Panghal A, Kumar Y, Kulriya PK, Shirage PM, Singh NL (2021) Structural assessment and irradiation response of $La_2Zr_2O_7$ pyrochlore: impact of irradiation temperature and ion fluence. J Alloys Compd 862:158556
27. Moon PK, Tuller HL (1988) Ionic conduction in the $Gd_2Ti_2O_7$- $Gd_2Zr_2O_7$ system. Solid State Ion 28:470–474
28. Stewart JR, Ehlers G, Wills AS, Bramwell ST, Gardner JS (2004) Phase transitions, partial disorder and multi-k structures in $Gd_2Ti_2O_7$. J Phys: Condens Matter 16(28):L321
29. Kumar A et al (2022) Probing the short-range ordering of ion irradiated Gd_2Ti_2-$yZryO_7$ ($0.0 \leq y \leq 2.0$) pyrochlore under electronic stopping regime. J Nucl Mater 564:153682
30. Nakamura K, Mori M, Itoh T, Ohnuma T (2016) Theoretical and experimental investigation of defect formation/migration in $Gd_2Ti_2O_7$: general rule of oxide-ion migration in $A_2B_2O_7$ pyrochlore. AIP Adv 6(11):115003
31. Zhang FX, Wang JW, Lian J, Lang MK, Becker U, Ewing RC (2008) Phase stability and pressure dependence of defect formation in $Gd_2Ti_2O_7$ and $Gd_2Zr_2O_7$ pyrochlores. Phys Rev Lett 100(4):45503
32. Sharma SK et al (2020) Structural, dielectric and electrical properties of pyrochlore-type $Gd_2Zr_2O_7$ ceramic. J Mater Sci: Mater Electron 31:21959–21970
33. Akhbarifar S (2020) Thermoelectric properties and transport mechanisms of lead-and lead-yttrium ruthenate pyrochlores. The Catholic University of America
34. Drey DL et al (2020) Disorder in Ho_2Ti_2–$xZrxO_7$: pyrochlore to defect fluorite solid solution series. RSC Adv 10(57):34632–34650
35. Janish MT et al (2020) In-situ re-crystallization of heavily-irradiated $Gd_2Ti_2O_7$. Acta Mater 194:403–411
36. Suganya M et al (2022) Raman and photoluminescence spectroscopic studies on structural disorder in oxygen deficient $Gd_2Ti_2O_7$-δ single crystals. Cryst Res Technol 57(4):2100287
37. Park SJ et al (2018) The effective fingerprint detection application using $Gd_2Ti_2O_7$: Eu3+ nanophosphors. J Alloys Compd 741:246–255
38. Ćulubrk S, Antić Ž, Marinović-Cincović M, Ahrenkiel PS, Dramićanin MD (2014) Synthesis and luminescent properties of rare earth (Sm3+ and Eu3+) Doped $Gd_2Ti_2O_7$ pyrochlore nanopowders. Opt Mater (Amst) 37:598–606
39. Xia J, Lei L, Dai X, Ling J, Li Y, Xu S (2018) Excitation-dependent multi-color emissions in Yb/Er/Eu: $Gd_2Ti_2O_7$ pyrochlore for anti-counterfeiting. Mater Res Bull 107:213–217. https://doi.org/10.1016/j.materresbull.2018.07.027
40. Kulriya PK, Yao T, Scott SM, Nanda S, Lian J (2017) Influence of grain growth on the structural properties of the nanocrystalline $Gd_2Ti_2O_7$. J Nucl Mater 487:373–379

Graphical User Interface (GUI): Characterization Technique for Photonic and Plasmonic Structures

Pushpa Bindal and Ayasha Malik

1 Introduction

As we are aware that invention of lasers in 1960 revolutionized the field of optical fiber communication. The information carrying capacity of these optical fibers is high and losses are low. Active research in this area made the ultrafast internet possible in today's world. It is possible to send more than 10 terabits of information per second through a hair thin optical fiber, which is equivalent to 150 million telephone calls.

As shown in Fig. 1, an optical fiber is a hairlike material having a cylindrical geometry. It consists of a high index medium known as 'core', surrounded by a slightly lower index medium known as 'cladding'. A plastic coating covers the fiber to protect it from damages. The laser light incident on the fiber at suitable angles can propagate as its 'modes' which are transverse field distributions propagating through the fiber unchanged in form except for a phase change. In order to fully exploit the advantages of optical fibers, optical waveguides, plasmonic waveguides having metallic interfaces and devices made with them, it is extremely important to understand their modes and hence the need to develop the tools to evaluate the propagation characteristic of these modes.

'Graphical user interface' or 'GUI' is a form of interface that enables users to communicate with the application program using visual elements, symbols, and metaphors. In the context of Scilab, an open-source programming language, the GUI is an application software that provides users with an interactive environment to perform modeling, statistical analysis, numerical optimization, and other scientific computations [1]. By leveraging symbols and other visual elements, the GUI facilitates user communication with Scilab and displays output results in graphical as well as tabular formats. This makes the GUI an extremely useful asset for simulators

P. Bindal (✉) · A. Malik
Department of Physics, Kalindi College (University of Delhi), East Patel Nagar, New Delhi 110008, India
e-mail: pushpabindal@kalindi.du.ac.in

S. B. Krupanidhi et al. (eds.), *Recent Advances in Functional Materials and Devices*, Springer Proceedings in Materials 37, https://doi.org/10.1007/978-981-99-6766-7_6

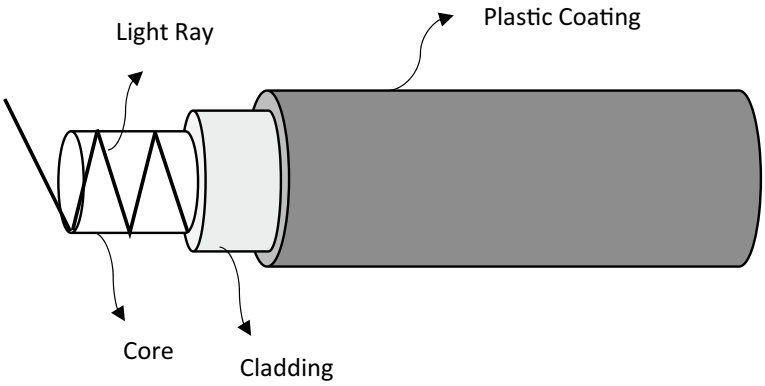

Fig. 1 Cross-sectional view of an optical fiber

of physics problems, as it allows users to visualize the simulation results and make decisions based on the data [2].

This paper presents a tool that can easily be used to solve and examine photonic and plasmonic structures in a simple and accessible manner. The tool includes a graphical user interface for studying photonics problems such as planar waveguides and directional couplers made of plasmonic planar waveguides. The waveguidance phenomenon and characterization in these structures can be effectively visualized through graphs. In the past few years, a lot of theoretical and experimental work has been carried out on plasmonic waveguides and devices made with them [3] and therefore the current study of these waveguides is highly relevant.

2 Working and Development of GUI

Graphical User Interface (GUI) development involves designing user interfaces using built-in components rather than writing long programs. One must install "guibuilder" from the module manager atoms in order to begin developing GUI [4, 5]. After installation, GUI builder display can be accessed by typing "guibuilder" on the command line as shown in Fig. 2a.

The GUI builder consists of two parts, namely the GUI builder palette and graphical window as shown in Fig. 2b. The GUI builder palette contains various built-in components such as push buttons, radio buttons, toolbars, text boxes, edit boxes, sliders, check boxes, and more [6]. One can create different GUIs exhibiting a variety of visual representations by choosing suitable icons and dragging them into the graphical window. Once the GUI is designed, the corresponding code for the same will be generated at the back end, which can be altered if required [4].

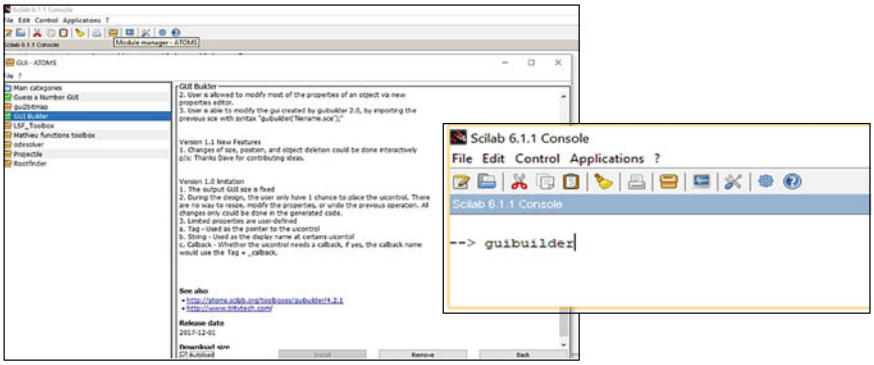

Fig. 2(a). Guibuilder Insatallation

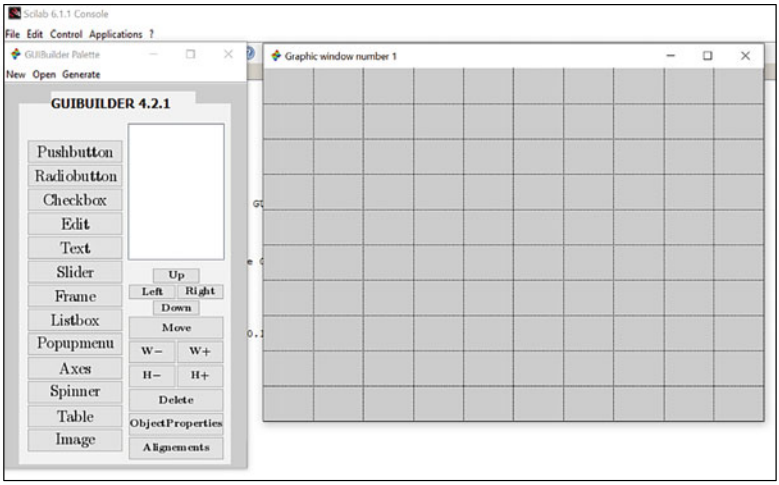

Fig. 2(b). Guibuilder consist of gui palatte and graphic window

Fig. 2 **a** Guibuilder insatallation, **b** Guibuilder consist of GUI palatte and graphic window

The illustration (see Fig. 3) shows a GUI with text boxes for input and output parameter tags, sliders for continuous values, and pushbuttons to retrieve output results and graphs. The edit boxes labeled “input 1” and “input 2” are for inserting input parameters, while “method 1” and “method 2” display output. The right area is for displaying graphs. Input parameters can be changed via sliders, and edit boxes.

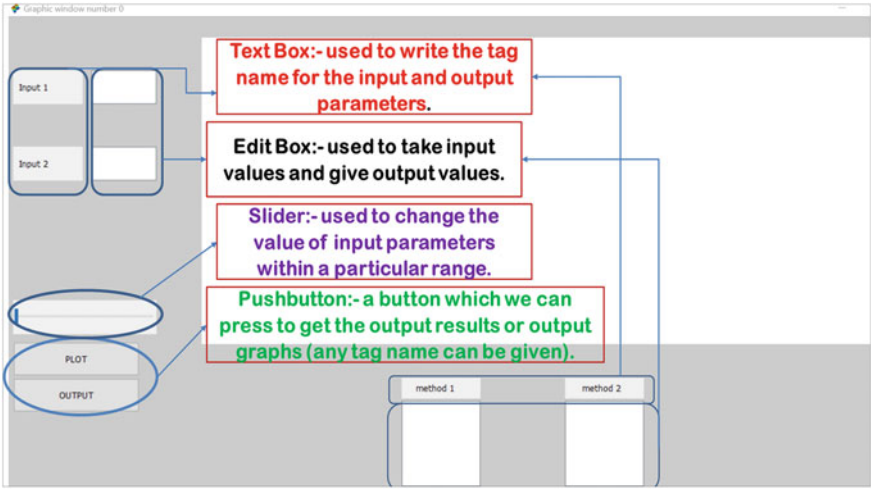

Fig. 3 Graphical User Interface (GUI): an instance

3 Modeling

3.1 Symmetric and Antisymmetric Modes of Planar Waveguide

We have considered a step index planar waveguide (shown in Fig. 4) of width 'a' with n1, n2 as refractive indices of its core and cladding medium. As we are well aware, waveguidance of light waves takes place by total internal reflection in the waveguide.

Solving the Maxwell's equations for the structure, one arrives at the scalar wave equation for TE modes of the weakly guiding approximation [7]

$$\frac{d^2\psi}{dx^2} + \left[k_0^2 n^2(x) - \beta^2\right]\psi = 0 \tag{1}$$

where ψ is the modal field, k_0 is the free space wave number, $n^2(x)$ is the refractive index distribution shown in Fig. 4b and β is the propagation constant. Taking care of the continuity conditions for modal field and its derivative at the boundaries, one obtains the transcendental equations for transverse electric (TE) mode as:-

$$\text{Symmetric mode: } p\tan p = \left[\left(\frac{V}{2}\right)^2 - p^2\right]^{\frac{1}{2}} \tag{2a}$$

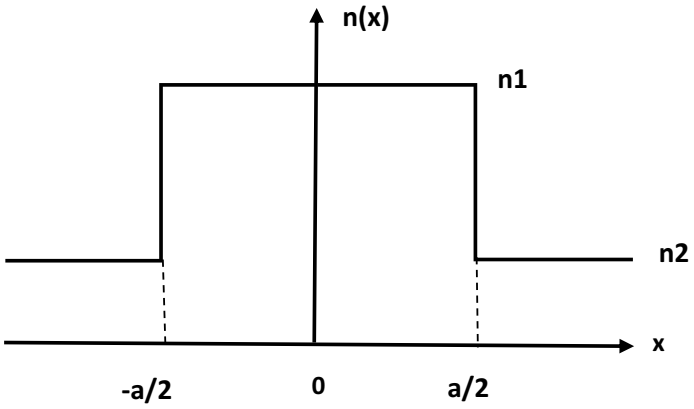

(a). Refractive index distribution

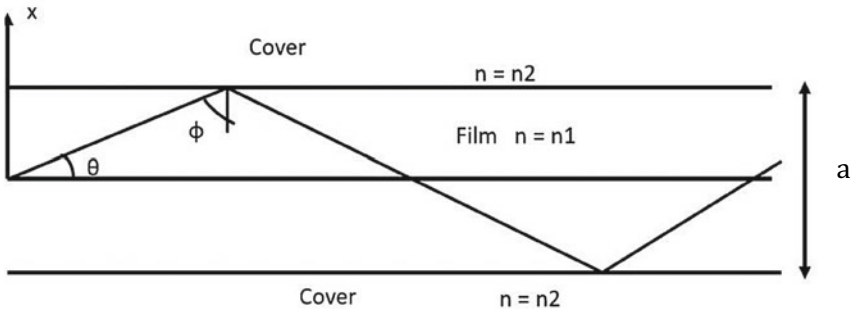

(b). Step index planar waveguide

Fig. 4 **a** Refractive index distribution, **b** Step index planar waveguide

$$\text{Antisymmetric mode: } -p\cot p = \left[\left(\frac{V}{2}\right)^2 - p^2\right]^{\frac{1}{2}} \tag{2b}$$

where $p = \frac{ma}{2}$; $\mathrm{m} = \left[k_0^2 n1^2 - \beta^2\right]^{\frac{1}{2}}$.

V is a dimensionless waveguide parameter, $V = k_0 \mathrm{a}\left(n1^2 - n2^2\right)^{1/2}$.

We have developed a GUI to obtain symmetric and antisymmetric modes of the planar waveguides as shown in Fig. 5a, b.

Fig. 5(a): $n1 = 1.503$, $n2 = 1.5$, a = 4 μm and λ = 0.5 μm

Fig. 5(b): $V = 10$.

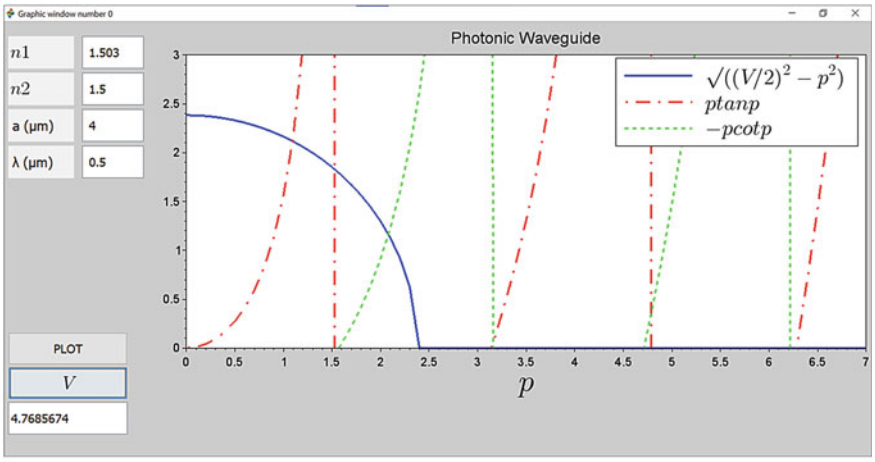

(a)

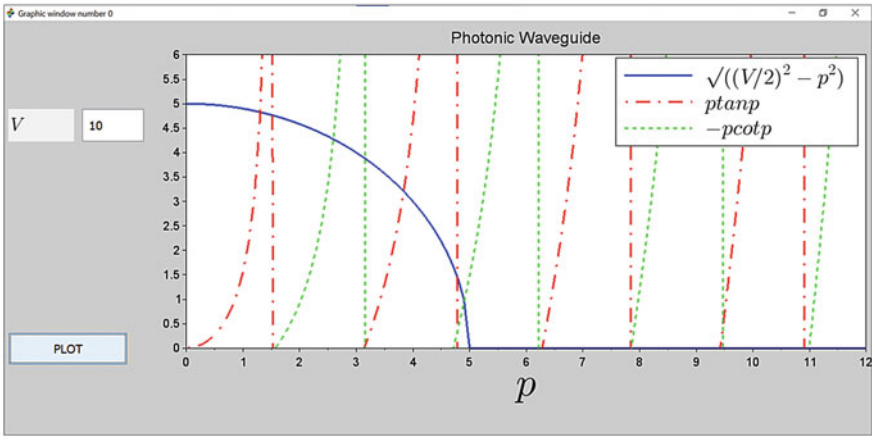

(b)

Fig. 5 **a** GUI for symmetric and antisymmetric modes of planar waveguide. **b** GUI for symmetric and antisymmetric modes of planar waveguide when value of 'V' is given

3.2 Plasmonic Planar Waveguide

Here, we have considered a plasmonic planar waveguide as shown in Fig. 6, having a metal interface at one boundary, making the field vanish at that interface, thereby generating plasmons at the interface. We also developed GUI for the same to obtain modes of the plasmonic planar waveguide [7] (see Fig. 7). The refractive index distribution for the plasmonic planar waveguide is given in Eq. (3).

$$\mathrm{n(x)} = \mathrm{n1 \text{ for } 0 < x < t} \tag{3a}$$

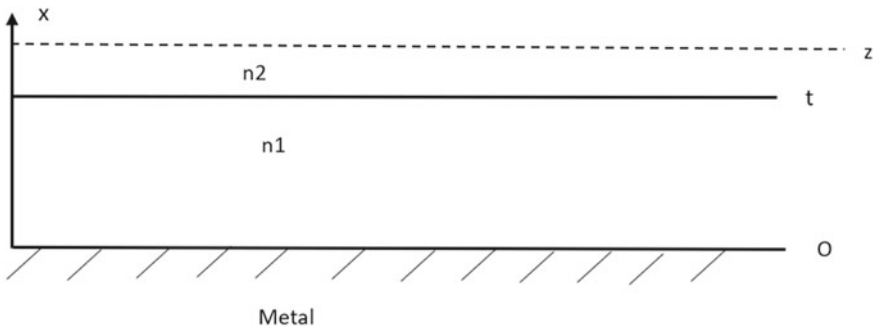

Fig. 6 Plasmonic planar waveguide with dielectric on one side and metal on other

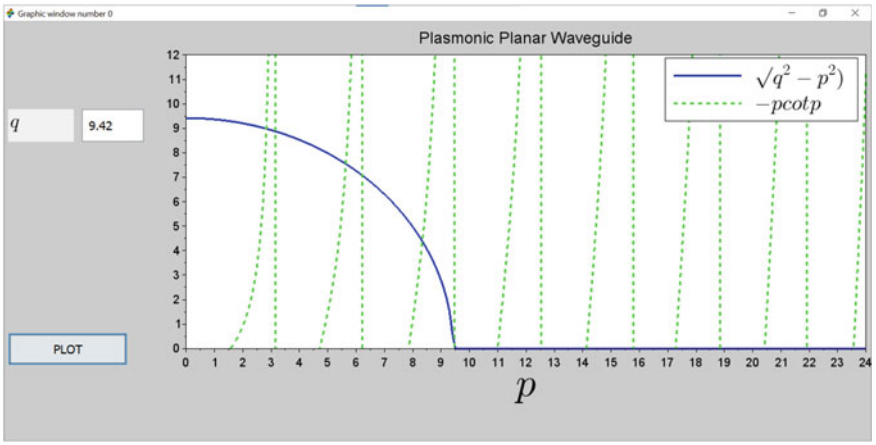

Fig. 7 GUI created to obtain modes of plasmonic planar waveguide

$$\mathrm{n(x)} = \mathrm{n2 \text{ for } x} > \mathrm{t} \tag{3b}$$

modal field would vanish at x = 0, transcendental equation for transverse electric (TE) mode is given by:-

$$-p\cot p = \left[q^2 - p^2\right]^{\frac{1}{2}} \tag{4}$$

where, $q = k_0 t\left(n1^2 - n2^2\right)^{1/2}$

and $p = t\left[k_0^2 n1^2 - \beta^2\right]^{\frac{1}{2}}$

Results are shown in Fig. (7) for $q = 3\pi$.

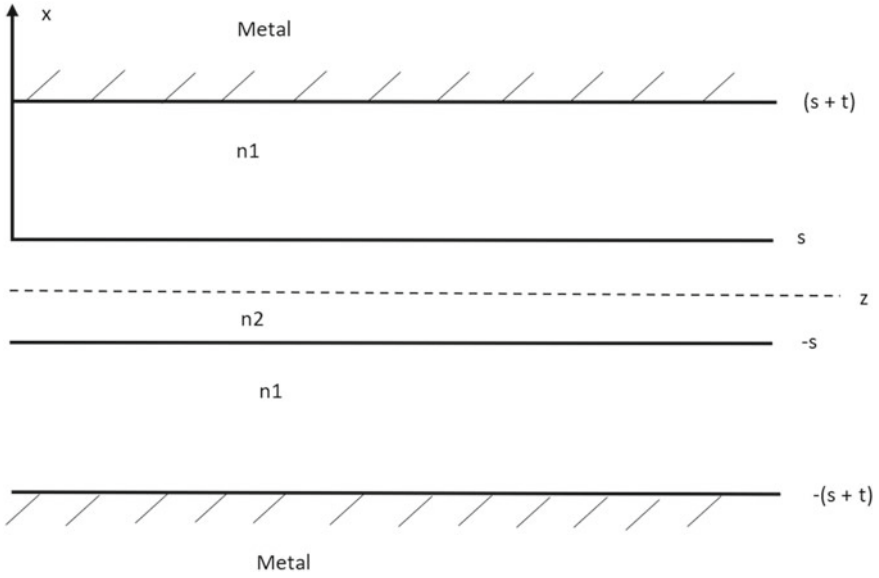

Fig. 8 Directional coupler consisting of two plasmonic planar waveguide

3.3 Directional Coupler Consisting of Plasmonic Planar Waveguides

We also developed a GUI for a directional coupler made with two identical plasmonic waveguides (see Fig. 8). Results of modal analysis of this directional coupler are shown in Fig. 9a, b.

For this structure with a metal boundary at $|x| = s + t$ (as shown in Figure above):-

$$n(x) = n2 \text{ for } |x| < s \tag{5a}$$

$$n(x) = n1 \text{ for } s < |x| < s + t \tag{5b}$$

We have assumed $n2 < \beta/k_0 < n1$ for this waveguide.

Transcendental equation for symmetric and antisymmetric transverse electric (TE) mode is given by:-

$$-\frac{\left(q^2 - p^2\right)^{1/2}}{p}\tan p = (\text{cothus})^{\pm 1} \tag{6}$$

where, q and p are same as for single plasmonic waveguide defined above and

$$u^2 = \beta^2 - k_0^2 n2^2$$

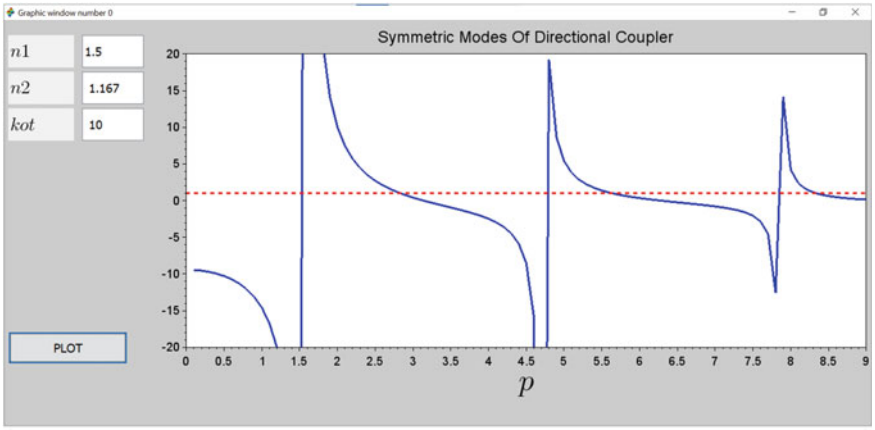

(a)

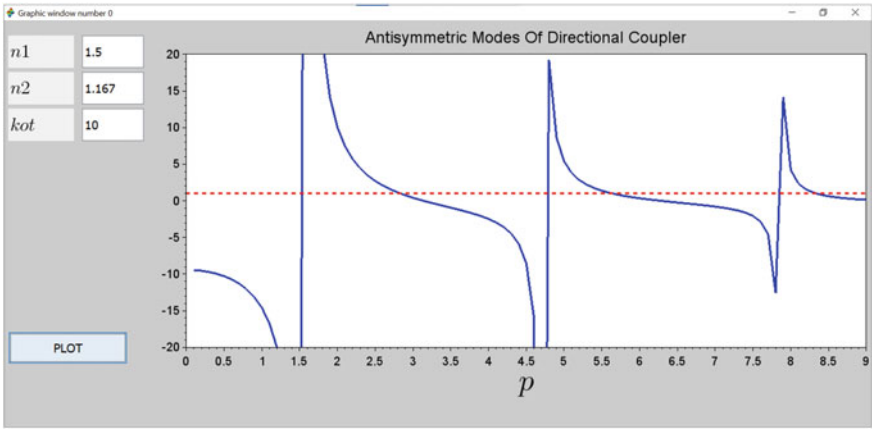

(b)

Fig. 9 **a** GUI for symmetric modes of directional coupler, **b** GUI for antisymmetric modes of directional coupler

$+$ and $-$ signs correspond to symmetric and antisymmetric modes respectively.

We have considered $n1 = 1.5$, $n2 = 1.167$, $k_0 t = 10$, (t/s) $= 0.2$ to develop GUI for the symmetric and antisymmetric modes of the directional coupler as shown in Fig. 9a, b. The results shown in Figs. 5a, 7 and 9a, b are displayed in Tables 1, 2, 3 and 4 for planar waveguide, plasmonic waveguides and Directional coupler along with manual results.

4 Comparison Table

For Planar Waveguide.

Table 1 Values of p for T.E. mode of planar waveguide

Mode	Manual	GUI
Symmetric	1.094	1.094
Antisymmetric	2.081	2.081

Table 2 Values of p for T.E. mode of plasmonic planar waveguide

Manual	GUI
2.836	2.829
5.641	5.639
8.339	8.340

Table 3 Values of p for symmetric T.E. mode of directional coupler

Manual	GUI
2.821	2.822
5.600	5.606
8.237	8.269

Table 4 Values of p for antisymmetric T.E. mode of directional coupler

Manual	GUI
2.849	2.841
5.682	5.681
8.476	8.381

For Plasmonic Planar Waveguide.
For Directional Coupler.

5 Conclusion

In conclusion, the creation of graphical user interface that enables precise determination of roots of the symmetric and antisymmetric modes of a planar waveguide and the symmetric modes of directional couplers has been carried out. It can prove to be a significant step toward virtual laboratory, which is a need of the hour. This approach of characterization to the photonic and plasmonic structures will provide researchers a potent tool to explore these structures more thoroughly, leading to new innovations. The accurate roots obtained through this approach demonstrate its effectiveness and reliability, making it a valuable tool for researchers. Overall, graphical user interface will help in the development of the field of photonics and plasmonics, enabling researchers to study these structures more precisely and intelligently.

6 Applications

Scilab's Graphical User Interface (GUI) is a potent tool that has numerous applications in various fields. GUI can assist users rapidly and readily see the data they are working with in pre-computational analysis. Additionally, it can help enhance the basic understanding of physics concepts by offering a simple and interactive platform for learning and experimentation. The user-friendliness of GUI makes it the perfect tool for problem-solving and simulation in a variety of applications, including fluid dynamics, picture enhancement, and signal processing, etc. [2]. GUI is a valuable and adaptable tool that can help with a variety of facets of scientific study and research. It can also help experimentalists working with plasmonic integrated circuits [3] to verify and also improve their results.

References

1. Nagar S (2017) Introduction to Scilab: for engineers and scientists. Apress
2. Serway RA, Jr. Jewett JW (2015) Physics for Scientists and Engineers:Technology Update. Brooks/Cole Pub Co.
3. Fang Y, Sun M (2015) Nanoplasmonic waveguides: towards applications in integrated nanophotonic circuits. Light: Sci Appl 4:e294. https://doi.org/10.1038/lsa.2015.67
4. https://www.scilab.org/application-development-gui-building
5. https://en.wikipedia.org/wiki/Scilab
6. https://atoms.scilab.org/toolboxes/guibuilder
7. Ghatak A, Thyagarajan K (1998) Introduction to fiber optics. Cambridge University Press, Cambridge. Reprinted by Foundation Books, New Delhi (2008)

Effect of Synthesis Conditions on the Photoluminescent Properties of Eu Doped Gadolinium Oxide Phosphors

Kajal Kaushik, Ruby Priya, Harmanpreet Kaur, Kulwinder Singh, and O. P. Pandey

1 Introduction

Rare-earth activated phosphors have appealing applications in the optoelectronic and display devices as their emission spectra is sharp, intense, and narrow. The emission properties depend on various factors among which host lattice and dopant play a vital role. Rare-earth (RE) oxides are the promising host matrices. Among the various RE-oxides, Gd_2O_3 is an appropriate host matrix for the europium (Eu) ions [1–4]. This is for the reason that ionic radii of europium ions are close to gadolinium ions and both the elements have same valency [5–7].

Gd_2O_3:Eu is a bi-probe as it can show paramagnetic as well as luminescent behavior. These properties make it useful in potential applications such as opto-electronic devices and biomedical applications. It exhibits sharp, narrow, and intense emission bands under UV excitation. Till now, synthesis of Gd_2O_3:Eu has been reported by various routes. Among the various methods, co-precipitation route is a promising chemical method for the synthesis of pure cubic Gd_2O_3 phosphors. Earlier reports showed that cubic phase Gd_2O_3:Eu has improved luminescent characteristics as compared to monoclinic crystal phase [8–10].

K. Kaushik · R. Priya (✉) · H. Kaur
Department of Physics, University Institute of Sciences, Chandigarh University, Mohali, Punjab 140413, India
e-mail: ruby.e10411@cumail.in

K. Singh
University Centre for Research and Development, Chandigarh University, Mohali, Punjab 140413, India

O. P. Pandey
Functional Materials Lab, School of Physics and Materials Science, Thapar Institute of Engineering and Technology, Patiala, Punjab-140, India

S. B. Krupanidhi et al. (eds.), *Recent Advances in Functional Materials and Devices*, Springer Proceedings in Materials 37, https://doi.org/10.1007/978-981-99-6766-7_7

In the present work, we have synthesized Gd_2O_3:4mol%Eu phosphors by co-precipitation route with the variation of temperature and pH during synthesis. The synthesized phosphors are characterized by various techniques.

2 Materials and Methods

Starting precursors such as gadolinium nitrate hexahydrate (99.99%), and europium nitrate hexahydrate (99.99%) have been purchased from Alfa Aesar. Ammonia solution (25 wt%,) and ethanol (99.9%) were used as solvents and acquired from Loba Chemie Pvt. Limited. Synthesis process involves the dissolution of stoichiometric quantities of gadolinium as well as europium precursors for the preparation of 0.1 M. To this solution, pH at 8 and 10 was maintained through dropwise addition of ammonia solution. The solution was aged for 24 h, centrifuged followed by water and ethanol washing using Whatman filter paper. After drying at 60 °C, precipitates were heat treated for 4 h at 800 °C in the programmed muffle furnace followed by grounding (to form uniform powder) to use for various characterizations respectively.

3 Characterization Techniques

X-ray diffraction (XRD) diffractograms were obtained with the help of XRD diffractometer (Panalytical X'Pert Pro) in the range from 10° to 80° with a step interval of 0.0131° at normal scan rate. Exstar TG/DTA 6300 was used to obtain thermographs corresponding to different samples in nitrogen environment. The heating rate was set to 10 °C/min. Field-emission scanning electron microscopic (FESEM) images were taken at operating voltage of 20 kV using Carl Zeiss FESEM. The emission spectrums of different phosphors were acquired with the help of Xenon lamp incorporated fluorescence spectrophotometer (Agilent Technologies- Model Cary Eclipse).

4 Results and Discussion

4.1 XRD Results

Figure 1a, b represents the XRD diffractograms of as-prepared precipitates at pH 8 and 10. All XRD peaks resemble to the standard ICDD card (01-083-2037) of $Gd(OH)_3$ phase having hexagonal crystal structure. The space group symmetry of characterized sample is P63/m. Matching of all the diffraction peaks indicates the high purity of $Gd(OH)_3$. High crystallinity of $Gd(OH)_3$ phase is confirmed from sharp as well as intense diffraction peaks. Depending upon TG results, the obtained

samples are calcined at 800 °C to ensure the complete crystallization into the oxide phase.

XRD patterns of Gd_2O_3 prepared at pH 8 and 10 after calcining $Gd(OH)_3$ at 800 °C are presented in Fig. 2a, b. After careful investigation, diffraction patterns have been matched through standard ICDD card 03-065-3181, confirmed the establishment of pure Gd_2O_3 phase with BCC crystal structure having Ia-3 (206) group symmetry. Absence of impurity peak(s) due to $Gd(OH)_3$ infers the Gd_2O_3 single phase formation. Further, high crystallinity of prepared Gd_2O_3 was revealed from sharp as well as intense diffraction peaks. This shows that hydroxides are completely converted into oxides.

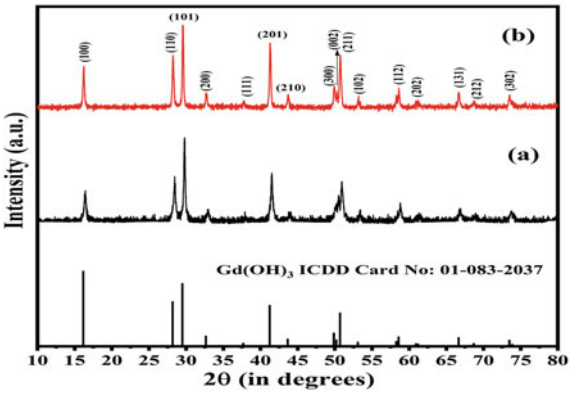

Fig. 1 Diffraction patterns of samples synthesized at **a** pH = 8, and **b** pH = 10, respectively

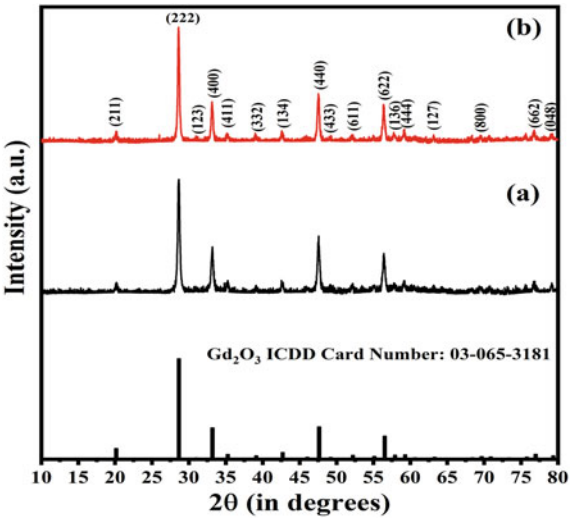

Fig. 2 XRD patterns of Gd_2O_3 calcinated samples synthesized at **a** pH = 8, and **b** pH = 10

4.2 Thermal Behavior of As-Synthesized Samples

The thermal behavior of prepared $Gd(OH)_3$ powders at different pH values are analyzed via TG/DTG curves, as shown in Fig. 3. The TG curves represent two stages at which weight loss can be clearly seen. The sample synthesized at pH 8 shows different weight loss stages around 323.24 and 410.81 °C, respectively. The weight losses corresponding to these temperatures are ~6.08 and ~6.71%, respectively. However, in the case of sample synthesized at pH 10, weight losses are observed at 306.21, and 419.41 °C, and the corresponding weight losses are ~8.95 and ~4.11%, respectively. The variation in the temperature and weight losses in the TG curves indicates the formation of intermediate products during calcination. In literature, it is reported that lanthanide hydroxides have the LnOOH phase as an intermediate product when dehydration of $Ln(OH)_3$ takes place [11]. Based on this, dehydration of the synthesized $Gd(OH)_3$ is considered to following dehydration steps:

$$Gd(OH)_3 \rightarrow GdOOH + H_2O \quad (1)$$

$$2GdOOH \rightarrow Gd_2O_3 + H_2O \quad (2)$$

The total experimental weight loss for $Gd(OH)_3$ prepared at pH = 8 and 10 is 12.79% and 13.1%, respectively. These experimentally determined values are very close to the theoretical value of weight loss of $Gd(OH)_3$, i.e. 12.97% [12, 13].

The micrographs of Gd_2O_3:4mol%Eu calcined at 800 °C and synthesized at pH (8 and 10) are shown in Fig. 4a, b. Samples prepared at pH 8 do not have particular morphology, as shown in Fig. 4a. The sample consists of irregular shape particles having rod-like features. The length of the rods is found to be in the range 200–400 nm and diameter around 90–150 nm. The average size of the particles lies in the range 55–90 nm. However, samples synthesized at pH 10 (Fig. 4b) have uniform

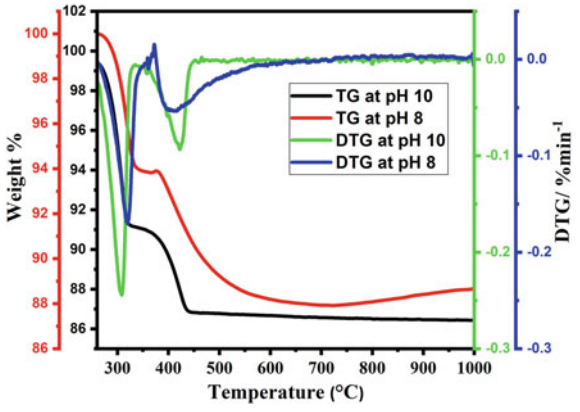

Fig. 3 TG/DTG curves of as-prepared samples at pH 8 and 10

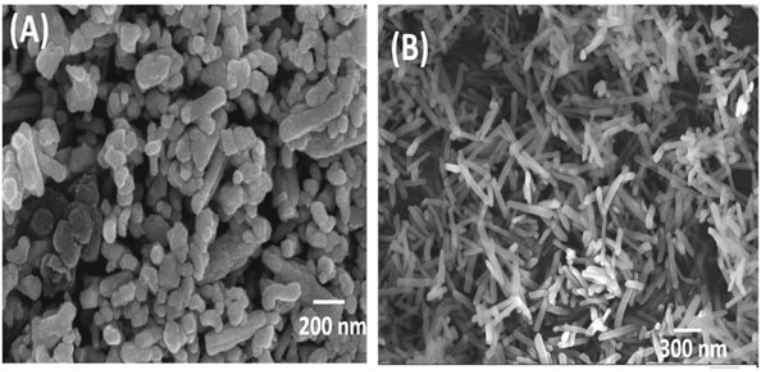

Fig. 4 FESEM micrographs of Gd_2O_3:4 mol%Eu phosphors obtained at **a** pH 8 and **b** pH 10

rod-like morphology with nano dimensions. The rod-like morphology is related to the self or induced scrolling mechanism [14]. The diameter of the rods is found in the range 70–120 nm, and the length around 200–500 nm.

4.3 Photoluminescence Results

The effect of pH as well as calcination temperature on luminescent characteristics of Gd_2O_3:4mol% is also investigated. Emission spectra of Gd_2O_3:4mol% with respect to pH and calcination temperature are shown in Fig. 5. The obtained spectrums comprise sharp, intense, and narrow emission peaks. Emission bands observed at approximately 592, 612, 625, 650, and 705 nm correspond to europium ion transitions, i.e., $^5D_0 \rightarrow {}^7F_{1,2,3,4}$ respectively [15]. Among all the peaks, the peak observed at 612 nm ($^5D_0 \rightarrow {}^7F_2$) has the highest intensity, which is hypersensitive and dominant emission transition.

Cubic Gd_2O_3 exhibits two symmetry sites, i.e., C_2 and S_6, having 3:1 ratio respectively. From which non-inversion symmetry is possessed C_2 symmetry sites whereas inversion symmetry is occupied by S_6 symmetry sites. As soon as europium occupies S_6 sites, peak corresponding to the 592 nm dominates. The emission peak at 612 nm dominates if europium ions occupy C_2 sites in Gd_2O_3 lattice [16].

Figure 5 also cleared that PL emission increases with rise in calcination temperature and is found maximum at 800 °C. Further increase in calcination temperature, i.e., 800 °C beyond leads to decrease in the PL intensity due to enlargement of non-radiative transitions. On the other hand, emission intensity is observed maximum at pH 10 compared to the sample synthesized at pH 8. The fall in PL intensity at low pH is attributed to the non-uniform morphology, irregular shapes, and agglomeration observed in the samples. The maximum PL is obtained for the sample, which is synthesized at pH 10, and calcined at 800 °C.

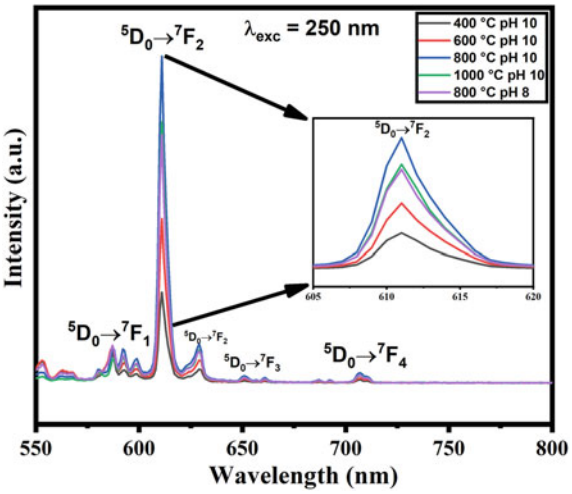

Fig. 5 PL emission spectra of Gd_2O_3:4 mol%Eu phosphors synthesized at different pH and temperature values

5 Conclusion

The uniform shape, phase pure, and crystalline Gd_2O_3:4 mol%Eu samples were synthesized via co-precipitation route. XRD patterns confirmed the cubic phase of Gd_2O_3 samples. FESEM results revealed the rod type morphology of the samples synthesized at pH 10, while mixed particle and rod-like morphology was obtained at pH 8. Moreover, PL emission intensity was found higher for samples prepared at pH 10, which is due to the uniform morphology of the samples. Moreover, with increase in temperature, PL intensity was found to increase and was maximum for samples calcined at 800 °C.

Acknowledgements Authors are highly grateful to Sukhvir Singh for his constant support and encouragement. Authors are thankful to SAI labs, TIET, Patiala for XRD characterizations. Authors also acknowledge the support provided by Dr. Puneet Sharma and Dr. B.N. Chudasama, TIET for PL and TG results.

References

1. Chaudhary S, Kumar S, Umar A, Singh J, Rawat M, Mehta SK (2017) Sens Actuators B Chem 243:579–588
2. Chen J, Shi Y, Shi J (2004) J Mater Res 19:3586–3591
3. Kumar RGA, Hata S, Gopchandran KG (2013) Ceram Int 39:9125–9136
4. Dhananjaya N, Nagabhushana H, Nagabhushana BM, Rudraswamy B, Shivakumara C, Ramesh KP, Chakradhar RPS (2011) Phys. B Phys. Condens. Matter. 406:1645–1652
5. Jain A, Hirata GA (2016) Ceram Int 42:6428–6435
6. Li J, Zhu Q, Li X, Sun X, Sakka Y (2011) Acta Mater 59:3688–3696
7. Ansari AA, Ahmad N, Labis JP (2019) J Photochem Photobiol A Chem 371:10–16

8. Wang Z, Wang P, Zhong J, Liang H, Wang J (2014) J Lumin 152:172–175
9. Iwako Y, Akimoto Y, Omiya M, Ueda T, Yokomori T (2010) J Lumin 130:1470–1474
10. Majeed S, Shivashankar SA (2014) J. Mater Chem C 2:2965–2974
11. Thongtem T, Phuruangrat A, Ham J, Lee S, Thongtem S (2010) CrystEngComm 12:2962–2966
12. Kaur G, Sharma P, Priya R, Pandey OP (2020) J Alloys Compd 822:153450
13. Priya R, Pandey OP (2018) Vacuum 156:283–290
14. Boopathi G, Gokul Raj S, Ramesh Kumar GR, Mohan (2018) Indian J Phys 92:715–724
15. Li Y, Hong G (2007) J Lumin 124:297–301
16. Lin CC, Lin KM, Li YY (2007) J Lumin 126:795–799

Extraction of Carbon from Biomass-Based Bamboo and Coconut Husk for Enhancement of High-Performance Supercapacitor

Giriraj Dandekar, Gauresh Godkar, Omkar Salvi, Brijeshkumar Yadav, Mahadev Sonavane, and Rounak Atram

1 Introduction

Nowadays, everything is powered by electricity, including your mobile phone, laptop, and so on. As a result, a range of energy technologies, including traditional fossil fuels and sustainable options like solar panels, are employed globally to meet the growing energy demand. However, with the rapid increase in population and energy consumption, the importance of green energy has become paramount [1, 2]. To meet these demands, energy storage devices like batteries, capacitors, supercapacitors, and fuel cells are crucial. While batteries can store energy, they cannot charge rapidly, and capacitors, while quick to charge, have limited storage capacity [1, 3]. To overcome these limitations, researchers have turned to supercapacitors as a promising solution. The supercapacitor is a one-of-a-kind energy storage technology that outperforms batteries in a variety of ways. It is an electrochemical device with a high energy density, power density, and capacity, allowing it to charge faster and store more energy than batteries. Supercapacitors have many advantages, including a fast cycle rate, high power density, durability, extended life, and environmentally benign operation. Supercapacitors have wide-ranging applications in various fields, including the military, electric vehicles, and the medical sector, among others [4]. Based on their charge-storing mechanism, supercapacitors are divided into two types: Electric Double Layer Capacitors (EDLC) and Pseudocapacitors. EDLC stores charge faradaically, whereas Pseudocapacitors stores charge non-faradaically.

G. Dandekar · G. Godkar · O. Salvi · R. Atram (✉)
Department of Physics, M.M College of Arts, N.M. Institute of Science, H.R.J College of Commerce, Bhavans College, Andheri-(W), Mumbai 400058, India
e-mail: rounak.atram@bhavans.ac.in

B. Yadav · M. Sonavane
Department of Physics, The Institute of Science, Dr. Homi Bhabha State University, 15, Madam Cama Road, Fort, Mumbai 400032, India

S. B. Krupanidhi et al. (eds.), *Recent Advances in Functional Materials and Devices*, Springer Proceedings in Materials 37, https://doi.org/10.1007/978-981-99-6766-7_8

Carbonaceous materials such as Graphene, CNT, CNF, biomass-derived carbon, and rGO are typically utilized as EDLC electrode materials, whereas metal oxides and conducting polymers are employed as Pseudocapacitors electrode materials [1, 3]. The properties of the electrode material and the electrolyte heavily influence the optimal performance of a supercapacitor [5, 6]. The surface area and pore size of the electrode material, in particular, are significant parameters influencing energy storage capacity and charge transfer efficiency [7, 8]. Carbonaceous materials such as graphite, carbon fibers, and carbon nanotubes have been intensively explored as possible electrode materials for supercapacitors, as have more recent innovations such as graphene, carbon black, activated carbon, biochar, hollow spheres, and mesoporous carbon [5, 7]. Biomass-derived carbon is a significant area of research due to its low cost, abundance, and renewable nature and may be extracted from a variety of biomass wastes [1, 3, 5]. In this study, we focus on comparing biomass-derived carbons from Bamboo and Coconut husk, specifically as electrode materials for supercapacitors. Both materials were chosen for their vast availability and unique properties: Bamboo has a high absorption capacity and extraordinary porous microstructure, while Coconut husk is an extremely fibrous material [9, 10]. The morphological and electrochemical properties of the biomass-derived carbons (BB-400 and CHB) were analyzed through various characterizations. Our results indicate that BB-400 demonstrates favorable electrochemical behavior and could be a promising candidate for supercapacitor applications.

2 Experimental

The pyrolysis and activation of waste biomass materials were performed in lab-scale facilities. The grade of the used chemicals was Analytical and was employed without further purification.

2.1 Sample Preparation

The parts of Bamboo and Coconut husk were collected from the campus of Bhavan's College, Andheri (w), Mumbai, India. After that, both were fragmented into smaller pieces and dried in sunlight until all visible moisture had evaporated [11–13].

2.2 Preparation of BB-400

These collected samples were washed thoroughly with distilled water to remove adhering soil and dust and dried at 125 °C in a Hot Air Oven for 3 h. The next step was to initiate the torrefaction process in the Muffle Furnace at 250 °C for 3 h, after

Fig. 1 Schematic showing preparation of BB-400

which the material was cooled overnight [11–13]. Subsequently, the sample was ground using a mortar and pestle and filtered through layers of cloth. Then, the same filtered sample was placed in silica crucibles and enclosed with numerous layers of aluminum foil to minimize interaction with ambient air except air trapped between gaps of vessels and material being physically activated, resulting in a low-oxygen environment [14]. Now, these samples were filled in tightly sealed crucibles and this setup was put into Muffle Furnace at 400 °C for 2 h for carbonization. [14] (Fig. 1).

2.3 Preparation of CHB Carbon

After we collected the raw CHB, it was kept in a hot air oven for 3 h at 1100 °C for the moisture removal process. Then, CHB was crushed into fine pieces in a mortar and pestle and filtered through layers of cloth. Torrefaction was then initiated for 2 h at 200 °C in a Muffle Furnace. Finally, the carbonization was carried out in a Muffle Furnace for 2 h at 400 °C. It was accompanied by a restricted supply of oxygen. Thus, we extracted the carbon [15] (Fig. 2).

3 Characterization

To study the morphological structure and topology of the samples, such as roughness or smoothness, the samples were examined under a scanning electron microscope (SEM EVO 18, Carl ZEISS, Department of Physics, RTM Nagpur University, India.

Fig. 2 Schematic showing preparation of CHB carbon

The Electrochemical Analysis of BB-400 and CHB Carbon was carried out to determine the performance of the materials. The electrochemical properties of the materials were studied using Cyclic Voltammetry (CV), Galvanostatic Charge Discharge (GCD), and Electrochemical Impedance Spectroscopy (EIS) on the potentiostat in a 1 M H_2SO_4 electrolyte using a three-electrode device with Ag/AgCl serving as the reference electrode, platinum serving as the counter electrode, and the synthesized carbon materials serving as the working electrode.

4 Result and Discussion

4.1 Scanning Electron Microscopy

The SEM images of both materials revealed distinct morphologies. The BB-400 (Fig. 3a) derived carbon material exhibited random-sized pores distributed all over the surface and an excellent interconnected wire fence-like structure. In contrast, CHB-derived carbon showed a rough surface with the occurrence of an agglomeration of bulky particles with tiny and irregular pores between them. These SEM images confirm the previously reported literature that bamboo-derived carbon has a high absorption capacity and extraordinary porous microstructure [9]. This comparison of SEM images for BB-400 and CHB-derived carbon sheds light on the impact of

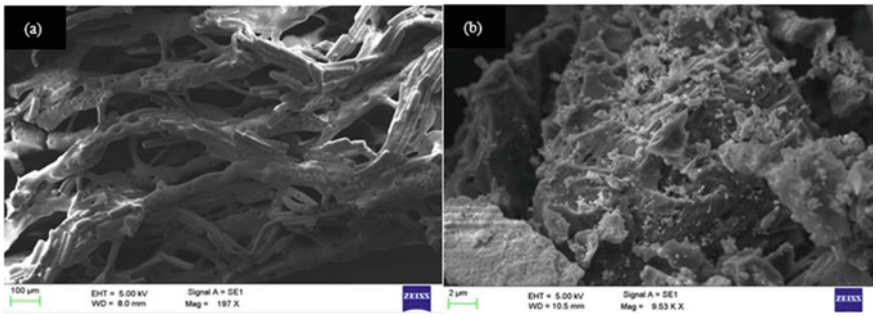

Fig. 3 SEM image of **a** BB-400 at a magnification of 197X, **b** CHB carbon at a magnification of 9.53KX

precursor biomass on the morphology and, therefore, the performance of carbon-based materials. This comparison shows that the biomass used for carbonization has a considerable impact on the shape of the produced carbon material and, as a result, the electrochemical performance of supercapacitor electrodes [5, 7].

4.2 Cyclic Voltammetry

The CV studies were conducted utilizing a three-electrode setup. To assess the capacitance behavior of the materials, CV measurements were performed at different potential windows and scan rates. BB-400 material displayed an almost ideal capacitive behavior, as evidenced by the nearly rectangular shape of the CV curves [16–18]. However, at higher scan rates of 75 mV/s, the CV curves showed some deviations from the ideal rectangular shape, indicating a quasi-rectangle shape at lower scan rates. Despite this, the shape of the CV curve remained unchanged at higher scan rates, suggesting a high degree of chemical stability of the material [19, 20]. In contrast, the CHB carbon also exhibited a quasi-rectangular-like shape in the CV curves, with two redox peaks observed at 0.5 V and 0.3 V. Interestingly, there was a significant increase in the area of the current from 10 mV/s to 100 mV/s, indicating that the material is highly conductive [21]. Furthermore, the oxidation peaks shifted to the right, while the reduction peak shifted to the left with increasing scan rates, which suggests that the material may have a higher resistance to oxidation than reduction [18, 21] (Fig. 4).

4.3 Galvanostatic Charge Discharge

The Galvanostatic Charge Discharge (GCD) analysis of BB-400 showed promising results in terms of its capacitive performance for supercapacitor applications. The

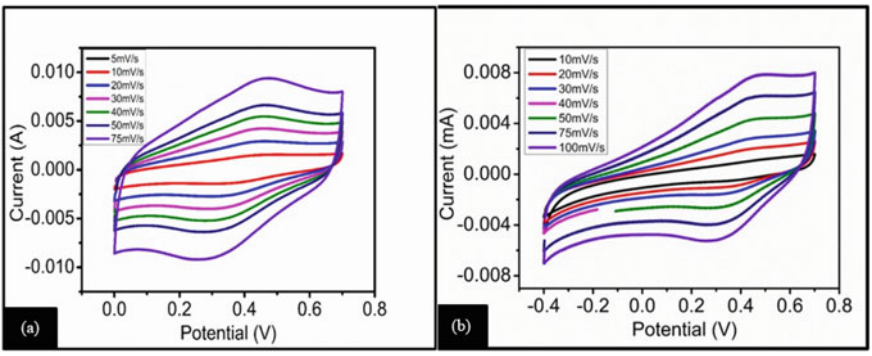

Fig. 4 Cyclic voltammetry of **a** BB-400, **b** CHB carbon

GCD curve exhibited a perfect triangular shape without any IR drop, indicating the reversible nature of the sample and its chemical stability. This behavior is crucial for the long-term stability and reliable operation of supercapacitors [18]. Based on the results of the GCD curves in Fig. 5, the specific capacitance values of the BB-400 were computed. Moreover, the specific capacitance of BB-400 was found to be higher at lower current densities, achieving a maximum value of 188.36 Fg^{-1} at 0.50 Ag^{-1}. However, the specific capacitance decreased to 87 Fg^{-1} at a higher current density of 7 Ag^{-1}. This behavior suggests that BB-400 exhibits good capacitive retention at higher current densities, making it an excellent candidate for high-performance supercapacitors [21]. CHB carbon also showed a standard triangular shape, with a plateau region observed in the potential window range of −0.3 to −0.4 V at a lower current density of 0.5 Ag^{-1}. This behavior is due to a slow charge adsorption of the material, indicating low electrolyte penetration at lower current density [22, 23]. However, at higher current density, no plateau region was observed, suggesting a highly conductive nature of the material. On the other hand, CHB carbon showed a higher specific capacitance of 124 Fg^{-1} at of current density of 1 Ag^{-1}, this value drops to 27 Fg^{-1} at a current density of 5 Ag^{-1}. The discharging time of GCD curves for both materials decreased with increasing current densities [24, 25]. From the description of the GCD curves, it can be concluded that BB-400 is a more suitable material for high current density applications due to its good capacitive retention, while CHB carbon is suitable for low current density applications due to its slow charge adsorption behavior [24].

The specific capacitance of BB-400 and CHB carbon was calculated by [23, 25]

$$C_s = \frac{I \times \Delta t}{m \times \Delta V} \tag{1}$$

where I (in A) is the discharge current, Δt (in s) is the discharge time, ΔV (in V) is the change in working potential and M (in g) is the mass of material.

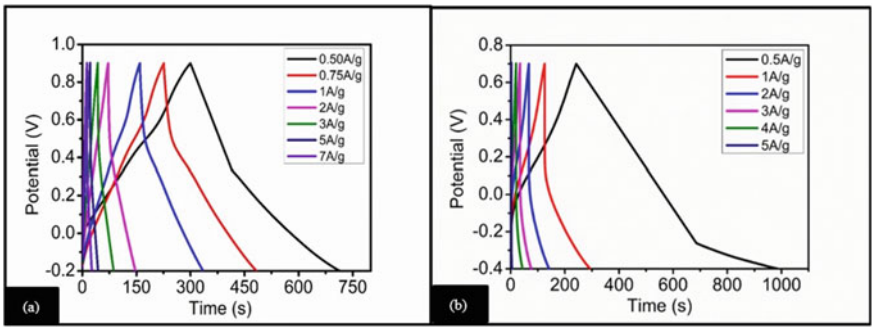

Fig. 5 GCD curves of **a** BB-400, **b** CHB carbon

4.4 Electrochemical Impedance Spectroscopy

EIS measurements were performed on both BB-400 and CHB carbon electrodes to investigate their resistive behavior and these results show that BB-400 and CHB carbon exhibit significant differences in their electrochemical properties. For BB-400, EIS measurements were conducted in the frequency range of 1 MHz to 1 MHz and a small distorted semicircle was observed. This semicircle can be attributed to the charge-transfer process at the electrode–electrolyte interface. The steeper slope in the lower frequency regime indicates that BB-400 has low diffusive resistance of electrodes due to fast ion diffusion [26]. On the other hand, for CHB carbon, EIS measurements were performed in the frequency regime of 0.1–100 kHz. The high-frequency intercept at the real part (Z') indicates the combinational resistance, including the ionic resistance of the electrolyte, intrinsic resistance of active material, and contact resistance of active material and current collector [23, 26]. A semicircle of ~225 Ω was observed in the intermediate frequency region of the Nyquist plot. As we know, the size of the semicircle is directly proportional to the charge transfer resistance (R_{ct}). Therefore, the smaller the semicircle, the faster the charge transfer kinetics of the material [23] (Fig. 6).

This semicircle observed for CHB carbon indicates that the charge transfer resistance at the electrode–electrolyte interface is significant. This means that the transfer of charge is not as efficient as in BB-400, and there is a higher chance of losing energy during the transfer process. Whereas the low charge transfer resistance of BB-400 makes it a promising material for supercapacitor applications.

4.5 Ragone Plot

A Ragone plot, which displays the relation between energy density and power density, can be used to compare the performance of different supercapacitor materials. At low power densities, CHB carbon has the maximum energy density of 5.2 $Whkg^{-1}$

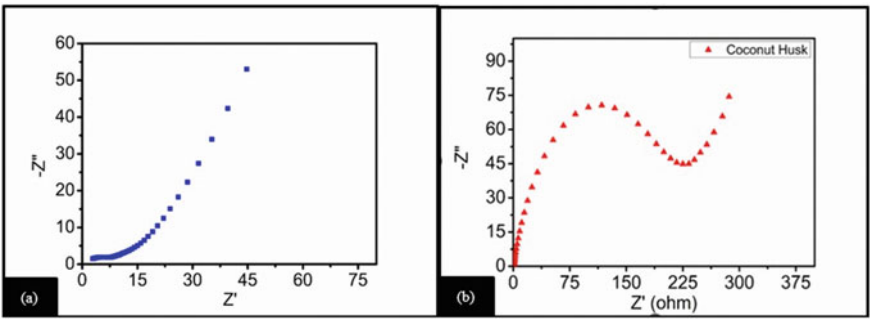

Fig. 6 Nyquist plot of **a** BB-400, **b** CHB carbon

at a power density of 68.57 Wkg^{-1}. However, when the power density grows, the energy density of CHB carbon declines substantially, reaching 1.13 $Whkg^{-1}$at the greatest power density of 271 Wkg^{-1}. As opposed to CHB carbon, BB-400 achieves a greater energy density at higher power densities, with a 3.67 $Whkg^{-1}$ energy density at a 963.67 Wkg^{-1} power density. Results indicate that both materials have their advantages and disadvantages in terms of power and energy density. CHB has a high energy density at low power densities, however, this energy density cannot be maintained at greater power densities. BB-400, on the other hand, has a lower energy density at low power densities but can sustain a reasonably high energy density at higher power densities [27–29]. These statistics are significant because they emphasize how crucial it is to select the right material for each individual application when using supercapacitors. For example, if the application demands a high energy density at a low power density, CHB carbon may be the ideal option. But, BB-400 could be a better option if the application requires a high-power density at higher energy densities (Fig. 7).

The ED and PD of BB-400 and CHB carbon were calculated by [3, 6, 23]

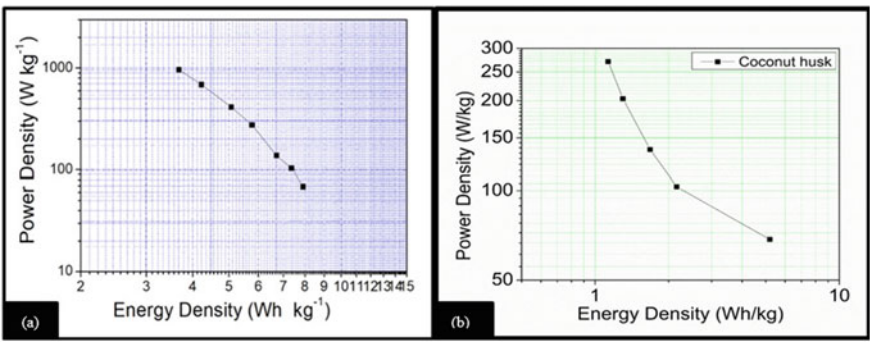

Fig. 7 Ragone plot of **a** BB-400, **b** CHB carbon

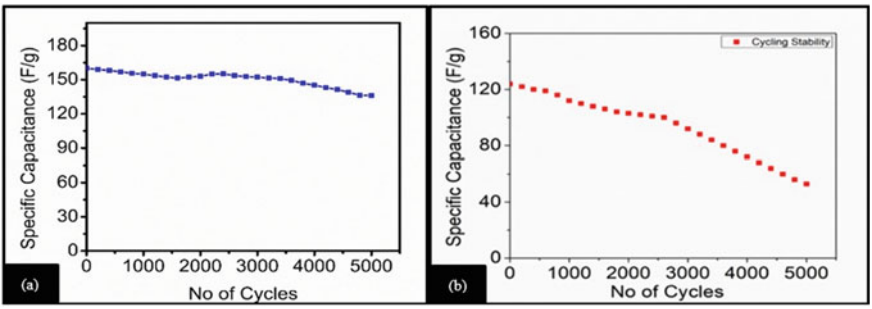

Fig. 8 Cyclic performance of **a** BB-400, **b** CHB carbon

$$Energy\ Density(ED) = \frac{1}{2 \times 3.6} \times C_s \times V^2 \tag{2}$$

$$Power\ Density(PD) = \frac{3600 \times ED}{\Delta t} \tag{3}$$

4.6 Cycling Stability

Cyclic stability is a crucial factor to take into account when assessing the effectiveness of supercapacitors for real-world applications. It refers to a supercapacitor's ability to sustain capacitance and charge storage capacity through repeated charge–discharge cycles. In this regard, a number of variables, including the materials used in the fabrication of electrodes, electrolytes, the operating voltage range, and the charging/discharging current density, might impact the cyclic stability [26]. The results showed that both materials exhibited a reduction in capacitance during their initial phases of the cycling test. However, BB-400 revealed amazing stability even after 5000 cycles with over 80% retention, but CHB carbon showed a considerable decline in retention after 3000 cycles. This implies that the BB-400 is more suited for long-term energy storage applications that demand steady and consistent performance through several cycles (Fig. 8).

5 Conclusion

In this work, the carbon from bamboo biomass and coconut husk biomass was successfully prepared using the carbonization method. SEM images showed BB-400 has a greater porosity than CHB carbon. Using characterization techniques like CV, GCD, and EIS, the electrochemical performance of carbon electrodes made

from BB-400 and CHB was assessed. The BB-400 demonstrated improved electrochemical performance and great stability from the CV curves. At a current density of $1 Ag^{-1}$, CHB demonstrated a high specific capacitance of $124 Fg^{-1}$ and demonstrated about 60% stability after 5000 charge and discharge cycles. The CHB carbon has a high power density of $271 Wkg^{-1}$ as well as a high energy density of $5.2 Whkg^{-1}$. A high specific capacitance of $188.36 Fg^{-1}$ at $0.50 Ag^{-1}$ of current density was demonstrated by the BB-400. Moreover, it has a high power density of $963.67 Wkg^{-1}$ and a high energy density of $7.91 Whkg^{-1}$. It has shown a good performance of 80% for Electrochemical Cyclic Stability at 5000 cycles. Proving that carbon extracted from bamboo is an excellent material for supercapacitors.

References

1. Saini S, Chand P, Joshi A (2021) Biomass-derived carbon for supercapacitor applications. J Energy Storage 39:102646. https://doi.org/10.1016/j.est.2021.102646
2. Graetzel M, Janssen R, Mitzi D et al (2012) Materials interface engineering for solution-processed photovoltaics. Nature 488:304–312. https://doi.org/10.1038/nature11476
3. Castro-Gutiérrez J, Celzard A, Fierro V (2020) Energy storage in supercapacitors: focus on Tannin-derived carbon electrodes. Front Mater 7:217. https://doi.org/10.3389/fmats.2020.00217
4. Bhat MY et al (2023) Frontiers and recent developments on supercapacitor's materials, design, and applications: transport and power system applications. J Energy Storage 58:106104. https://doi.org/10.1016/j.est.2022.106104
5. Enock TK, King'ondu CK, Pogrebnoi A, Jande YAC (2017) Status of biomass-derived carbon materials for supercapacitor application. Int J Electrochem.https://doi.org/10.1155/2017/6453420
6. Sim CK, Majid SR, Mahmood NZ (2019) Durable porous carbon/$ZnMn_2O_4$ composite electrode material for supercapacitor. J Alloy Compd 803:424–433. https://doi.org/10.1016/j.jallcom.2019.06.220
7. Simon P, Gogotsi Y (2008) Materials for electrochemical capacitors. Nat Mater 7(11):845–854. https://doi.org/10.1038/nmat2297
8. Abeykoon NC, Garcia V, Jayawickramage RA, Perera W, Cure J, Chabal YJ, ... Ferraris JP (2017) Novel binder-free electrode materials for supercapacitors utilizing high surface area carbon nanofibers derived from immiscible polymer blends of PBI/6FDA-DAM: DABA. RSC Adv 7(34):20947–20959.https://doi.org/10.1039/C7RA01727H
9. Yang C-S, Jang YS, Jeong HK (2014) Bamboo-based activated carbon for supercapacitor applications. Curr Appl Phys 14(12):1616–1620. https://doi.org/10.1016/j.cap.2014.09.021
10. Nayar NM (2016) The coconut: phylogeny, origins, and spread. Academic Press. https://doi.org/10.1016/B978-0-12-809778-6.00005
11. Pandey A, Negi S, Binod P, Larroche C (eds) (2014) Pretreatment of biomass: processes and technologies. Academic Press. ISBN: 978-0-12-800080-9
12. Rautiainen M (2014) Torrefied and carbonized wood, fuel properties, and turn of an exothermic reaction
13. Amer M, Elwardany A (2020) Biomass carbonization. In: Qubeissi MA, El-kharouf A, Soyhan HS (eds) Renewable energy—Resources, challenges and applications. IntechOpen. https://doi.org/10.5772/intechopen.90480
14. Sivaraj R, Rajendran V, Gunalan GS (2010) Preparation and characterization of activated carbons from Parthenium biomass by physical and chemical activation techniques. E-Journal of Chem 7(4):1314–1319. ISSN: 0973-4945

15. Erman VMN, Taslim R (2020) Activated carbon Monolith derived from coconut husk fiber as electrode material for supercapacitor energy storage. J Phys: Conference Series 1655(1):012164. IOP Publishing. https://doi.org/10.1088/1742-6596/1655/1/012164
16. Hsia B (2013) Materials synthesis and characterization for micro-supercapacitor applications. The University of California, Berkeley. UMI Number: 3616556
17. Ortega EO, Hosseinian H, Meza IBA, López MJR, Vera AR, Hosseini S (2022). Material characterization techniques and applications. https://doi.org/10.1007/978-981-16-9569-8
18. Marcus NA (2015) A survey of electrochemical supercapacitor technology
19. Dos Reis GS, Larsson SH, de Oliveira HP, Thyrel M, Claudio LE (2020) Sustainable biomass activated carbons as electrodes for battery and supercapacitors—A mini-review. Nanomaterials (Basel) 10(7):1398. https://doi.org/10.3390/nano10071398
20. Yang X, Fei B, Ma J, Liu X, Yang S, Tian G, Jiang Z (2018) Porous nanoplatelets wrapped carbon aerogels by pyrolysis of regenerated bamboo cellulose aerogels as supercapacitor electrodes. Carbohydr Polym 180:385–392.https://doi.org/10.1016/j.carbpol.2017.10.0133
21. Wang Y, Liu Y, Chen Z, Zhang M, Liu B, Xu Z, Yan K (2022) In situ growth of hydrophilic nickel-cobalt layered double hydroxides nanosheets on biomass waste-derived porous carbon for high-performance hybrid supercapacitors. Green Chem Eng 3(1):55–63 https://doi.org/10.1016/j.gce.2021.09.001
22. Taer E, Taslim R, Putri AW, Apriwandi A, Agustino A (2018) Activated carbon electrode made from coconut husk waste for supercapacitor application. Int J Electrochem Sci 13(12):12072–12084. https://doi.org/10.20964/2018.12.19
23. Alzaid M, Alsalh F, Zahir Iqbal M (2021) Biomass-derived activated carbon-based hybrid supercapacitors. J Energy Storage 40:102751. https://doi.org/10.1016/j.est.2021.102751
24. Kumar N, Kim SB, Lee SY, Park SJ (2022) Recent advanced supercapacitor: a review of storage mechanisms, electrode materials, modification, and perspectives. Nanomaterials (Basel) 12(20):3708. https://doi.org/10.3390/nano12203708
25. Cao X, Li Z, Chen H, Zhang C, Zhang Y, Gu C, Xu X, Li Q (2021) Synthesis of biomass porous carbon materials from bean sprouts for hydrogen evolution reaction electrocatalysis and supercapacitor electrode. Int J Hydrogen Energy 46(36):18887–18897. https://doi.org/10.1016/j.ijhydene.2021.03.038
26. Baig MM, Gul IH, Baig SM, Shahzad F (2021) The complementary advanced characterization and electrochemical techniques for electrode materials for supercapacitors. J Energy Storage 44:103370. https://doi.org/10.1016/j.ijhydene.2021.09.094
27. Zequine C, Ranaweera CK, Wang Z, Singh S, Tripathi P, Srivastava ON, Kumar Gupta B et al (2016) High performance and flexible supercapacitors based on carbonized bamboo fibers for wide temperature applications. Sci Reports 6(1):1–10
28. Wang J, Wang Z, Yu H, Wu W, Zhang J, Li J (2022) Designing a novel type of multifunctional bamboo surface based on an RGO/AG coating. Arab J Chem 15(12):104332. https://doi.org/10.1016/j.arabjc.2022.104332
29. Zhang G, Chen Y, Chen Y, Guo H (2018) Activated biomass carbon made from bamboo as electrode material for supercapacitors. Mater Res Bull 102:391. https://doi.org/10.1016/j.materresbull.2018.03.006

Biopolymer-Based Biosensors: Fabrication and Properties

Rakhi Pandey and Garima Mathur

1 Introduction to Biosensor

The necessity of monitoring important processes and their parameters in numerous sectors has directed the development of devices for analysis known as biosensors [1]. The development of these devices has given solutions for a broad range of applications that involve discovery of drugs, diagnostic technology, biomedicine, food processing environmental monitoring, defense, and protection [1]. A biosensor is an apparatus that monitors physiological or chemical operations by producing signals directly linked to the amount of analytes within the reaction. Wearable biosensors are associated with the body or specific parts of human body in the form of gloves, tattoos, clothes, and implants, permitting in-vivo monitoring, data collection, and calculation to be accomplished using mobile or portable equipment. The possible applications of wearable biosensors in human health monitoring and personalized treatment are driving up demand for their fabrication and development [2]. The integration of automated and independent biosensors into public facilities (such as transit hubs, schools, and workplaces) is intended to enhance the safety of the public by informing the public to potential biological hazards. These are self-contained assimilated devices that generate qualitative and partially quantitative statistical information using an element for biological recognition linked to a transduction component [3].

Generally, biosensors can be categorized in three parts (Fig. 1).

(a) An element that is sensitive to biological response that produces signal by interacting with the targeted analyte. This material generally includes tissues, enzymes, cell receptors, and nucleic acids.
(b) Transducer that acts as a physicochemical detector for the quantification of signal that has produced from sensing element.

R. Pandey · G. Mathur (✉)
Technology Solutions for Soil and Water Remediation (TSSR), Department of Biotechnology, Jaypee Institute of Information Technology, Uttar Pradesh, A-10, Sector-62, Noida 201309, India
e-mail: garimacity@gmail.com

S. B. Krupanidhi et al. (eds.), *Recent Advances in Functional Materials and Devices*, Springer Proceedings in Materials 37, https://doi.org/10.1007/978-981-99-6766-7_9

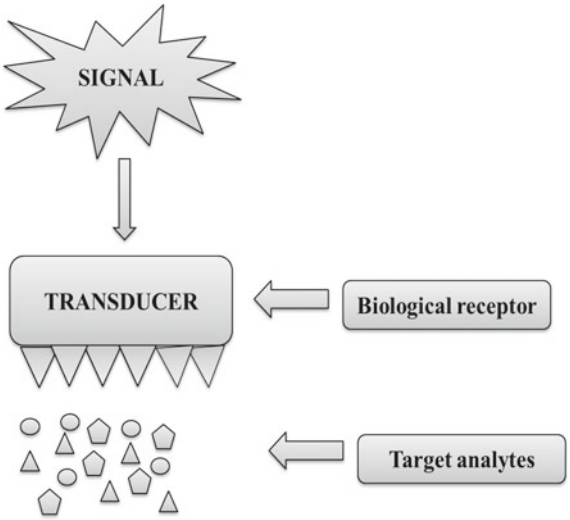

Fig. 1 General representation of strategy of biosensor [1]

(c) A system that is used for the processing of signals [4].

Traditional 'off-site' analysis necessitates sending the samples to a laboratory for examination. These procedures provide the best quantification accuracy and the lowest detection limits, but they are costly, time intensive, and require the employment of highly skilled staff. Because of the aforementioned limitations, there has been a lot of interest in biosensor technology. In recent years, there has been amazing progress in the area of biosensor growth and development, with growing applications in a broad spectrum of fields [4] (Fig. 2).

Fig. 2 Different applications of biosensors [5, 6]

2 Why Biopolymers are Used to Make Biosensor?

Efficiently leveraging the interaction that exists between the biorecognition component and the analyte is an essential component for successful biosensor development. This demands the biorecognition component to be effectively immobilized or attached onto the sensor interface. Several sophisticated immobilization strategies that serve much effectively in retaining the bioreceptor near to the transducer for intuitive monitoring of the signal that has been biochemically released. Furthermore, the biosensor material must be biocompatible in order for the bioreceptor to remain functional. The biorecognition factors are sensitive toward environmental factors including pH, strength of ionization, temperature, and so on. As a result, the immobilizing matrix must be effective in protecting the bioreceptor from circumstances that are destructive to its activation. The immobilizing matrix must facilitate easy passage of the analyte to the bioreceptor without acting as an obstacle, while also preventing bioreceptor leakage through the matrix [7]. Biopolymers are a particular variety of material that meets several of the discussed requirements and so finds widespread use in the production of biosensors.

Polymeric macromolecules derived from organisms that are living called biopolymers. Biopolymers may be divided into three types based on their monomeric units:

(a) Polypeptides—that contains the small units of amino acids such as hemoglobin.
(b) Polynucleotides—made up of nucleotide smaller units e.g. RNA, DNA.
(c) Polysaccharides—that are made up of chain of carbohydrates e.g. chitosan, cellulose.

Biopolymers, in contrast to their synthetic substitutes, have a clearly defined three-dimensional framework that is essential for their functioning [8].

Biopolymers, since they are created by nature, have a high monodispersity compared to synthetic polymers, which have a high polydispersity [8]. In general, dispersity of polymers defines the ratio of average weight and number of average molecular weight. It explains the spatial arrangement of molar masses and the polymerization degree [9]. Monodispersity generally indicates molecules have almost same polymerization degree and relative molecular mass whereas polydisperse means molecules with different degree of polymerization and molecular weight ratio [9]. Biopolymers are environmentally beneficial because natural processes involving enzymes or bacteria can reduce them to elemental entities. The ultimate result of these polymers' natural degradation may be again absorbed in the environment with minimal carbon traces. The other benefit of biopolymers that has been observed is that they have a wide range of chemical and structural properties since they are derived from natural resources such as plants or organisms that live. Chitosan is one of the dominantly used biopolymers that helps in the development of biosensor [8, 10]. Biopolymers have numerous benefits in the context of biosensor usage, which are explored in the following sections [8].

3 Bioresponsive

A number of biopolymers are bioresponsive, meaning that their characteristics vary in response to inputs from physiologically relevant substances such as glucose, enzymes, ATP, antibodies, and so on. Bioresponsive materials have the ability to react selectively to specific chemicals. We can see this in case of glycosaminoglycan biopolymer chondroitin sulphate which selectively binds to the receptors of CD44 that have an overexpression in cancer cells. This aids in the identification of cancer cells as well as their adhesion [11]. The majority of biopolymers have been demonstrated for fabricating hydrogels which is a three-dimensional network of polymers. Hydrogels can be engineered to modify their characteristics by collapsing or swelling or by their phase transitions from gel to solution or vice versa in response to external stimuli such as temperature, ionic strength, solvent polarity, electric/magnetic field, light, or tiny (bio) molecules. Different types of stimuli are there for bioresponsive hydrogel systems. In one of them hydrogel materials are changed to include very small molecules that predominantly attach to biomacromolecules that include receptors for proteins or antibodies. In other stimuli substrates that are sensitive toward enzymes such as short peptides are used for the modification of hydrogels. Third, systems may contain biomacromolecules, which include enzymes that detect tiny biomolecules [12].

4 Biocompatibility

Because of their natural biology, biopolymers interact favorably with biological systems and aid in the protection of the biosensor's biorecognition unit. It has been claimed that the cells were not only capable of attaching to composite film of biopolymer while being viable, as well as multiplying on the film after long-lasting culture. Researchers noted that modification of polylactic acid biomaterials has been demonstrated to able to modulate the expression of a wide variety of genes involved in cell cycle, metabolism, and ultimately stimulates proliferation of cells and also plays a role in differentiation. In vitro biocompatibility experiments utilizing the MTT test found that the quantity of pectin boosted cell viability [13].

5 Matrix of Immobilization

Biopolymers serve as an effective immobilization matrix for biorecognition entities such as enzymes, entire cells, and so on. Physical trapping of biological entities inside the biopolymer can be used to immobilize them. Alternatively, various novel strategies for trapping and secretion of biological species in situ under moderate circumstances have been documented in the literature. Biopolymers also improve

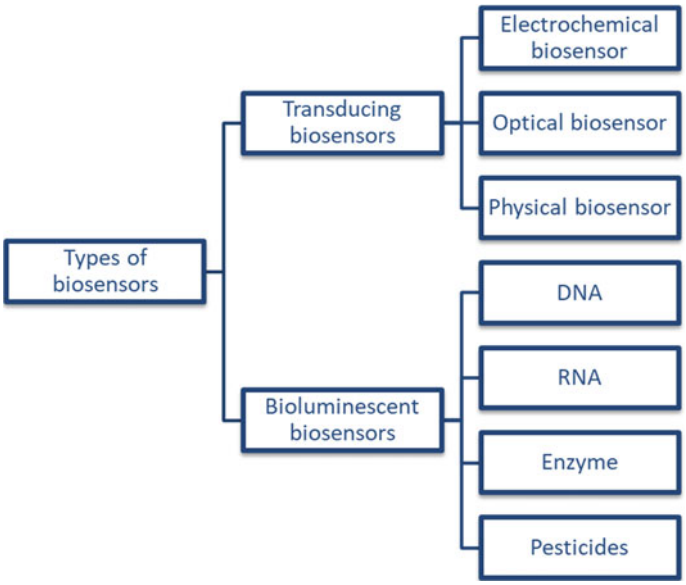

Fig. 3 Biosensors that are based on chitosan [15]

the composite's adherence to the electrode for sensing measures. These materials possess excellent water permeability, allowing for efficient electrolyte diffusion over the surface of biosensors. This alleviates the issues and limits related to diffusion obstacles [14].

Chitosan is one of the important biopolymers that are used in the making of a biosensor. Chitosan-based biosensor has been investigated because of unique characteristics and physicochemical properties of chitosan. There are a number of organic polymers, out of them chitosan is the one that has the physical benefits of high mechanical strength, hydrophilic nature, and ease of processing, as well as the biocompatibility of chemicals, bio-environmental stability, and chemical modification capacity. Over the last decade, there have been observations of biosensors being developed utilizing chitosan as the substrate material rather than traditional inorganic materials [15, 16]. Majorly there are two types of biosensors reported based on chitosan: (a) Transducing biosensor and (b) Bioluminescent biosensor (Fig. 3).

6 Fabrication of Chitosan Biosensor

See Fig. 4.

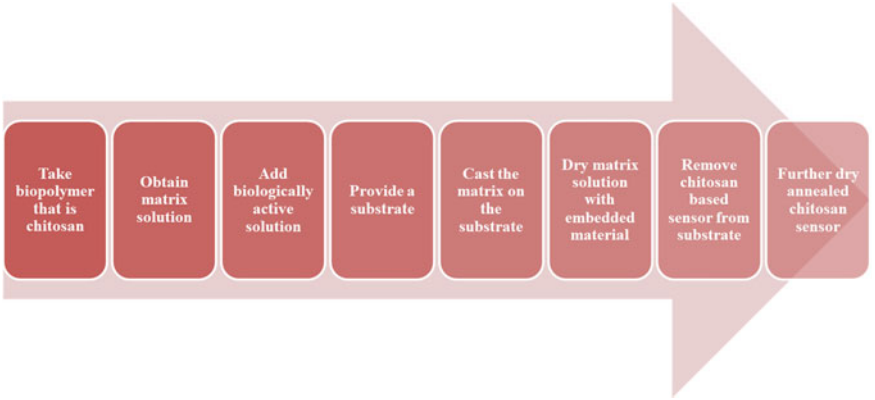

Fig. 4 Schematic diagram of fabrication of chitosan-based biosensor [17]

7 Properties of Chitosan-Based Biosensor

Chitosan is a potential natural material for sensing elastic strain sensors due to its exceptional biological compatibility, biodegradability, zero toxicity, and outstanding mechanical characteristics. Because of its reactive groups, chitosan has remarkable capabilities that may be exploited as a stage for complicated modifications to provide remarkable features. Physical modifications, chemical modifications, and grafting of CS, in particular, allow the production of chitosan polymers with specific functionalities [18].

Chitosan-based amperometric biosensors are useful in the detection of many compounds and in some cases they also maintain high recovery rates. These biosensors play a crucial role in the detection of glucose, ethanol, ascorbic acid, phenols, acetaminophen, and hydrogen peroxide [15].

Chitosan-based voltametric biosensors are being used for the sensing of catechol, neotame, amitrole, luteolin, bisphenol A, hydroquinone, and organophosphates. Electrochemical biosensors are being developed for the detection of phenolic compounds [15].

Chitosan-based potentiometric biosensor was used to detect urea in blood serum samples. Four procedures were employed to create this sort of sensor. Starting with the adsorption, the next was reticulation in collaboration with glutaraldehyde dilute solution, then glutaraldehyde activation is done when combined with solution of enzyme, and the last was immobilization of the enzyme on the prepared membranes of chitosan [15].

Optical biosensors are manufactured at nanoscale of versatile biomaterials and constitute the most prominent nanotechnologies associated with biological applications primarily because of its biocompatibility and biodegradability. This matrix was employed in the production of optical glucose biosensors. This type of biosensor could detect antibody titers in serum samples [15].

Physical biosensors are piezoelectric biosensors that have been developed by crosslinking carboxymethyl chitosan. The biosensor inhibited bovine serum albumin and lysozyme from binding. The constructed biosensors provided a low-cost as well as fast immunoglobulin.

Bioluminescent biosensors contain bioluminescence which is the generation of light in biological systems. The energy that is produced from ATP conversion to AMP is used to generate oxyluciferin, CO_2, and light during the oxidation of firefly D-luciferin. Adenosine triphosphate is the primary currency of energy in living cells, is found in cells and defines the energy level of the cell. As a result, the quantity of measured ATP corresponds to the number of live cells and characterizes the "well-being" of the cultivated cells [19].

Stability is defined as the degree of sensitivity to environmental alterations in and around the biosensing system. These disruptions might create a drift in the output signals of a biosensor that is being measured. This might result in a measurement inaccuracy and decrease the precise and accurate outputs of the biosensor. For maintaining the biological activity that is required for the important functioning of sensors a layer that is biocompatible should be present between receptors and surface of electrode. This layer is known as the interface whose stability directly influences the interaction of analytes which in turn influences the sensing performance of the biosensor [22].

In situations where a biosensor requires extensive incubation stages or constant monitoring, stability is the most important attribute. Electronics and transducers might have temperature-sensitive responses, which can affect biosensor stability. The affinity is generally defined as the degree or extent analyte will bind to the receptor, which is an important factor that might impact stability. The degeneration of the bioreceptor over time is another factor that impacts measurement stability. Other concerns with sensors include the viability of structures in the applications of sensor, which has received little attention, and toxicity, which varies depending on the physical qualities of the material type [20].

There are certain limits to the widespread use of chitosan-based biosensors. The key concern is about the ways biosafety changes by the effect of nanoparticles. As a result, the amount and cytocompatibility of various nanoparticles need to be studied. The second point is that biosensor reusability must be enhanced. This necessitates investigating the process of electrode contamination and developing interfaces of sensor that should have anti-fouling capabilities [22]. The main disadvantage of different types of biosensors is very poor interferences and selectivity [21]. Furthermore, the potential of chitosan-based bioelectronics sensors to access biological information and activate signals has to be investigated further [22]. One of the most difficult difficulties is sensitivity, which is determined by the thickness of the sensor layer. If sensing layer is very thin it may lead to the exposure of electrode surface, lowering the ratio of noise to signal and sensitivity. If the sensor layer is excessively thick, the observed AC impedance current decreases, preventing electron transmission between layers and lowering sensitivity. Tiny molecules alone often produce very few observable responses, which is generally not easy to quantify, particularly

in real and common samples in which target molecule concentration is generally very low [23].

8 Conclusion

Biosensors are becoming the basic need for the people with the modernization of the world. Different type of biosensors helps in the detection of different pollutants/ contaminants that are generally unfavorable to living things. Biosensors exhibit a broad number of applications in the different sectors. So with the increasing demand safety and efficacy issue related to biosensor comes into existence. To overcome that biopolymers have been chosen instead of synthetic and harmful chemicals. Chitosan is one of the biopolymers that is used in the fabrication of biosensors. Chitosan has some unique properties which makes it a promising material for the making of biosensor. There has not been much work done with biopolymers in biosensor making but now it is being researched due to its advantageous properties over the existing one. Challenges are associated with the stability of transducer and bioreceptor affinity in the fabrication of biosensor. Very low selectivity and interference property is one of the limiting factors of different types of biosensors.

9 Statements and Declarations

Contributions:The authors listed above have equal contributions. The submitted work is part of the doctoral research of Miss Rakhi Pandey, done under the guidance of Dr. Garima Mathur.

Conflict of Interest:The authors declare that they have no conflict of interest in the publication.

Funding:The authors did not receive support from any organization for the submitted work.

Competing Interests:The authors have no financial and nonfinancial competing interests to declare that are relevant to the content of this article.

Acknowledgements The authors are grateful to the Department of Biotechnology, Jaypee Institute of Information Technology, Noida, Uttar Pradesh, India for providing necessary facilities to execute this work.

References

1. Tetyana P, Shumbula PM, Njengele-Tetyana Z (2021) Biosensors: Design, development and applications. Nanopores. IntechOpen
2. Sharma A, Badea M, Tiwari S, Marty JL (2021) Wearable biosensors: an alternative and practical approach in healthcare and disease monitoring. Molecules 26(3):748
3. Altug H, Oh SH, Maier SA, Homola J (2022) Advances and applications of nanophotonic biosensors. Nat Nanotechnol 17(1):5–16
4. Nikhil B, Pawan J, Nello F, Pedro E (2022) Introduction to biosensors. Essays Biochem 60(1):1–8
5. Mehrotra P (2016) Biosensors and their applications–A review. J Oral Biol Craniofacial Res 6(2):153–159
6. Vigneshvar S, Sudhakumari CC, Senthilkumaran B, Prakash H (2016) Recent advances in biosensor technology for potential applications–an overview. Front Bioeng Biotechnol 4:11
7. Scala-Benuzzi ML, Piguillem Palacios SV, Takara EA, Fernández-Baldo MA (2023) Biomaterials and biopolymers for the development of biosensors. In: Biomaterials-Based sensors: Recent advances and applications, pp 3–24
8. Sawant SN (2017) Development of biosensors from biopolymer composites. Biopolymer composites in electronics. Elsevier, pp 353–383
9. Gilbert RG, Hess M, Jenkins AD, Jones RG, Kratochvil P, Stepto RFT (2009) Dispersity in polymer science. Pure Appl Chem 81(2):351–353
10. Sobhan A, Muthukumarappan K, Wei L (2021) Biosensors and biopolymer-based nanocomposites for smart food packaging: Challenges and opportunities. Food Packag Shelf Life 30:100745
11. Radhakrishnan K, Tripathy J, Datey A, Chakravortty D, Raichur AM (2015) Mesoporous silica–chondroitin sulphate hybrid nanoparticles for targeted and bio-responsive drug delivery. New J Chem 39(3):1754–1760
12. Ulijn RV, Bibi N, Jayawarna V, Thornton PD, Todd SJ, Mart RJ, Smith AM, Gough JE (2007) Bioresponsive hydrogels. Mater Today 10(4):40–48
13. Amarnath CA, Venkatesan N, Doble M, Sawant SN (2014) Water dispersible Ag@ polyaniline-pectin as supercapacitor electrode for physiological environment. J Mater Chem B 2(31):5012–5019
14. Bilal M, Iqbal HMN (2019) Naturally-derived biopolymers: Potential platforms for enzyme immobilization. Int J Biol Macromol 130:462–482
15. Chauhan S, Thakur A (2023) Chitosan-based biosensors-A comprehensive Review. Mater Today: Proc
16. Yu J, Wu J (2019) Recent development in chitosan nanocomposites for surface-based biosensor applications. Electrophoresis 40(16–17):2084–2097
17. Madej-Kiełbik L, Gzyra-Jagieła K, Jóźwik-Pruska J, Dziuba R, Bednarowicz A (2022) Biopolymer composites with sensors for environmental and medical applications. Materials 15(21):7493
18. Nath N, Chakroborty S, Vishwakarma DP, Goga G, Yadav AS, Mohan R (2023)Recent advances in sustainable nature-based functional materials for biomedical sensor technologies. Environ Sci Pollut Res:1–25
19. Rahimirad N, Kavoosi S, Shirzad H, Sadeghizadeh M (2019) Design and application of a bioluminescent biosensor for detection of toxicity using Huh7-CMV-Luc cell line. Iran. J. Pharm. Res.: IJPR 18(2):686
20. Naresh V, Lee N (2021) A review on biosensors and recent development of nanostructured materials-enabled biosensors. Sensors 21(4):1109
21. Song M, Lin X, Peng Z, Xu S, Jin L, Zheng X, Luo H (2021) Materials and methods of biosensor interfaces with stability. Frontiers in Materials 7:583739

22. Wu S, Wu S, Zhang X, Feng T, Wu L (2023) Chitosan-based hydrogels for bioelectronic sensing: Recent advances and applications in biomedicine and food safety. Biosensors 13(1):93
23. Kivirand K, Min M, Rinken T (2019) Challenges and applications of impedance-based biosensors in water analysis. Biosens Environ Monit:2–4

Synthesis Cum Structural, Mechanical, Optical and Piezoelectric Studies of L(+)-Tartaric Acid Crystals Adulterated with Malachite Green and Trypan Blue Dyes

Preetika Dhawan, Karan Grover, and Harsh Yadav

1 Introduction

Crystal engineering in the present era is utilized to expedite a wide variety of its applicative uses owing to various physical, chemical, and mechanical properties along with optical transparency, photoluminescence yield, piezoelectric, ferroelectric, and dielectric behaviour, nonlinear optical behaviour, magnetic behaviour, etc. [1, 2]. Crystals can take on several forms such as polymorphs, solvates, hydrates, and so on, altering structural, and physio-chemical properties such as hygroscopicity, solubility, and compaction behaviour including purity of the chemical and its composition with the distribution of size and shape of the crystal [3–6]. Numerous studies in the avenue of organic, inorganic, and semi-organic materials for nonlinear optics (NLO) have been carried out in the past years, owing to the growing demand for inexpensive and simply processable materials for photonics applications [7]. The materials chosen for this study are organic as they can easily emanate monomer or dimer forms thus making them favourable for controlled crystallization [4, 8].

L(+)-tartaric acid (TA) is an excellent organic NLO compound [7]. Many tartrate-based compounds are widely useful in industrial applications like in transducers, and linear and nonlinear mechanical devices because of their outstanding dielectric, ferroelectric, piezoelectric, and NLO attributes [9, 10]. L(+)-tartaric acid or dextro-tartaric acid is the readily available version of the acid. It is possible to synthesize levotartaric acid or D(–)-tartaric acid which is the mirror-image form, as well as mesotartaric acid which is the achiral form [10]. Tartaric acid is more water soluble, can be crystallized into larger sizes, and is less expensive than aminoacid-based NLO

P. Dhawan · K. Grover · H. Yadav (✉)
Department of Physics, Netaji Subhas University of Technology, Dwarka, New Delhi 110078, India
e-mail: harsh@nsut.ac.in

S. B. Krupanidhi et al. (eds.), *Recent Advances in Functional Materials and Devices*, Springer Proceedings in Materials 37, https://doi.org/10.1007/978-981-99-6766-7_10

compounds [1]. This study aims in growing TA single crystals from conventional solution growth technique via the slow evaporation method.

The novelty of this study, however, lies in the analysis of characteristic behavioural changes in TA when it is subjected to the inclusion of organic dyes in dopant amounts and this includes the study of optical, structural, and piezoelectric properties and even the powder handling for pharmaceutical purposes [11]. The dyeing technique is a facile way to incorporate NLO active chromophores into the single crystal lattice thereby facilitating applications in the field of solid-state photonic devices. Because single crystals are anisotropic, have intrinsic polarization and huge thermal conductivity and have lesser scattering centres, they are an appealing host matrix for dye molecules [12].

For the aforesaid purpose, two dyes have been separately chosen i.e. malachite green (MG) and trypan blue (TB). The cationic dye known as MG is used widely in the paper, rubber, and plastic industries as well as in the manufacturing of ink, and textile dyes, particularly for wood and silk and ink research. The indicator of pH is yet another function [13]. Trypan blue is a type of azo dye which when doped into the host materials shows quality NLO absorption phenomena [14]. Furthermore, TB is a cotton textile dye. It is used as an essential stain in biosciences for colouring dead cells. Trypan blue is extensively used in microscopy or cell counting purposes and laboratory mice for tissue viability testing [15]. This study, thus, lays out a comparison between unadulterated TA-grown crystals with that of MG dye-adulterated TA and TB dye-adulterated TA crystals in terms of their structural attributes, and optical and piezoelectric properties. A study of the mechanical property, i.e., microhardness behaviour of unadulterated TA crystal has also been laid out in this article.

2 Experimental Methodology

2.1 Synthesis and Growth

Single crystals of unadulterated L-tartaric acid (TA) ($C_4H_6O_6$) (extrapure 99.7%-AR ACS) along with 0.01 mol% malachite green dye (MG) ($C_{48}H_{50}N_4O_4.2C_2H_2O_4$) adulterated TA and 0.01 mol% trypan blue dye (TB) ($C_{34}H_{24}N_6Na_4O_{14}S_4$) adulterated TA crystals were synthesized from their respective homogeneous aqueous solutions (pH = 3) by slow evaporation technique. 0.01 mol% describes that adulteration was deliberately performed in a dopant amount. The solvent so chosen in all three scenarios was deionized water with the solutions being stirred magnetically for a few hours. 120 mm Whatman papers were utilized to occlude the impurities present in all the solutions. Thereafter, all three solutions were kept undisturbed for some weeks to let the solutions attain their supersaturated states that would emanate crystal growth via steady evaporation at room temperature. Optical images are recorded in Fig. 1 showing the flat transparent single crystals and dye inclusion in the designated sectors of the crystals.

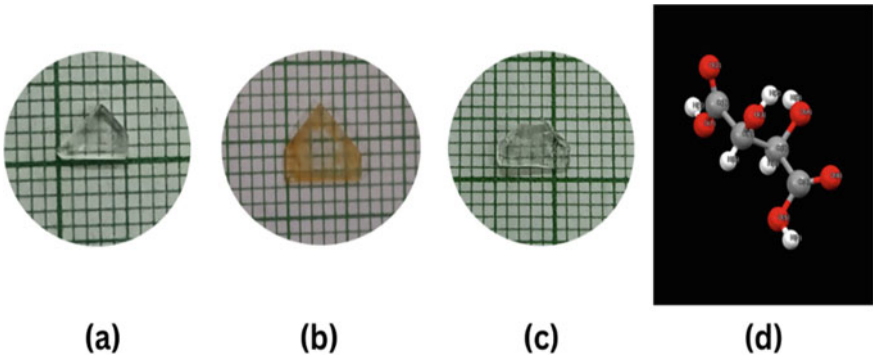

Fig. 1 Optical images of the as-grown **a** Unadulterated TA crystal, **b** MG adulterated TA crystal, **c** TB adulterated TA crystal, **d** structure of L(+)-tartaric acid

2.2 Characterizations

Powder X-ray diffraction (XRD) estimations were accomplished from EMPYREAN diffractometer system at room temperature ($\lambda = 1.5405$ Å for Cu K_α X-ray source). Furthermore, XRD refinement of the structural parameters of all three above-mentioned crystals was done employing EXPO2014 software. The UV–visible transmittance pattern was traced using a Shimadzu UV-2600i spectrometer (200–800 nm). The photoluminescence (PL) emission spectrum was further recorded employing a fluorescence spectrometer (model: QM-8450–11; 450W Xe lamp source). The Fourier transform infrared (FTIR) spectrum of all the crystals was traced on a Nicolet iS50 FTIR Tri-detector with a Gold flex spectrometer in the 400 to 4000 cm^{-1} range. Piezoelectric (d_{33}) analysis was performed via PM300 Piezo Meter system (model: PIEZOTEST, tapping force = 0.25 N, frequency = 110 Hz). The Vickers microhardness technique was utilized in studying the variation of hardness with the application of external load using a diamond indenter with a 10 s constant duration time and 4 s load-unload time via the Mitutoyo HM-220 machine.

3 Results and Discussion

3.1 X-ray Diffraction and Structural Refinement

Crushed crystals of unadulterated, MG and TB adulterated TA were analyzed by the Debye Scherrer method in the 2θ range of 8–80° at room temperature with Cu K_α radiation (wavelength = 1.5405 Å). The XRD graphical patterns of the unadulterated and dye-adulterated samples of TA are shown in Fig. 2, with peaks of (hkl) reflection properly indexed. The relatively intense peaks in the XRD data demonstrate that

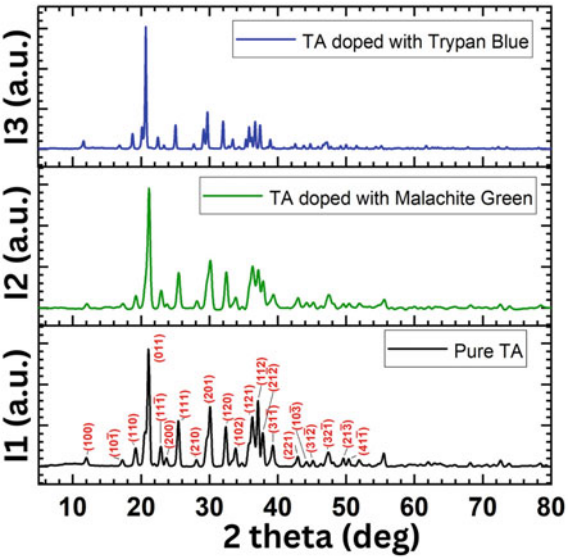

Fig. 2 XRD (experimental) (Intensity—2 theta) pattern of unadulterated TA (I1), MG adulterated TA (I2), TB adulterated TA (I3)

the formed material has a high degree of crystallinity with the (011) plane showing the dominant intense peak. EXPO2014 software employing the Le Bail technique was further utilized to optimize and refine the lattice parameters [16] of unadulterated and dye adulterated TA samples along with the determination of indexed (hkl) reflection planes and feasible space group (Fig. 3). The quality of refinement has been ascertained using weighted/unweighted profile R-factors. TA crystal unit cell specifications matched well with the reported literature [1, 7–10, 17]. The insertion of MG or TB dye caused straining of the TA lattice structure, resulting in a modest shift in unit cell values designated as a, b, and c (in Å). Crystal system (monoclinic) and space group ($P2_1$), however, remained unchanged in the three cases (see Table 1). As a result, XRD examination verifies the existence of dye molecules in the TA crystal lattice.

3.2 UV–Vis Spectral Analysis

The UV–Vis transmittance of a crystal is affected by various parameters, including its thickness, optically active functional units, orientation, impurities, structural defects, dislocations, etc. [18]. The transparency in the UV–visible region affects an NLO material's optoelectronic efficiency. According to Fig. 4 (a), which shows the optical transmission spectrum of the entitled crystals in the 200–800 nm range, the UV characteristic cut-off wavelength is reportedly 232 nm. The characteristic absorption peak at 624 nm for MG dye affirmed its presence in the TA crystal while the characteristic absorption peak at 584 nm for TB dye affirmed its presence in the TA crystal. The

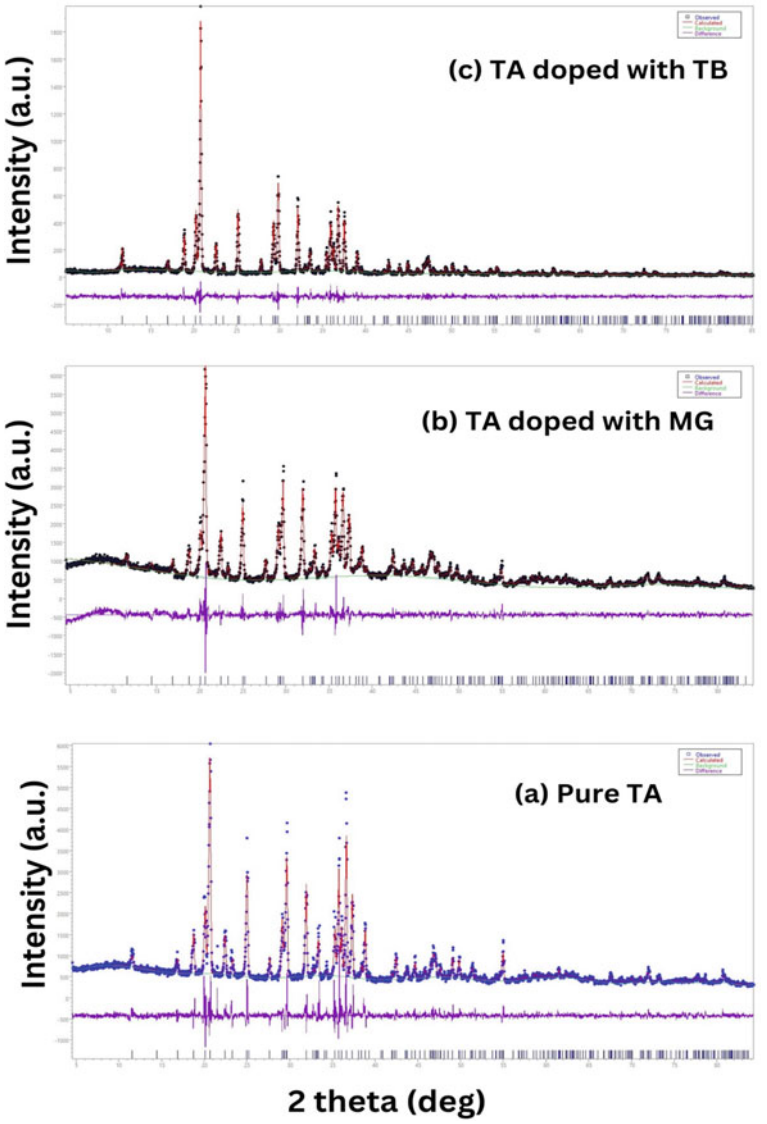

Fig. 3 XRD (refined) (Intensity—2 theta) pattern of unadulterated TA, MG adulterated TA, TB adulterated TA

percentage transmittance in both the dye adulterated cases, however, was reduced. These values fairly matched with that in the reported literature [1, 7, 8, 13, 19]. Additionally, Fig. 4b shows the Tauc plot which describes that the values of E_g, the optical energy band gap are 5.31 eV for unadulterated TA, 5.32 eV for MG adulterated TA, 5.22 eV for TB adulterated TA by the determination of x-axis intercept of the linearly

Table 1 Comparison between pure and dye-adulterated TA crystals based on XRD refinement

Type	Pure TA	TA adulterated with malachite green dye	TA adulterated with trypan blue dye
Refined cell parameters	a = 7.75 Å, b = 6.02 Å, c = 6.23 Å	a = 7.74 Å, b = 6.01 Å, c = 6.22 Å	a = 7.71 Å, b = 5.99 Å, c = 6.20 Å
	α = 90°, β = 100.19°, γ = 90°	α = 90°, β = 100.13°, γ = 90°	α = 90°, β = 100.17°, γ = 90°
Space group	$P2_1$	$P2_1$	$P2_1$
Crystal system	Monoclinic	Monoclinic	Monoclinic
Weighted/unweighted profile R-factor	$R_p = 7.53$, $R_{wp} = 8.61$	$R_p = 6.82$, $R_{wp} = 8.90$	$R_p = 12.22$, $R_{wp} = 9.87$
Software	EXPO2014	EXPO2014	EXPO2014

fitted tauc plot. The direct optical band gap of the three crystals is suggested by this investigation with the variation in the values confirming the dyes inclusion in TA. Thus, TA along with its dye adulterated attributes are approvingly efficacious for optical applications due to their wide band gap, excellent transmittance, and low value of cutoff wavelength.

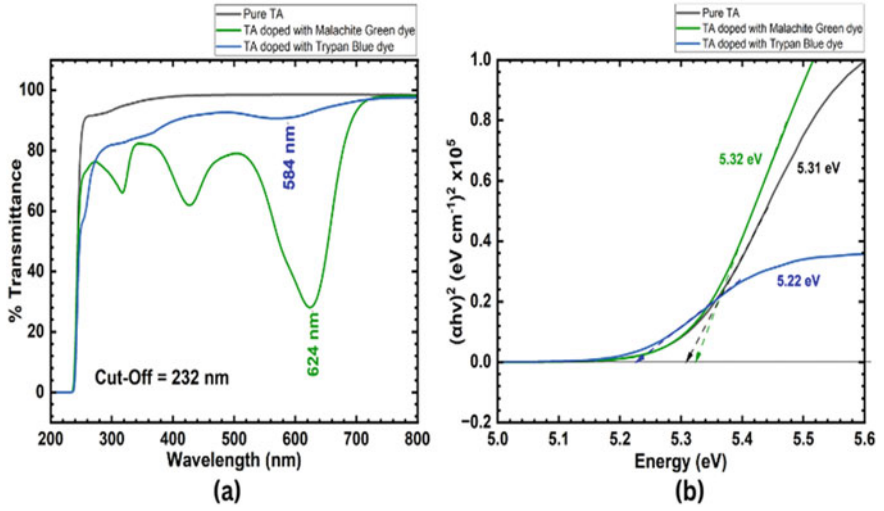

Fig. 4 **a)** UV–Vis transmission spectra, **b)** scaled Tauc Plots of unadulterated and dye-adulterated TA

3.3 Photoluminescence Spectroscopy

Any material's photoluminescence (PL) emission can reveal the manifestations of defects in a single crystal and aid in the analysis of changes to the local atomic configuration of the crystal structure [12]. The luminescence spectra of TA, MG adulterated TA, and TB adulterated TA crystal at an excitation of 250 nm were recorded at room temperature are shown in Fig. 5. To achieve this, their respective solid samples were preferred since the dye molecules showing fluorescing character intermingle in the water molecules and produce modest emission. At 393 nm, the developed crystal's strong emission peak was seen corresponding to violet emission and is in good agreement with the reported literature [7]. The intensity of violet emission, however, reduced on account of dye adulteration in both the cases for TB adulterated TA as well as for MG adulterated TA. The sharpness of the emission peaks on the other hand enhanced with TB or MG dye inclusion. This quenching in violet emission intensity can be attributed to molecular interactions like molecular rearrangements, complex formation in the ground state, energy transfer-related reactions and collisional quenching between fluorophore (TA) and quencher (TB or MG) dye molecules [12, 20, 21].

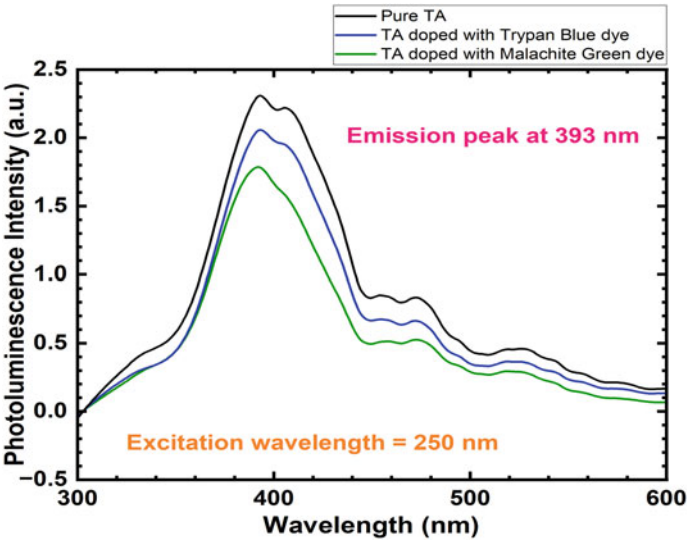

Fig. 5 Photoluminescence spectra of unadulterated and dye-adulterated TA

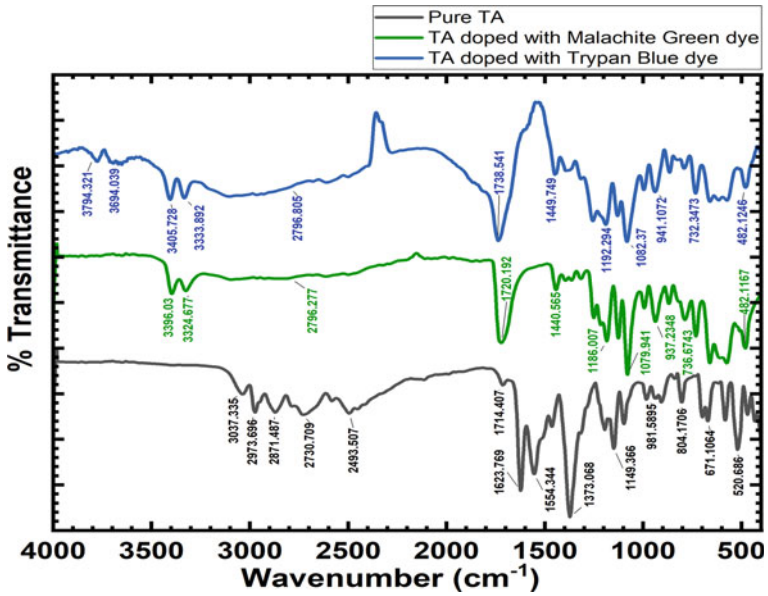

Fig. 6 FTIR spectral analysis of unadulterated and dye-adulterated TA

3.4 FTIR Spectroscopy

To identify the type of chemical bonds in each substance, FTIR spectroscopy is proven to be a beneficial approach. It has an operating range from 4000 to 400 cm^{-1}. FTIR spectrum brings forth details on the material's molecular structure, bond strength, and normal modes of vibration. Additionally, the analysis of the FTIR spectra's absorption bands' strength, location, and shape reveals details about various existing vibrational groups in the sample [22]. The broad peak overridden by small peaks in the range from 3400–2400 cm^{-1} is because of the occurrence of O–H stretching vibration in the carboxyl group of TA [7, 23]. The still stronger peak detected at around 1738 cm^{-1} points to the presence of C = O with a slight shift in these values for dye-adulterated crystals [1]. The weak peaks between 1450 and 1100 cm^{-1} occur as a result of simultaneous C–O stretching and O–H deformation [1, 9]. Peaks towards 480 cm^{-1} pertains to COOH torsions [9] (see Fig. 6).

3.5 Piezoelectric Measurements

A polar crystalline substance's capacity to generate an electric charge with regard to an external mechanical stress is known as piezoelectricity. The molecular potential energy surface achieves its stable global minima as a result of the association between

the molecular moment and the externally applied electric field in the material. The geometric response of the organic system to an electric field relies on H-bonding and π- π stacking interactions. The gross piezoelectric effect is determined by the displacement of the hydrogen bond length and the shielding of π–π stacking [24]. The piezoelectrical measurements (d_{33} responses) of the entitled crystals were accomplished at ambient temperature for the synthesized crystals in different orientations as shown in Fig. 7 employing identical crystals (with dimensions around 5 × 5 × 1 mm^3) of pure TA, MG adulterated TA, TB adulterated TA. It was observed that piezoelectric charge coefficient values decreased slightly in MG adulterated TA crystal while the same enhanced in all the chosen orientations in TB adulterated TA crystal. The reason for the same is that on account of TB dye adulteration, charge asymmetry was enhanced thereby inducing numerous dipoles in the synthesized crystal lattice by the subjection of externally applied pressure.

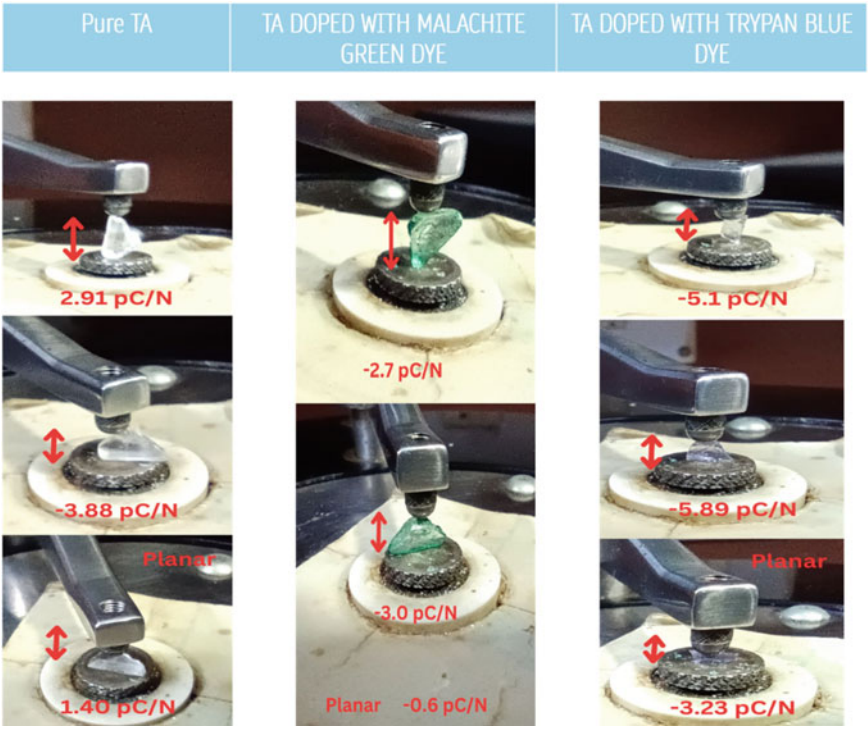

Fig. 7 Piezoelectric values at different orientations of unadulterated and dye-adulterated TA crystals

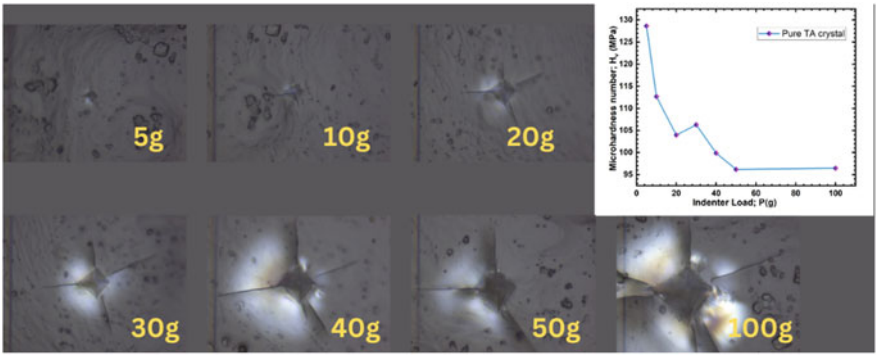

Fig. 8 50X microscopic images of indentation imprints of TA crystal as well as the variation of Vicker's microhardness number (MPa) at several loads of diamond indenter (5, 10, 20, 30, 40, 50 and 100 g)

3.6 Hardness

A material's hardness, a crucial solid-state attribute that gauges how resistant it is to local deformation, is a vital mechanical property of a sample under study [25]. The hardness of the as-grown crystal was assessed using the Vickers microhardness method. Vickers microhardness number (H_v; kg/ mm^2; MPa) was computed from the formula $H_v = 1.8544\ P/d^2$ (kg/mm^2) $= 0.1891\ F/d^2$ (N/mm^2 = MPa), where d stands for the average length along two diagonals of the indent (mm) and P stands for the external indenter load (kg), F is the applied indenter force (N). The load was gradually varied from 5–100 g. The TA single crystal's microhardness number (H_v) vs indenter load (P) is plotted in Fig. 8. When the indenter load was enhanced from 5 to 100 g, the hardness number declined to demonstrate the normal indentation size effect (ISE behaviour). The typical indentation size effect (ISE), which manifests as a sharp decline in hardness with applied loads, is caused by the internal stress developed at significant indentation load which was being liberated in the form of cracks. Due to the crystal surface stacking up after 50 g, the value of the hardness number is practically constant up to around 300 g post which at 500 g load, the crystal broke apart [3, 12].

4 Conclusion

This article recapitulates the effective solution growth of high-quality good sized single crystals of unadulterated, malachite green dye adulterated and trypan blue dye adulterated tartaric acid in dopant amounts. Powder XRD patterns and their refinement successfully affirmed the growth and cell parameters of the entitled crystals thereby revealing that all three crystals attribute to the monoclinic system of crystals

having a space group $P2_1$. Slight changes in the values of intensities and 2-theta shifts corresponding to dye adulteration were observed. The UV–visible spectroscopic study of the crystals demonstrated that they are suitable for nonlinear optical applications due to their broader optical band gaps and lower cut-off at 232 nm. Characteristic absorption peaks for both dyes were affirmed using this technique. It was observed that the band gap slightly increased with MG adulteration while it decreased with TB adulteration (5.31 eV for unadulterated TA, 5.32 eV for MG adulterated TA, and 5.22 eV for TB adulterated TA). When stimulated by a 250 nm excitation source, the PL spectroscopy detected a violet emission peak at 393 nm. Sharpness increased and PL intensity, however, decreased with dye adulteration. Functional groups were further confirmed with that reported in the literature. Moreover, piezoelectric charge coefficient values (along different orientations) increased in TB adulterated TA while it decreased in MG adulterated TA. Furthermore, TA crystal reportedly exhibited ISE behaviour in its microhardness analysis. Conclusively, all three crystals can potentially serve as good candidates for optoelectronic applications while TB adulterated TA crystal showed better piezoelectric performance over MG adulterated TA crystal.

Acknowledgements Preetika Dhawan is highly grateful for sincere supervision and guidance of Dr. Harsh Yadav, Assistant Professor, Netaji Subhas University of Technology, Dwarka, Delhi. The authors are also highly thankful to the Vice Chancellor, NSUT, Delhi for sponsoring and funding this research work. They would also like to acknowledge Prof. Binay Kumar, CGRL, Department of Physics, University of Delhi for providing piezoelectric measurement facility.

CrediT Authorship Contribution Statement **Preetika Dhawan**: Conceptualization, Methodology and Investigation, Writing. **Karan Grover**: Data Curation and validation. **Harsh Yadav**: Review and Supervision.

Declaration of Competing Interest The authors declare that they have no known competing financial interests or personal relationships that could have appeared to impact the work reported in this paper.

References

1. Martin Britto Dhas SA, Suresh M, Bhagavannarayana G, Natarajan S (2007) Growth and characterization of l-Tartaric acid, an NLO material. J Cryst Growth 309:48–52. https://doi.org/10.1016/j.jcrysgro.2007.09.008
2. Balashova E, Zolotarev A, Levin AA, Davydov V, Pavlov S, Smirnov A, Starukhin A, Krichevtsov B, Zhang H, Li F, Luo H, Ke H (2023) Crystal structure, Raman, FTIR, UV-Vis Absorption, Photoluminescence spectroscopy, TG–DSC and Dielectric properties of new semiorganic crystals of 2-Methylbenzimidazolium Perchlorate. Mater 16. https://doi.org/10.3390/ma16051994
3. Dhawan P, Saini A, Goel S, Tyagi N, H. Yadav H (2022) A systematic study of the third-order nonlinear optical co-crystal of bis-((diisopropyl)ammonium) dichromate: X-ray, Hirshfeld surface, Optical, and Mechanical analysis. J Mol Struct 1270. https://doi.org/10.1016/j.molstruc.2022.133869
4. Sun Y, Tilbury CJ, Reutzel-Edens SM, Bhardwaj RM, Li J, Doherty MF (2018) Modeling olanzapine solution growth morphologies. Cryst Growth Des 18:905–911. https://doi.org/10.1021/acs.cgd.7b01389

5. Goswami PK, Thaimattam R, Ramanan A (2013) Multiple crystal forms of p-aminosalicylic acid: Salts, salt co-crystal hydrate, co-crystals, and co-crystal polymorphs. Cryst Growth Des 13:360–366. https://doi.org/10.1021/cg3015332
6. Ter Horst JH, Cains PW (2008) Co-crystal polymorphs from a solvent-mediated transformation. Cryst Growth Des 8:2537–2542. https://doi.org/10.1021/cg800183v
7. Moovendaran K, Jayaramakrishnan V, S. Natarajan S (2014) Optical studies on L-tartaric acid and L-Prolinium tartrate. Photonics Optoelectron 3(9). https://doi.org/10.14355/jpo.2014.0301.02.
8. Anis M, Shkir M, Baig MI, Ramteke SP, Muley GG, AlFaify S, Ghramh HA (2018) Experimental and computational studies of L-tartaric acid single crystal grown at optimized pH. J Mol Struct 1170:151–159. https://doi.org/10.1016/j.molstruc.2018.05.073
9. Bhattacharjee R, Jain YS, Bist HD (1989) Laser Raman and infrared spectra of tartaric acid crystals. J Raman Spectrosc 20:91–97. https://doi.org/10.1002/jrs.1250200206
10. Fukami T, Tahara S, Yasuda C, Nakasone K (2016) Structural refinements and thermal properties of L(+)-Tartaric, D(−)-Tartaric, and Monohydrate Racemic Tartaric Acid. Int J Chem 8:9. https://doi.org/10.5539/ijc.v8n2p9
11. Liu F, Hooks DE, Li N, Rubinson JF, Wacker JN, Swift JA (2020) Molecular crystal mechanical properties altered via dopant inclusion. Chem Mater 32:3952–3959. https://doi.org/10.1021/acs.chemmater.0c00433
12. Goel S, Sinha N, Yadav H, Joseph AJ, Hussain A, Kumar B (2020) Optical, piezoelectric and mechanical properties of xylenol orange doped ADP single crystals for NLO applications. Arab J Chem 13:146–159. https://doi.org/10.1016/j.arabjc.2017.03.003
13. Kanwal F, Rehman R, Bakhsh IQ (2018) Batch wise sorptive amputation of diamond green dye from aqueous medium by novel Polyaniline-Alstonia scholaris leaves composite in ecofriendly way. J Clean Prod 196:350–357. https://doi.org/10.1016/j.jclepro.2018.06.056
14. Kamatchi K, Sriram S, Sangeetha K, Anuranjani E, Durairaj M, Sabari Girisun TC (2021) Enhanced third order nonlinear optical properties of methyl orange dye doped potassium penta borate octa hydrate (MOPPB) Single crystals using CW diode laser for optical limiting applications. J Mater Sci: Mater Electron 32:15171–15181. https://doi.org/10.1007/s10854-021-06067-2
15. Fang IJ, Trewyn BG (2012) Application of mesoporous silica nanoparticles in intracellular delivery of molecules and proteins. Methods Enzymol:41–59. Academic Press Inc. https://doi.org/10.1016/B978-0-12-391860-4.00003-3
16. Altomare A, Cuocci C, Giacovazzo C, Moliterni A, Rizzi R, Corriero N, Falcicchio A (2013) Expo. 2014. J Appl Cryst 46:1231–1235. http://www.ba.ic.cnr.it/softwareic/expo/contact-us/
17. Stern F, Bievers CA (1950) The crystal structure of tartaric acid. Acta Cryst 3. https://doi.org/10.1107/S0365110X50000975
18. Phan VT, Do TTP, Nguyen DT, Nguyen KD, Vo TTN, Le ATQ, Huynh DT (2021) Growth, ultraviolet-visible, vibrational, photoluminescence and second harmonic generation studies of Amaranth and EDTA co-doped KDP crystals. Opt Quantum Electron. 53. https://doi.org/10.1007/s11082-020-02677-y
19. Kathiresan G, Vijayakumar K, Sundarrajan AP, Kim HS, Adaikalam K (2021) Photocatalytic degradation efficiency of ZnO, GO and PVA nanoadsorbents for crystal violet, methylene blue and trypan blue dyes. Optik (Stuttg) 238. https://doi.org/10.1016/j.ijleo.2021.166671
20. Goel S, Sinha N, Hussain A, Joseph AJ, Yadav H, Kumar B (2018) Sunset yellow dyed triglycine sulfate single crystals: enhanced thermal, mechanical, optical and di-/piezo-/ferro-/pyro-electric properties. J Mater Sci: Mater Electron 29:13449–13463. https://doi.org/10.1007/s10854-018-9470-9
21. Goel S, Sinha N, Yadav H, Hussain A, Kumar B (2016) Effect of crystal violet dye on the structural, optical, mechanical and piezoelectric properties of ADP single crystal. Mater Res Bull 83:77–87. https://doi.org/10.1016/j.materresbull.2016.05.023
22. Reena Priya J, Mercina M, Nancy MP, Mary Linet J, Arul Martin Mani J (2022) Synthesis and characterization of rhodamine B and methylene blue doped potassium hydrogen phthalate single crystals. Mater Today Proc 65:385–390. https://doi.org/10.1016/j.matpr.2022.06.459

23. Shkir M (2016) Effect of titan yellow dye on morphological, structural, optical, anddielectric properties of zinc(tris) thiourea sulphate single crystals. J Mater Res 31(8). https://doi.org/10.1117/2.1201401.005298
24. Yadav H, Sinha N, Kumar B (2016) Modified low temperature Czochralski growth of xylenol orange doped benzopheone single crystal for fabricating dual band patch antenna. J Cryst Growth 450:74–80. https://doi.org/10.1016/j.jcrysgro.2016.06.035
25. Fernandes JM, Mahendra K, Udayashankar NK (2020) Effect of Erioglaucine dye dopant on the structural, optical, mechanical, electrical and nonlinear properties of ammonium dihydrogen phosphate single crystal. Opt Mater (Amst) 110. https://doi.org/10.1016/j.optmat.2020.110528

Investigating the Morphological Evolution, Electron Paramagnetic Resonance, & Electrical Properties of Barium Titanate with Sn-Incorporation

Sachin Kumar, Anurag Pritam, Vaibhav Shrivastava, O. P. Thakur, and Vandna Luthra

1 Introduction

Researchers widely use barium titanate (BT) based perovskite ceramics for their dielectric properties, structural stability, and environmentally friendly nature [1, 2]. The highest value of BT's dielectric constant is typically found near its Curie temperature, which is approximately ca. 120 °C [3]. Many modern applications such as MLCCs (Multi-layer ceramic capacitors), and FeRAM (Ferroelectric Random Access Memory) require a high dielectric constant over a broad temperature range. Some researchers have utilized tin (Sn) to lower the transition temperature and achieve high dielectric constant near RT. [4, 5] The ionic radius of tin in its 6-coordinate state is larger than that of titanium (R_{Sn} (69.0 pm) > R_{Ti} (60.5 pm)) [6]. As a result, tin occupies more void space at B-site than the titanium ions, causing the decrease of structural transition temperature from tetragonal to cubic [7].

Sn-incorporated BT ($Ba(Ti_{1-z}Sn_z)O_3$) is a binary solid solution composed of non-ferroelectric $BaSnO_3$ ($T_c = -260$ °C) and ferroelectric $BaTiO_3$ ($T_c = 120$ °C). The transition temperature of the solid solution can be controlled by varying their concentrations [8]. Besides, the properties of Sn-incorporated BT are expected to

S. Kumar (✉)
Department of Physics & Astrophysics, University of Delhi, Delhi 110007, India
e-mail: sachscientist@gmail.com

S. Kumar · V. Luthra
Department of Physics, Gargi College, Siri Fort Road, New Delhi 110049, India

A. Pritam · V. Shrivastava
Department of Physics, Shiv Nadar University, G.B. Nagar, Greater Noida 201314, India

O. P. Thakur
Solid State Physics Laboratory, Timarpur, Delhi 110054, India

S. B. Krupanidhi et al. (eds.), *Recent Advances in Functional Materials and Devices*,
Springer Proceedings in Materials 37, https://doi.org/10.1007/978-981-99-6766-7_11

be tuned by the composition and the processing conditions [9]. Wei et al. (2011) incorporated tin at B-site in BT and optimized the sintering temperature for the whole series from 0 to 100 mol% incorporation. It has been reported that a higher sintering temperature or soaking time is required for tin incorporation at the B-site with an increase in tin doping due to its relatively large ionic radius and mass as compared to native titanium ion. Horchidan et al. observed the highest value of dielectric constant (~10,000) for 10 mol% tin-doped sample, sintered at 1300 °C for 4 h [7]. Kalyani et al. synthesized different compositions of tin-doped BT using two-step sintering and studied the variation in phase transition temperatures [10]. Nath et al. investigated the variation in the density of tin-doped BT samples with varying sintering temperatures from 1150 to 1400 °C and an increase in the density was observed with an increase in sintering temperature [11]. Wang et al. synthesized compositions of tin and zirconium doping in BT ($Ba(Ti_{0.94}Sn_{0.06-x}Zr_x)O_3$ for $0.00 \leq x \leq 0.06$) at sintering temperature from 1450 to 1550 °C [4]. It has been observed that higher soaking time or sintering temperature is required for tin incorporation at the B-site with an increase in tin doping [12].

Different sintering temperatures and soaking times have been used to optimize the dielectric properties for several tin doping compositions but there is a lack of discussion over the centralized idea of morphological development and corresponding defect concentration. Therefore, the present work emphasizes on these areas along with other structural and ferroelectric investigations. The EPR has been used to understand the nature of defects and to the best of our knowledge has rarely been investigated for this system. Such investigations provide insights into the process of material formation and develop an understanding of the structure–property relationship.

2 Experimental Technique

The present study involved synthesizing tin-doped BT powders using a solid-state ceramic route, with the formula $BaTi_{1-z}Sn_zO_3$; $z = 0$, 0.02, 0.05, 0.07, and 0.1. The samples were given labels BT, BTS2, BTS5, BTS7, and BTS10, respectively. The synthesis process involved mixing barium carbonate (Sigma-Aldrich, 99.9% purity), titanium oxide (Merck, > 99% purity), and stannic oxide (Loba Chemie, 99.8% purity) in the required stoichiometric proportions. The mixture was then milled for 24 h using a horizontal bar roller ball mill with IPA. The resulting suspension was subsequently dried for 8 h at 100 °C and then calcined at 1200 °C for 3 h.

The pellets were then pressed using a uniaxial pellet-pressing machine after grinding the powders with 2% by weight Poly Vinyl Alcohol. Subsequently, the pellets were sintered at 1300 °C for 3 h. The XRD patterns were obtained using a Rigaku Ultima-IV X-ray diffractometer, Cu-kα radiation of 1.5418 Å. The lattice parameters were determined through Rietveld refinement. The strain and crystallite sizes were calculated using Williamson Hall plots. The SEM micrographs were obtained from the fractured portions of the pellets on a Jeol-JSM 6610LV, and the particle size was measured using imageJ software. Furthermore, the sintered powder

was subjected to room temperature (RT) EPR study using a Bruker EMX EPR spectrometer. The Lande's g-factor for a specific resonance peak was calculated using the formula.

$$g = \frac{h.v_o}{\mu_B.H} \tag{1}$$

where h is Planck's constant. ν_o is the operating frequency (9.876 GHz). μ_B and H are Bohr Magnetron (9.274×10^{-24} J/T) and the corresponding applied magnetic field. The dielectric measurements were taken on these samples in the temperature range from RT to 300 °C. The PM-300 piezo-meter was used to measure the piezoelectric charge coefficient (d_{33}) of the samples after they were polled at room temperature for 30 min with 15 kV/cm. Polling aligns the ferroelectric domain in the direction of the applied electric field. Thereafter, domains give a collective response, whereas, in an unpolled sample randomly oriented domains generate random electric fields on applying pressure and as a result, a very low d_{33} value is obtained. The P-E hysteresis loops were obtained at RT using a hysteresis loop tracer based on a modified Sawyer and Tower circuit provided by M/s Marine India Pvt. Ltd. in Delhi.

3 Results and Discussion

3.1 X-Ray Diffraction

The X-ray diffraction (XRD) patterns in Fig. 1. revealed that the samples had a tetragonal phase formation conforming to JCPDS #83–1875 [3]. A small carbonate peak at approximately 28°, was observed only in the BTS10 sample [13]. Furthermore, an observable shift toward lower 2θ values was noticed with an increase in the tin doping concentration, for all the peaks corresponding to different planes. The peak position of (110) peak has been mentioned below to quantify this effect (Fig. 1ii, Table 1). Lattice strain and crystallite size of these samples are also mentioned in Table 1. The given samples showed an increase in crystallite size with an increase in tin doping concentration. Tin substitution expands the lattice structure and its influence can also be noticed in the increase in the value of lattice volume (Table 1) [5].

As shown in Fig. 1iii, an increase in tin doping level resulted in a decrease in the splitting of (002) and (200) peaks at approximately 45°. The peak situated at a lower 2θ value indicates the longer c lattice parameter, whereas the shorter a and b parameters generate a peak at a higher 2θ value. Furthermore, the decrease in average tetragonality was found to be associated with a decrease in the c/a ratio (Table 1) [7].

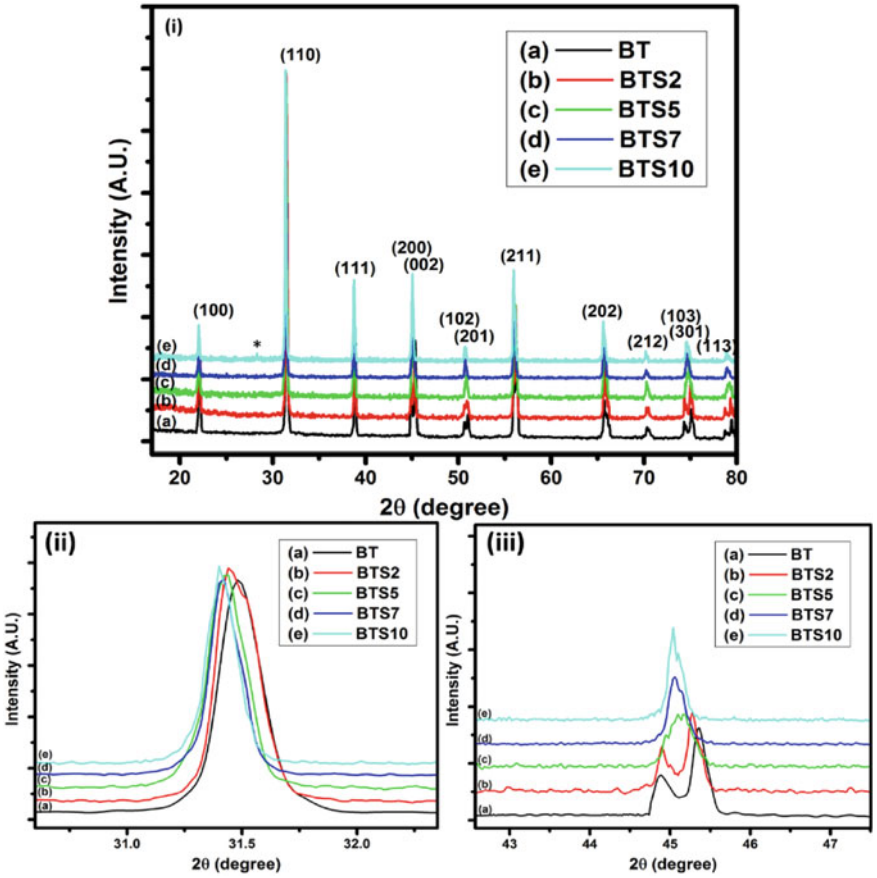

Fig. 1 **i** X-ray diffraction patterns of tin-doped BT ($BaTi_{1-z}Sn_zO_3$) **ii** An enlarged plot of the (110) peak **iii** An enlarged plot of the splitting of (200) and (002) peaks ca. 45°

3.2 Scanning Electron Microscopy (SEM)

The SEM micrographs of tin-doped BT samples were taken from the fractal portions of the sintered pellets (Fig. 2). The intra-granular breaking instead of inter-granular breaking was usually observed while capturing the SEM images for $\leq$ 5 mol% tin doping. Therefore, many fractal portions were investigated to obtain SEM images of grains with clear boundaries. Nath et al. have also shown the SEM micrographs with intra-granular breaking for tin-doped barium titanate samples [11]. The intra-granular breaking, as well as the grains with clear boundaries, are visible in Fig. 2ii.

Figure 2i shows the SEM micrograph of the undoped BT, whose average grain size was ca. 6 μm. Figure 2ii and iii show the microstructure of BTS2 and BTS5 having an average grain size of ca. 16 and ca. 58 μm, respectively. An increase in the grain size with the tin doping to a certain level has been noticed by researchers [14].

Table 1 The (110) peak position, lattice strain, crystallite size, lattice parameters, volume, and c/a ratio of the samples under investigation

Sr. no	Sample	(110) Peak position	Lattice Strain	Crystallite size (nm)	Lattice parameter, a or b (Å)	Lattice parameter, c (Å)	Lattice volume ($Å^3$)	c/a
1	BT	31.46	2.91×10^{-3}	52.34	3.9934	4.0301	64.2690	1.0092
2	BTS2	31.44	3.19×10^{-3}	56.64	3.9990	4.0300	64.4470	1.0077
3	BTS5	31.43	3.88×10^{-3}	67.68	4.0045	4.0202	64.4682	1.0039
4	BTS7	31.42	5.82×10^{-3}	99.83	4.0131	4.0177	64.7041	1.0012
5	BTS10	31.40	5.31×10^{-3}	92.51	4.0148	4.0187	64.7756	1.0010

This can be attributed to the liquid phase formed due to the isovalent substitution of tin for titanium which forms a eutectic in $BaTiO_3$ and $BaSnO_3$ systems [15, 16].

The SEM micrographs of BTS7 are shown in Fig. 3. at different magnifications. These figures provide information about the formation process of bigger particles by the combination of smaller grains. In the case of synthesis via a solid-state method, the grain size depends upon the sintering temperature [4], sintering time [17], and diffusion length[18] of the contributing ions at that temperature. In Fig. 3i, the micrograph was taken at a lower magnification to get a broader view of surface morphology. It can be observed from the morphology (Fig. 3i) that the small grains are fusing among each other to form a bigger particle. The representative white lines are marked along the tentative grain boundary. Figure 3ii is a higher magnification of the same morphology at the position of that white line rectangular box as shown in Fig. 3i. Figure 3ii shows the micrograph of these grain boundaries. Furthermore, in Fig. 3iii the image at even higher magnification shows that the small grains are 0.96 μm in size. The basic difference between the accumulation and the grain boundary is that the grains across the boundary are not diffusing into each other.

3.3 Electron Paramagnetic Resonance (EPR)

The EPR patterns of the undoped and tin-doped barium titanate samples are given in Fig. 4. The EPR signals corresponding to barium and titanium vacancies are observed at $g = 1.974$ and $g = 2.004$, respectively [19, 20]. The undoped BT showed a minor bump dedicated to barium vacancies at $g = 1.974$. In the case of tin-doped samples, an intense barium vacancy peak was observed for BTS2 and its intensity reduced with an increase in tin doping concentration. Barium vacancies are shallow defects at the grain surface [21]. While the signal for titanium vacancy at $g = 2.004$ was

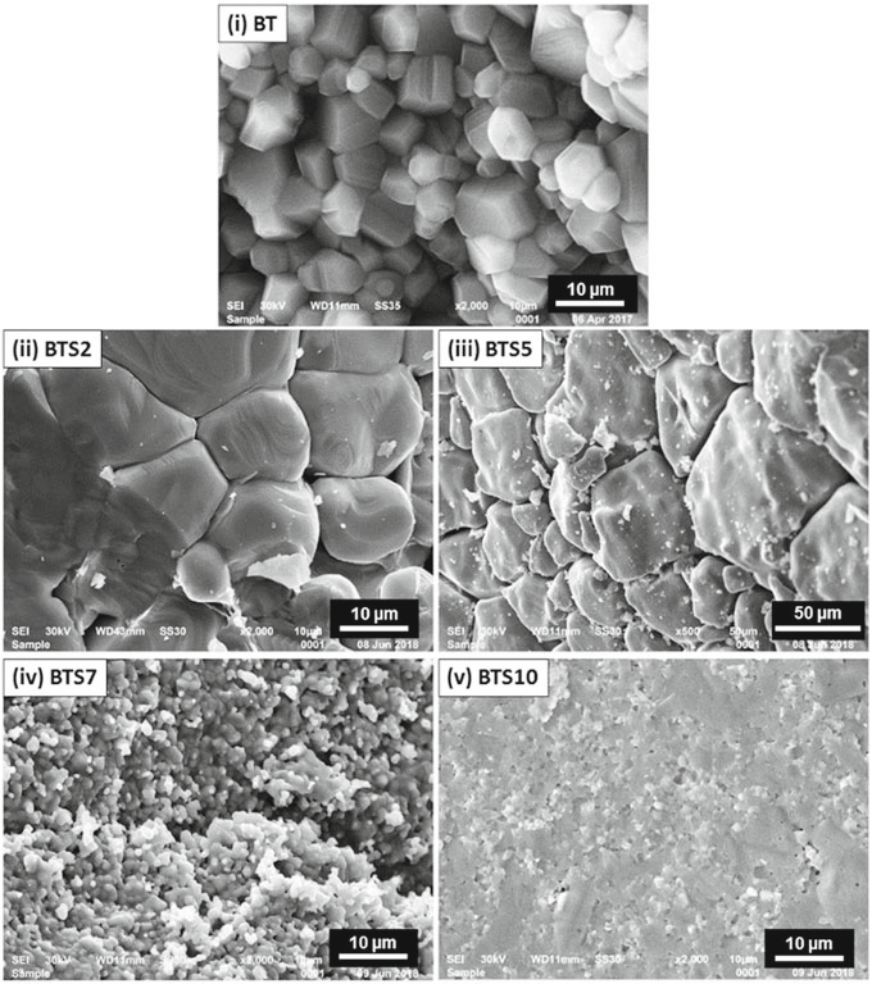

Fig. 2 SEM images of **i** BT **ii** BTS2 **iii** BTS5 **iv** BTS7 **v** BTS10 samples

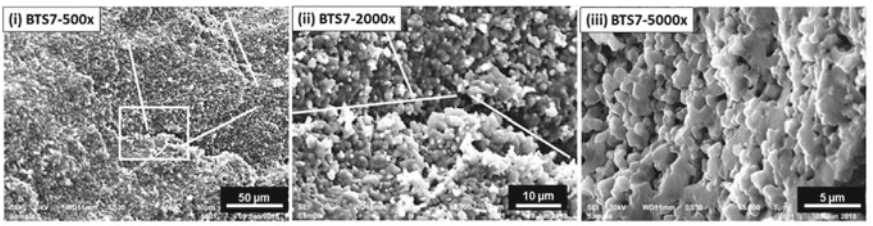

Fig. 3 SEM images of BTS7 at **i** 500, **ii** 2000, and **iii** 5000 magnifications

found to increase with the increase in tin doping concentration. The increase in the number of defects like B-site vacancy could be attributed to the fact that tin is a relatively heavier element than titanium and tin ions were not able to diffuse up to the required length and occupy all the stoichiometrically available titanium sites. Therefore, the intensity of titanium vacancy peak increases with an increase in tin-doping concentration. The partial substitution of tin at B-site in barium titanate has also been addressed by Veselivonic et al. by Rietveld refinement of the XRD data and XRF (X-ray Fluorescence) spectroscopy [8].

A group of 6 equidistant peaks (sextet) can also be seen emerging with increasing doping concentration because of the increase in cubic nature in the system [22, 23]. This has been reported in the literature as the hyperfine structure of Manganese ion [22]. In the present study, the separation between the consequent peaks in the present work is close to 83 Gauss. This confirms that the observed peaks are because of the presence of Mn^{2+} ions in the sample having a spin of 5/2 [23].

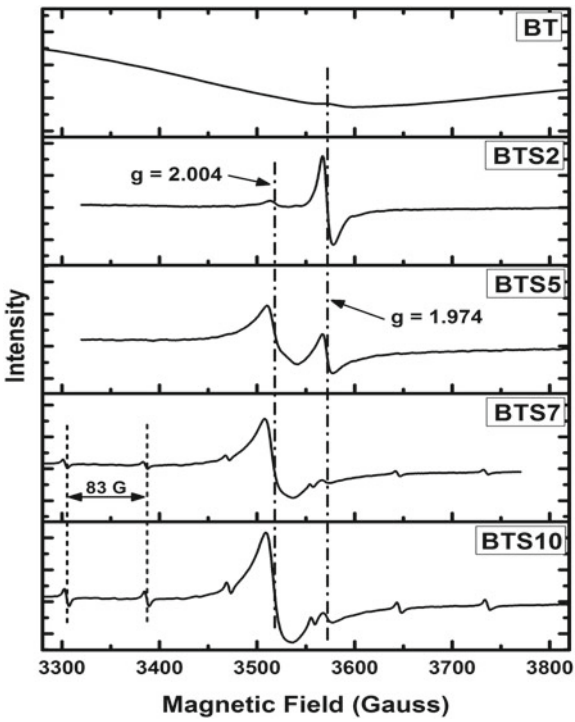

Fig. 4 The EPR data of undoped and tin-doped barium titanate samples

3.4 *Dielectric Properties*

Figure 5i shows the plots of dielectric constant with respect to temperature at 1 kHz frequency. Figure 5ii and iii represent the dielectric constant vs temperature curves of BTS2 and BTS10 samples at different frequencies.

A composition-dependent variation in T_c and dielectric constant is observed. The maximum value of the dielectric constant has been observed for BTS2 at a transition temperature of 106 °C. The values of the T_c and the respective dielectric constants are shown in Table 2 for various samples. It has been noticed from the XRD pattern that Sn incorporation decreases the average tetragonality of the material (Fig. 1iii).

This infers a decrease in the polarization density of the material with tin doping, which is contrary to the enhancement in its dielectric constant. Shi et al. have investigated the enhancement of dielectric constant in BT because of tin incorporation and

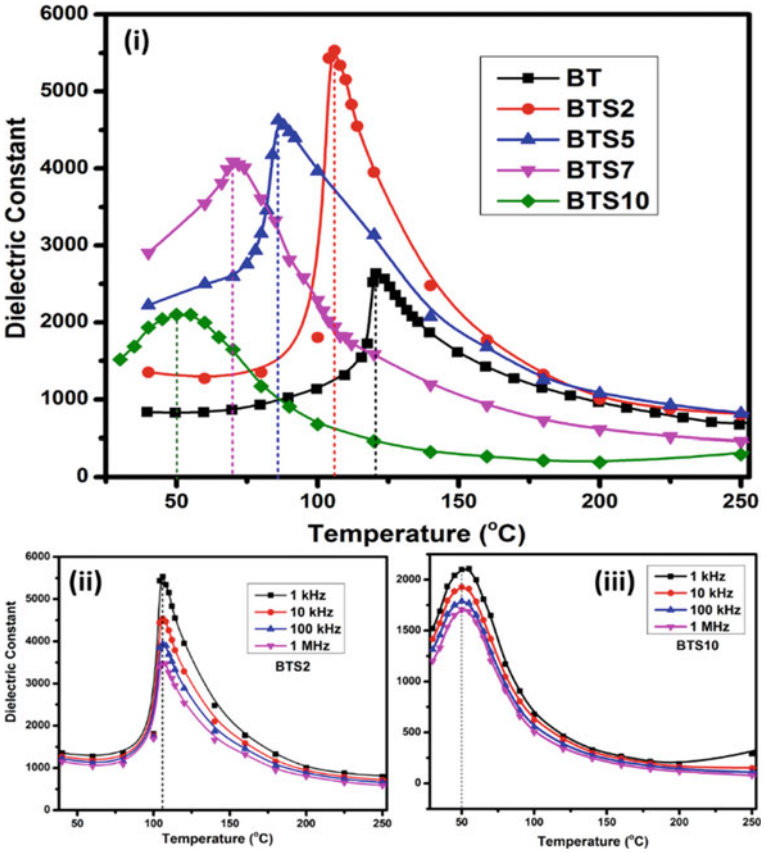

Fig. 5 **i** Dielectric constant with respect to temperature for different doping concentrations **ii** dielectric constant vs. temperature curves for BTS2 and **iii** BTS10 at different frequencies

Table 2 The values of the transition temperature, dielectric constant at 40 °C and T_c (1 kHz), and diffusivity coefficient of the samples under investigation

Sr. no	Sample name	Transition temperature (T_c) (°C)	Dielectric const. at 40 °C (1 kHz)	Dielectric const. at T_c (1 kHz)	(γ) Diffusivity coefficient
1	BT	120	837	2637	1.083 ± 0.009
2	BTS2	106	1352	5533	1.187 ± 0.019
3	BTS5	86	2224	4625	1.230 ± 0.014
4	BTS7	70	2903	4086	1.342 ± 0.016
5	BTS10	50	1934	2099	1.807 ± 0.048

it was observed that besides the increase in an average symmetry, tin doping distorts the lattice structure and increases the local polarization forming polar regions [24]. Therefore, the increase in the dielectric constant of BTS2 could be attributed to doping-induced structural distortions. The extent of the enhancement in local polarization with tin doping is a temperature-dependent process as it can be generalized from the literature that different tin doping compositions show their optimum values of dielectric constant for different sintering temperatures [19, 25, 26]. The maximum value of dielectric constant was observed for 2 mol% tin-doping levels when the samples were sintered at 1300 °C.

For doping concentrations above 2 mol%, the decrease in tetragonality becomes more significant than local polarization, causing the dielectric constant to decrease at its transition temperature. The sample BTS7 demonstrated the highest value of dielectric constant near room temperature (at 40 °C) due to its transition temperature being closer to room temperature, combined with an optimal sintering temperature.

The data was analyzed using the Modified Curie–Weiss Law [26]. A gradual increase in diffusivity from BT ($\gamma = 1.08$) to BTS7 ($\gamma = 1.34$) was observed, but its value increases high for BTS10 samples ($\gamma = 1.80$). This sample also showed a low dielectric constant. With the increase in tin content, the peak of the dielectric permittivity becomes progressively more diffused (BTS10), but the peak position doesn't change (Fig. 5iii). Therefore, the high value of diffusivity coefficient ($\gamma = 1.80$) and broad transition in BTS10 sample (Fig. 5iii) manifests DPT (Diffuse Phase Transition) behavior [27]. The incorporation of dopant ions such as tin in the place of a native titanium ion distorts the long-range uniformity and gives rise to the increase in diffusivity [28]. The increasing number of B-site vacancy defects has also been discussed in the EPR investigation, which can also be a contributing factor to the increasing diffusivity with an increase in tin doping concentration.

3.5 P-E Hysteresis Loop

P-E hysteresis loops of the tin-doped BT samples are shown in Fig. 6. The maximum remnant polarization ($2P_r$) was observed to be 11.56 μC/cm^2 for BTS2. However, the value of remnant polarization was found to decrease with an increase in tin doping. However, Horchidan et al. have observed an increase in remnant polarization up to 5 mol% tin doping in BT which decreases afterward [27]. Besides, the minimum value of coercivity was also observed for BTS2. Its value increased for BTS5 and started decreasing thereafter. It can also be noticed that the saturation polarization is also found to be the maximum for BTS2 sample (Table 3), which can be correlated with the highest value of the dielectric constant obtained for this sample.

As the tin content increased, a reduction in both the maximum and remnant polarization was observed. This can be attributed to the non-ferroelectric nature of $BaSnO_3$, leading to a decrease in polarization [29]. Furthermore, increased Sn doping caused $BaTiO_3$ to transition to DPT and then relaxor behavior, resulting in

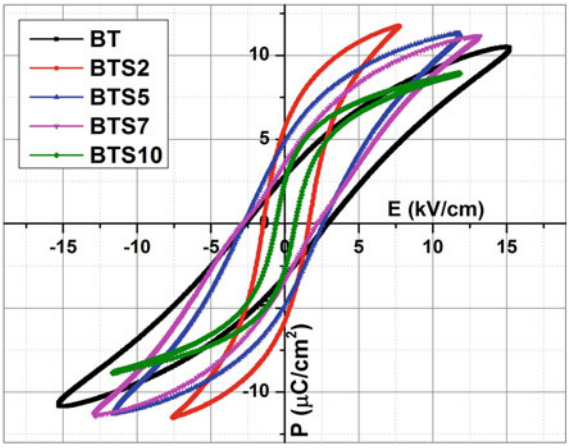

Fig. 6 Plots demonstrating the P-E hysteresis loops of the undoped and tin-doped BT samples

Table 3 The $2P_r$ (remanence), $2E_c$ (coercivity), P_s (saturation polarization), and piezoelectric coefficient (d_{33}) of the samples under investigation

Sr. No	Sample	($2P_r$) Remanence (μC/cm^2)	($2E_c$) Coercivity (kV/cm)	Saturation Polarization (P_s) (μC/cm^2)	d_{33} (pC/N)
1	BT	5.9	5.54	10.6	79
2	BTS2	11.56	3.08	11.64	114
3	BTS5	9.88	5.36	11.26	48
4	BTS7	7.00	5.04	11.22	26
5	BTS10	5.17	1.26	8.19	16

slender hysteresis loops with lower polarization and coercive field, values given in Table 3.

3.6 Piezoelectric Coefficient (d_{33})

The maximum value of d_{33} was observed for BTS2 sample. It decreases after 2 mol% doping because of the dominance of cubic nature. It has been stated by researchers that the switching of dipoles is more accessible and quicker if the energy barrier for polarization switching is low [30, 31]. It has also been established that the energy barrier for polarization switching decreases with an increase in tin content in BT [31]. The high value of the piezoelectric coefficient (d_{33}) can be correlated with the lower value of coercivity for BTS2 than the coercivity of its adjoining samples (Table 3). High saturation polarization from the P-E hysteresis loop (Fig. 6) and high dielectric constant observed for BTS2 sample suggest the existence of enhanced polarization for this composition and could be a reason for its high piezoelectric coefficient.

4 Conclusion

The tetragonal structure of these samples was confirmed using XRD. Moreover, in SEM micrographs the particle size increased till 5 mol% tin-doping and small grain microstructure forming big accumulations was observed for 7 mol% tin doping. EPR data exhibited an increase in titanium vacancies with tin doping because of the diffusion-limited substitution process. The intensity of Mn^{2+} hyperfine peaks was also found to increase with an increase in tin doping. The diffusion-limited substitution can be supported by the increase in vacancy defects with the increase in tin doping concentration. The BTS2 sample showed the highest value of the dielectric constant at its transition temperature because of an increase in polarization initiated by doping-induced distortions. It is also evident from the P-E hysteresis loop of BTS2 showing the highest value of saturation (P_s), remnant polarization ($2P_r$) and the lowest value of coercive field ($2E_c$). Tin-doped samples achieved their saturation polarization at a lower electric field than undoped BT because of the decrease in domain switching energy. The piezoelectric coefficient (d_{33}) of BTS2 was also found to be the maximum because of faster domain switching and enhanced polarization.

Acknowledgements We are thankful to Star College Grant, Gargi College-wide SAN/No.102/IFD/DBT/SAN/1911/2008-09 (Department of Biotechnology). We are thankful to Principal, Gargi College and USIC instrumentation facility, University of Delhi for providing various facilities.

References

1. Yoon DH (2006) Tetragonality of barium titanate powder for a ceramic capacitor application. J Ceram Process Res 7(4):343–354
2. Chen WP, Shen ZJ, Guo SS, Zhu K, Qi JQ, Wang Y, Chan HLW (2008) A strong correlation of crystal structure and Curie point of barium titanate ceramics with Ba/Ti ratio of precursor composition. Phys B Condens Matter 403(4):660–663
3. Kumar S, Thakur OP, Luthra V (2018) Modulating the effect of yttrium doping on the structural and dielectric properties of Barium titanate. Phys Status Solidi A 215(7):1700710
4. Wang N, Zhang BP, Ma J, Zhao L, Pei J (2017) Phase structure and electrical properties of Sn and Zr modified $BaTiO_3$ lead-free ceramics. Ceram Int 43(1):641–649
5. Wei X, Yao X (2007) Preparation, structure and dielectric property of barium stannate titanate ceramics. Mater Sci Eng B 137(1–3):184–188
6. Dean JA (1999) Lange's Handbook of chemistry, 15th ed. McGraw Hills
7. Horchidan N, Ianculescu AC, Curecheriu LP, Tudorache F, Musteata V, Stoleriu S, Dragan N, Crisan D, Tascu S, Mitoseriu L (2011) Preparation and characterization of barium titanate stannate solid solutions. J Alloys Compd 509(14):4731–4737
8. Veselinović, L., Mitrić, M., Mančić, L., Vukomanović, M., Hadžić, B., Marković, S., Uskoković, D (2014) The effect of Sn for Ti substitution on the average and local crystal structure of $BaTi_{1-x}Sn_xO_3$ ($0 \leq x \leq 0.20$). J Appl Crystallogr 47(3):999–1007
9. Cai W, Fan Y, Gao J, Fu C, Deng X (2011) Microstructure, dielectric properties and diffuse phase transition of barium stannate titanate ceramics. J Mater Sci 22(3):265–272
10. Kalyani AK, Brajesh K, Senyshyn A, Ranjan R, Kalyani AK, Brajesh K, Senyshyn A, Ranjan R (2016) Orthorhombic-tetragonal phase coexistence and enhanced piezo-response at room temperature in Zr, Sn, and Hf modified $BaTiO_3$. Appl Phys Lett 252906(2014):1–5
11. Nath AK, Medhi N (2012) Density variation and piezoelectric properties of $Ba(Ti_{1-x}Sn_x)O_3$ ceramics prepared from nanocrystalline powders. Bull Mater Sci 35(5):847–852
12. Lu DY, Guan DX (2017) Photoluminescence associated with the site occupations of Ho^{3+} ions in $BaTiO_3$. Sci Rep 7(1):1–8
13. Ashiri R (2016) RSC Advances nanocrystals from mechanically activated $BaCO_3$ and TiO_2 powders : innovative mechanochemical. RSC Adv 6(21):17138–17150
14. Ansaree MJ, Upadhyay S (2017) Study of phase evolution and dielectric properties of Sn-doped barium titanate. Emerg. Mater. Res. 1817(4):21–28
15. Bilous A, V'Yunov O, Kovalenko L (2001) (Ba, Y)(Ti, Zr, Sn)O_3-based PTCR materials. Ferroelectrics 254(1–4):91–99
16. Matsuo Y, Sasaki H (2019) Exaggerated grain growth in Liquid-Phase sintering of $BaTiO_3$. J. Am. Ceram. Soc. Notes. 12:471
17. Bongkarn T, Wattanawikkam C (2009) The preparation of $Ba(Sn_{0.1}Ti_{0.9})O_3$ ceramics via a solid state reaction method. Ferroelectrics 382(1):56–61
18. Miao S, Pokorny J, Pasha UM, Thakur OP, Sinclair DC, Reaney IM (2009) Polar order and diffuse scatter in $Ba(Ti_{1-x}Zr_x)O_3$ ceramics. J Appl Phys 106(11):1–6
19. Dunbar TD, Warren WL, Tuttle BA, Randall CA, Tsur Y (2004) Electron paramagnetic resonance investigations of Lanthanide-Doped barium titanate: dopant site occupancy. J Phys Chem B 108(3):908–917
20. Kolodiazhnyi T, Petric A (2003) Analysis of point defects in polycrystalline $BaTiO_3$ by electron paramagnetic resonance. J Phys Chem Solids 64(6):953–960
21. Lu DY, Sun XY, Toda M (2006) Electron spin resonance investigations and compensation mechanism of europium-doped barium titanate ceramics. Jpn J Appl Phys 45(11):8782–8788
22. Choudhury D, Pal B, Sharma A, Bhat SV, Sarma DD (2013) Magnetization in electron-and Mn-doped $SrTiO_3$. Sci Rep 3:1–4
23. Slipenyuk AM, Glinchuk MD, Bykov IP, Yurchenko LP, Mikheev VA, Frenkel OA, Tkachenko VD, Garmash EP (2003) Study of $BaTiO_3$ ceramics doped with Mn and Ce or Nb and Sr. Condens Matter Phys 6(2):237–244

24. Shi T, Xie L, Gu L, Zhu J (2015) Why Sn doping significantly enhances the dielectric properties of $Ba(Ti_{1-x}Sn_x)O_3$. Sci Rep 5:8–11
25. Xiaoyong W, Yujun F, Xi Y (2003) Dielectric relaxation behavior in barium stannate titanate ferroelectric ceramics with diffused phase transition. Appl Phys Lett 83(10):2031–2033
26. Horchidan N, Ianculescu AC, Vasilescu CA, Deluca M, Musteata V, Ursic H, Frunza R, Malic B, Mitoseriu L (2014) Multiscale study of ferroelectric-relaxor crossover in $BaSn_xTi_{1-x}O_3$ ceramics. J Eur Ceram Soc 34(15):3661–3674
27. Shvartsman VV, Kleemann W, Dec J, Xu ZK, Lu SG (2006) Diffuse phase transition in $BaTi_{1-x}Sn_xO_3$ ceramics: An intermediate state between ferroelectric and relaxor behavior. J Appl Phys 99(12):1–8
28. Jha PA, Jha AK (2013) Effects of yttrium substitution on structural and electrical properties of barium zirconate titanate ferroelectric ceramics. Curr Appl Phys 13(7):1413–1419
29. Kalyani AK, Krishnan H, Sen A, Senyshyn A, Ranjan R (2015) Polarization switching and high piezoelectric response in Sn-modified $BaTiO_3$. Phys Rev B−Condens Matter Mater Phys 91(2):1–13
30. Zhu L, Zhang B, Zhao L, Li S, Zhou Y, Shi X, Wang N (2016) Large piezoelectric effect of $(Ba, Ca)TiO_3$ – $xBa(Sn, Ti)O_3$ lead-free ceramics. J Eur Ceram Soc 36:1017–1024
31. Liu W, Wang J, Ke X, Li S (2017) Large piezoelectric performance of Sn doped $BaTiO_3$ ceramics deviating from quadruple point. J Alloys Compd 712:1–6

Photoluminescence and Optical Studies of a Temperature Sustainable Dy^{3+} Doped Silicate Phosphor for Photonic Applications

Vibha Sharma, Shreya Maurya, and A. S. Rao

1 Introduction

In today's lighting and display industries, rare-earth ions-activated luminescent materials are widely used, particularly in phosphor-converted white LEDs. The efficiency of w-LEDs is significantly influenced by the characteristics of luminescent materials. Phosphors with good efficiency, tunable luminescence, and high thermal stability are needed to boost the performance of white LEDs [1]. The majority of currently available w-LEDs are using a blue-emitting (450–470 nm) diode, which activates a $Y_3Al_5O_{12}:Ce^{3+}$ (YAG:Ce) phosphor and causes it to generate yellow light. This w-LED does not have a red-emitting component, hence the hue of the light it emits is incomplete. The color rendition values of the above-mentioned w-LEDs are not very close to perfect white light because of the lack of blue-excitable and red-emitting phosphor systems in these devices [2]. A standard method for creating white light uses RGB (red, green, and blue) phosphors in n-UV LED chips. However, maintaining a balanced proportion of red, blue, and green phosphors to get white emission is difficult and using three phosphors requires adding more dopants, which increases the cost of LEDs. To reduce expenses, it is therefore required to dope a single rare earth ion. With at least two distinct emission bands in the blue and yellow regions, Dy^{3+} is the most reliable rare earth ion for producing white light. To achieve optimal white light, researchers have been experimenting with a variety of methods. Another essential feature that influences the effectiveness of emitting devices is the choice of host material. Silicates are regarded as dazzling luminescent hosts for solid-state illumination, particularly for white light-emitting diodes, due to their strong chemical-physical stability and high-temperature stability [3, 4]. Numerous studies have recently used the Dy^{3+} ion as a dopant and silicates as the host material to increase the luminous

V. Sharma · S. Maurya · A. S. Rao (✉)
Department of Applied Physics, Delhi Technological University, New Delhi-110 042, Bawana Road, India
e-mail: drsrallam@gmail.com

S. B. Krupanidhi et al. (eds.), *Recent Advances in Functional Materials and Devices*, Springer Proceedings in Materials 37, https://doi.org/10.1007/978-981-99-6766-7_12

characteristics of phosphor [5–8]. Currently, there are no papers available describing luminescence studies of Dy^{3+} doped KCS phosphors. In the present research work, we have prepared Dy^{3+} doped KCS phosphor using the traditional solid-state reaction method and its structural and luminescence behavior was examined using XRD, DRS, PL, and TDPL characterizations. The results obtained show that the as-prepared phosphor is a favorable candidate for near UV-based white LEDs.

2 Experimental

2.1 Phosphor Preparation

The Dy^{3+} ions activated KCS phosphor for white light-emitting applications was prepared using conventional solid-state synthesis. The raw ingredients (K_2CO_3, 99.9%), calcium carbonate ($CaCO_3$ 99.9%), silicon oxide (SiO_2 99.99%), and dysprosium oxide (Dy_2O_3 99.9%) were first weighed in accordance with the nominal composition of phosphor, and then completely mixed and ground for two hours using an agate mortar and pestle. The sample was prepared in accordance with the chemical equation given below:

$$2K_2CO_3 + (1-x)CaCO_3 + 3SiO_2 + (x/2)Dy_2O_3 = K_4Ca_{1-x}Dy_xSi_3O_9 + \text{Gaseousproducts} \quad (1)$$

here x = 0, 0.3.

The ground sample was kept in an alumina crucible and then heated to 850° C in an electric furnace for 6 h. After cooling down, the product was finally ground for further characterizations [9, 10].

2.2 Characterization Techniques

The crystal structures of as-synthesized Dy^{3+} doped phosphor were determined using X-ray diffraction method using the Bruker X-ray Diffractometer, model-D8 Advance (With Cu-Kα source of radiation, λ = 1.5406), and data were collected over the 20° to 60° range. Diffused Reflectance Spectrum (DRS) was recorded using JASCO (V-770) spectrophotometer and used to calculate the optical bandgap of Dy^{3+} doped phosphor. PL emission and excitation spectrum were captured using a JASCO (FP-8300) spectrofluorophotometer (1.0 nm resolution). Temperature-dependent photoluminescence properties were investigated using a FLAME-S-XR1-ES spectrometer and a central heating system section.

3 Results and Discussion

3.1 XRD Analysis

Figure 1 represents the X-ray diffraction patterns for undoped KCS phosphor and 0.3 mol% of Dy^{3+} ions doped KCS phosphor. The XRD patterns show complete agreement with the standard data from JCPDS Card No. 00–039-1427. The as-prepared samples were crystallized in a single-phase cubic structure. The estimated lattice parameters are a = b = c = 15.9446 Å, V = 4053.60 $Å^3$ and α=β=γ=90°. The Debye–Scherrer equation was used to estimate the crystallite size [11].

$$L = \frac{k\lambda}{\beta_c cos\theta_B} \tag{2}$$

where L represents the crystallite size, k is the shaped factor ($k \sim 0.94$) and λ = 1.5406 Å is wavelength of X-ray, respectively. β_c is FWHM and θ_B denotes the Bragg's angle, respectively. The typical crystallite size for the KCS ground sample is found to be 113.49 nm.

Scherrer's formula can produce inaccurate results when used to compute crystallite size because as the crystallite size grows, the effects of instrumental broadening and strain broadening become more pronounced. Another method of calculating crystallite size is Williamson Hall (W–H) Plot which considers additional factors such as instrumental broadening, strain broadening, and other crystallographic parameters to provide a more accurate characterization of the crystallite. By plotting β_{hkl} cosθ on y-axis against 4 sinθ on x-axis, shown in Fig. 2, we can evaluate the strain component from the slope and the crystallite size component from the y-intercept [12].

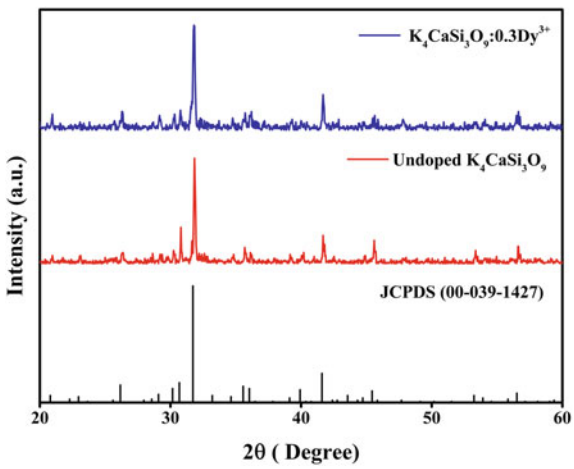

Fig. 1 XRD of un-doped and Dy^{3+} doped KCS phosphors

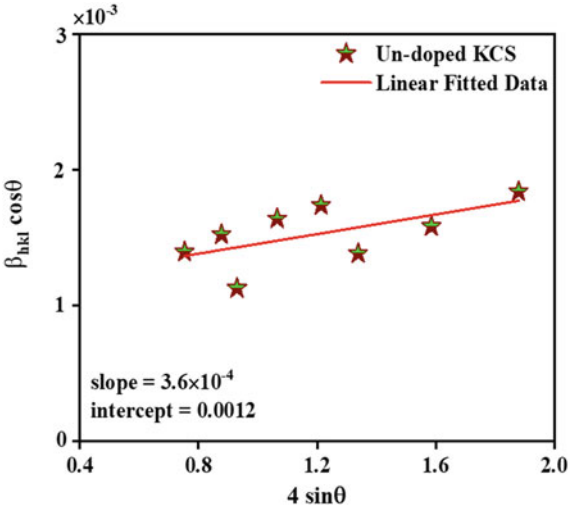

Fig. 2 Williamson Hall Plot for undoped KCS phosphor

$$\beta_{hkl}\cos\theta_B = \frac{k\lambda}{L} + 4\,\varepsilon\,\sin\theta_B \tag{3}$$

where L, k, ε, and λ represent the average crystallite size, shape factor (~0.94), strain, and wavelength of X-ray (1.5406 Å), respectively. β_{hkl} and θ are full width at half maxima and the Bragg's angle, respectively. The average crystallite size for the as-prepared KCS phosphor using W–H plot approach is found to be 125.8 nm. This result is in consonance with the crystallite size calculated by using Scherrer's formula.

3.2 Diffused Reflectance Spectroscopy Studies

UV–Vis Spectroscopy is used to measure how much light an individual molecule absorbs. The reflectance spectrum of 0.3 mol% doping of Dy^{3+} ions in KCS phosphor obtained in the 200–1400 nm range is shown in Fig. 3. The spectrum reveals a wide excitation band centered at 254 nm, which is analogous with the charge transfer between O^{2-} and Dy^{3+} ions [13]. The f-f transition of Dy^{3+} corresponds to the weak absorption peaks at 350 nm and 425 nm [13]. The transitions from the ground state of $^6H_{15/2}$ to the $^6F_{5/2}$, $^6F_{7/2}$, $^6F_{9/2} + {}^6H_{7/2}$, and $^6F_{11/2} + {}^6H_{9/2}$ states can be attributed to the peaks at 798, 894, 1072, and 1268 nm of wavelengths respectively [13].

The Kubelka–Munk (K-M) theory was used to transform reflectance data into absorption data. The K-M function is employed in order to compute the band gap of the KCS:0.3Dy^{3+} phosphor [14]:

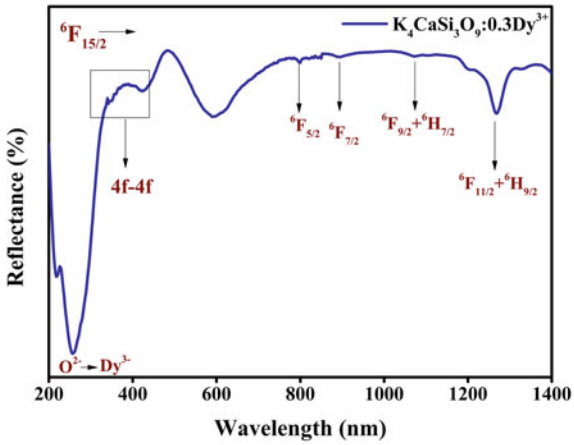

Fig. 3 Diffused reflectance spectra of 0.3 mol% of Dy^{3+} doped KCS phosphor

$$F(R) = \frac{(1-R)^2}{2R} = \frac{Q}{S} \tag{4}$$

Here, R represents the diffused reflectance of the sample, Q denotes the absorption coefficient and S is the scattering coefficient. The Tauc's relation correlates with the band gap (E_g) and linear absorption coefficient (α) of a material [15]:

$$\alpha h\nu = K\left(h\nu - E_g\right)^{1/2} \tag{5}$$

where $h\nu$ is energy of photon, E_g represents the band gap, and K is a constant. By using the Eq. (4), the Tauc's relation in Eq. (5) can be modified and represented as:

$$[F(R)h\nu]^2 = C\left(h\nu - E_g\right) \tag{6}$$

Using the plot of $[F(R)h\nu]^2$ *versus* $h\nu$ by using the Eq. (6), the band gap value (E_g) is obtained by extrapolation of the linear fitted regions to $[F(R)h\nu]^2 = 0$. Figure 4 shows the linear fit plot of as-prepared phosphor. The value of direct bandgap for the phosphor was found to be 3.8 eV which is lower than the values found in earlier reported works for $LiCaBO_3$:Dy^{3+} (4.85 eV) and NCBP:0.07Dy^{3+} phosphors (4.30 eV) [16, 17].

3.3 Photoluminescence Spectral Studies

Figure 5 shows the PL excitation and emission spectra of Dy^{3+} doped KCS phosphor recorded in the range of 200–400 nm and 400–700 nm respectively. The transitions from $^6H_{15/2} \rightarrow {}^6P_{3/2}, {}^4I_{9/2}, {}^6P_{7/2}, {}^6P_{5/2}, {}^4K_{17/2}, {}^4G_{11/2}, {}^4I_{15/2}$ are attributed to the highly

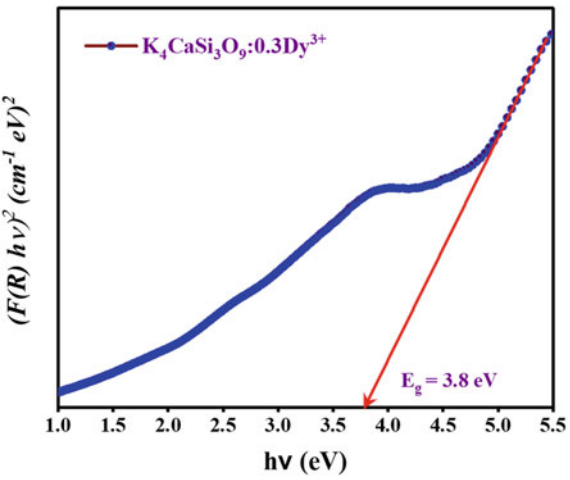

Fig. 4 Tauc's plot for Dy^{3+} ions doped KCS phosphor

intense peak at 350 nm and somewhat less intense peaks at 325, 338, 350, 365, 388, 425, and 452 nm in the excitation spectrum respectively [18]. The highest intensity peak among them is centered at 350 nm which shows that the as-prepared Dy^{3+} ions doped phosphor can be excited at 350 nm wavelength effectively. When the phosphor was agitated at 350 nm, concurrent emanation of blue (489 nm), yellow (576 nm), and a less intense red (673 nm) colors were yielded owing to the $^4F_{9/2} \rightarrow {}^6H_{15/2}$, $^4F_{9/2} \rightarrow {}^6H_{13/2}$ and $^4F_{9/2} \rightarrow {}^6H_{11/2}$ transitions, respectively [19]. This indicates that the as-prepared phosphor can contribute in the production of white light. To emphasize the impact of Dy^{3+} ions activated phosphor on luminescent emission, the CIE 1931 × and y coordinates were calculated using the emission spectra at 350 nm as depicted in Fig. 6. The value of Color Rendering Index (CRI) is 52 as obtained from PL data and the value of coordinates was calculated to be x = 0.2353 and y = 0.3015 which lies in the white region.

3.4 Temperature-Dependent Photoluminescence (TD-PL)

One of the key characteristics that makes phosphor materials suitable for use in a variety of light emanating devices is how temperature affects their photoluminescence properties. Phosphors used in lighting equipment often need strong thermal stability owing to the high operating temperature (120–150 °C) of UV/blue LED chips [20]. Hence, the TDPL studies of the as-prepared phosphor have been carried out under λ_{ex} = 350 nm to investigate the thermal stability by varying the temperature from 18 to 170 °C. Fig. 7 shows the variation in intensity of $^4F_{9/2} \rightarrow {}^6H_{13/2}$ transition by taking the initial intensity as 100% at 18°C. The PL intensity starts decreasing with increase in temperature and at 170°C, the emission intensity was 64.2% of the initial. The significant thermal durability of the Dy^{3+} doped silicate

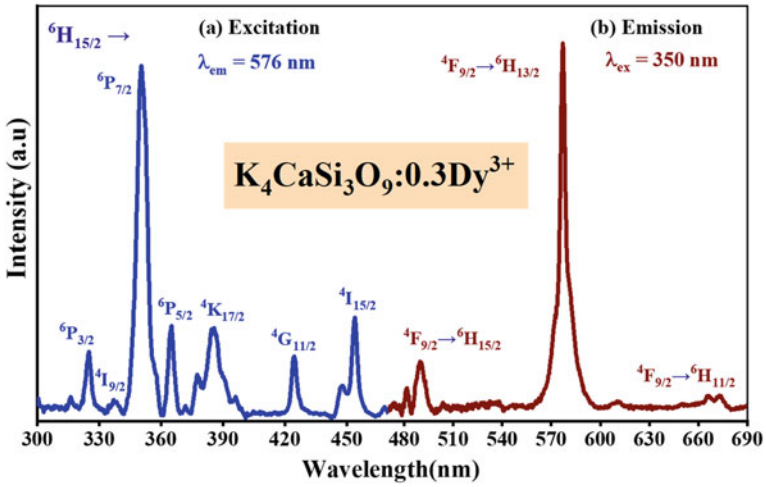

Fig. 5 PL excitation and emission spectrum of Dy^{3+} doped KCS phosphor

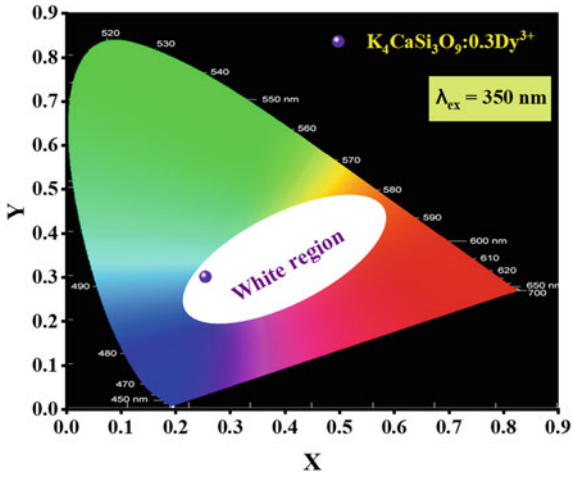

Fig. 6 CIE chromaticity coordinates of Dy^{3+} doped KCS phosphor

phosphor is indicated by this much retaining of the luminescence intensity at 170 °C.

Furthermore, the activation energy is calculated using Arrhenius equation [21]:

$$\frac{I_0}{1 + B\,exp(-\Delta E/KT)} \tag{7}$$

where k is the Boltzmann constant (8.67×10^{-5} eV K^{-1}), B is a constant, and ΔE is the activation energy. I_0 and I_t represents the intensity at 18 °C and temperature T

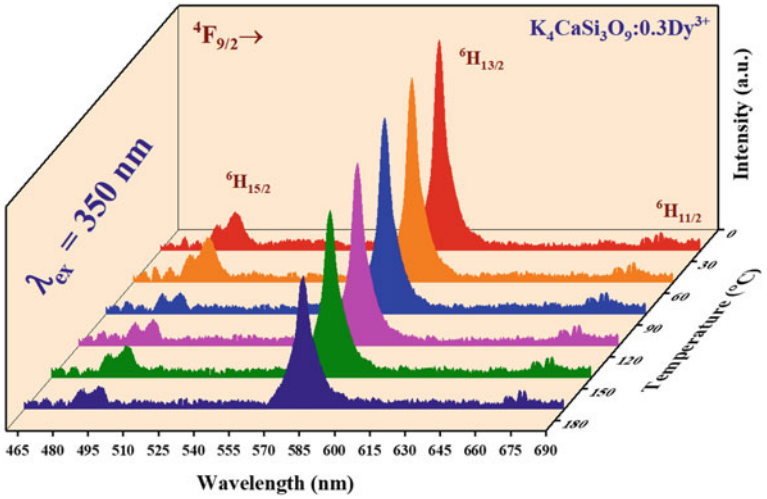

Fig. 7 Temperature-dependent PL spectrum of 0.3 mol% of Dy^{3+} doped KCS phosphor

(°C) respectively. In order to calculate ΔE, the slope's value is calculated by fitting $\ln[(I_0/I_T)-1]$ versus $1/k_BT$ (as demonstrated in Fig.8). ΔE is equal to 0.30 eV for as-synthesized Dy^{3+} phosphors, which is greater than the values found in earlier investigations for $Ca_3Bi(PO_4)_3$:6Dy^{3+} (0.223 eV) [22] and BZPO:Ce^{3+}, Dy^{3+}/Tb^{3+} phosphors (0.15 eV) [23].

Comparatively high value of ΔE indicates their thermal stability and supports their prospective use in solid-state lighting device [24].

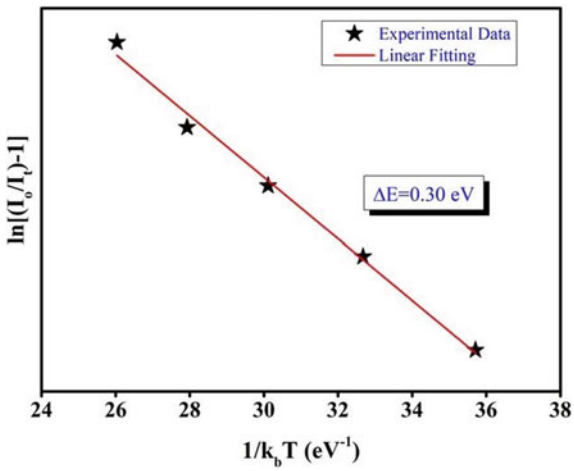

Fig. 8 Activation energy of 0.3 mol% of Dy^{3+} doped KCS phosphor

4 Conclusions

In the present work, Dy^{3+} activated phosphors were prepared using solid-state synthesis route and analyzed using XRD, DRS, PL, and TDPL characterizations. The phase purity and the cubic structure are exhibited through XRD analysis. The optical band gap is calculated to be 3.8 eV using Tauc's Plot. In PL spectra under excitation of 350 nm, a relatively high intensity peak is obtained at 576 nm. Furthermore, according to TDPL characteristics, the intensity remains 64.2% at 170 °C, demonstrating the phosphor's good thermal stability. All the aforementioned findings enable us to conclude that the as-prepared Dy^{3+} doped silicate phosphor is a very suitable candidate for application in white LEDs excited by n-UV light.

Declaration of Competing Interest The authors declare that they have no known competing financial interests or personal relationships that could have appeared to influence the work reported in this paper.

References

1. Tong X, Zhou H, Zhang H, Han J, Zhang X (2022) Effect of ionic couple substitution on the enhanced photoluminescence properties of (BaMg)1–x(KxAl10+x)O17:Eu2+ phosphor for white LEDs application. J Lumin 246:118825. https://doi.org/10.1016/j.jlumin.2022.118825
2. Lohia N, Jaiswal VV, Bishnoi S, Swati G, Sharma SN, Mohapatra M, Haranath D (2020) Novel multi-wavelength excitable single-component phosphor system for application in white-LEDs. Ceram Int 46:4079–4085. https://doi.org/10.1016/j.ceramint.2019.09.212
3. Öztürk E (2017) Photoluminescence properties of Eu3+-activated Silicate Phosphors. High Temp Mater Process 36:635–640. https://doi.org/10.1515/htmp-2015-0263
4. Chaware PJ, Choudhari YD, Borikar DM, Rewatkar KG (2022) Photoluminescence and Judd-Ofelt analysis of Eu3+ doped akermanite silicate phosphors for solid state lighting. Opt Mater (Amst) 133:112945. https://doi.org/10.1016/j.optmat.2022.112945
5. Tang H, Sun H, Zhang X, Bai Z, Mi X, Liu X (2023) Tunable emission in Dy3+/Eu3+-doped BaLu2Si3O10 trisilicate structure for white light-emitting diode applications. J Alloys Compd 934:168068. https://doi.org/10.1016/j.jallcom.2022.168068
6. Al-Mashhadani TA, Kadhim FJ (2023) Photoluminescence properties of sliver-dysprosium co-doped silica obtained by sol–gel method. J Sol-Gel Sci Technol:553–560. https://doi.org/10.1007/s10971-023-06098-7
7. Reddy L (2023) A review of the efficiency of white light (or other) emissions in singly and Co-doped Dy3+ Ions in different host (Phosphate, Silicate, Aluminate) Materials. J Fluoresc. https://doi.org/10.1007/s10895-023-03250-y
8. Golja DR, Dejene FB, Kim JY (2022) Doped with dysprosium for white solid-state lighting, 2022
9. Yuan B, Wang X, Tsuboi T, Huang Y, Seo HJ (2012) A new yellowish-green-emitting phosphor: Eu2+-doped K 4CaSi3O9. J Alloys Compd 512:144–148. https://doi.org/10.1016/j.jallcom.2011.09.050
10. Zhao L, Fan F, Chen X, Wang Y, Li Y, Deng B (2018) Luminescence and thermal-quenching properties of silicate-based red-emitting K4CaSi3O9:Eu3+ phosphor. J Mater Sci Mater Electron 29:5975–5981. https://doi.org/10.1007/s10854-018-8571-9
11. Kaur S, Rao AS, Jayasimhadri M (2017) Spectroscopic and photoluminescence characteristics of Sm3+ doped calcium aluminozincate phosphor for applications in w-LED. Ceram Int 43:7401–7407. https://doi.org/10.1016/j.ceramint.2017.02.129

12. Kaur S, Jayasimhadri M, Rao AS (2017) A novel red emitting Eu3+doped calcium aluminozincate phosphor for applications in w-LEDs. J Alloys Compd 697:367–373. https://doi.org/10.1016/j.jallcom.2016.12.150
13. Kumar V, Manhas M, Bedyal AK, Swart HC (2017) Synthesis, spectral and surface investigation of novel CaMgB2O5:Dy3+ nanophosphor for UV based white LEDs. Mater Res Bull 91:140–147. https://doi.org/10.1016/j.materresbull.2017.03.037
14. Cao C, Wei S, Zhu Y, Liu T, Xie A, Noh HM, Jeong JH (2020) Synthesis, optical properties, and packaging of Dy3+ doped Y2WO6, Y2W3O12, and Y6WO12 phosphors. Mater Res Bull 126:110846. https://doi.org/10.1016/j.materresbull.2020.110846
15. Rohilla P, Rao AS (2022) Synthesis optimisation and efficiency enhancement in Eu3+ doped barium molybdenum titanate phosphors for w-LED applications. Mater Res Bull 150:111753. https://doi.org/10.1016/j.materresbull.2022.111753
16. Roshan A, Sourav B, Jairam D (2017) Temperature dependent photoluminescence of LiCaBO 3 phosphor. J Mater Sci Mater Electron 28:17168–17176. https://doi.org/10.1007/s10854-017-7645-4
17. Rathnakumari EA, Jayachandiran M, Kennedy SMM (2019) Optik Color tunable and energy transfer mechanism of Dy 3 + and Eu 3 + rare earth ions activated NaCaBi 2 (PO 4) 3 eulytite type phosphor for NUV excitable warm white light emitting diodes. Opt Int J Light Electron Opt 186:221–230. https://doi.org/10.1016/j.ijleo.2019.04.048
18. Sahu IP (2016) Luminescence properties of dysprosium doped barium alumino-silicate phosphors prepared by the solid state reaction method. J Mater Sci Mater Electron 27:13134–13147. https://doi.org/10.1007/s10854-016-5459-4
19. Sahu IP, Bisen DP, Brahme N (2015) Structural characterization and optical properties of dysprosium doped strontium calcium magnesium di-silicate phosphor by solid state reaction method. Displays 38:68–76. https://doi.org/10.1016/j.displa.2015.03.002
20. Sahu MK, Jayasimhadri M, Haranath D (2022) Temperature-dependent photoluminescence and optical thermometry performance in Ca3Bi(PO4)3:Er3+ phosphors. Solid State Sci 131:106956. https://doi.org/10.1016/j.solidstatesciences.2022.106956
21. Anu N, Deopa AS (2022) Rao, Structural and luminescence characteristics of thermally stable Dy3+ doped oxyfluoride strontium zinc borosilicate glasses for photonic device applications. Opt Laser Technol 154:108328. https://doi.org/10.1016/j.optlastec.2022.108328
22. Sahu MK, Mula J (2019) White light emitting thermally stable bismuth phosphate phosphor Ca3Bi(PO4)3:Dy3+ for solid-state lighting applications. J Am Ceram Soc 102:6087–6099. https://doi.org/10.1111/jace.16479
23. Wang L, Xu M, Zhao H, Jia D (2016) Luminescence, energy transfer and tunable color of Ce3+, Dy3+/Tb3+ doped BaZn2(PO4)2 phosphors. New J Chem 40:3086–3093. https://doi.org/10.1039/c5nj03148f
24. Chang S, Fu J, Wang K, Sun X, Ma Y, Bai G, Liu G, Wang Y, Tang M (2022) Correlating doping with the stability and color rendition of red phosphors. Mater Adv:6529–6538. https://doi.org/10.1039/d2ma00617k.

Exploration of Molybdenum Disulfide Nanostructures Through Raman Mode Detection

A. P. Sunitha and K. Nayana

1 Introduction

Bulk form of MoS_2 is having a layered structure (Fig. 1) [1–7]. MoS_2 when thinned from bulk to two-dimensional layers, the indirect bandgap (1.2 eV) transforms to direct type (1.8 eV) [4–23]. Two-dimensional MoS_2 films have layered structure with each layer containing one molybdenum atom sandwiched between two Sulphur atoms as shown in Fig. 1 [24]. Covalent bonding between molybdenum and sulphur is very strong as compared to weak van der Waals' bonding between the layers. Frequency of different vibrational modes of MoS_2 depends on the bonding, interlayer coupling, chemical environment of constituent atoms, etc. [25]. Raman scattering can be used as an effective tool to analyze the structure and composition of such materials [26]. From Raman scattering data, information about the size of crystal [4, 16, 27–32], thickness of thin films [33, 34], percentage of mechanical strain in the layers [35–38], temperature effects [12, 23, 39, 40], effect of doping percentage [41–43], adhesion of other atom layers [44], influence of defective centers in the deposited samples, etc., can be analyzed [45]. It can also be used to determine the composition [46] and to find the effect of coupling [31, 39] between layers.

A. P. Sunitha (✉) · K. Nayana
Department of Physics, Government Victoria College, Affiliated to University of Calicut, Palakkad, Kerala 678001, India
e-mail: sunithaganesh@gvc.ac.in

K. Nayana
Department of Physics, N. S. S. College, Affiliated to University of Calicut, Ottapalam, Kerala 679103, India

S. B. Krupanidhi et al. (eds.), *Recent Advances in Functional Materials and Devices*, Springer Proceedings in Materials 37, https://doi.org/10.1007/978-981-99-6766-7_13

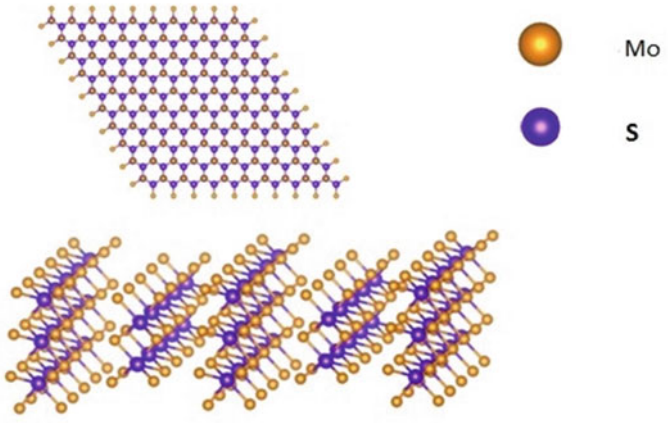

Fig. 1 Layered structure of MoS_2

2 Basics of Raman Spectroscopy

Sir C. V. Raman, through his experiments, noticed the presence of some additional wavelengths in scattered light than the wavelength of incident sunlight [47–49]. He published the papers in nature in 1928 [47, 48]. Experiments with about sixty dustless liquids [48, 49] and high-density gases [47] had shown the same behavior in scattered light. High polarization comparable to ordinary scattering, feeble intensity of other wavelength components in scattered light [48], and its coherent behavior [47] led him to the concept of Raman scattering than the concept of fluorescence. As the part of tentative explanation, he assumed that the partial scattering by the molecule results in the shift of wavelength [49]. He explained that the shift and intensity of the wavelengths depends on the molecules of the sample [49] and chemical environment of the molecules [47] respectively. In the inaugural speech at south Indian science academy, he explained the ground of blue color of sky, deep sea, and the opalescence of ice is because of the secondary radiation additionally scattered than the incident radiation from the molecules [50].

In Raman spectroscopy, monochromatic light from a source excites the molecules from ground electronic energy state to higher virtual or excited states. The virtual state energies are far below the energies of electronic excited state [51]. Molecules in higher (virtual/excited) state can jump down to ground state by emitting radiation. If the higher state is virtual/excited, corresponding Raman spectra is known as non-resonance/resonance Raman spectra. Emitted wavelength can be equal or not equal to the incident wavelength. Emission of same wavelength is known as Rayleigh scattering. Most of the light follows Rayleigh scattering. But a few of light can scatter with higher wavelength, known as Stokes' lines and a few light rays scatter with lower wavelength known as anti-Stokes' lines (Fig. 2.) [52, 53].

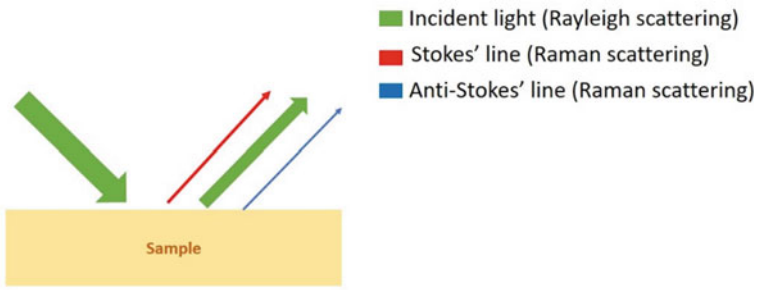

Fig. 2 Raman and Rayleigh scattering from a sample

According to Maxwell–Boltzmann distribution law, most of the molecules in a sample are in ground state and as a result, Stokes' lines are more intense than anti-Stokes' lines [51]. Only 10^{-5} portion of the incident light scatters like Stokes' or anti-Stokes' lines [51]. So, minimum of 10^8 number of atoms essential for normal Raman scattering is to be noticeable [54]. Interaction between molecular vibrations and incident light results in Raman spectra, only if the molecular polarizability changes during vibration. Such vibrations are known as Raman active vibrations [55]. During the particular mode of vibration, polarizability change is quantified as the intensity of resultant spectra [55]. The position, width, and intensity of Stokes' and anti-Stokes' lines can explain the structure and vibrational modes of sample used. Most common light sources used in Raman spectra are in ultraviolet–visible region [53, 56].

Depending on the instrumentation and working principle, different Raman spectroscopies are there. Dispersive Raman spectroscopy (DRS), Fourier transform Raman spectroscopy (FTR), surface enhanced Raman spectroscopy (SRS), Tip enhanced Raman spectroscopy (TRS), resonance Raman spectroscopy (RRS), and confocal Raman spectroscopies (CRS) are some of them. In the DRS, scattered light gets dispersed before recording, and the spectrum is noisy in the visible region due to fluorescence [56]. To overcome this, near infrared wavelength is used in modern DRS with a charge coupled device (CCD) as the detector [57, 58]. Wang et al. reported that the near infrared DRS with CCD detector has greater sensitivity than the FTR spectroscopy [59]. Raman spectra of samples in aqueous form and samples at very high temperature of the order of above 1000 ^{0}C can be detectable in DRS [57]. In FTR, scattered light gets Fourier transformed before recording [57]. Wavelength of laser light used in FTR, is in infrared (IR) region (most commonly, Nd: YAG laser with 1064 nm wavelength) [56–58]. So, fluorescence can easily be omitted in FTR than DRS [56]. In the SRS, analyte is adsorbed on metal nanoparticles. Their rough surface provides surface plasmon to enhance the electric field, and consequently the intensity of scattered photons [54, 55, 60, 61]. So, the cross section of Raman scattering is increased in SRS, compared to normal Raman scattering [53]. Compared to normal Raman scattering, intensity of scattered light in SRS is ten lakh times higher [60]. So, it is very powerful to analyze the structure of low-concentrated analyte [55]. In TRS, a metal tip rather than metal nanoparticles will provide surface plasmon [55, 62].

Strain [61], defects [62], and heterostructure analysis [63] are possible by SRS and TRS. In the RRS, the energy of incident photons is in resonance with the electronic transitions of sample molecules [64, 65]. In the case of MoS_2 nanofilms, wavelengths at the two excitonic peaks in photoluminescence spectra can be used in RRS as laser wavelength. Most commonly using laser light of 633 nm is corresponding to the B-excitonic peak of MoS_2 nanofilm of energy 1.96 eV [24, 33, 66]. Helium–neon laser and diode laser can have a wavelength corresponding to 1.96 eV [55]. Under resonance condition, the intensity and number of peaks in Raman spectra are high compared to non-resonance scattering [33]. Since, the intensity of resonance Raman spectra is higher than non-resonance Raman spectra, only a few concentrations of analyte are needed for getting the spectra [53]. In CRS, backscattered laser beam is re-focused through a pin hole [55]. High resolution and purity of spectra can be confirmed by this method. Sample with a volume of femtolitre is enough for confocal Raman spectroscopy [54]. Depth profiling and structural analysis of sample can be done by CRS [42, 43, 66–68].

2.1 Vibrational Modes of MoS_2

Bulk MoS_2 belongs to D_{6h} point group. It contains 6 atoms per unit cell [69, 70]. At point of Brillouin zone, bulk MoS_2 possesses 18 vibrational modes; 3 acoustic and 15 optical. $2A_{2u,}$ $2E_{1u}$, $A_{1g,}$ $2E_{2g,}$ $E_{1g,}$ $2B_{2g}$, B_{1u}, E_{2u} are representing different vibrational modes of bulk MoS_2 [33, 69, 71–73]. $A_{2u,}$ and E_{1u} have both acoustic and IR active optical modes [25, 74, 75]. 'E' modes are degenerate (double) modes. A and B are non-degenerate modes [69]. $A_{1g,}$ $2E_{2g,}$ and E_{1g} vibrations are Raman active. $A_{2u,}$ E_{1u} are IR active. $2B_{2g}$, B_{1u}, and E_{2u} are both IR and Raman inactive [69]. Monolayer MoS_2 has 9 number of vibrational modes, because of 3 atoms per unit cell [69]. Bilayer or even number of layers of MoS_2 has 18 number of vibrational modes.

$A_{1g,}$ $2E_{2g,}$ and E_{1g} are the four Raman active modes of vibrations of bulk MoS_2. A_{1g} mode belongs to out-plane vibration of Sulphur atoms. E_{2g} ($E^1{}_{2g}$ and $E^2{}_{2g}$) modes belong to in-plane vibrations of both molybdenum and Sulphur atoms. E_{1g} corresponds to in-plane vibration of Sulphur atoms (Fig. 3.) [33, 74]. E_{1g} with wavenumber 286 cm^{-1} is absent in backscattering configuration, due to the same direction of electric field of incident light and plane of MoS_2 [33, 76–79]. When this direction changes, E_{1g} mode will appear [80]. But due to Rayleigh scattering, it is difficult to detect [81]. ${E_{2g}}^2$ with wavenumber 32 cm^{-1} can be detectable only if the detector is detectable in the same wavenumber range [25, 76]. Or cross polarizer can be implemented to block Rayleigh components which help to recognize ${E_{2g}}^2$ mode [82]. In monolayer or few layers of MoS_2 crystal, this mode acts as shear mode with red shift [82–85]. In non-resonance Raman spectroscopy, bulk MoS_2 is characterized by two Raman active modes—${E_{2g}}^1$ mode at 382 cm^{-1} and A_{1g} mode at 407 cm^{-1}.

The modes correspond to E_{2g} and A_{1g} in bulk belong to E' and A_1' representations for nanostructures which have odd number of layers. If number of layers are even, it

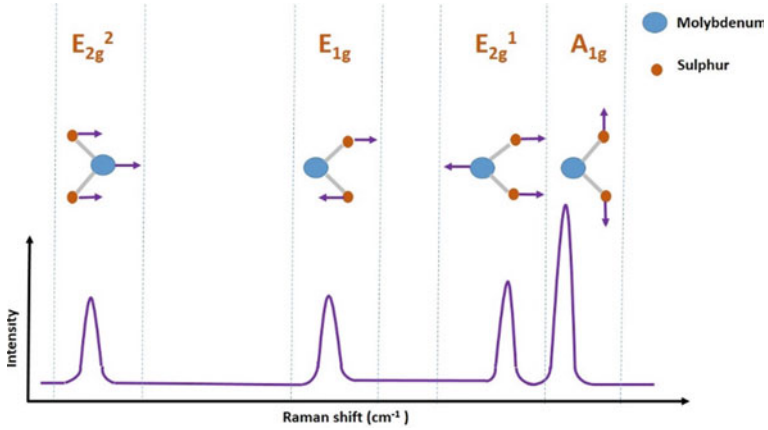

Fig. 3 Graphical representation of prominent MoS_2 vibrations and corresponding peaks in Raman spectra

changes to E_g and A_{1g} respectively. A_1', $2A_2''$, $2E'$, and E'' are the vibrational modes in monolayer [33, 69]. One A_2'' and one doubly degenerate E' correspond to acoustic translational modes and others are optical modes [25]. All optical modes except A_2'' are Raman active and A_2'' is IR active [25, 75]. A_{1g}, B_{1u} in bulk matches with A_1' in monolayer [69]. Similarly, B_{2g}^{1}, A_{2u} matches with A_2'', E_{1u}, E_{2g}^{1} matches E' and E_{1g}, E_{2u} matches with E'' [69].

2.2 Shear and Breathing Modes

Below 50 cm^{-1}, there are two major peaks for MoS_2 crystal, known as shear (E_{2g}^{2}) and breathing modes (B_{2g}^{2}) [38, 83, 86, 87]. Both have N-1 number of vibrational modes for N number layered crystal. If N is even, breathing mode vibrations are Raman inactive. But N/2 number of doubly degenerate shear modes are Raman active. If N is odd, (N-1)/2 number of breathing modes and N-1 number of shear modes are Raman active [38]. Analyzing these modes gives information about the interlayer coupling and number of layers [38, 86, 87].

3 Factors Affecting Raman Spectra

3.1 Temperature of Sample

For nanofilm or few layers of MoS_2, position and width of $E_{2g}{}^1$ and A_{1g} peaks depend on the temperature of sample. When temperature increases both peaks get red shifted [81, 88–90]. Thermal expansion and anharmonic phonon coupling are the reasons for the red shift [90, 91]. When temperature increases, the thermal expansion and hence lattice parameter expansion of the crystal occur which results in lowering of interatomic interaction and hence the red shift [90]. Similarly, when temperature increases, phonon coupling also increases, which contributes to the red shift [88]. But for $E_{2g}{}^1$ in-plane vibration, thermal expansion contribution is very less compared to the A_{1g} out-plane vibration. Hence, A_{1g} is red shifted than $E_{2g}{}^1$ [91]. Temperature-dependent frequency (ν_T) shift can be explained using the Eq. 1 and Eq. 2.

$$\nu_T = \nu_0 + \chi T \tag{1}$$

$$\nu_T = \nu_0 + \left[\frac{d\nu}{dT}\right]\Delta T + \left[\frac{d\nu}{dV}\right]\Delta V \tag{2}$$

where, ν_0 is the frequency at absolute zero temperature. In Eq. 1, χ is the first order temperature coefficient. [67, 84, 90, 92–94]. Equation 1 includes only linear approximation of frequency with temperature. Higher order terms are neglected here [33]. From experimentally observed peak shifts, temperature coefficient for each mode can be calculated. In Table 1, experimentally determined temperature coefficients of MoS_2 by various researchers are listed. In Eq. 2, the term $[\frac{d\nu}{dT}]\Delta T$ represents temperature-dependent phonon coupling or anharmonicity and the term $[\frac{d\nu}{dV}]\Delta V$ represents the thermal expansion or phonon–phonon interaction [67, 92, 95]. Decay of phonon to low-energy phonons is known as phonon–phonon interaction [95]. Phonon coupling occurs due to three phonon and four phonon scattering [33, 67, 92, 93, 96]. Equation 3 gives the contribution due to three phonons $A_3[1 + \frac{2}{e^x-1}]$ and four phonons $A_4[1 + \frac{3}{e^y-1} + \frac{3}{(e^y-1)^2}]$ processes.

$$\left[\frac{d\nu}{dT}\right]\Delta T = A_3\left[1 + \frac{2}{e^x - 1}\right] + A_4\left[1 + \frac{3}{e^y - 1} + \frac{3}{(e^y - 1)^2}\right] \tag{3}$$

where, $x = \frac{h\nu}{KT}$, $y = \frac{h\nu}{3KT}$ and A_3, A_4 are the three phonon and four phonon scattering coefficients. A_4 is much higher than A_3 which indicates that four phonon process are dominant in temperature-dependent Raman scattering [92, 96]. Both three and four phonon scattering occurs due to anharmonicity [97]. Using Gruneisen constant model, the thermal expansion term can be deduced as follows

$$\left[\frac{d\nu}{dV}\right]\Delta V = \nu_0 e^{(-3\gamma \int_0^T \alpha dT)} - \nu_0 \tag{4}$$

For bulk MoS_2, $E_{2g}{}^1$ Gruneisen parameter (ϒ) is nearly 0.21 and for A_{1g} mode, it is nearly 0.42 [96], even though Gruneisen parameter varies with number of layers of sample. Difference in the value of ϒ for two modes indicates that A_{1g} mode has higher thermal shift than $E_{2g}{}^1$ mode [96, 98]. Thermal expansion coefficient (α) is a temperature-dependent factor and for monolayer MoS_2, thermal expansion coefficient is positive [41, 69].

Najmaei et al. reported that the temperature-dependent red shift of $E_{2g}{}^1$ and A_{1g} peaks vary with the thickness of sample [81]. From monolayer to six number of layers, they got significant red shift. But for number of layers greater than six, red shift is very negligible. Again, the red shift of $E_{2g}{}^1$ is small compared to A_{1g} mode. Stiffening of $E_{2g}{}^1$ mode, when it thinned from many layers to single layer reduces the red shift and softening of bonds at higher temperature enhances the red shift in A_{1g} mode.

Full width at half maximum (FWHM) of the same peaks are getting broaden, when the temperature increases. Phonon–phonon and phonon-electron interactions at higher temperature leads to the broadening of peaks [81, 84, 88, 95, 99]. Decay of phonon to electron hole pair is known as phonon-electron interaction [95]. Crystallinity of sample inversely affects the FWHM [84].

As per Xue et al. reported, intensity of Raman peaks decreases when temperature of sample increases from 10 to 300 K [73]. But Deepu. et al. reported some anomalous results of intensity with temperature [33]. Under the decrease of temperature, the A and B exciton peaks deviate toward higher wavenumber. So, under resonance Raman scattering, deviation of B exciton from 633 nm reduces the intensity and deviation of A exciton to the place of B exciton (633 nm) enhances the intensity. Hence, at temperatures between 300 and 160 K intensity reduces and below 160 K, intensity enhances rapidly. Annealing at high temperature increases the intensity of peaks in Raman spectra, which denotes annealing enhances the crystallinity [34].

Table 1 Temperature coefficients of MoS_2

Sample	Temperature range (K)	χ of $E_{2g}{}^1$ cm^{-1} K^{-1}	χ of A_{1g} cm^{-1} K^{-1}	Reference
Few layer	83 to 523	−0.0132	−0.0123	84
Few layered nanosheet	77 to 623	−0.016	−0.011	88
Monolayer	298 to 573	–	−0.013	89
Few layer nanosheet	78 to 543	−0.0105	−0.0141	90
Monolayer	303 to 448	−0.013	−0.016	91
Monolayer	70 to 350	−0.0124	−0.0143	93

3.2 Laser Power

When laser power increases, both $E_{2g}{}^1$ and A_{1g} modes are red shifted [76, 81, 90]. This is because of the softening of phonon energies of both modes under increasing laser power [90]. Temperature and laser power have the same effect on the shifting and broadening of Raman peaks. This is because, increase in laser power results in the local increase of temperature of the sample at the vicinity of point of incidence of laser beam on sample [84]. Laser power should be very small in the order of micro or milli Watts to avoid overheating or damage of the sample [61, 79, 90]. When laser power increases from very low value, distinct new peaks will arise [100]. Broadening of peaks also happens, when laser power increases [98]. Ortega et al. explained the relation between line width and laser power using uncertainty principle [98]. When laser power increases, due to the large value of anharmonic coupling, life time of phonon gets reduced. By uncertainty principle, lifetime of phonon is inversely proportional to line width of peaks.

Thermal conductivity (K) of the crystal can be deduced from the graph plotted between the variations of laser power (Δp) with peak shift in wavenumber ($\Delta\nu$) of vibrational modes. Equation 5 gives the thermal conductivity for a film of thickness d [67, 84, 90].

$$K = \frac{\chi}{2\pi d}\left(\frac{\Delta\nu}{\Delta p}\right)^{-1} \tag{5}$$

Sahoo et al. calculated thermal conductivity of few layers of MoS_2 sample as 52 W/mK at room temperature [84], by Eq. 5. It is similar to the result obtained by Yen et al. as (30.5 to 38.5) W/mK [101] and 23.2 W/mK is obtained by Cai et al. [69] for monolayer MoS_2 at room temperature.

3.3 Size and Number of Layers of MoS_2

Size of MoS_2 crystal affects the position, intensity, and width of peaks in Raman spectra. Studies of Raman scattering shows intensity of mode A increase when thinned from bulk [84]. Positions of $E_{2g}{}^1$ and A_{1g} mode show opposite trends when it moves from bulk to single nanolayer. Compared to bulk MoS_2, Raman peak $E_{2g}{}^1$ of two-dimensional MoS_2 is blue shifted. But, A_{1g} mode of the same is red shifted [81, 83]. In two-dimensional crystal, when the number of layers reduces, same effect will happen. But A_{1g} mode is more redshift than the blue shift of $E_{2g}{}^1$ mode [81]. Strong thickness dependence of A_{1g} mode can be influenced by van der Waal force. In a very few layered structure, magnitude of out-of-plane compressive force constant is larger than the magnitude of in-plane shear force constants. So out-of-plane frequencies are larger than the in-plane frequencies. Screening effect causes red shift in A_{1g} than in $E_{2g}{}^1$ [102]. In the case of in-plane vibration mode long-range coulomb force is

dominant than inter-layer van der Waals forces and the stiffening of bonds results in slight blue shift of $E_{2g}{}^{1}$ mode [24]. Peak gap between $E_{2g}{}^{1}$ and A_{1g} mode depends on number of layers of two-dimensional MoS_2 [34]. For one-layer MoS_2, peak gap is of the order of 18 cm^{-1}. If it increases up to 22 cm^{-1}, crystal may contain two or three number of layers [33]. Deepu et al. reported the energy gap corresponding to 23.6 cm^{-1} belongs to two- or three-layer thick MoS_2 and 25.3 cm^{-1} belongs to multilayer MoS_2 [33].

Peak width broadening occurs when the size of MoS_2 crystal reduces from bulk to two-dimensional [91]. For bulk MoS_2 uncertainty in momentum is negligible due to large uncertainty in size as in Eq. 6 [64, 83].

$$\Delta x \cdot \Delta p \approx h \tag{6}$$

So, phonons at center only participate in Raman scattering. When the thickness reduces to two-dimensional, phonons near the center also will participate in Raman scattering [64, 83]. Contribution of phonon vibrations other than center results in phonon confinement effect and peak broadening. In two-dimensional films, commonly, peak width decreases, when number of layers of MoS_2 decreases [83, 103, 104]. This can also be explained by the increasing uncertainty in momentum and increasing phonon confinement effect, when number of layers decreases. But Lee et al. [103] and Luo et al. [83] reported the same effect that, FWHM increases from two layer of MoS_2 to one layer. Luo explained this anomalous effect by stating that in monolayer MoS_2, phonons with large momentum are absent because of the direct bandgap of monolayers [83].

3.4 Strain

Both uniaxial and biaxial strain can be applied into a two-dimensional crystal to investigate its effects [61, 105]. Both can change the effective mass, carrier mobility, and bandgap of crystal [105, 106]. Strain can change the direct bandgap of monolayer of MoS_2 to indirect [61, 105–107]. Uniaxial strain applied to the two-dimensional layer of crystal results in the shifting and splitting of $E^{'}$ peak [85, 108]. $A_1{}^{'}$ mode is comparatively unchanged due to strain [85, 109] and under strain $E_{2g}{}^{1}$ mode splits into two, one corresponds to vibration of molecule along the direction of applied field and other corresponds to perpendicular direction of field [110]. Intensity ratio of E and A modes gives a clue to the nature of applied strain [41]. If arm chair strain is present in the sample along any arbitrary direction, then E' phonon mode is split into two branches-E_{pl} and E_{pr}. For compressive strain, E_{pl} blue shifts. For tensile strain, it red shifts [108]. The intensity of A_1' mode is maximum in direction perpendicular to strain and minimum parallel to direction of strain [41].

3.5 Doping and Defects

Doping in MoS_2 crystal affects the Raman spectra. n-type doping gives in red shift of A_{1g} [41, 43, 109] and p-type of doping give in blue shift of the same peak [110, 111]. But generally, E_2g^1 peak is unaffected by the doping. In n-type doped crystal, a greater number of electrons in conduction band softens the out-plane vibration and red shift of the A_{1g} peak will occur. Due to a greater effect of electron–phonon interaction, broadening of the peak also will happen [42, 43]. But for p-type doping, reduction of peak broadening will occur [44].

Defects in MoS_2 crystal also alter the Raman peaks. Sulphur vacancies in monolayer MoS_2 crystal caused red shift in $E^{'}$ mode [45]. Hye et al. reported the changes in Raman spectra due to physisorption and chemisorption of atmospheric gas molecules in MoS_2 crystal [44]. By changing the laser irradiation time, they examined the changes of Raman peaks in the presence of ambient gas. For low laser irradiation time, blue shift of A_{1g} peak and unshift of E_{2g} peak are explained by the p-type doping or physisorption in crystal due to the presence of atmospheric gases like oxygen and water. Due to the absence of strain, unshift of E_{2g} mode happens. For long laser irradiation time, reduction of intensity of both A_{1g} and E_{2g} is explained by the chemisorption or permanent damage of crystal due to the same gases.

3.6 Pressure

When pressure applied to the MoS_2 crystal increases, both $E_{2g}{}^1$ and A_{1g} modes are blue shifted. But, A_{1g} mode shifts more than $E_{2g}{}^1$ mode [72, 73, 112]. It is explained by the fact that, for A_{1g} mode, the pressure coefficient is higher than the $E_{2g}{}^1$ mode. Week van der Waal forces participating in out-plane vibration are strongly affected by the external pressure applied. The pressure can reduce the amplitude of out-plane vibration, which causes the blue shift of frequency [72, 112]. Li et al. reported that, the four-layer MoS_2 film regains its original Raman spectra, when the pressure of 20.7 GPa is removed, which indicates that the crystal can withstand such high pressure without damaging the structure [73]. Some other effects are also reported under high pressure on MoS_2 crystal. Appearance of shoulder peak [113] and new peak [72], lowering of intensity [72, 73, 110], broadening of peaks [73, 113], and splitting of peaks [114–116] are some of them.

3.7 Davydov Splitting

Davydov splitting in Raman spectra is caused by the interlayer interaction between the layers in a two-dimensional crystal [117]. Number of splitting in one peak is related to the number of layers. For odd number of layers (N), one peak split into

(N + 1)/2 number of Raman active and (N-1)/2 number of infrared active peaks under resonance. If N is even, one peak splits into N/2 number of Raman active and infrared active peaks [33, 117]. For crystals like MX_2, the vibrational modes depend upon the number of layers of the material. Raman active $E^{'}$ mode in one layer splits into Raman active $E_g^{'}$ and IR active E_u modes in two layer and bulk samples [24, 46]. X atoms in adjacent layers have spring coupling, which intensify the frequency of $E_g^{'}$ with respect to E_u. That is the degeneracy of E mode in one layer is lifted into two layers because of the interaction between the layers. This is called Davydov splitting. The mutually exclusive infrared and Raman doublets are called Davydov pairs. Anomalous frequency trends in this Davydov splitting are also reported in which the frequency of E_u is greater than E_g. The IR active $A_2^{''}$ mode in one-layer MX_2 splits into two modes in two layers (Raman active $A_{1g}^{'}$ and IR active A_{2u}). Also, Raman active $A_1^{'}$ in one layer splits into IR active A_{2u} and Raman active A_{1g} [2] [117].

3.8 Methods of Synthesis

Depending on the methods of synthesis of MoS_2 nanostructures, peak positions of characteristic modes may be varied. MoS_2 fabricated by dip coating, SILAR method, ultrasonication assisted fabrication (UAF) and modified thermal evaporation techniques exhibited different peak separation (Δ) between E_{2g} and A_{1g} vibrations [118]. According to the precursor used in dip coating, annealing temperature of MoS_2, sonication time in UAF, and cationic precursor used in SILAR method, peak separations vary [118]. It indicates that the vibration modes of MoS_2 nanostructures depend on the fabrication methods and chemical and physical environment of the sample. As explained in Sect. 3.3, about 20 cm^{-1} of Δ is expected between E_{2g} and A_{1g} vibrations in monolayer MoS_2. Table 2 indicates Δ of monolayer MoS_2 dependence on the method of synthesis also.

3.9 Resonance

As explained in introduction, if the applied laser wavelength is equivalent to bandgap of nanostructure, resonance Raman scattering will occur. Intensity and number of peaks in resonance Raman spectra are higher than non-resonance Raman spectra. Photoluminescence spectra of MoS_2 show two peaks near 1.83 eV and 1.98 eV which can be used in resonance Raman spectra as laser light energy [33]. Li et al. used 671 nm (1.85 eV) laser [74], and H Li used 632.8 nm (1.96 eV) laser source [24] for resonance spectra. In resonance Raman spectra, beyond the peaks belongs to vibrations at center, vibrations at M point and K point can also be detectable [65, 66]. Longitudinal acoustic peaks and in phase-out phase addition of some vibrations are also present in resonance Raman spectra [65, 74, 114]. Li et al. reported the peak

Table 2 Dependence of synthesis methods on monolayer MoS_2 peak separation between $E_{2g}{}^1$ and A_{1g}

Synthesis method	Peak position of $E_{2g}{}^1$ cm^{-1}	Peak position of A_{1g} cm^{-1}	Δ cm^{-1}	Reference
Mechanical exfoliation	384.6	403.4	18.8	24
Chemical Vapor Deposition	384	403	19	45
Mechanical exfoliation	382.3	402.1	19.8	114
Chemical Vapor Deposition	384.5	404.7	20.2	119
Mechanical exfoliation	389.2	407	17.8	120

near 454 cm^{-1} due to the double wavenumber of longitudinal acoustic wave at M point and peak at 180 cm^{-1} and 634 cm^{-1} due to out-phase and in-phase addition of $A_{1g}{}^1$ and LA(M) modes respectively [24]. Mignuzzi reported peak at 227 cm^{-1} for LA(M) and peaks near 154 cm^{-1},180 cm^{-1} and 187 cm^{-1} for transverse acoustic at M point, out-plane transverse acoustic at M point and transverse acoustic at K point respectively [66].

4 Conclusion

Different types of Raman scattering spectroscopic studies are effectively used in the analysis of structural and vibrational modes of two-dimensional materials. In this chapter, a review about Raman scattering data analysis of layered Molybdenum disulphide nanofilms is done. It gives light to different vibrational modes of MoS_2 and information about the systemic or sample parameters which influences the appearance of different modes. Major Raman peaks of MoS_2 are E_{2g} and A_{1g}. Analyzing the position, broadening, and intensity of Raman peaks, physical and chemical properties of crystal can be understood. Various factors like temperature, laser power, size and number of layers of crystal, pressure and strain applied can alter Raman spectra. MoS_2 crystal exhibits red shift of both E_{2g} and A_{1g} peaks with increase in temperature and laser power. Similarly, MoS_2 exhibits blue shift of E_{2g} and red shift of A_{1g} under reduction of size and number of layers. Red/blue shift of A_{1g} for n/p doping and blue shift of both $E_{2g}{}^1$ and A_{1g} mode in increase of pressure are noted. Anomalous results in the variation of intensity of peaks are reported under temperature, pressure, and laser power changes. Defects in crystal also result in intensity variations. Davydov splitting of peaks happens due to the interlayer interaction between the layers. Number of splitting of peaks depends upon the number of layers of crystal. When the temperature or laser power increases and the size or number of layers

reduces, width of the peaks gets broaden. All these factors lead to the conclusion that Raman spectroscopy is an effective tool to analyze the structure of nanostructures including MoS_2.

Acknowledgements Nil.

References

1. Li X, Zhu H (2015) Two-dimensional MoS_2: Properties, preparation, and applications. Journal of Materiomics 1(1):33–44
2. Debabrat K, Chetia L, Gazi A (2013) Ahmed. Investigation of Optical Properties of MoS_2 Derivative with Tungsten.
3. Yakov E, Thomas J (2010) Risdon. Molybdenum disulfide in lubricant applications—A review. Proceedings of the 12 Lubricating Grease Conference.
4. Zhou, W et al. (2013) Synthesis of few-layer MoS_2 nanosheet-coated TiO_2 nanobelt heterostructures for enhanced photocatalytic activities. Small 9(1): 140–147
5. Kan M et al (2014) Structures and phase transition of a MoS_2 monolayer. J Phys Chem C 118(3):1515–1522
6. Tonndorf, P et al. (2013) Photoluminescence emission and Raman response of monolayer MoS_2, $MoSe_2$, and WSe_2. Optics express 21(4): 4908–4916
7. Ataca C et al (2011) A comparative study of lattice dynamics of three-and two-dimensional MoS_2. J Phys Chem C 115(33):16354–16361
8. Zhang H et al. (2014) Molybdenum disulfide (MoS_2) as a broadband saturable absorber for ultra-fast photonics. Optics express 22(6): 7249–7260.
9. Bozheyev F, Damir V, Renata N (2016) Pulsed cathodoluminescence and Raman spectra of MoS_2 and WS_2 nanocrystals and their combination MoS_2/WS_2 produced by self-propagating high-temperature synthesis. Applied Physics Letters 108(9): 093111.
10. Gołasa K et al (2014) Resonant Raman scattering in MoS_2 From bulk to monolayer. Solid State Commun 197:53–56
11. Eda G et al. (2011) Photoluminescence from chemically exfoliated MoS_2. Nano letters 11(12): 5111–5116.
12. Jin-Mun Y et al. (2013) Efficient work-function engineering of solution-processed MoS_2 thin-films for novel hole and electron transport layers leading to high-performance polymer solar cells. J Materials Chemistry C 1(24): 3777–3783.
13. Jing-Yuan W et al. (2014) Photoluminescence of MoS_2 prepared by effective grinding-assisted sonication exfoliation. J Nanomaterials.
14. Pagona G et al. (2015) Exfoliated semiconducting pure 2H-MoS_2 and 2H-WS_2 assisted by chlorosulfonic acid. Chemical Communications 51(65): 12950–12953.
15. Garadkar KM et al (2009) MoS_2: Preparation and their characterization. J Alloy Compd 487(1–2):786–789
16. Mingxiao Y et al. (2015) Recent advancement on the optical properties of two-dimensional molybdenum disulfide (MoS_2) thin films. Photonics. 2(1). Multidisciplinary Digital Publishing Institute.
17. Chen C et al. Growth of large-area atomically thin MoS_2 film via ambient pressure chemical vapor deposition. Photonics Research 3(4): 110–114.
18. Ponomarev EA et al (1998) Highly oriented photoactive polycrystalline MoS_2 layers obtained by van der Waals rheotaxy technique from electrochemically deposited thin films. Sol Energy Mater Sol Cells 52(1–2):125–133
19. Mak KF et al. (2010) Atomically thin MoS_2 : a new direct-gap semiconductor. Physical review letters 105(13): 136805.

20. Britnell L et al. (2013) Strong light-matter interactions in heterostructures of atomically thin films. Science 340(6138): 1311–1314.
21. Hwang WS et al. (2013) Comparative study of chemically synthesized and exfoliated multilayer MoS_2 field-effect transistors. Applied Physics Letters 102(4): 043116.
22. Patil RS (1999) Electrosynthesis of the molybdenum disulphide thin films and characterization. Thin Solid Films 340(1–2):11–12
23. Pawar SM et al (2011) Recent status of chemical bath deposited metal chalcogenide and metal oxide thin films. Curr Appl Phys 11(2):117–161
24. Li H et al. (2012) From bulk to monolayer MoS_2: evolution of Raman scattering. Advanced Functional Materials 22(7): 1385–1390.
25. Sandoval, SJ et al. (1991) Raman study and lattice dynamics of single molecular layers of MoS 2. Physical Review B 44(8): 3955.
26. John AP, Thenapparambil A, Madhu T (2020) Strain-engineering the Schottky barrier and electrical transport on MoS_2. Nanotechnology 31(27): 275703.
27. Terrones H et al. (2014) M. a. T. Nguyen, AL Elías, TE Mallouk, L. Balicas, MA Pimenta, and M. Terrones. Scientific Reports 4(10): 1038.
28. Zhang X et al. (2015) Measurement of lateral and interfacial thermal conductivity of single- and bilayer MoS_2 and $MoSe_2$ using refined optothermal Raman technique. ACS applied materials & interfaces 7(46): 25923–25929.
29. Zhao Y et al. (2013) Interlayer breathing and shear modes in few-trilayer MoS_2 and WSe_2. Nano letters 13(3): 1007–1015.
30. Feng N et al. Magnetism by interfacial hybridization and p-type doping of MoS_2 in Fe_4N/MoS_2 superlattices: a first-principles study. ACS applied materials & interfaces 6(6): 4587–4594.
31. Merki D et al. (2011) Amorphous molybdenum sulfide films as catalysts for electrochemical hydrogen production in water. Chemical Science 2(7): 1262–1267.
32. Smith RJ et al. (2011) Large-scale exfoliation of inorganic layered compounds in aqueous surfactant solutions. Advanced materials 23(34): 3944–3948.
33. Kumar D et al. (2021) Davydov splitting, resonance effect and phonon dynamics in chemical vapor deposition grown layered MoS_2. Nanotechnology 32(28): 285705.
34. Keng-Ku L et al. (2012) Growth of large-area and highly crystalline MoS_2 thin layers on insulating substrates. Nano letters 12(3): 1538–1544.
35. Kite SV et al (2017) Effect of annealing temperature on properties of molybdenum disulfide thin films. J Mater Sci: Mater Electron 28(21):16148–16154
36. Dobisz EA, Louay AE (2004) Nanoengineering: Fabrication, Properties, Optics, and Devices. SPIE.
37. Lee J-U, Kim M, Cheong H (2015) Raman spectroscopic studies on two-dimensional materials. Applied Microscopy 45(3):126–130
38. Zhang X et al (2013) Raman spectroscopy of shear and layer breathing modes in multilayer MoS_2. Phys Rev B 87(11):115413
39. Shi Y, Li H, Li L-J (2015) Recent advances in controlled synthesis of two-dimensional transition metal dichalcogenides via vapour deposition techniques. Chem Soc Rev 44(9):2744–2756
40. Wang Z et al. (2016) Chemical dissolution pathways of MoS_2 nanosheets in biological and environmental media. Environmental science & technology 50(13): 7208–7217.
41. Kukucska G, Koltai J (2017) Theoretical investigation of strain and doping on the Raman spectra of monolayer MoS_2. Physica status solidi (b) 254(11): 1700184
42. Chakraborty B et al. (2012) Symmetry-dependent phonon renormalization in monolayer MoS_2 transistor. Physical Review B 85(16): 161403
43. Birmingham B et al. (2019) Probing the effect of chemical dopant phase on photoluminescence of monolayer MoS_2 using in situ Raman microspectroscopy. J Phys Chem C 123(25): 15738–15743.
44. Oh HM et al. (2016) Photochemical reaction in monolayer MoS_2 via correlated photoluminescence, Raman spectroscopy, and atomic force microscopy. ACS nano 10(5): 5230–5236.

45. Parkin WM et al. (2016) Raman shifts in electron-irradiated monolayer MoS_2. ACS nano 10(4): 4134–4142.
46. Mak KF et al. (2012) Control of valley polarization in monolayer MoS_2 by optical helicity. Nature nanotechnology 7(8): 494–498.
47. Raman CV. (1928) A change of wave-length in light scattering. Nature 121(3051): 619–619.
48. Raman CV, Kariamanikkam SK. (1928) The optical analogue of the Compton effect. Nature 121(3053): 711–711.
49. Raman CV (1944) The nature and origin of the luminescence of diamond. Proceedings of the Indian Academy of Sciences-Section A. 19(5) Springer India.
50. Raman CV (1928) A new radiation. Indian J Phys 2:387–398
51. Ferraro JR (2003) Introductory raman spectroscopy. Elsevier
52. Smith E, Geoffrey D (2019) Modern Raman spectroscopy: a practical approach. John Wiley & Sons v.
53. Kudelski A (2008) Analytical applications of Raman spectroscopy. Talanta 76(1):1–8
54. Kneipp K et al. (1999) Ultrasensitive chemical analysis by Raman spectroscopy. Chemical reviews 99(10): 2957–2976.
55. Rostron P, Safa G, Dina G (2016) Raman spectroscopy, review. laser 21: 24.
56. Sadeghi-Jorabchi H et al (1990) (1990) "Determination of the total unsaturation in oils and margarines by Fourier transform Raman spectroscopy.". J Am Oil Chem Soc 67(8):483–486
57. Yang D, Ying Y (2011) Applications of Raman spectroscopy in agricultural products and food analysis: A review. Appl Spectrosc Rev 46(7):539–560
58. Hanlon EB et al (2000) Prospects for in vivo Raman spectroscopy. Phys Med Biol 45(2):R1
59. Wang Y, McCreery RL (1989) Evaluation of a diode laser/charge coupled device spectrometer for near-infrared Raman spectroscopy. Anal Chem 61(23):2647–2651
60. Stiles PL et al. (2008) Surface-enhanced Raman spectroscopy. Annu. Rev. Anal. Chem. 1: 601–626.
61. Moe YA et al. (2018) Probing evolution of local strain at MoS_2-metal boundaries by surface-enhanced Raman scattering. ACS applied materials & interfaces 10(46): 40246–40254.
62. Kato R et al. (2019) Probing nanoscale defects and wrinkles in MoS_2 by tip-enhanced Raman spectroscopic imaging. Applied Physics Letters 114(7): 073105.
63. Anbazhagan R et al. (2048) Surface-enhanced Raman scattering of alkyne-conjugated MoS_2: a comparative study between metallic and semiconductor phases. Journal of Materials Chemistry C 6(5): 1071–1082.
64. Arora AK et al. (2007) Raman spectroscopy of optical phonon confinement in nanostructured materials. Journal of Raman Spectroscopy: An International Journal for Original Work in all Aspects of Raman Spectroscopy, Including Higher Order Processes, and also Brillouin and Rayleigh Scattering 38(6): 604–617.
65. Gołasa K et al (2014) Multiphonon resonant Raman scattering in MoS_2. Appl Phys Lett 104(9):092106
66. Mignuzzi S et al. Effect of disorder on Raman scattering of single-layer MoS_2. Physical Review B 91(19): 195411.
67. Balandin AA et al. (2008) Superior thermal conductivity of single-layer graphene. Nano letters 8(3): 902–907.
68. Islam MR et al. (2014) Tuning the electrical property via defect engineering of single layer MoS_2 by oxygen plasma. Nanoscale 6(17): 10033–10039.
69. Cai Y et al. (2014) Lattice vibrational modes and phonon thermal conductivity of monolayer MoS_2. Physical Review B 89(3): 035438.
70. Soni H, Jha PK (2015) Ab-initio study of dynamical properties of two dimensional MoS_2 under strain. AIP Adv 5(10):107103
71. Ghosh PN, Maiti CR (1983) Interlayer force and Davydov splitting in 2 H− MoS_2. Physical Review B 28(4): 2237
72. Bandaru N et al. (2014) Effect of pressure and temperature on structural stability of MoS_2. J Phys Chem C 118(6): 3230–3235

73. Li X et al. (2016) Pressure and temperature-dependent Raman spectra of MoS_2 film. Applied Physics Letters 109(24): 242101
74. Verble JL, Wieting TJ (1970) Lattice mode degeneracy in Mo S_2 and other layer compounds. Phys Rev Lett 25(6):362
75. Evarestov RA, Bandura AV (2018) Infrared and Raman active vibrational modes in MoS_2-based nanotubes: Symmetry analysis and first-principles calculations. J Comput Chem 39(26):2163–2172
76. Virsek M et al. (2009) Raman characterization of MoS_2 microtube. physica status solidi (b) 246(11–12): 2782–2785
77. Zhang X et al (2016) Review on the Raman spectroscopy of different types of layered materials. Nanoscale 8(12): 6435–6450
78. Frey GL et al (1999) Raman and resonance Raman investigation of MoS_2 nanoparticles. Physical Review B 60(4): 2883
79. Sun Y et al (2014) Probing local strain at MX_2–metal boundaries with surface plasmon-enhanced raman scattering. Nano letters 14(9):5329–5334
80. Ding Y et al (2020) Raman tensor of layered MoS_2. Optics letters 45(6):1313–1316
81. Najmaei S et al (2012) Thermal effects on the characteristic Raman spectrum of molybdenum disulfide (MoS_2) of varying thicknesses. Appl Phys Lett 100(1):013106
82. Plechinger G et al (2012) Raman spectroscopy of the interlayer shear mode in few-layer MoS_2 flakes. Applied Physics Letters 101(10): 101906
83. Luo X et al (2013) Anomalous frequency trends in MoS_2 thin films attributed to surface effects. Physical Review B 88(7): 075320
84. Sahoo S et al (2013) Temperature-dependent Raman studies and thermal conductivity of few-layer MoS_2. J Phys Chem C 117(17): 9042–9047
85. Wang Y et al (2013) Raman spectroscopy study of lattice vibration and crystallographic orientation of monolayer MoS_2 under uniaxial strain. Small 9(17): 2857–2861
86. Huang S et al (2016) Low-frequency interlayer Raman modes to probe interface of twisted bilayer MoS_2. Nano letters 16(2):1435–1444
87. Chen S-Y et al (2015) Helicity-resolved Raman scattering of MoS_2, $MoSe_2$, WS_2, and WSe_2 atomic layers. Nano letters 15(4): 2526–2532
88. Thripuranthaka M et al (2014) Temperature dependent Raman spectroscopy of chemically derived few layer MoS_2 and WS_2 nanosheets. Appl Phys Lett 104(8):081911
89. Yalon E et al (2017) Temperature-dependent thermal boundary conductance of monolayer MoS_2 by Raman thermometry. ACS applied materials & interfaces 9(49): 43013–43020.
90. Shen P et al (2021) Temperature and laser-power dependent Raman spectra of MoS_2/RGO hybrid and few-layered MoS_2. Physica B: Condensed Matter 604: 412693
91. Lanzillo NA et al (2013) Temperature-dependent phonon shifts in monolayer MoS_2. Applied Physics Letters 103(9): 093102
92. Lin J et al (2011) Anharmonic phonon effects in Raman spectra of unsupported vertical graphene sheets. Physical Review B 83(12):125430
93. Taube A et al (2014) Temperature-dependent nonlinear phonon shifts in a supported MoS_2 monolayer. ACS applied materials & interfaces 6(12): 8959–8963
94. Calizo I et al (2007) Temperature dependence of the Raman spectra of graphene and graphene multilayers. Nano Lett 7(9):2645–2649
95. Yan Y et al (2013) Facile synthesis of low crystalline MoS_2 nanosheet-coated CNTs for enhanced hydrogen evolution reaction. Nanoscale 5(17): 7768–7771
96. Najmaei S, Pulickel MA, Lou J (2013) Quantitative analysis of the temperature dependency in Raman active vibrational modes of molybdenum disulfide atomic layers. Nanoscale 5(20): 9758–9763
97. Feng T, Lindsay L, Ruan X (2017) Four-phonon scattering significantly reduces intrinsic thermal conductivity of solids. Phys Rev B 96(16):161201
98. Lin Z et al (2021) Thermal expansion coefficient of few-layer MoS_2 studied by temperature-dependent Raman spectroscopy. Scientific reports 11(1): 7037

99. Ko PJ et al (2015) Laser power dependent optical properties of mono-and few-layer MoS_2. Journal of nanoscience and nanotechnology 15(9): 6843–6846
100. Chang CH, Chan SS (1981) Infrared and Raman studies of amorphous MoS_2 and poorly crystalline MoS_2. J Catal 72(1):139–148
101. Yan R et al (2014) Thermal conductivity of monolayer molybdenum disulfide obtained from temperature-dependent Raman spectroscopy. ACS nano 8(1): 986–993
102. Zhang G-Y, Lan GX, Yu-Fang W (1991) Lattice vibration spectroscopy. Ch 4: 112–113
103. Lee C et al (2010) Anomalous lattice vibrations of single-and few-layer MoS_2. ACS nano 4(5): 2695–2700
104. Xu K et al (2017) Doping of two-dimensional MoS_2 by high energy ion implantation. Semiconductor Science and Technology 32(12): 124002
105. Phuc HV et al (2018) Tuning the Electronic Properties, Effective mass and carrier mobility of MoS_2 monolayer by strain engineering: first-principle calculations. Journal of Electronic Materials 47(1): 730–736
106. Peelaers H, Van de Walle CG (2012) Effects of strain on band structure and effective masses in MoS_2. Physical Review B 86(24): 241401
107. Yun WS et al (2012) Thickness and strain effects on electronic structures of transition metal dichalcogenides: 2H-MX_2 semiconductors (M= Mo, W; X= S, Se, Te). Physical Review B 85(3): 033305
108. Yue Q et al (2012) Mechanical and electronic properties of monolayer MoS_2 under elastic strain. Physics Letters A 376(12–13): 1166–1170
109. Velicky M et al (2020) Strain and charge doping fingerprints of the strong interaction between monolayer MoS_2 and gold. The journal of physical chemistry letters 11(15): 6112–6118
110. Saigal N et al (2018) Effect of lithium doping on the optical properties of monolayer MoS_2. Applied Physics Letters 112(12): 121902
111. Cortijo-Campos S, Carlos P, De Andrés A (2022) Size effects in single-and few-layer MoS_2 nanoflakes: impact on Raman phonons and photoluminescence. Nanomaterials 12(8): 1330
112. Bagnall AG et al (1980) Raman studies of MoS_2 at high pressure. Physica B+ C 99(1–4): 343–346
113. Yan Y et al (2016) Interlayer coupling affected structural stability in ultrathin MoS_2: an investigation by high pressure Raman spectroscopy. J Phys Chem C 120(43): 24992–24998
114. Yang M et al (2017) Anharmonicity of monolayer MoS_2, $MoSe_2$, and WSe_2: a Raman study under high pressure and elevated temperature. Applied Physics Letters 110(9): 093108
115. Bertolazzi S, Brivio J, Kis A (2011) Stretching and breaking of ultrathin MoS_2. ACS Nano 5(12):9703–9709
116. Chi Z-H et al (2014) Pressure-induced metallization of molybdenum disulfide. Phys Rev Lett 113(3): 036802
117. Song QJ et al (2016) Physical origin of Davydov splitting and resonant Raman spectroscopy of Davydov components in multilayer $MoTe_2$. Phys Rev B 93(11):115409
118. Sunitha AP (2018) Growth and characterization of MoS_2 nanostructures for optoelectronic device applications, PhD. Thesis in Physics
119. Tsai M-L et al (2014) Monolayer MoS_2 heterojunction solar cells. ACS nano 8(8): 8317–8322
120. Li L et al (2015) Raman shift and electrical properties of MoS_2 bilayer on boron nitride substrate. Nanotechnology 26(29): 295702

Electronic and Optical Properties of Transparent Conducting Perovskite $SrNbO_3$: Ab Initio Study

Rakesh Kumar, Patel Maneshwar Rai, Nitesh K. Chourasia, Manish Kumar, Arun Kumar Singh, Aavishkar Katti, and Ritesh Kumar Chourasia

1 Introduction

Perovskite, which occurs naturally and artificially, is used in our references as an example of how research throughout the world has made truly important strides toward the effective utilization of every attribute of every element categorization. As a platform for broad study on the electronic states and physical characteristics of transition metal oxides (TMOs) for human needs, perovskite oxides (ABO_3) have been intensively studied by researchers. For the First-principles investigation, we considered A = Sr and B = Nb, respectively, where A and B correspond to different cations. Similar to $SrVO_3$ perovskite TMOs with a d1 electronic configuration is strontium niobium oxide (SNO). When compared to 4d TMOs, a large range of studies have been conducted on 3d TMOs; however, Oka et al study on 4d TMOs [1] has described the high conductivity of stoichiometric SNO. The fact that bulk samples

Authors Rakesh Kumar and Nitesh K. Chourasia contributed equally to the present research work.

R. Kumar · P. M. Rai · A. K. Singh
University Department of Physics, Lalit Narayan Mithila University, Darbhanga, 846004, Bihar, India

R. Kumar · R. K. Chourasia (✉)
Post Graduate Department of Physics, Samastipur College (A constituent college of L.N.M.U. Darbhanga, 846004, Bihar, India), Samastipur, India

N. K. Chourasia
School of Physical Sciences, Jawaharlal Nehru University, New Delhi 110067, India

M. Kumar
Department of Physics, ARSD College, University of Delhi, New Delhi 110021, India

A. Katti (✉)
Department of Physics, Dr. Vishwanath Karad MIT World Peace University, Pune, Maharashtra 411038, India
e-mail: aavishkarkatti89@gmail.com

S. B. Krupanidhi et al. (eds.), *Recent Advances in Functional Materials and Devices*, Springer Proceedings in Materials 37, https://doi.org/10.1007/978-981-99-6766-7_14

display metallic electrical conduction, as well as photocatalytic activity for both UV and visible windows, has received significant interest in the scientific community. Mathieu Mirjolet et al. [2, 3] examined the Sr-deficient powder of $Sr_{1-x}NbO_3$, a material that's metallic and exhibits lovely red color indicating an optical absorption process, and found that TMOs based on 3d and 4d metals have great potential for plasmonic applications. In the study of the SNO band diagram, Suresh Thapa et al. discovered that Nbt2g band crosses the Fermi level and suggests metallic nature [4]. To demonstrate the potential of SNO as a UV transparent conduction medium, Yoonsang Park et al. presented a combined DFT and experimental study [5, 6].

With the above inspiration and the great utility of such metal perovskite, material, our present research is also focused on the cubic system of bulk SNO for the understanding of metallic character and optical properties using DFT, keeping in mind the framework discussed above from various literature. This is because the behavior of perovskite oxides holding 4d TM ions is expected to be quite different in comparison to similar and more extensively studied 3d compounds [7–9]. Due to their dynamic (electron mobility, carrier density, and electrical resistivity) and static (absorption, refractive index, and loss function) properties at room temperature, the family of SNO has attracted major attention for optoelectronic device applications. Since d1-type TMOs have potential applications as the next generation of transparent electrode materials and are a leading contender to displace traditional TCOs like tin-doped indium oxide (ITO) [8], there is a vital need for us to research the electrical and optical behavior of SNO, as already suggested by our objective. Due to hybridization with the surrounding oxygen ions in the crystal and a reduction in on-site Coulomb interaction, SNO has a higher electrical conductivity. This is also due to its longer 4d electronic states, which give it a more metallic character and diminishing electronic correlation.

2 Theoretical Details

For a clear vision of the present research work, the theoretical details are divided into the following categories:

2.1 Material Details

$SrNbO_3$ has a (cubic) perovskite structure, resembling $CaTiO_3$ in phase, and crystallizes in the cubic Pm-3 m space group with 5 independent atoms per unit cell in the oxidation states O^{2-}, Sr^{2+}, and Nb^{4+}, respectively. SrO_{12} cuboctahedra are created when Sr^{2+} bonds with twelve equivalent O^{2-}atoms, sharing corners with twelve equivalent SrO_{12} cuboctahedra, faces with six comparable SrO_{12} cuboctahedra, and faces with equivalent NbO_6 octahedra. NbO_6 octahedra are created when

Nb^{4+} bonds with six equivalent O^{2-}atoms, sharing faces with eight equivalent SrO_{12} cuboctahedra and corners with an additional six NbO_6 octahedra.

2.2 DFT Theories

The success and application of DFT may be attributed to certain extremely astute realizations made by Kohn, Hohenberg, and Sham around the middle of 1960s. DFT was created by reformulating the many-body issue as an analogous single-particle problem and focusing instead on the density of electrons as the primary one to solve. Since its inception in condensed matter physics, it has developed into a powerful tool for material science, nanotechnology, solid-state chemistry, and other computational sub-disciplines. For instance, the Schrodinger equation has trouble with the many-body system because 10 electrons need 30 dimensions, which makes it difficult to get precise answers. From this point on, DFT is effective. The many-body problem's approximations are merely briefly given here. Using these theories and approximations, DFT is developed, which operates in terms of electron density rather than just classical electrons [10, 11]. The Schrödinger equation is solved to determine an atom's ground state energy in known terms:

$$\widehat{H}\psi(\{r_i\},\{R_l\}) = E\psi(\{r_i\},\{R_l\} \tag{1}$$

2.2.1 The Born–Oppenheimer (BO) Estimation:

The Born–Oppenheimer approximation is one of the key concepts that underlie the description of the quantum states of molecules and enables the separation between the motion of the nuclei and the motion of the electrons [12]. By taking into account the following mathematics, presented in general form, it is possible to see how the Schrödinger equations employ the fact that the mass of an atomic nucleus is considerably more than the mass of an electron:

$$\psi(\{r_i\},\{R_l\}) = \psi_N\{R_l\}x\psi_e\{r_i\} \tag{2}$$

here, ψ_N = Nuclei wave function and ψ_e = Electron wavefunction.

2.2.2 The Hohenberg Kohn (HK) Postulates

It consists of two fundamental postulates that were put out by Hohenberg and Kohn [13]. The first theorem states that the total ground state energy or external potential of a many-electron system is an exclusive function of the electron density.

$$E = E_o[\rho_o(r)] \tag{3}$$

here ρ(r) is density function.

But according to the second postulate, the actual ground-state electron density is the one that minimizes the functional's total energy.

$$E[\rho(r)] > E_o[\rho_o(r)] \tag{4}$$

2.2.3 The Kohn Sham (KS) Strategy

According to this technique, the KS equation may be used to convert a multi-electron system with ground state eigenvalues into a single electron problem. The formula is as follows:

$$\rho(r) = \sum_{i=1}^{N} |\varphi_i(r)|^2 \tag{5}$$

$|\varphi_i(r)|^2$ is a unit electron wave function.

2.3 *Exchange–Correlation Approximations (ECA) Energy Functionals*

We all are already aware that, exchange–correlation functional E_{XC} is a crucial component of DFT. LDA/LSDA (local spin density approximation), GGA (generalized gradient approximation), and BLYP (hybrid density functional) are only a few of the approximation methods that have been developed. Sham introduced LDA's core idea [14] for the first time in 1965. In 1986, Perdew and Wang presented GGA [15, 16], which was based on the LDA potential function, and indicated that in addition to the system's local electron density, the exchange energy and correlation energy also rely on the density gradient. Compared to LDA, which is better for metals but less effective for semiconductors, GGA is employed in all sorts of materials.

$$E_{XC}^{LDA}[\rho] = \int \rho(r)\varepsilon_{XC}[\rho(r)]dr \tag{6}$$

$$E_{XC}[\rho] = \int \rho(r)\varepsilon_{XC}(\rho(r))dr + E_{xc}^{GGA}(\rho(r), \nabla\rho(r)) \tag{7}$$

2.4 Electronic Structure Calculations and Properties

Determining a material's electrical structure is the major goal of atomistic simulations. The calculations of wave functions, often referred to as eigenstates, and related eigenvalues, or energies, of electrons surrounding stationary nuclei are the subject of this work. The knowledge of electronic ground states provides knowledge of stability, vibrational properties with a variety of thermal properties, elastic properties, and transport phenomena like diffusivity, ionic conductivity, and dielectric properties. Excited states convey knowledge of electronic transport phenomena and optical properties. This study plays a crucial role in the delicate development of microscopic phenomena as well as in the classification of materials as conductors, semiconductors, insulators, or superconductors. Following are explanations of its electrical band structure (a) and density of states (b) [17].

a. **Band Structure**
Each energy level divides into N energy levels, creating an energy continuum, as the N atoms form a solid and move towards one another at a distance equal to the lattice constant. This group of continuum energy levels is referred to as an energy band. The quantum mechanical approach offers a comprehensive grasp of the description of the band structure, as shown by the Schrodinger equation, which explains free electron mobility at a potential of zero.

$$\frac{d^2\psi}{dx^2} + \frac{2m}{\hbar^2}E\psi = 0 \tag{8}$$

The state of a free electron is represented by ψ (r) = Aexp(ikr) (wave function), which produces energy E as,

$$E(k) = \frac{\hbar^2 k^2}{2m} \tag{9}$$

where k = radius of considered sphere; ħ = planks constant; m = electron mass and above Eq. (9) is a dispersion relation and represents a single band.

b. **The Density of States (DOS)**
There are a relatively large number of energy levels in each band, and the number of them changes based on the material's composition. This constraint requires calculating the number of energy levels or states per unit of energy and per unit of physical space. States that there are per unit of energy "N" The definition of the electronic density of states "D" is "E" per unit volume "V" of the real space.

$$D = \frac{1}{V}\frac{dN}{dE} \tag{10}$$

$$D = \frac{1}{2\pi^2}\left(\frac{2m}{\hbar^2}\right)^{3/2} E^{1/2} \tag{11}$$

2.5 Optical Properties

We continue the research of SNO based on optical characteristics while keeping in mind that we have completed a variety of electronic structure calculations that serve as the foundation for calculating optical features. Materials can also be classified as translucent, opaque, or transparent in addition to this property. It frequently has to do with how responsive the material is to incoming electromagnetic radiation (E_MR). Due to exposure to E_MR, a number of intriguing features evolved depending on their metallic or non-metallic qualities. The energy E a photon carries is,

$$E = hv \tag{12}$$

Considering coefficients of absorptivity, reflectivity, and transmissivity as a,r,t, we have.

$$a + r + t = 1 \tag{13}$$

The incident photon's energy is absorbed by the electron during the microscopic treatment of E_MR interaction, causing E_MR to slow down and produce the refraction phenomena, which is measured by the refractive index. The dielectric function, a key microscopic characteristic that links the electrical structure to optical events, is the next significant variable. Here, the dielectric function E_r is described by two equations, the first equation is:

$$\mathrm{d(r, f)} = \varepsilon_r(\omega)\, \varepsilon_0 \mathrm{E(r, f)} \tag{14}$$

here,

"$d = \varepsilon_0 E + p$" is the displacement vector, "ε_0" is the constant for dielectric for the vacuum and "p" is the vector of polarization, and "f" is the frequency of energy, the 2nd equation is given by,

$$\varepsilon_r = n^2 \tag{15}$$

The refractive index function may be written with "n" being the refractive index as,

$$\hat{n} = n - ik \tag{16}$$

Since our case study of SNO is metal, we obtain an equation that consists of extinction coefficient "k" and plasma frequency "f_p" for the metal that defines the intra-band transition of electrons owing to E_MR absorption.

$$\mathrm{f}_p = \frac{ne^2}{\epsilon_0 m} \tag{17}$$

Theoretically by solving the equations, n(f)" and " k(f)" is obtained as,
"Refractive index"

$$\mathrm{n(f)} = \{\frac{\left[\varepsilon_1^2(\mathrm{f}) + \varepsilon_2^2(\mathrm{f})\right]^{1/2} + \varepsilon_1(\mathrm{f})}{2}\}^{1/2} \tag{18}$$

"Extinction Coefficient"

$$\mathrm{k(f)} = \{\frac{\left[\varepsilon_1^2(\mathrm{f}) + \varepsilon_2^2(\mathrm{f})\right]^{1/2} + \varepsilon_1(\mathrm{f})}{2}\}^{1/2} \tag{19}$$

here, ε_1 = real component; ε_2 = imaginary component; of dielectric function "ε_r" which is affected by the damping parameter in a real metal case, hence complex equation for the dielectric function becomes:

$$\varepsilon_\mathrm{r} = \varepsilon_1 + \mathrm{i}\varepsilon_2 \tag{20}$$

which are connected via frequency "f" by the Kramers–Kronig relation as;

$$\varepsilon_1(f) = 1 + \frac{2}{\pi}\int_0^\infty \frac{\omega\prime\varepsilon_2(f\prime)}{\omega'^2 - \omega^2} df\prime \tag{21}$$

A material's precise dielectric function equation can be used to predict how it will react electronically to an incoming photon, given as:

$$\varepsilon_\mathrm{r}(\mathrm{f}) = \varepsilon_1(\mathrm{f}) + \mathrm{i}\varepsilon_2(\mathrm{f}) \tag{22}$$

Typically, the real component ε_1(f) indicates the phase lag between the incident and induced polarized field component and the imaginary component ε_2(f) reflects energy loss. Calculating ε_2(f) involves comparing the momentum matrix components of the empty and occupied electronic states. Using "c" as the speed of light, equations describing several other significant optical characteristics are described below.
"Reflectivity"

$$R(f) = \frac{(n-1)^2 + \left(\frac{\alpha c}{2f}\right)^2}{(n+1)^2 + \left(\frac{\alpha c}{2f}\right)} \tag{23}$$

"Energy loss spectra"

$$L(f) = \frac{\varepsilon_2(f)}{\left[\varepsilon_1^2(f) + \varepsilon_2^2(f)\right]} \tag{24}$$

"Absorption Coefficient"

$$\alpha(f) = \frac{2f}{c}\left\{\frac{\left[\varepsilon_1^2(f) + \varepsilon_2^2(f)\right]^{1/2} - \varepsilon_1(f)}{2}\right\}^{1/2} \tag{25}$$

2.6 Computational Details

Ab-initio kind of computation, i.e., the First principal calculation has been performed using the WIEN2k package [18] based on DFT. The KS equations of DFT are solved using the full-potential (linearized) augmented plane-wave and local-orbitals [FP-(L) APW + lo] basis set to look at the different properties. In the current investigation, we use many software factors to comprehend the program's variety of applications by concentrating on electronic and optical aspects. We have used GGA for the XC functional constructed with the PBE prescription. The atomic coordinate-dependent visualization of the material unit cell, i.e., atomic structure, has been done using VESTA [19] (Visualisation for Electronic Structural Analysis) for a proper understanding of the considered cell.

For DFT calculations, we need a crystal information file (cif), which we obtained from the materials project site [20], from which $SrNbO_3$ cif has been obtained. The cif file reveals that the $SrNbO_3$ is a cubic crystal system, having a cubic lattice system that has been visualized from VESTA as shown in Fig. 1, comprising Hall Number P423, and International space group name and number Pm-3 m and 221 respectively.

We first proceeded with the optimization of the structure formed using the cif file, which includes atoms whose coordinates have been given in Table I. After optimization, we obtained the optimized structure. We performed spin-polarized calculations of the optimized cubic structure having lattice parameters a = b = c = 7.753399 Bohr, unit cell volume = 466.09710 $Bohr^3$, and convergence criteria for energy = 0.00001 Ry, force = 1mRy/au, and charge = 0.0001e have been applied. We have used GGA type of exchange–correlation functional for pseudopotential under Perdew-Burke-Ernzerhof, RKMAX = 7.0, smearing = TETRA, and energy separation between core and valence = -6.0 Ry with 10,000 k-points having div. 21 × 21 × 21 for all calculations for our whole study.

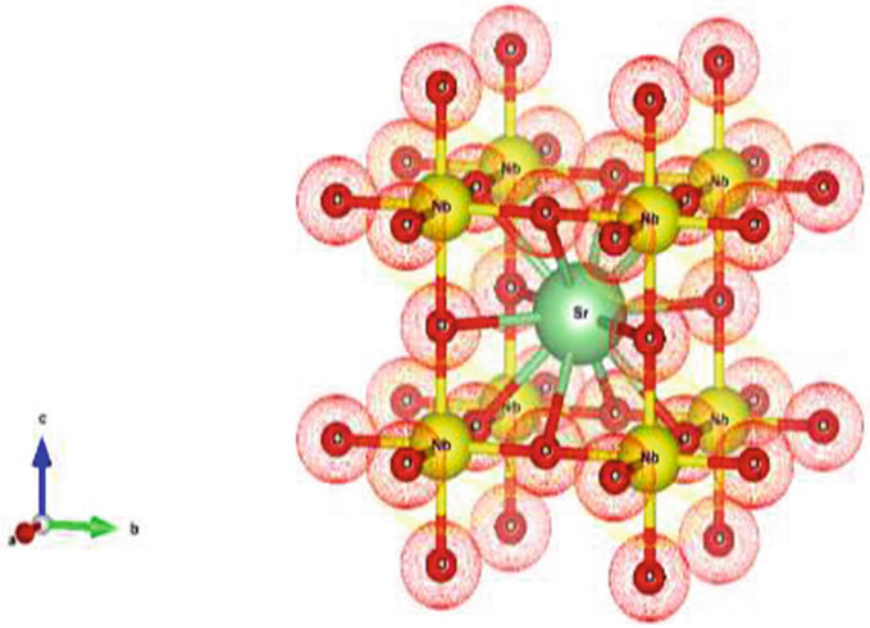

Fig. 1 Crystal structure visualisation of (SNO) $SrNbO_3$

Table 1 Considered atomic positions

Wyckoff	Atoms	x-coordinates	y-coordinates	z-coordinates
3d	O	0.5	0.0	0.0
		0.0	0.5	0.0
		0.0	0.0	0.5
1b	Sr	0.5	0.5	0.5
1a	Nb	0.0	0.0	0.0

3 Obtained Results and Discussions

In this section, the obtained results have been discussed based on below mentioned several subparts.

3.1 Structure Optimization

As we know "structure dictates the properties," thus structure optimization should be our priority. Therefore, theoretically speaking, geometric optimization must be carried out by relaxing the structure at various volumes, determining the global

minimum energy, and the proper pressure, and then fitting the structure with the appropriate equation of state (EoS). Figure 2 displays the results of using the Murnaghan EoS optimized structure, and Fig. 3 displays the results of the scf calculation's energy convergence plot.

The volume-energy curve shows that the minimum total energy has been obtained at a 3% change of volume w.r.t. initial structure, hence parameters corresponding to this value have been utilized further for all kinds of required calculations using DFT in the next sections.

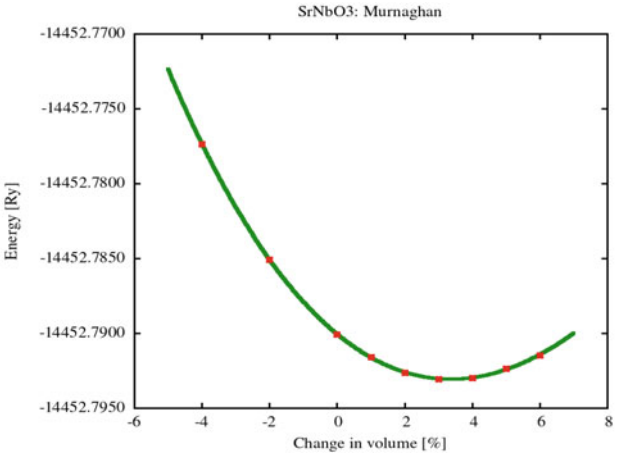

Fig. 2 Optimized energy-volume curve of $SrNbO_3$

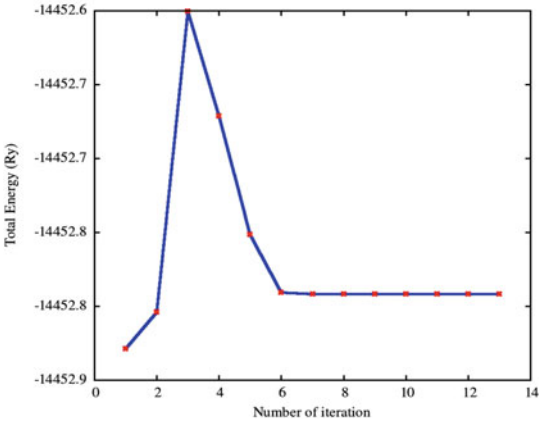

Fig. 3 Energy convergence plot of $SrNbO_3$

3.2 *Electronic Properties*

The electronic band structure Fig. 4 and DOS. Figure 5 contribute towards the formation of electronic properties and are mentioned below.

3.2.1 Electronic Band Structure

As discussed in the theory section Eq. (9) describes a dispersion relation that represents the single band too, keeping this fact in mind, we have come across the following electronic band structure of $SrNbO_3$, for both spins along the Brillion-zone integrations, which were carried out along the high symmetry points "R, Γ, X, M, Γ" for

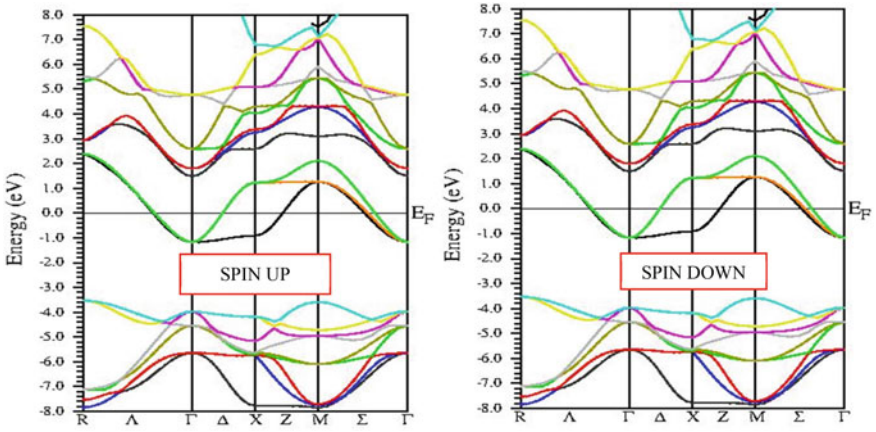

Fig. 4 Electronic band structure of $SrNbO_3$ for both spins (different orbital configuration)

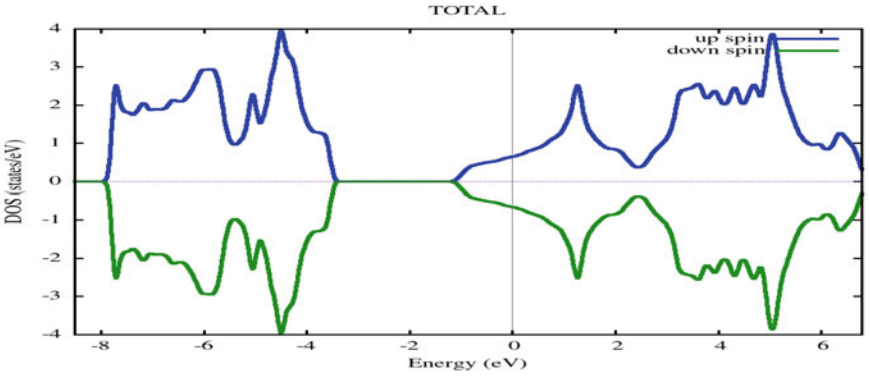

Fig. 5 Total density of state comprising up and down spin for overall $SrNbO_3$ (TCP) material

band structure calculations. Band structure of both up and down spins along the Fermi level (E_F) can be seen in Fig. 4 within the practical energy range -8 to 8 eV, respectively.

Further, we have come across the energy band gap of 0 eV that clarifies it as metallic, under the most common one, the parameter-free GGA functional developed by Perdew, Burke, Ernzerhof (PBE).

3.2.2 DOS and PDOS Calculations

The DOS and PDOS of each and every atom's contribution has been revealed in this section, where DOS represents the number of states available to electrons, it's the only function depending upon energy in DFT calculations. The total density of states TDOS of $SrNbO_3$ material for different orbital configurations is shown in Fig. 5 below.

For a better insight into DOS, PDOS of every atom in SNO is shown below in Fig. 6.

From Figs. 6, 7 and 8 we note that the region of energy range –8 eV to –3.5 eV approximately in the valence band is dominated by the p-states of O and from region –1 eV, at Fermi level and that at the conduction band to is dominated by the same p-state that sums up the total contribution of O in TDOS is mostly due to p orbital compared to s-orbital.

From Figs. 8 and 9, we see that the same region of energy (–8 eV to –3.5 eV) in "Nb" atom is dominated by d orbital even having "p" orbital contribution in significant number, but "s" states an absence in the PDOS of Nb and from the valence band of energy range -1 eV to conduction band crossing Fermi energy level is well supported with "d" & p-orbital but in less nature.

If we study the above plots in Figs. 10, 11, it follows the same trends as of "O" and "Nb" atom, the major difference is that in valence band "p" & "d" states both

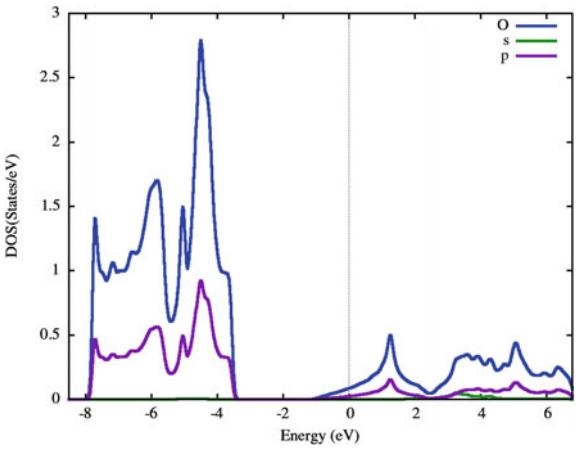

Fig. 6 PDOS of oxygen atom in up spin

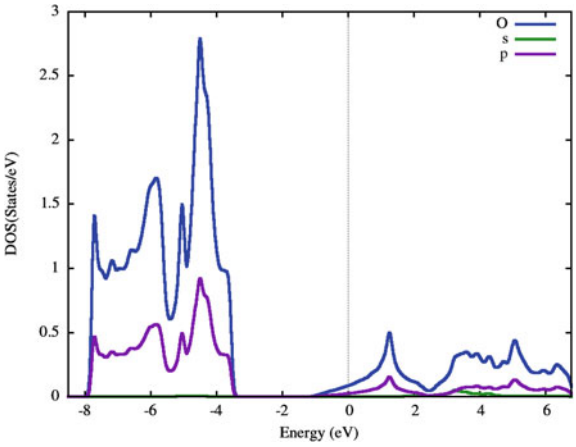

Fig. 7 PDOS of oxygen atom in down spin

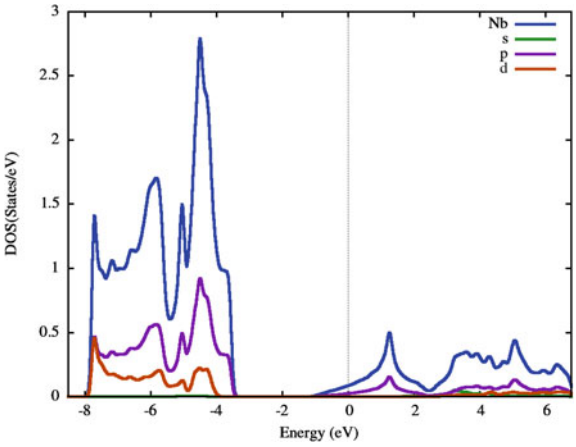

Fig. 8 PDOS of Niobium atom in up spin

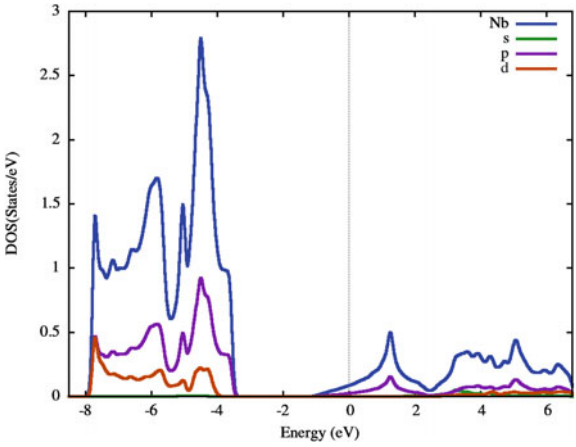

Fig. 9 PDOS of Niobium atom in down spin

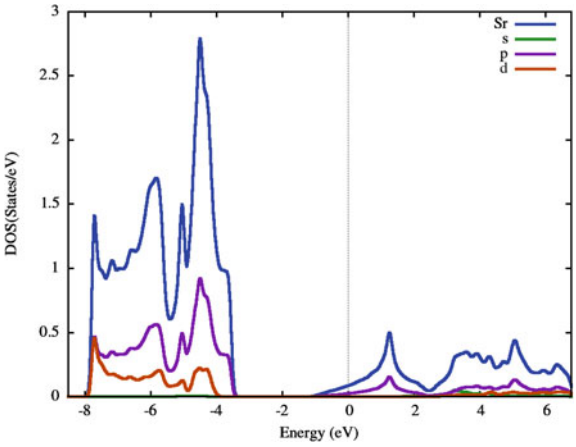

Fig. 10 PDOS of Strontium atom in up spin

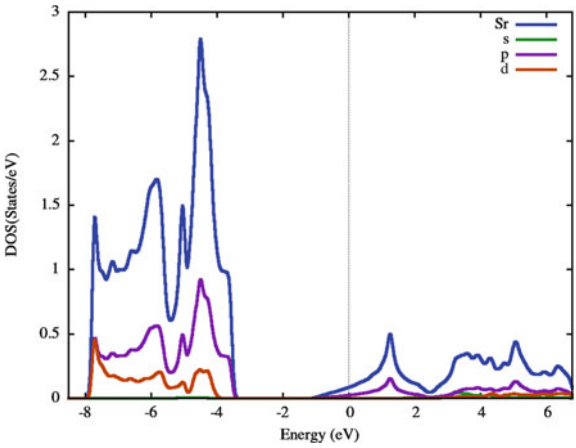

Fig. 11 PDOS of Strontium atom in down spin

contribute to domination in TDOS of SNO having d-orbital in dominating character but as soon we move from valence band towards Fermi than to conduction band, we see a rapid decrease in DOS contribution of all the s, p, d states.

3.3 Optical Properties

Keeping in mind that we have done all kinds of electronic structure calculations which form the basis for optical properties calculation. The calculated $\varepsilon_1(f)$ and $\varepsilon_2(f)$ for the strontium niobium oxide using PBE functionals are shown below. Figure 12 shows the reflectivity R(f) of SNO perovskite having minima at plasma edges. These

characteristics shown by SNO are due to the plasmonic excitation within the material, which causes the decline within the plots of reflectivity.

The n(f) in Fig. 13 shows the varying refractive index, which is the result of refraction within the material. We can conclude from both of the plots that there is negligible varying R(f) and almost constant n(f), which implies that there is not a much higher degree of refraction or reflectance within the material, it remains constant throughout the UV and visible light wavelength, bringing it in the category of transparent conducting perovskites.

The peak of the energy loss spectrum L(f) in Fig. 12 can be used for understanding the plasmonic resonance. In Fig. 13 spectra near approaching 0 eV, and the absorption coefficient is almost approaching 0. The refractive index in Fig. 10 approaches 1 and the absorption coefficient falls to 0 at energies above plasmon energy, demonstrating the transparency of the material. The measurement of optical conductivity, which is the extension of electrical transport to high (optical) frequencies, is quantifiable, contact-free, primarily responsive to charged responses, and it is based on polarized

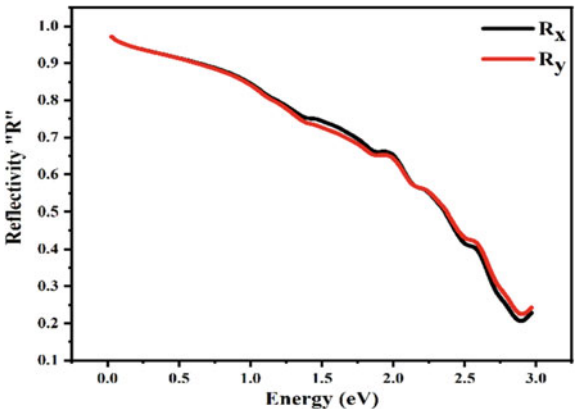

Fig. 12 Reflectivity through SNO

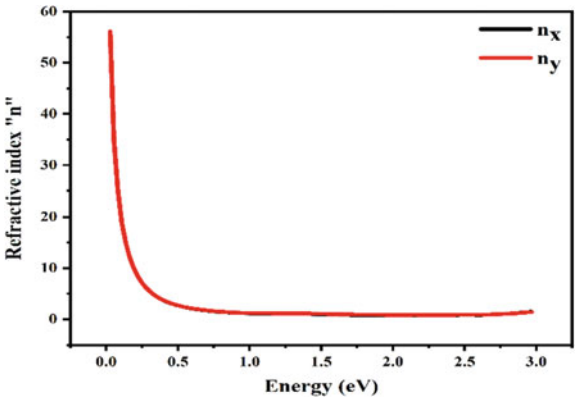

Fig. 13 Refractive index variation in SNO

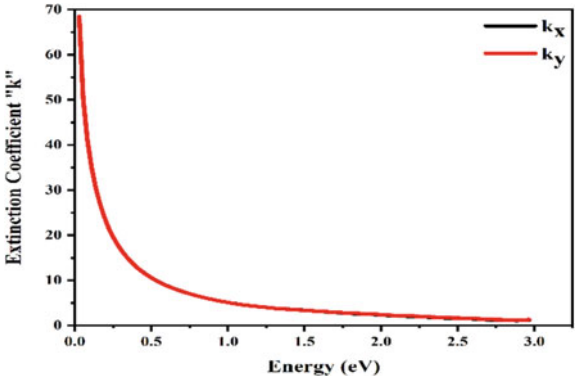

Fig. 14 Extinction coefficient of SNO

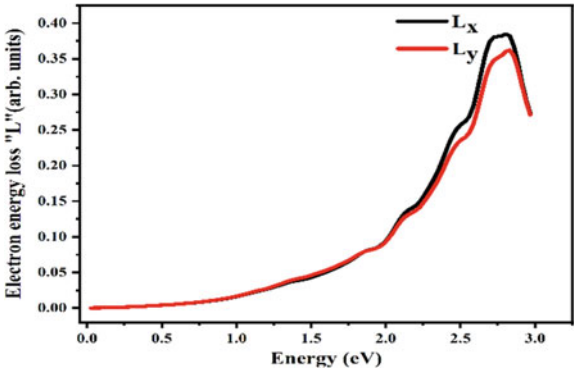

Fig. 15 Energy loss spectra of SNO

absorption spectra. Figure 14 explains the optical conductivity spectra that designate that SNO is optically active for visible to UV light. Overall Fig. 15 explains the degree of absorption or reflection radiation taking place through SNO, dependent on atomic, chemical, and structural composition as an intrinsic property.

4 Conclusions

Overall, the most recent method for examining a material's electronic structure is DFT, within the framework of the DFT FP-LAPW technique, employing GGA-PBE functionals, a thorough analysis of the cubic-structured SNO's structural, electrical, and optical aspects of the optimized crystal lattice are carried out very successfully, whose lattice parameters were comparable to earlier efforts. The study of electronic properties by both the calculated band structure and density of states has been strongly explained towards its metallic behavior. As the refractive index is approaching one and absorption spectra can be seen as a maximum within the photon energy implying

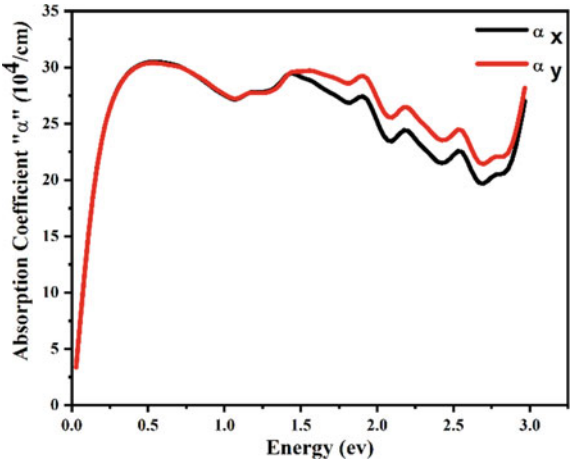

Fig. 16 Absorption coefficient of SNO

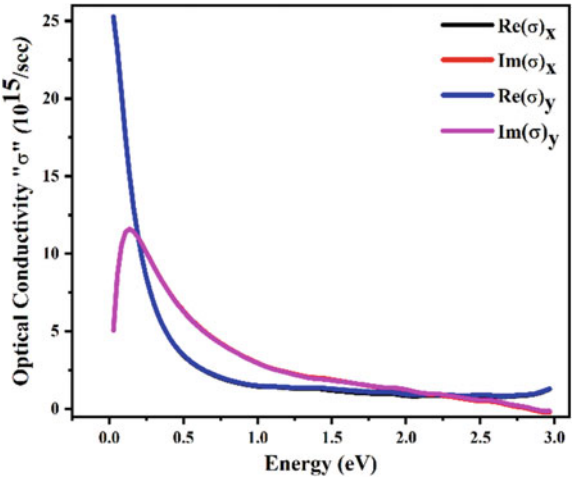

Fig. 17 Optical conductivity of SNO

the UV and visible window. Therefore, we can conclude that it transmits the whole incident light rays making it TCP. The result presented here in this work can be used and helpful as a road map for experimentalists for the futuristic application of this needful material especially in the optical aspect.

Acknowledgement Aavishkar Katti wishes to acknowledge financial assistance from DST-SERB, Govt. of India through the Core Research Grant awarded (vide File No. CRG/2021/004740).

References

1. Oka D, Hirose Y, Nakao S, Fukumura T, Hasegawa T (2015) Intrinsic high electrical conductivity of stoichiometric $SrNbO_3$ epitaxial thin films. Phys Rev B 92:205102
2. Mirjolet M, Kataja M, Hakala KT, Komissinskiy P, Alff L, Herranz G, Fontcuberta J (2021) Optical Plasmon Excitation in Transparent Conducting $SrNbO_3$ and $SrvO_3$ Thin Films. Advanced Optical Materials 9(17):2100520
3. Sun C, SearlesJD (2014) Electronics, Vacancies, Optical Properties and Band Engineering of Red Photocatalyst $SrNbO_3$: a computational investigation. The Journal of Physical Chemistry C 118(21), 11267–11270
4. Thapa S, Provence SR, Gemperline PT, Matthews BE, Spurgeon SR, Battles SL, Heald SM, Kuroda MA, Comes RB (2022) Surface stability of SrNbO3+δ grown by hybrid molecular beam epitaxy. APL Materials 10(9), 2166–532X
5. Park Y, Roth J, Oka D, Hirose Y, Hasegawa T, Paul A, Pogrebnyakov A, Gopalan V, Birol T, Engel-Herbert R (2020) $SrNbO_3$ as a transparent conductor in the visible and ultraviolet spectra. Commun Phys 3(102)
6. Kumar S (2021) Theoretical and experimental studies of $SrNbO_3$, SPAST Abs 1(01)
7. Wolfram T, Ellialtioglu S (2006) Electronic and optical properties of d-band Perovskites. Cambridge University Press
8. Bigi C, Orgiani P, Slawinska J, Fujii J, Irvine TJ, Picozzi S, Panaccione G, Vobornik I, Rossi G, Payne D, Borgatti F (2020) Direct insight into the band structure of $SrNbO_3$. Physical Review Materials 4:025006
9. Tariq S, Batool A, Faridi MA, Jamil MI, Mubarak AA, AkBAR NO (2017) Calculation of optical properties of SrNbO3 and SrNbO3.5 based on density functional theory DFT
10. Booth GH, Grüneis A, Kresse G, Alavi A (2013) Towards an exact description of electronic wavefunctions in real solids. Nature 493:365–370
11. Kohn W, Becke AD, Parr RG (1996) Density functional theory of electronic structure. J Phys Chem 100(31):12974–12980
12. Fernandez MF (2019). The Born-Oppenheimer approximation. https://doi.org/10.13140/RG.2.2.21650.91840,PY:2019/03/08
13. Hohenberg P, Kohn W (1964) Inhomogeneous electron gas. Phys Rev 136(3):B864
14. Kristyán S, Pulay P (1994) Can (semi) local density functional theory account for the London dispersion forces? Chem Phys Lett 229(3):175–180
15. Perdew JP, Yue W (1986) Accurate and simple density functional for the electronic exchange energy: Generalized gradient approximation. Phys. Rev. B Condense Matter 33(12):8800–8802
16. Perdew JP, Burke K, Ernzerhof M (1996) Generalized gradient approximation made simple. Phys Rev Lett 77(18):3865
17. Lamichhane A (2021) First-principles density functional theory studies on perovskite materials. Dissertations. 1518
18. Blaha P, Schwarz K, Tran F, Laskowski R, Madsen GK, Marks LD (2020) WIEN2k: An APW+lo program for calculating the properties of solids. The Journal of Chemical Physics 152(7), 074101
19. Momma K, Izumi F (2011) VESTA 3 for three-dimensional visualization of crystal, volumetric and morphology data. J Appl Crystallogr 44:1272–1276
20. Materials Project Homepage. https://materialsproject.org/materials/mp-7006 from database version v2022.10.28

Tribology of Spray Formed Aluminium-Based Materials

N. Raja, G. Gautam, S. K. Maurya, A. Sharma, S. Singh, A. K. Singh, and R. Pandey

1 Introduction

The aluminium-based materials (aluminium alloys and their composites) are the important engineering materials since last few decades owing to their characteristics such as less density, excellent mechanical and tribological properties, relatively low cost, good properties at high temperature and damping capacity, good electrical and thermal properties [1, 2]. These materials are generally used to make the parts for different sectors such as automotive, aerospace, marine and sports. The common parts of automotive sectors are cylinder blocks, cylinder liners, piston, piston insert rings and brake drums made by aluminium-based materials [3, 4]. These materials are generally upgraded via the incorporation of varying types of materials with different morphology. The particulate morphology of ceramic materials (carbide, boride and nitride of metals), intermetallics (trialuminide of nickel, iron, titanium and zirconium), solid lubricants and industrial waste are preferred over the other morphology to prepared aluminium-based materials due to their isotropic properties [5–11]. The

N. Raja
Department of Materials Science & Engineering, IITK, Kanpur, UP 208016, India

G. Gautam (✉) · S. K. Maurya
Department of Physics, Graphic Era Hill University, Dehradun, UK 248001, India
e-mail: gauravgautamm1988@gmail.com

A. Sharma
Department of Physics, Graphic Era Deemed to be University, Dehradun, UK 248001, India

S. Singh
Department of Physics, Bharati Vidyapeeth's College of Engineering, GGSIP University Delhi, New Delhi 110063, India

A. K. Singh · R. Pandey
Department of Physics, Atma Ram Sanatan Dharma College, University of Delhi, New Delhi 110021, India

S. B. Krupanidhi et al. (eds.), *Recent Advances in Functional Materials and Devices*, Springer Proceedings in Materials 37, https://doi.org/10.1007/978-981-99-6766-7_15

above-mentioned materials are utilized as a single or combined form in the fabrication of aluminium-based materials which depend on the requirement of properties for applications [12, 12]. There are many techniques to fabricate the aluminium-based materials, but the spray forming is an interesting technique. Because this technique has the fast deposition and solidification rates of metal, which assists to minimize the segregation & oxide content and also refining the particle size. Additionally, this technique has the ability to produce near-net shape materials [13]. This is a single-step technique in which sequential stages of atomization, droplet consolidation and deposition of liquid metal on a substrate occur in the inert atmosphere. This is also called spray casting, spray processing and spray deposition [15–17]. There are different materials based on aluminium fabricated by spray forming which are used in applications of different sectors [18–23]. Further, these fabricated materials are also employed for tribological applications [22]. Tribology is the study of three things wear, friction and lubrication and depends on many factors, especially the properties of materials, experimental parameters, etc. [24–27]. Therefore, in this chapter, the overview of the tribology of spray-formed aluminum-based materials is discussed in detail with the mechanism taking the different parameters related to the experiment and others.

2 Wear and Friction Behaviour of Aluminium-Based Materials

The wear is the progressive material loss under respective motion of two objects. It is generally represented by cumulative volume loss and wear rate. The wear rate is described as the volume loss per unit sliding distance; however, the volume loss is quantified by Eq. (1) [27].

$$\text{Volume loss} = \frac{\text{Mass loss}}{\text{Density}} \times 1000 \tag{1}$$

The units of volume loss, mass loss and density are millimeter cube (mm^3), gram (g) and gram per centimeter cube (g/cm^3), respectively.

The friction is the opposite force on an object by the other object under relative motion and it is represented by the coefficient of friction described as the force acting on the object per unit applied load as shown in Eq. (2) [7].

$$\text{Coefficient of friction} = \frac{\text{Friction force}}{\text{Applied force}} \tag{2}$$

The coefficient of friction is a number, not having a unit; however, the force and the applied load both have unit of newton (N).

There are different factors that control the wear and friction behavior of spray formed aluminium-based materials.

2.1 Experimental Factors

There are many experimental factors on which wear and friction behavior of spray-formed aluminium-based material affect such as sliding distance, applied load, sliding velocity, etc., however, in the subsections, the influence of sliding distance and applied load has been discussed in detail with responsible mechanisms.

2.1.1 Influence of Sliding Distance

In general, the variation plot of material volume loss with sliding distance consists of two regions, first is running-in wear and second is steady-state wear. Actually, during sliding, the input energy is used in two manners. First is plastic deformation that comes after the elimination of material, and the second is control of the friction force. The friction force is responsible for the generation of heat at the interface. So at the initial stage; the temperature is less and it is assumed that the wear of material occurs mainly by the plastic deformation and the value of it is very high. This is known as running-in wear. As the sliding continues, the temperature is high due to friction resulting the deformation is easy. When the temperature gets constant value via the dissipation of heat through the sample, then in this condition the wear is steady-state wear [28, 29].

The plot of coefficient of friction versus sliding distance indicates the steady state value after an initial high value in the spray-formed aluminium-based material [29]. The initial high coefficient of friction value is owing to the topographical features of the mating surfaces. At peak, there is a high pressure resulting in cold welding of the mating materials and an increase in the coefficient of friction.

Figure 1 shows the alteration of the material loss with sliding distance in the spray-formed aluminium-based material consisting of graphite particles. It clearly shows that the volume loss changes linearly with sliding distance without displaying the high value at the initial stage of sliding distance. The disappearing of the high value of volume loss at the initial siding distance is may be due to the less number of tests [30].

It is also observed from the worn surface analysis of the spray-formed aluminium-based material that at less sliding distance the worn surface indicates shallow grooves with less amount of plastic deformation while at a large sliding distance, the worn surface shows a high amount of plastic deformation with deep grooves and debris particles.

2.1.2 Influence of Load

The load is a key experiment factor influencing the wear rate and coefficient of friction with significant amount. Generally, the wear rate increases with an increasing value of applied load in wear test. This type of nature in wear rate with applied load is also

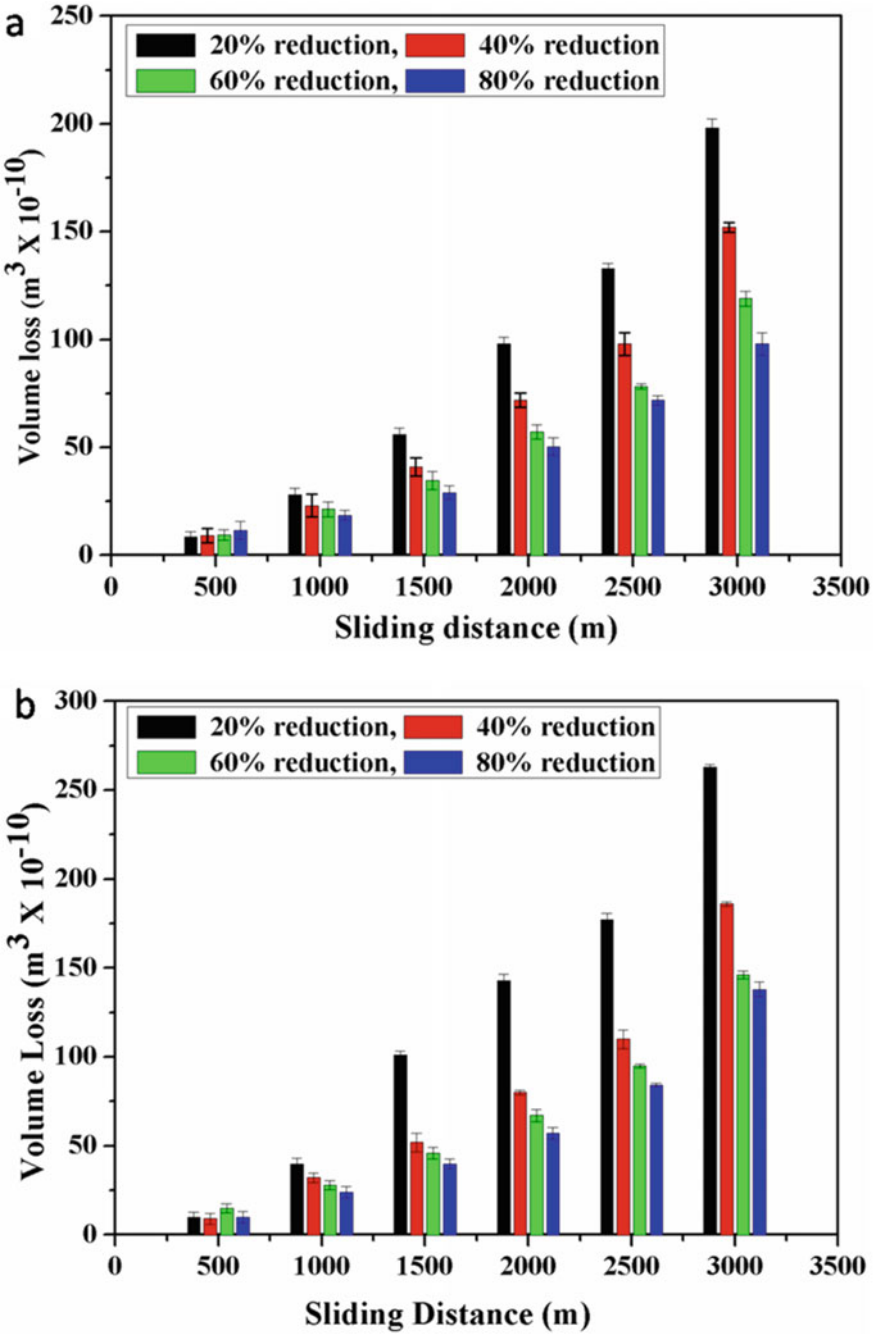

Fig. 1 The volume loss versus sliding distance in spray-formed aluminium-based material having graphite particles at **a** 20 N and **b** 40 N load [30]

observed in spray-formed aluminium-based materials [30]. There are many affecting parameters on which the wear rate and coefficient of friction depend while changing the applied load and that are the actual area of contact, debris particles, etc.

The materials always have a roughness on the surface, which indicates the presence of peaks and valleys. While wear, the actual area of contact between tribo surfaces is different than the apparent area and the value is less. As the applied load increases resulting in increase in the asperity deformation of the surface which enhances the actual area of contact and wear rate rises [31].

The particles present in the aluminium-based material may break under high load condition and rise in wear rate via third body wear [32].

In addition to the above-mentioned mechanism, the temperature at the interface between tribo surfaces can also arise owing to friction and oxide layer may be generated which try to reduce the wear rate of the material at less load condition. That's why at less load, the wear rate is less. However, at high load condition, the situation is different and the wear rate is high due to third body wear originated by the debris particles of broken thick oxide layer. At this time, the wear mechanism laters from mild/oxidative to severe/oxidative-metallic [26].

With the increase in applied load, the characteristics of the worn surfaces also change. At less load situation, the worn surface of the aluminium-based material exhibits mild deformation with the shallow grooves while at high load situation, the worn surface shows a high amount of plastic deformation, deep grooves, cracks and debris particles. The debris particles generated under high load condition shows different morphology with large sizes (Fig. 2). The EDS elemental analysis of these particles indicates that in high load situation, these particles consist of different elements like silicon, oxygen, carbon, aluminium and iron. This indicates the conversion of wear mechanism at high load situation, i.e. severe/oxidation-metallic from mild/oxidative [26].

2.2 Other Factors

2.2.1 Influence of Fabrication Technique

The wear and friction behavior of aluminium-based material is greatly affected by the techniques by which these materials are fabricated. The wear rate is lower in spray-formed materials than the other i.e. stir cast materials [32]. This is because of the improvement in microstructural features and the properties of materials by the spray forming technique.

2.2.2 Influence of Secondary Process

The wear and friction behavior of aluminium-based material is also affected via secondary processes like forging, rolling, etc. Figure 3 shows the influence of

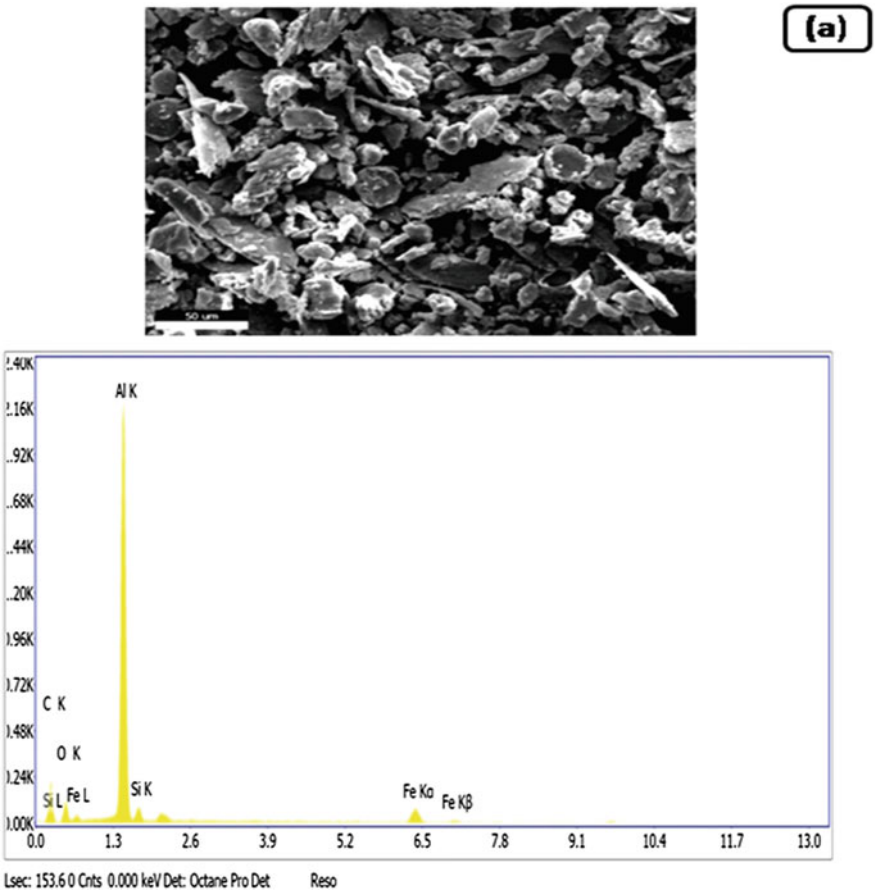

Fig. 2 **a** Debris particles with EDS spectrum and **b** EDS elemental mapping of different elements of spray-formed aluminium-based material having graphite particles [26]

secondary process namely rolling on the wear behaviour in the aluminium-based material [30]. The wear rate reduces as the amount of secondary process, i.e. rolling reduction increases. This is because of the improvement in physical, mechanical properties along with the refinement of the microstructural features.

The variation in mechanical properties with the rolling reduction is shown in Fig. 4 [26]. It clearly shows that the mechanical properties are improved by the increase in rolling reduction and contribute to the reduction of wear rate.

The worn surface features of the materials also change by the secondary process, i.e. rolling as shown in Fig. 5. At the less amount of rolling reduction, the worn surface of aluminium-based material displays a high quantity of plastic distortion, deep grooves, debris particles, and broke oxide layer, however, at the high amount of thickness reduction, the worn surface exhibits the less quantity of distortion, shallow grooves and smooth oxide layer.

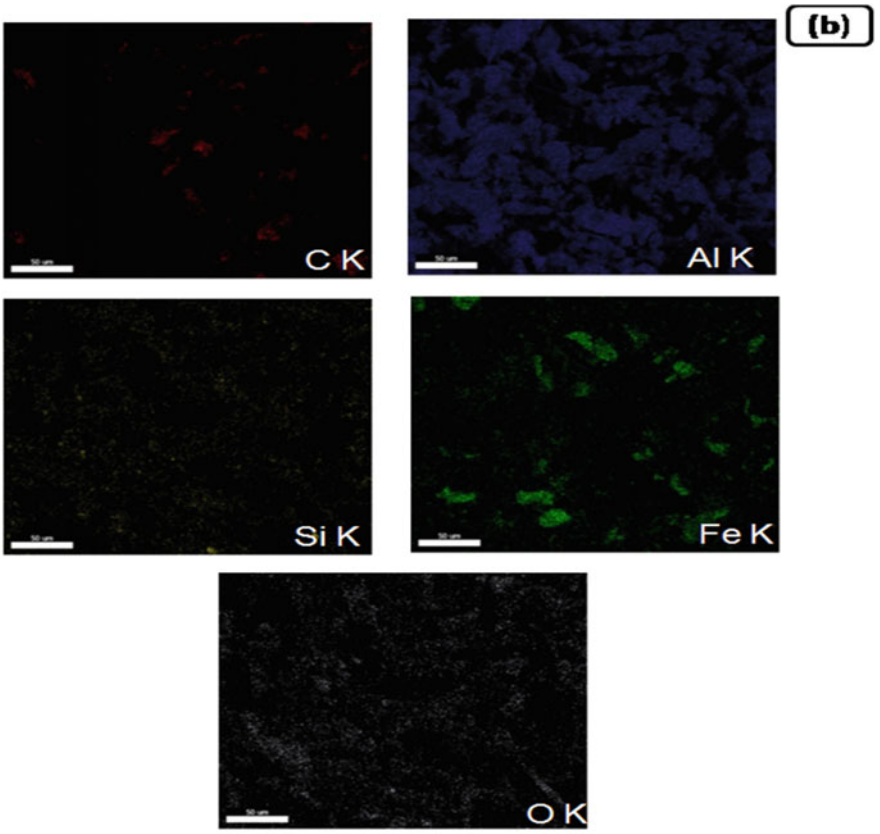

Fig. 2 (continued)

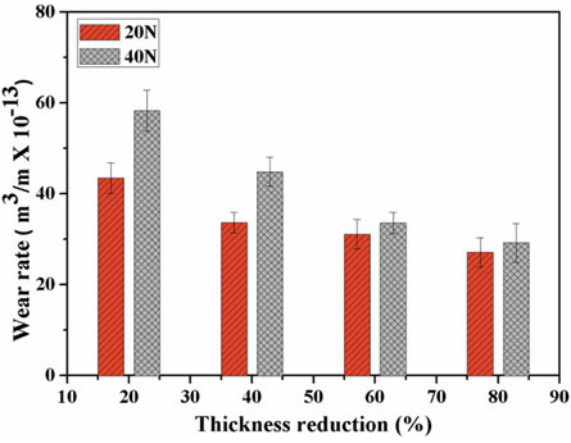

Fig. 3 Effect of secondary process, i.e. rolling thickness reduction (%) on the wear rate in spray-formed aluminium-based material having graphite particles [30]

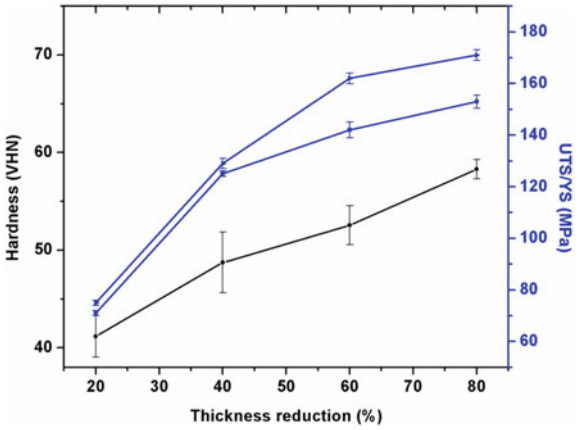

Fig. 4 The variation in mechanical properties with rolling thickness reduction (%) in spray-formed aluminium-based materials having graphite particles [26]

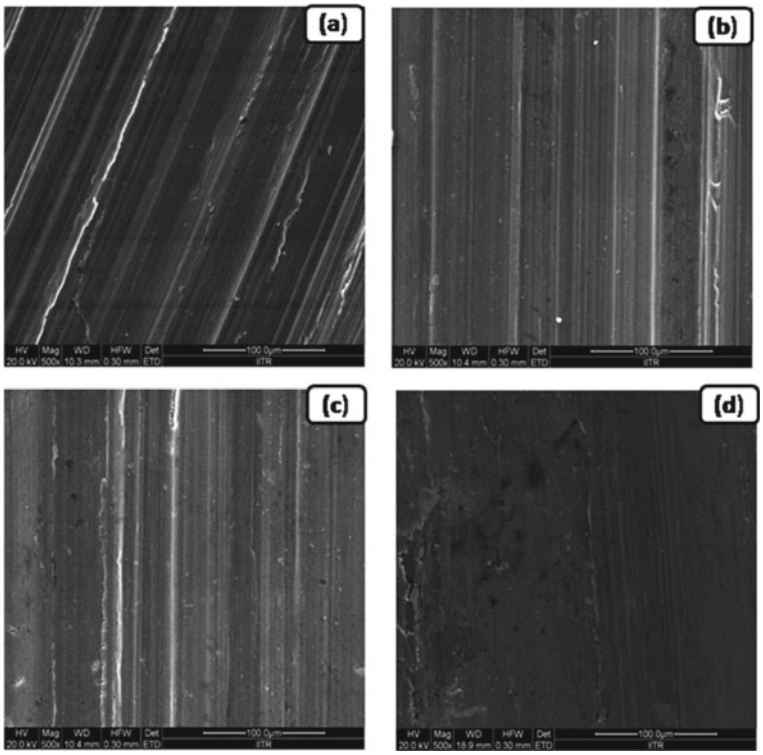

Fig. 5 Worn surface micrographs of spray-formed aluminium-based materials having graphite particles with thickness reduction (%) [26]

3 Summary

This work presents the tribology overview of spray-formed aluminum-based materials in detail with responsible mechanisms taking the different parameters related to the experiment and others. The importance of aluminium-based materials for making the different components of industries and the spray-forming technique is also addressed in detail. The experimental factors namely sliding distance and applied load effecting on wear and friction of spray-formed aluminum-based materials are well considered in detail with mechanisms, worn and debris analysis through different techniques. The other factors like fabrication technique and secondary process affecting the wear and friction are also explained. The wear and friction of the aluminium-based materials can be optimized through the different sets of experiment and other factors.

References

1. Gautam G, Mohan A (2015) Effect of ZrB_2 particles on the microstructure and mechanical properties of hybrid (ZrB_2+Al_3Zr)/AA5052 Insitu composites. J Alloy Compd 649:174–183
2. Kumar N, Gautam G, Gautam RK, Mohan A, Mohan S (2017) A study on mechanical properties and strengthening mechanisms of AA5052/ZrB_2 insitu composite. J Eng Mater Technol Trans ASME. 139: 011002–1–011002–8
3. Gautam G, Kumar N, Mohan A, Gautam RK, Mohan S (2016) Strengthening mechanisms of (Al_3Zr_{mp}+ZrB_{2np})/AA5052 hybrid composites. J Compos Mater 50:4123–4133
4. Gautam M, Gautam G, Mohan A, Mohan S (2019) Enhancing the performance of aluminium by chromium oxide. Materials Research Express. 6:126569
5. Kumar N, Gautam G, Gautam RK, Mohan A, Mohan S (2015) Synthesis and characterization of TiB_2 reinforced aluminium matrix composites: A Review. Journal of the Institution of Engineers (India): Series D. 97: 233–253
6. Mohan S, Gautam G, Kumar N, Gautam RK, Mohan A, Jaiswal AK (2016) Dry sliding wear behavior of Al-SiO_2 composites. Compos Interfaces 23:493–502
7. Gautam G, Kumar N, Mohan A, Gautam RK, Mohan S (2016) High temperature tensile and tribological behavior of hybrid (ZrB_2+Al_3Zr)/AA5052 insitu composite. Metall Mater Trans A 47A:4709–4720
8. Tan H, Wang S, Yu Y, Cheng J, Zhu S, Qiao Z, Yang J (2018) Friction and wear properties of Al-20Si-5Fe-2Ni-Graphite solid-lubricating composite at elevated temperatures. Tribol Int 122:228–235
9. Surappa MK (2003) Aluminium matrix composites: challenges and opportunities. Sadhana 28:319–334
10. Kumar N, Singh SK, Gautam G, Padap AK, Mohan A, Mohan S (2017) Synthesis and statistical modelling of dry sliding wear of Al 8011/6 vol. % AlB2 insitu composite. Materials Research Express. 4: 106514
11. Kumar N, Gautam G, Mohan A, Mohan S (2018) High temperature tensile and strain hardening behaviour of AA5052/9 vol. % ZrB_2 insitu composite. Materials Research. 21: 20170860
12. Gautam G, Ghose AK, Chakrabarty I (2015) Tensile and dry sliding wear behavior of in situ Al_3Zr+Al_2O_3-reinforced aluminum metal matrix composites. Metallurgical and Materials Transactions A. 46A: 5952–5961
13. Mohan A, Gautam G, Kumar N, Mohan S, Gautam RK (2016) Synthesis and tribological properties of AA5052 base insitu composites. Composite Interfaces. 23: 503–518

14. Cui C, Schulz A, Schimanski K, Zoch HW (2009) Spray forming of hypereutectic Al–Si alloys. J Mater Process Technol 209:5220–5228
15. Grant PS (1995) Spray forming. Progess in Materials. Science 39:497–545
16. Rohatgi PK, Ray S, Liu Y (1992) Tribological properties of metal matrix-graphite particle composites. Int Mater Rev 37(129–152):129–152
17. Gouthama R, G.B., Ojha SN (2007) Spray forming and wear characteristics of liquid immiscible alloys. Journal of Materials Processing Technology. 189: 224–230
18. Chourasiya SK, Si A, Singh G, Gautam G, Singh D (2019) A novel technique for automatic quantification of porosities in spray formed warm rolled Al-Si-Graphite composite. Materials Research Express. 6:116565
19. Zhou Y, Jihong LI, Nutt S, Lavernia EJ (2000) Spray forming of ultra-fine SiC particle reinforced 5182 Al-Mg. J Mater Sci 35:4015–4023
20. Bereta LA, Ferrarini CF, Kiminami CS, Botta WJF, Bolfarini C (2007) Microstructure and mechanical properties of spray deposited and extruded/heat treated hypoeutectic Al–Si alloy. Mater Sci Eng, A 448–451:850–853
21. Hariprasad S, Sastry SML, Jerina KL, Lederich RJ (1993) Microstructures and mechanical properties of dispersion-strengthened high-temperature Al-8.5Fe-1.2V-1.7Si alloys produced by atomized melt deposition process. Metallurgical Transaction A. 24: 865–873
22. Wang F, Liu H, Ma Y, Jin Y (2004) Effect of Si content on the dry sliding wear properties of spray-deposited Al-Si alloy. Mater Des 25:163–166
23. Raju K, Ojha SN, Harsha AP (2008) Spray forming of aluminium alloys and its composites: an overview. J Mater Sci 43:2509–2521
24. Gautam G, Kumar N, Mohan A, Mohan S (2018) Tribology of aluminium matrix composites. In: Davim JP (ed) Wear of Composite Materials. Germany, DE Gruyter
25. Sannino AP, Rack HJ (1995) Dry sliding wear of discontinuously reinforced aluminium composites: review and discussion. Wear 189:1–19
26. Mohan A, Gautam G, Kumar N, Mohan S (2020) Sustainable materials for tribological applications. In: Hashmi S, Choudhury IA (eds) Encyclopedia of renewable and sustainable materials. Vol. 1. Oxford: Elsevier
27. Chourasiya SK, Gautam G, Singh D (2019) Mechanical and tribological behavior of warm rolled Al-6Si-3Graphite self lubricating composite synthesized by spray forming process. SILICON 12:831–842
28. Gautam G, Kumar N, Mohan A, Mohan S, Singh D (2019) ZrB_2 nanoparticles transmuting tribological properties of Al_3Zr/AA5052 composite. J Brazilian Soc Mech Sci Eng 41: 469
29. Davis A, Eyre TS (1994) The effect of silicon content and morphology on the wear of aluminium-silicon alloys under dry and lubricated sliding conditions. Tribol Int 27:171–181
30. Anil M, Srivastava VC, Ghosh MK, Ojha SN (2010) Influence of tin content on tribological characteristics of spray formed Al–Si alloys. Wear 268:1250–1256
31. Chourasiya SK, Gautam G, Singh D (2020) Influence of rolling on wear and friction behaviour of spray formed Al alloy composites. Materials Today: Proceedings. https://doi.org/10.1016/j.matpr.2019.12.304
32. Rohatgi PK, Khorshid MT, Omrani E, Lovell MR, Menezea PL (2013) Tribology of metal matrix composites. In: Menezes PL et al (eds) Tribology for scientist and engineers: from basics to advanced concepts. Springer, New York
33. Chaudhury SK, Singh AK, Sivaramakrishnan CS, Panigrahi SC (2005) Wear and friction behavior of spray formed and stir cast Al–2Mg–11TiO_2 composites. Wear 258:759–767

Enhanced Structural and Optical Properties of Pr^{3+}Substituted Gadolinium Garnet Ferrite for Optical Devices Application

Anjori Sharma and Dipesh

1 Introduction

The importance of ferrites is increasing day by day. The reason is its uncountable applications, which increase its demand for new technologies [1–5]. Ferrites are known for excellent magnetic, insulating, structural stability, optical, optoelectrical, and dielectric properties. Due to good properties, ferrites are used in communication device, memory devices, optical storage, microwave absorption, antenna applications, and many more [6–11].

Ferrites are ceramic oxides that are categorized into three types: hexagonal ferrites, garnet ferrites, and spinel ferrites. All the ferrites have their own individual properties. Spinel ferrites and garnet ferrites are cubic in structure. Hexagonal ferrites have hexagonal structure. Garnet ferrites are superior than other ferrites because spinel ferrites are limited in high frequency region. Whereas hexagonal ferrites required higher preparation temperature. Due to very good dielectric, optical, magnetic, thermal, electromagnetic, and low losses [12–15], garnet ferrites are more fascinating nowadays. Garnet ferrites are used in communication devices, microwave devices, optical devices, antennas, optical isolators, and microwave absorption [16, 17]. Factors like sintering temperature, composition, morphology, preparation methods, and other factors affect the properties of ferrites. $R_3Fe_5O_{12}$ is the standard formula for iron garnets, whereby R is rare earth. Garnet ferrites have a cubic crystal structure with the Ia3d space group, and their magnetic characteristics depend on the presence of iron and rare earth cations. In garnet ferrites, there are three sites: dodecahedral site 24c, which is the largest and is occupied by the rare earth ion R^{3+}, octahedral site

A. Sharma (✉)
Department of Physics, Lovely Professional University, Phagwara, Punjab, India
e-mail: anjori.sharma1995@gmail.com

Dipesh
Department of Mathematics, Lovely Professional University, Phagwara, Punjab, India

S. B. Krupanidhi et al. (eds.), *Recent Advances in Functional Materials and Devices*,
Springer Proceedings in Materials 37, https://doi.org/10.1007/978-981-99-6766-7_16

16a, which is occupied by iron ion [Fe^{3+}], and tetrahedral site 24d, which is occupied by iron ion (Fe^{3+}).

Garnet ferrites can be synthesized in a variety of ways. Ball milling is a process that requires a very high temperature; it is extensively utilized, but it has a disadvantage in the form of product inhomogeneity. Many researchers are interested in the hydrothermal technique because it provides a fast rate of heating and efficient reaction kinetics, resulting in a high yield. Another interesting method is the sol—gel method, which provides higher uniformity in the garnet phase due to the rate of mixing, however, this process is limited by the longer time required to dry the gel. Furthermore, the sol—gel auto-combustion method is superior because it solves the problem of gel drying by using a fuel such as citric acid. Substitution can improve the characteristics properties of garnet ferrites. Scandium replacement in the octahedral position increases magnetic properties, while aluminum and gallium substitution in the tetrahedral site decreases it. The use of non-magnetic aluminum instead of magnetic iron ion in YIG alert structural and magnetic properties.

Large number of researches have been carried out on the effect of composition and substitution variation on garnet ferrites. Akhtar et al. [18] have observed that by Cerium (Ce^{3+}) substitution in GdIG, the crystallite size decreases. Yousaf et al. [14] have examined that with substitution of samarium [Sm^{3+}] in YIG the variation in band gap from 1.7 electron Volt to 1.88 electron Volt has been noticed. A. Sharma et al. [19] have examined the influence of substitution of yttrium [Y^{3+}], bismuth [Bi^{3+}], lanthanum [La^{3+}] on GdIG and found that crystallite size varies with substitution. Also, they found that with variation of substitution content, band gap value differs from 3.7 eV to 3.9 eV. M.N. Akhtar [21] has observed that lattice constant does not vary with incorporation of cerium [Ce^{3+}] in GdIG whereas particle size lies between 80–98 nm. M.R. Khalief et al. [20] have examined the influence of Dy^{3+} on Ce^{3+}, Bi^{3+} substitution on YIG. They found that all the prepared samples had impurity of CeO_2.

From the above discussion, it has been found that substitution in garnet ferrites can alert the properties. The motive of this research is to explore the influence of new substitution on GdIG for better structural as well as optical properties. By best of the knowledge no work is done on substitution of praseodymium (Pr^{3+}) in GdIG ($Pr_xGd_{3-x}Fe_5O_{12}$ for x = 0.5, 1.0, and 1.5).

2 Materials and Method

Praseodymium doped Gadolinium iron garnet ($Pr_xGd_{3-x}Fe_5O_{12}$ for x = 0.5, 1.0 and 1.5) was prepared using sol—gel auto-combustion method. Gadolinium (III) nitrate [Gd $(NO_3)_3.6H_2O$], ferric (III) nitrate [Fe $(NO_3)_3.\ 6H_2O$], Praseodymium (III) nitrate [Pr $(NO_3)_3.\ 6H_2O$] and citric acid ($C_6H_8O_7.H_2O$) of AR grade were used as precursors. The precursors were weighed according to stoichiometric formula and added into 100 ml of distilled water. The formation of garnet ferrite according to stoichiometric ratio is mentioned in the equation below:

$$3Gd\,(NO_3)_3 \cdot 6H_2O + 3Fe\,(NO_3)_3 \cdot 6H_2O + x\,Pr_3(NO_3)_3 \cdot 6H_2O \rightarrow Pr_xGd_{3-x}Fe_5O_{12}$$

The solutions were kept for stirring for thirty minutes in order to form clear solution. In order to maintain the pH approximately 7, ammonia solution was added into the solutions with constant stirring. Then the solution kept for stirring and heating until the gel form. After that, heat is increased to $200-250^{\circ}$ C until gel swells up and auto-combustion reactions start. Finally, powders were obtained after proper drying of samples. These obtained samples were finely ground. The obtained powder was sintered in muffle furnace for 6 h at 1200 ° C temperature.

The phase formation in the praseodymium substituted garnet ferrite ($Pr_xGd_{3-x}Fe_5O_{12}$ for x = 0.5, 1.0, and 1.5) was examined with X-ray diffraction (XRD) spectroscopy of Bruker D8 Advance company. The morphological properties were investigated by field emission scanning electron microscope (FESEM) of JEOL JSM-7610F Plus. The optical features were examined with ultra-violet visible spectroscopy (UV—Vis) of Shimadzu UV—vis 1800 spectrophotometer and fluorescence spectroscopy.

3 Results and Discussions

3.1 Structural Analysis

With X-ray diffraction pattern the structural properties of praseodymium substituted gadolinium iron garnet ($Pr_xGd_{3-x}Fe_5O_{12}$ for x = 0.5, 1.0, and 1.5) were evaluated. Figure 1 represents the XRD pattern of $Pr_xGd_{3-x}Fe_5O_{12}$ (x = 0.5,1 .0, 1.5 represented by PrG1, PrG2, and PrG3, respectively). The diffraction patterns of prepared samples concluded that the gadolinium iron garnet (GdIG) phase is dominating over other phases. The obtained results of the samples were further compared with JCPDS no. 72–0141 of pure GdIG. The cubic structure of prepared samples with space group Ia3d has been assured by miller indices values at (321), (400), (420), (422), (521), (532), (444), (640), (642), (800), (840), (842), and (664) [21]. With more addition of Pr in samples, i.e., from x = 0.5 to 1.5 the impurity phase (Fe_2O_3) has been observed. This impurity phase is due to stoichiometric modification in dodecahedral site [22]. Also, the higher intense peak (420) became less sharp with increase in Pr content in samples. This implies that the sample is becoming less crystalline with higher substitution of Pr. The crystallite size for the samples has been calculated using Debye Scherer Method (Eq. 1) [23].

$$D = \frac{k\lambda}{\beta cos\theta} \tag{1}$$

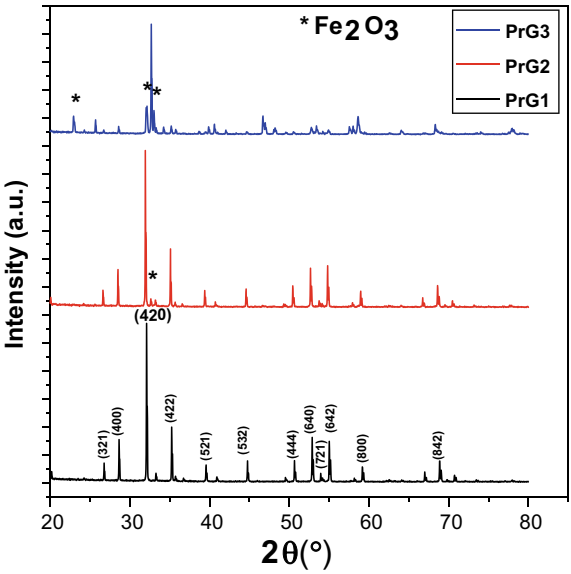

Fig. 1 XRD pattern of PrxGd3-xFe5O12 **a** x = 0.5, **b** 1.0, and **c** 1.5

Here k, λ, β, and θ represent Scherer constant (0.9), X-ray wavelength (0.15406 nm), Full width half maxima (FWHM) and peak position, respectively.

The calculated value of crystallite size "D," lattice constant "a," microstrain "ε" and dislocation density "δ" is tabulated in Table 1. It has been examined that the crystallite size decreases with increase in Pr substitution. The variation in crystallite size with substitution is due to presence of impurities. These impurities further affect the growth of crystal [24]. Second reason of variation can be stress and strain due to Pr substitution which produces defect in lattice [21].

The morphology of Pr substituted samples was examined by the micrographs obtained from FESEM. Figure 2a–c represents the micrographs of the sample PrG1, PrG2, and PrG3. From the deep analysis of micrographs, it can be concluded that all the samples contain spherically shaped grains which is in accordance with literature

Table 1 Calculated values of structural parameters: 2 θ, β, D, a, ε, δ for prepared compositions

Sample	Sample code	2θ(°)	β	hkl	D(nm)	a (Å)	ε (10^{-3})	δ (nm^{-2})
$Pr_xGd_{3-x}Fe_5O_{12}$ (x = 0.5)	PrG1	32.12	0.15	420	52.8	12.45	2.7	0.35
$Pr_xGd_{3-x}Fe_5O_{12}$ (x = 1.0)	PrG2	31.90	0.17	420	46.6	12.51	2.6	0.46
$Pr_xGd_{3-x}Fe_5O_{12}$ (x = 1.5)	PrG3	32.70	0.18	420	44.1	12.23	2.8	0.51

[21]. With increase in Pr^{3+}substitution, agglomeration has been observed. Figure 2a–c represents size distribution histogram of the samples. The large number of grains are obtained at 0.71 μm, 1.1 μm, 77 nm for PrG1, PrG2, and PrG3 sample, respectively.

Line intercept method (Eq. 2) [25] was used to calculate the grain size and tabulated in Table 2.

$$grain\ size = \frac{1.5L}{mn} \tag{2}$$

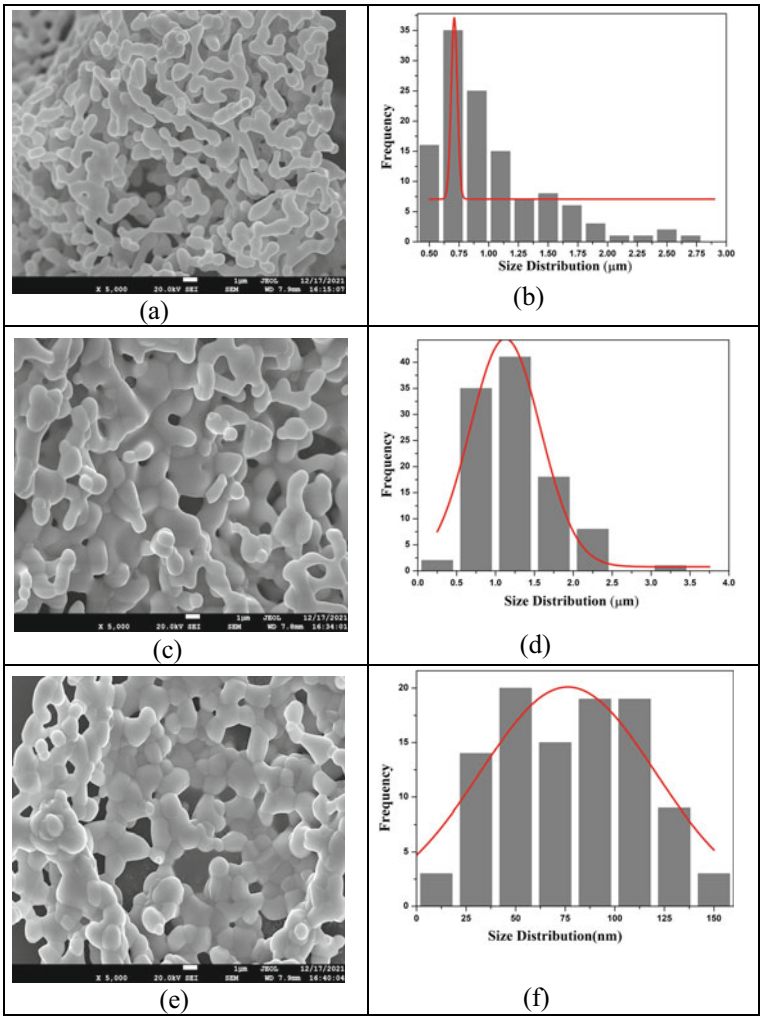

Fig. 2 Micrographs of samples **a** PrG1, **c** PrG2, **e** PrG3 and Gaussian fitted histograms (**b**) PrG1 **b** PrG2 **f** PrG3

Table 2 Calculated grain size of **a** PrG1, **b** PrG2, **c** PrG3

Sample	Grain size (μm)
PrG3	0.308
PrG1	0.271
PrG2	0.401

Here L, m, n represent the line length, magnification mentioned in micrographs, number of grain's intersepts respectively.

The ionic radii of substituted element, temperature, porosity, and method of preparations affect the grain size of the samples [28].

Optical Properties Analysis

The optical properties of the materials depend upon many factors but energy band gap (Eg) and absorption coefficient (α) are very crucial features. These features decide the importance of ferrites for optoelectronic devices. UV—Vis spectroscopy was used to study optical property of $Pr_xGd_{3-x}Fe_5O_{12}$. Figure 3 represents the absorption versus wavelength graph for samples PrG1, PrG2, and PrG3. The absorbance in all samples has been observed up to 280 nm, after that samples show transmittance. A shift in absorbance has been noticed with a change in composition from x = 0.5 to 1.5. The absorbance in the materials depends upon factors like energy band and uneven surface [26]. Figure 4a–c represents $(\alpha h\nu)^2$ versus $(h\nu)$ graphs which are plotted to calculate band gap of the samples. It has been observed that band gap of sample $Pr_xGd_{3-x}Fe_5O_{12}$ first decreases from 4.6 eV to 4.5 eV for x = 0.5 to 1.0. After that, the band gap increases from 4.5 eV to 4.7 eV. The change in bandgap depends upon several factors like crystallite size, impurity, concentration of substituents, and morphology [27].

In order to study the luminescence property and to analyze the energy band gap with related to most strong position of sub band gap fluorescence spectroscopy was studied. Figure 5 represents the fluorescence spectroscopy of $Pr_xGd_{3-x}Fe_5O_{12}$ sample. The excitation wavelength is around 270 nm which is chosen from the obtained UV spectroscopy. At this excitation wavelength it has been observed that

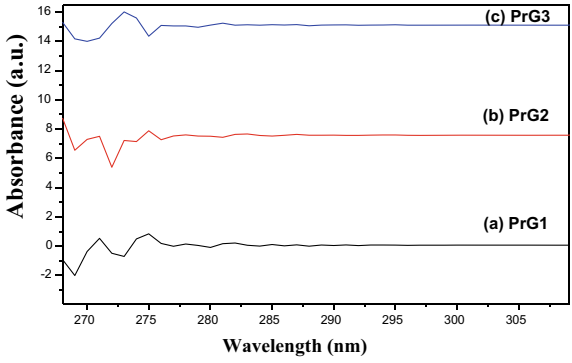

Fig. 3 Absorbance versus wavelength spectra of PrxGd3-xFe5O12 **a** PrG1 **b** PrG2 and **c** PrG3

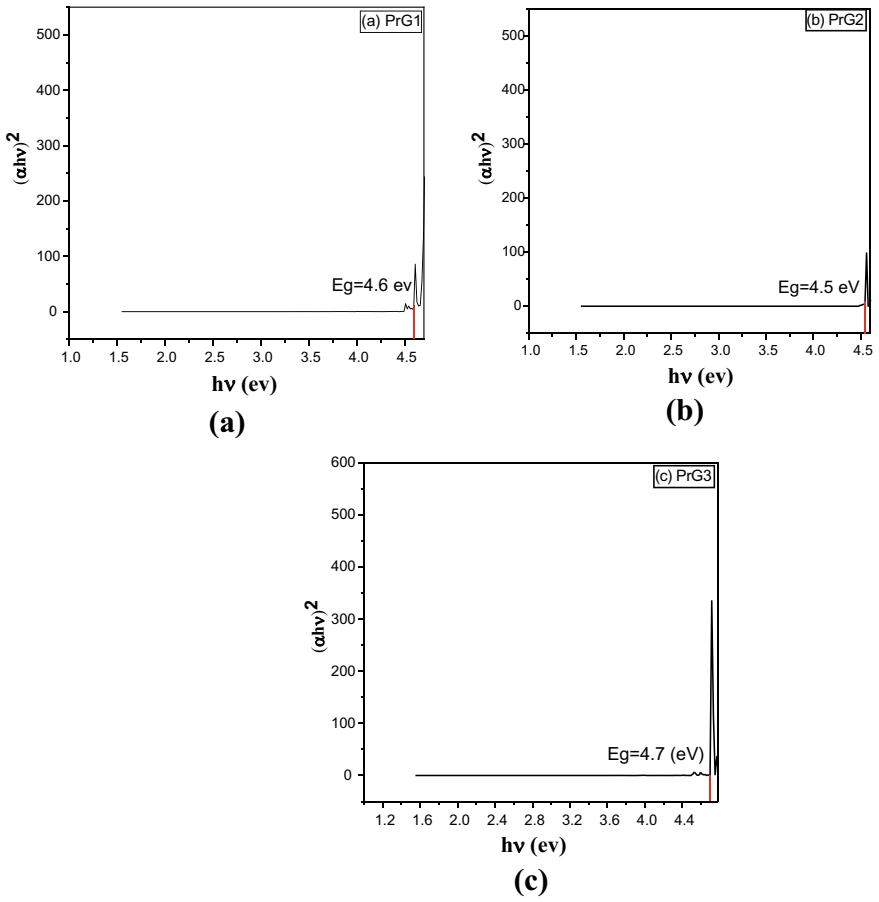

Fig. 4 Calculated band gap of PrxGd3-xFe5O12 **a** PrG1 **b** PrG2 and **c** PrG3

all three samples emit red color, i.e., at 650 nm region. The reason of such emission is presence of nitrates group in prepared samples [26]. A shift has been observed with increases in Pr concentration in $Pr_xGd_{3-x}Fe_5O_{12}$. The intensity of the sample increases with increase in Pr concentration. The reason of increase in fluorescent intensity is because of increase in distance between GdIG and dopant (Pr) [28]. This implies that increases in concentration of dopant increase the emission property. Such properties of $Pr_xGd_{3-x}Fe_5O_{12}$ make it suitable to be used in optical storage and optical devices.

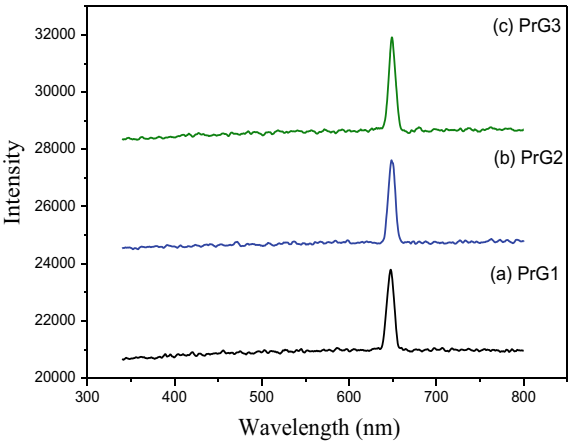

Fig. 5 Fluorescence emission spectra of PrxGd3-xFe5O12 **a** PrG1 **b** PrG2 and **c** PrG3

4 Conclusion

Sol—gel auto-combustion process was carried out to prepare $Pr_xGd_{3-x}Fe_5O_{12}$ for x = 0.5,1.0 and 1.5. XRD confirms the formation of garnet phase in Pr substituted GdIG. It has been observed that with increase in Pr content in garnet ferrite impurity phases were formed. Crystallite size, lattice constant, microstrain and dislocation density also vary with change in Pr content. From FESEM it has been observed that maximum number of grains lies in 0.71 μm, 1.1 μm, 77 nm for x = 0.5, 1.0, and 1.5 sample respectively. The bandgap evaluated from UV—Vis spectra was found in 4.5 eV to 4.7 eV range. From fluorescence spectroscopy it has been found that with increases in concentration of dopant, emission property enhanced.

References

1. Tatarchuk T, Naushad M, Tomaszewska J, Kosobucki P, Myslin M, Vasylyeva H, Ścigalski P (2020) Adsorption of Sr (II) ions and salicylic acid onto magnetic magnesium-zinc ferrites: isotherms and kinetic studies. Environ Sci Pollution Res 27(21):26681–26693
2. Tatarchuk T, Shyichuk A, Sojka Z, Gryboś J, Naushad M, Kotsyubynsky V, Kowalska M, Kwiatkowska-Marks S, Danyliuk N (2021) Green synthesis, structure, cations distribution and bonding characteristics of superparamagnetic cobalt-zinc ferrites nanoparticles for Pb (II) adsorption and magnetic hyperthermia applications. J Molecular Liquids 328:115375
3. Tatarchuk T, Myslin M, Lapchuk I, Shyichuk A, Murthy AP, Gargula R, Kurzydło P, Bogacz BF, Pędziwiatr AT (2021) Magnesium-zinc ferrites as magnetic adsorbents for Cr (VI) and Ni (II) ions removal: cation distribution and antistructure modeling. Chemosphere 270:129414
4. Kozlovskiy AL, Kenzhina IE, Zdorovets MV (2020) FeCo–Fe2CoO4/Co3O4 nanocomposites: Phase transformations as a result of thermal annealing and practical application in catalysis. Ceram Int 46(8):10262–10269
5. Zdorovets MV, Kozlovskiy AL (2020) Study of phase transformations in Co/CoCo2O4 nanowires. J Alloy Compd 815:152450

6. Akhtar MN, Khan MA, Ahmad M, Nazir MS, Imran M, Ali A, Sattar A, Murtaza G (2017) Evaluation of structural, morphological and magnetic properties of CuZnNi (CuxZn0. 5− xNi0. 5Fe2O4) nanocrystalline ferrites for core, switching and MLCI's applications. J Magnet Magnetic Mater 421:260–268
7. Rubinger CPL, Gouveia DX, Nunes JF, Salgueiro CCM, Paiva JAC, Graça MPF, Andre P, Costa LC (2007) Microwave dielectric properties of NiFe2O4 nanoparticles ferrites. Microw Opt Technol Lett 49(6):1341–1343
8. Ravinder D, Reddy P, Shalini P (2003) Frequency and composition dependence of dielectric behavior of copper substituted lithium ferrites. J Mater Sci Lett 22(22):1599–1601
9. Chen W, Dongsheng L, Wenwei W, Huaxin Z, Juan W (2017) Structure and magnetic properties evolution of rod-like Co0. 5Ni0. 25Zn0. 25DyxFe2− xO4 synthesized by solvothermal method. J Magnet Magnetic Mater 422:49–56
10. Jia Z, Misra RDK (2011) Magnetic sensors for data storage: perspective and future outlook. Mater Technol 26(4):191–199
11. Seongatae B, Won LS, Hirukawa A, Takemura Y, Youn J, Haeng GLS (2009) AC magnetic-field-induced healing and physical properties of ferrite nanocomposites for a hyperthermia agent in medicine. IEEE Transactions Nanotechnology 8:86–94
12. Sattar AA, Elsayed HM, Faramawy AM (2016) Comparative study of structure and magnetic properties of micro-and nano-sized GdxY3− xFe5O12 garnet. J Magn Magn Mater 412:172–180
13. Arun T, Vairavel M, Raj SG, Joseyphus RJ (2012) Crystallization kinetics of Nd-substituted yttrium iron garnet prepared through sol–gel auto-combustion method. Ceram Int 38(3):2369–2373
14. Yousaf M, Noor A, Xu S, Akhtar MN, Wang B (2020) Magnetic characteristics and optical band alignments of rare earth (Sm+ 3, Nd+ 3) doped garnet ferrite nanoparticles (NPs). Ceramics International 46(10):16524–16532
15. Praveena K, Srinath S (2014) Effect of Gd3+ on dielectric and magnetic properties of Y3Fe5O12. J Magn Magn Mater 349:45–50
16. Akhtar MN, Sulong AB, Ahmad M, Khan MA, Ali A, Islam MU (2016) Impacts of Gd–Ce on the structural, morphological and magnetic properties of garnet nanocrystalline ferrites synthesized via sol–gel route. J Alloy Compd 660:486–495
17. Kidoh H, Morimoto A, Shimizu T (1991) Synthesis of ferromagnetic Bi-substituted yttrium iron garnet films by laser ablation. Applied physics letters 59(2):237–239
18. Akhtar MN, Kashif A, Umer A, Ahmad T, Khan MA (2018) Structural elucidation, and morphological and magnetic behavior evaluations, of low-temperature sintered, Ce-doped, nanostructured garnet ferrites. Mater Res Bull 101:48–55
19. Sharma A, Godara SK, Srivastava AK (2021) Effect of Y3+, Bi3+, La3+ substitution on structural, optical and magnetic properties of gadolinium iron garnets. Materials Today: Proceedings
21. Akhtar MA, Sulong AB, Ahmad M, Khan MA, Ali A, Islam MU (2016) Impacts of Gd–Ce on the structural, morphological and magnetic properties of garnet nanocrystalline ferrites synthesized via sol–gel route. Journal of Alloys and Compounds 660:486–495
20. Khalifeh MR, Shokrollahi H, Arab SM, Yang H (2020) The role of Dy incorporation in the magnetic behavior and structural characterization of synthetic Ce, Bi-substituted yttrium iron garnet. Mater Chem Phys 247:122838
21. Mohaidat QI, Lataifeh M, Hamasha K, Mahmood SH, Bsoul I, Awawdeh M (2018) The structural and the magnetic properties of aluminum substituted yttrium iron garnet. Materials Research 21.
22. Sharma A, Godara SK, Maji PK, Srivastava AK (2021) Influence of Temperature on Structural and Magnetic Properties of Gd3AlxFe5− xO12 (x= 2). Crystal Research and Technology 2100109
23. Sharma A, Mahajan M, Mohammed I, Sinha S, Godara SK, Srivastava AK (2023) Effect of Sintering Temperature on the Structural, Dielectric, and Magnetic Properties of Garnet-Spinel Ferrite Composites for Use in L-Band Devices. Materials Performance and Characterization 12(1):64–78

24. Basavad M, Shokrollahi H, Ahmadvand H, Arab SM (2020) Structural, magnetic and magneto-optical properties of the bulk and thin film synthesized cerium-and praseodymium-doped yttrium iron garnet. Ceram Int 46(8):12015–12022
25. Sharma A, Mohammed I, Godara SK, Srivastava AK (2022) Low dielectric losses and enhanced magnetic property of ErIG (x)/YIG (1− x) (x= 0.5) composite for antenna applications. Bulletin of Materials Science 45(4): 248
28. Yousaf M, Noor A, Xu S, Akhtar MN, Wang B (2020) Magnetic characteristics and optical band alignments of rare earth (Sm+ 3, Nd+ 3) doped garnet ferrite nanoparticles (NPs). Ceramics International 46(10): 16524–16532
26. Chavan P (2021) Facile Synthesis, Diffused Reflectance Spectroscopy & Fluorescence Studies of Ni0. 5− xMg0. 5CuxFe2O4 Nanoparticles. Journal of Fluorescence 31(4):1023–1028
27. Chavan P, Naik LN, Belavi PB, Chavan GN, Kotnala RK (2017) Synthesis of Bi3+ substituted Ni-Cu ferrites and study of structural, electrical and magnetic properties. Journal of Alloys and Compounds 694:607–612
28. Talukdar S, Rakshit R, Krämer A, Müller FA, Mandal K (2018) Facile surface modification of nickel ferrite nanoparticles for inherent multiple fluorescence and catalytic activities. RSC advances 8(1):38–43

Investigation on Structural, Dielectric and Ferromagnetic Properties of Yttrium Doped Nickel Ferrites ($NiY_{0.05}Fe_{1.95}O_4$) Prepared by Modified Sol–gel Route

Nisha Yadav, Prachi Jain, and O. P. Thakur

1 Introduction

Magnetic nanoparticles have currently become the hottest topic to discuss among the researchers because of their extremely good physical and chemical properties. Among them, nickel ferrite comes under the category of soft spinel ferrites having some Fe^{3+} ions occupying the tetrahedral or A sites of the inverse spinel structure, while some Ni^{2+} ions and few Fe^{3+} ions occupy the octahedral or B sites [1]. Nickel ferrites nanoparticles find suitable for their applications in gas sensing and humidity sensing, dye degradation, MERAM and RERAMs, switching device applications, electronic, electrical and catalytic applications [2]. They come under the category of multiferroics because they are capable enough to exhibit more than two ferroic orderings at the same time. It can also exhibit M-E coupling effect in which electric field can be varied by magnetic field or vice-versa [3]. Also, nickel ferrites have low eddy current loss, high expansion coefficient, low saturation magnetic moment, high electrical resistivity and high chemical as well as electrical stability [4]. The multiferroics can be used to study the various applications performed in day-to-day life. Nickel ferrites are utilized as good core materials for power transformers in electronics and telecommunication because they have high electrical resistivity and low coercivity [5]. The 4f orbital of rare earth elements interacts with transition metal 3d electrons while being filtered by the 5 s and 5p orbitals. The reported electrical and magnetic properties of spinel ferrites are considerably impacted by the addition of rare-earth elements. The reason behind the doping of yttrium is to increase the porosity in the sample so that the material can be suggested to show good water sensing properties. Yttrium has been chosen as a dopant because it has the capability

N. Yadav · P. Jain · O. P. Thakur (✉)
Materials Analysis and Research Laboratory, Department of Physics, Netaji Subhas University of Technology, Dwarka, New Delhi 110078, India
e-mail: opthakur@nsut.ac.in

S. B. Krupanidhi et al. (eds.), *Recent Advances in Functional Materials and Devices*, Springer Proceedings in Materials 37, https://doi.org/10.1007/978-981-99-6766-7_17

to reduce the coercivity of the pure nickel ferrite by decreasing its saturation magnetization. Less coercivity can be useful in many applications like fabricating soft core of transforms, high storage density recorders, etc. [6]. Thus this material can be suggested for many useful future applications and so we have fabricated the Y-doped cobalt ferrite nanoparticles having particle size <40 nm using sol–gel cost-effective auto combustion route.

2 Experimental Procedure

Yttrium doped $NiFe_2O_4$, ($NiY_xFe_{2-x}O_4$ where x = 0.05) nanoparticles (NPs) were synthesized using modified auto-combustion sol–gel method. Ferric Nitrate (99% purity, Loba Chemie) Yttrium(III) nitrate hexahydrate (99% purity, Sigma-Aldrich) and Nickel(II) Nitrate hexahydrate (98% purity, Loba Chemie) were mixed in stoichiometric ratio in distilled water separately using a magnetic stirrer for 30 min each. Then citric acid with ethylene glycol as a chelating agent in a ratio of 3:7 was added. With continuous 3 h of heating and stirring leads to formation of viscous YNFO gel. This formed YNFO gel is again heated to 200 °C until formation of dry brown powder takes place. The obtained powder was then grounded using pestle mortar for 10 min to form fine YNFO sample. This sample is then sintered at 700 °C for 5 h with the rise of 5°C/min in a muffle furnace and then circular pellets of diameter 10 mm were formed and characterization was done further to investigate its properties.

3 Results and Discussion

3.1 Structural Analysis

The inset of Fig. 1 shows the XRD pattern of the yttrium doped nickel ferrite ($NiY_xFe_{2-x}O_4$ where x = 0.05) prepared by using sol–gel citrate method. All the peaks were correctly indexed using JCPDS card number # 074–2081. The nanocrystalline nature has been confirmed from the sharpened peaks as depicted by Fig. 1a while Fig. 1b shows that crystallite size varies linearly with the Bragg's diffraction angles. Using the Debye–Scherrer equation, the sample's crystallite size was determined to be around 15.4229 nm.

$$D = k\lambda/\beta Cos\theta \tag{1}$$

where K is the Scherrer constant, D is the crystallite size, FWHM is the full-width half maxima (FWHM), θ is the Bragg's diffraction angle, and λ is the wavelength of Cu–kα radiations.

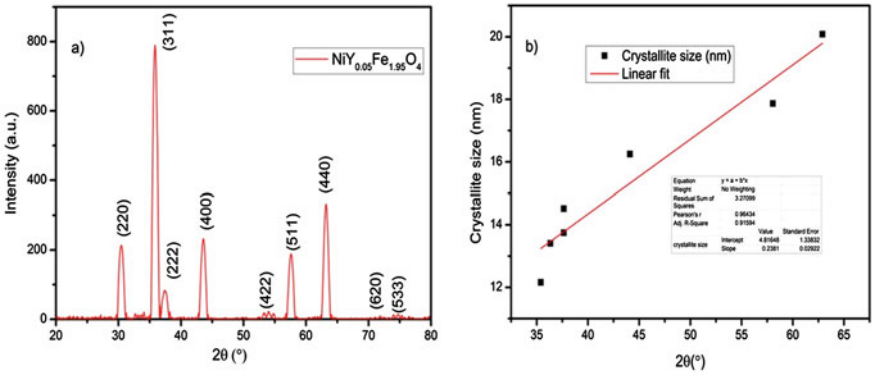

Fig.1 **a** X-Ray diffraction patterns of yttrium doped nickel ferrites, **b** Crystallite size vs bragg's angle

3.2 Morphological Analysis

FESEM (Field Emission Scanning electron microscopy) images have been obtained using Zeiss instrument as shown in Fig. 3a, b respectively. The grain size of the prepared samples have been calculated using ImageJ software and it comes around 34 nm. The particles obtained are circular in shape with huge amount of porosity can be observed. Also, with doping of yttrium in nickel ferrite, the particle size has also increased to ±20% ($NiY_{0.05}Fe_{1.95}O_4$) (Fig. 2).

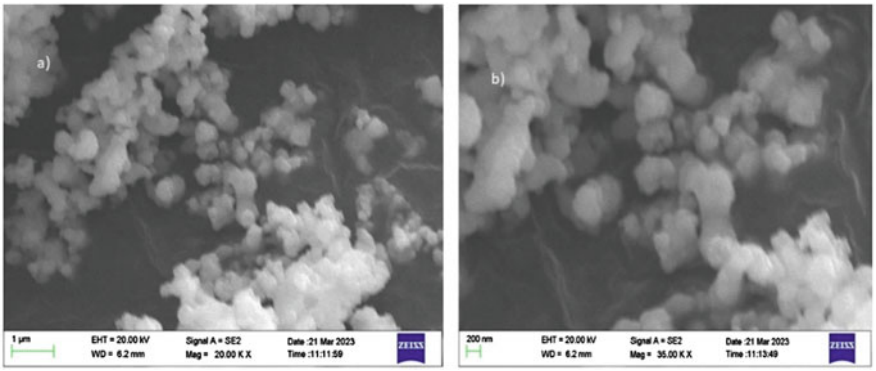

Fig. 2 **a** FESEM image of Yttrium doped nickel ferrites nanoparticles

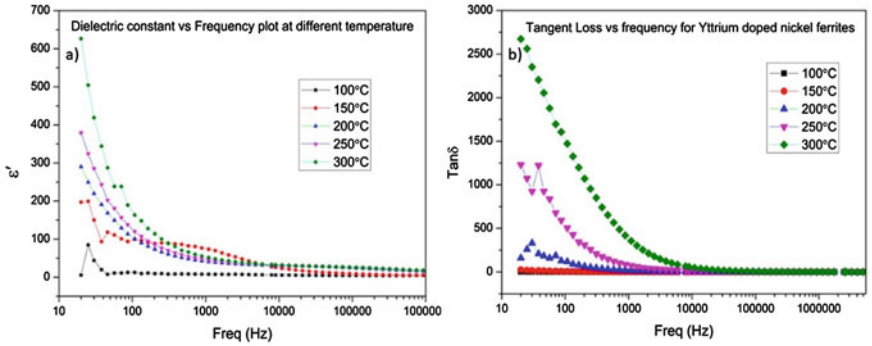

Fig. 3 **a** ε' against frequency at room temperature for yttrium doped nickel ferrite pellets sintered at 800 °C **b** and tangent loss with frequency from 10 Hz to 1 MHz

3.3 Dielectric Properties

The inset of Fig. 3 shows the two plots where Fig. 3a exhibits the plot of ε' (dielectric permittivity) against frequency from 10 Hz to 1 MHz at room temperature (RT) while Fig. 3b shows the tangent loss with frequency at different temperature ranging from 100 °C till 300 °C. The Fig. 3a plot indicates that ε' decreases with increase in frequency or we can say dielectric constant is higher at lower frequency and dielectric constant declines at higher frequency. The presence of dipolar relaxation processes is described by the significant step-like decreasing behaviour of dielectric constant with frequency. Figure 3b plot shows that the loss tangent is rising with the rise in temperature and lowers as the frequency range widens. The loss tangent's essentially insignificant value at higher frequency range suggests their use in high density storage device application [7].

3.4 Ferromagnetic Properties

The ferromagnetic properties in the prepared sample have been measured using VSM (vibrating spin magnetometer) which gives the variation of magnetization with the applied field as shown in Fig. 4. The M–H loop of yttrium doped nickel ferrite has very less coercivity which makes it useful for recording device, transformer cores and magnetic shielding device applications [8]. Also, the high value of saturation magnetization is also observed upon the yttrium doping. Very less value of coercivity has shown that prepared material perceives a soft magnets type nature which means that the magnetic characteristics of nickel ferrites doped with yttrium will be simpler to manage.

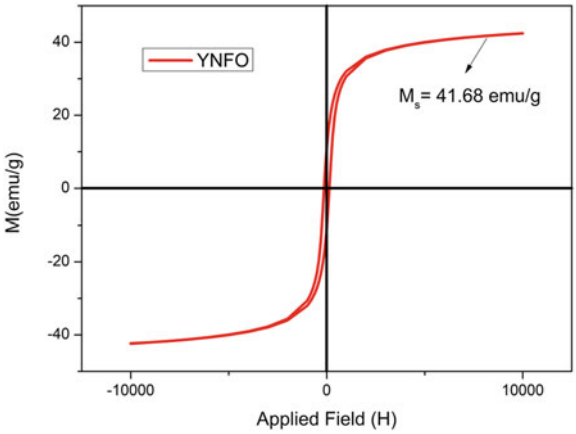

Fig. 4 M–H loop for yttrium doped nickel ferrite nanoparticles at RT

4 Conclusion

The yttrium-doped nickel ferrites ($NiY_{0.05}Fe_{1.95}O_4$) effectively prepared using the affordable sol–gel auto-combustion technique. The XRD, FESEM, Dielectric and VSM analysis has been done to check the structural, dielectric and ferromagnetic properties of the material respectively. Very fine-sized nanoparticles (15 nm) have been prepared using this synthesis technique. The FESEM images show the spherical shape particles of Y^{3+} doped nickel ferrites. The dielectric constant and tangent loss have been increased with the rise in temperature. The soft magnetic nature of nickel ferrites has been confirmed by the VSM analysis. Due to the porous nature, the material can be very useful for studying humidity sensors and hydroelectric cell applications.

References

1. Jankov S, Armaković S, Tóth E, Skuban S, Srdic V, Cvejic Z (2019) Understanding how yttrium doping influences the properties of nickel ferrite–combined experimental and computational study. Ceram Int 45(16):20290–20296
2. Sinha A, Dutta A (2020) Structural, optical, and electrical transport properties of some rare-earth-doped nickel ferrites: A study on effect of ionic radii of dopants. J Phys Chem Solids 145:109534
3. Gatelytė A, Jasaitis D, Beganskienė A, Kareiva A (2011) Sol-gel synthesis and characterization of selected transition metal nano-ferrites. Mater Sci 17(3):302–307
4. Stojanović G, Srdić V, Maletin M (2008) Electrical properties of yttrium-doped Zn and Ni–Zn ferrites. Physica Status Solidi (a) 205(10):2464–2468
5. Sileo EE, Jacobo SE (2004) Gadolinium–nickel ferrites prepared from metal citrates precursors. Physica B 354(1–4):241–245
6. Khan AA, Khan SN, Mir A (2022) Structural and electromagnetic characterization of yttrium doped copper ferrite. J Magn Magn Mater 559:169510

7. Ahmad U, Afzia M, Shah F, Ismail B, Rahim A, Khan RA (2022) Improved magnetic and electrical properties of transition metal doped nickel spinel ferrite nanoparticles for prospective applications. Mater Sci Semicond Process 148:106830
8. Yousuf MA, Jabeen S, Shahi MN, Khan MA, Shakir I, Warsi MF (2020) Magnetic and electrical properties of yttrium substituted manganese ferrite nanoparticles prepared via micro-emulsion route. Results Phys 16:102973

Thermoelectric and Optical Properties of Half–Heusler Compounds RbYX (X = Si, Ge): a First Principle Study

Dinesh Kumar and Prakash Chand

1 Introduction

The research scholars and technologist have concentrated their efforts recently on studying the intelligent and multifunctional compounds that can be utilized for various applications, including robotics, sensors, optoelectronics, solar and photovoltaic, thermoelectric, spintronics, and other sustainable and clean energy applications [1–4]. It is very concerning that the world climate is at risk as a result of steadily rising carbon emissions and other dangerous pollutants. There is a need to stop the destruction of our environment and for that, the search for clean and environmentally friendly sustainable energy sources like thermoelectric power, solar radiation power, and wind power has increased in the last decade. In contrast to the use of dissipated energy, the large amount of solar energy that the sun continuously emits can be captured and turned into appropriate electrical energy for mankind by using photovoltaics. A number of distinct kinds of substances, including chalcogenides, hybrid and oxide-perovskites, organic substances, and half-Heusler alloys have been investigated as promising solar and thermoelectric materials [5–10]. The majority of researchers and scientists have drawn their attraction toward half-Heusler materials due to their excellent optoelectronics and thermoelectric applications. Apart from this, these materials can be used for spintronics, laser diodes, alternates for electrodes of batteries, superconducting materials [11–18]. Fredrich Heusler, a German mining engineer and chemist, discovered Heusler alloys in 1903, which led to the development of the Heusler materials family [19]. The space group for the half-Heusler compounds is F–43 m and can be categorized in two groups on the basis

D. Kumar · P. Chand (✉)
Department of Physics NIT, Kurukshetra 136119, India
e-mail: prakash@nitkkr.ac.in

D. Kumar
Department of Applied Sciences and Humanities, PIET, Samalkha, Panipat 132102, India

S. B. Krupanidhi et al. (eds.), *Recent Advances in Functional Materials and Devices*,
Springer Proceedings in Materials 37, https://doi.org/10.1007/978-981-99-6766-7_18

of 8 valence electron valence count (VEC) and 18 VEC. The thermoelectric performance and efficiency of the devices can be determined using dimensionless figure of merit (ZT). Further, the ZT can be calculated in terms of S^2 (Seeback coefficient), σ (electrical conductivity), absolute temperature (T), and the thermal conductivity (κ) that is given by $ZT = S^2\sigma T/\kappa_{total}$. Consequently, substances with poor thermal conductivity and high power factors ($S^2\,\sigma$) can act as promising candidates. for future thermoelectric devices [20]. Since Zerrouki et al. [21] discovered that Nb-based Co, Sn, Fe, Sb half-Heusler alloys are mechanically stable, anisotropic in nature, and brittle in opposition to elastic deformation, they hypothesized that these alloys could make potential thermoelectric and photovoltaic candidates. Mostari et al. [22] were studied the mechanical properties of RUVAs alloy with varying pressure and found that the material is stable below pressure 40 GPa and above becomes unstable. This is due to the phase transition. Sahni et al. [23] have investigated 8-electron (I–II–V) half–Heusler (h–H) substances that may be suitable for thermoelectric, solar, and topological insulator applications through organized simulations. Previously various physical properties of RbSrX (X = C, Si, Ge) are studied, and found that the considered alloys are mechanically stable [24]. The literature research leads to the conclusion that there has not been much research done on the optical and thermoelectric characteristics of newly discovered materials. Therefore, it encourages us to study the elastic, optical, and thermoelectric characteristics of RbYX (X = Si, Ge) having 8 VEC. These properties have not yet been studied to the best of our understanding.

2 Methodology

To examine the thermoelectric and optical characteristics of RbYX (X = Si, Ge), we used the WIEN2K—simulation tool and full potential—LAPW technique [25, 26]. The density functional theory (DFT) with GGA-PBE exchange potential is used to study these properties. The extension of the electronic wave function takes into account the number of valence electrons. To analyze the electronic properties, density functional theory (DFT) with method is used. A $10 \times 10 \times 10$ k-point mesh is employed for the electronic study of the compound. The cut-off energy of -6.0 Ry, RMTKMax of 7, and k-points of 1000 are used in this study in the first Brillouin zone. The k-mesh of $18 \times 18 \times 18$ was used for 6000 k-points for the optical and DOS properties of the compounds. The BoltzTraP2 method is utilized to calculate the thermoelectric properties. The properties like electrical conductivity (σ), Seebeck coefficient (S), and thermal conductivity (κ) were studied using a dense k-point mesh. To find Kohn–Sham equations, the WIEN2k algorithm uses the full potential-LAPW method [27]. The extended wave function that we employed in the present study is given as:

$$\psi_G^k(r) = \begin{cases} \frac{1}{\sqrt{V}} e^{i(k+G)r} \text{interstitial region} \\ \sum_{l,m} \left(A_{lm}^{\alpha,k+G} u_l^{\alpha}(r, E_o) \right) + B_{lm}^{\alpha,k+G} \text{inside muffin} - \text{tin} \\ \dot{u}_l^{\alpha}(r, Eo) Y_m^l(r) \end{cases} \quad (1)$$

3 Results and Discussions

Initially, the lattice parameters (in angstrom) were determined. We compute the total energy for the aforementioned compounds with a half–Heusler structure calculated as a function of the lattice constant. By minimizing the total energy, the constants for the equilibrium lattice were discovered.

3.1 Structural Properties

We have optimized the structure in order to achieve the stability using Brich-Murnaghan's equation [28]. The stable structure is obtained at the minimum amount of energy. The space group 216 (F–43 m) is used for the considered compounds. The atoms of the RbYX (X = Si, Ge) alloys are placed at Wyckoff positions (0, 0, 0), (1/2, 1/2, 1/2), and (1/4, 1/4, 1/4). The crystal structures of RbYX (X = Si, Ge) are shown in Fig. 1a–b. The volume optimization has been done for each possible configuration of each compound using the Murnaghan equation of state. Figure 2a–b depicts the volume versus energy curves, and the curve with the minimum energy and electronegativity sequence should be taken into account.

The optimized parameters are shown in Table 1.

The energy and pressure are determined using Murnaghan's state equations which are given by [29]

$$E(V) = E_O + \left[\frac{BV}{B_P} \left(\frac{1}{(B_P - 1)} \left(\frac{V_O}{V} \right)^{B_P} + 1 \right) - \frac{BV_O}{(B_P - 1)} \right] \quad (2)$$

$$P(V) = \frac{B}{B_P} \left\{ \left(\frac{V_O}{V} \right)^{B_P} - 1 \right\} \quad (3)$$

where E(V) and P(V) represent the energy and pressure as a function of volume, E_O and V_O are the reference energy and volume, B_P denotes the pressure derivative of the bulk modulus. The investigated structural parameters are illustrated in Table 2.

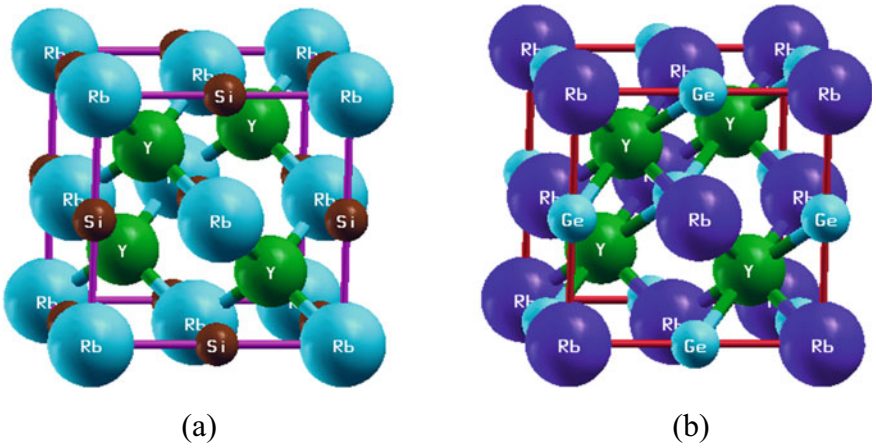

Fig. 1 **a**–**b** Crystal structure of half–Heusler alloys **a** RbYSi **b** RbYGe

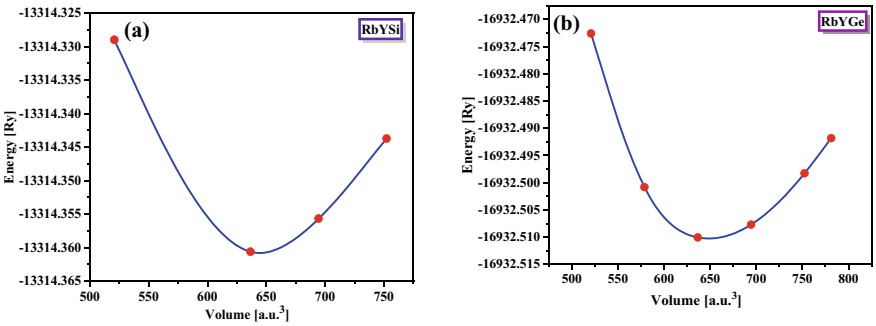

Fig. 2 **a**–**b** Total energy optimization per formula unit of half–Heusler alloys **a** RbYSi **b** RbYGe

Table 1 The optimized lattice parameter (a_o), optimized volume, bulk modulus, and pressure derivative (BP) of alloys

Alloy	Lattice constant (a_o)	Volume (V_0)	Bulk modulus (GPa)	B.P	Band gap (eV)
RbYSi	7.22	635.88	31.38	4.30	0.61 (Direct)
RbYGe	7.27	650.07	28.78	4.48	0.63 (Direct)

3.2 Electronic Properties

Initially, we analyzed the density of states (DOS) configuration of the RbYX (X = Si, Ge) having 8 valence electrons which provide a deep understanding of the electronic structure. TheTDOS and PDOS plots of each alloy are illustrated in Figs. 3a–d and 4a–d. The vertical region on 0 eV is known as the Fermi energy level and left region of this level is the valence band and the right region represents the conduction band.

Table 2 The Wyckoff positions, electronegativity, and optimized energy of alloys

Alloy	Atom	Wyckoff position	Electronegativity	Energy (Ry)
RbYSi	Rb	(0, 0, 0)	0.82	−13,314.3
	Y	$\left(\frac{1}{2}, \frac{1}{2}, \frac{1}{2}\right)$	1.22	
	Si	$\left(\frac{1}{4}, \frac{1}{4}, \frac{1}{4}\right)$	1.9	
RbYGe	Rb	(0, 0, 0)	0.82	−16,932.5
	Y	$\left(\frac{1}{2}, \frac{1}{2}, \frac{1}{2}\right)$	1.22	
	Ge	$\left(\frac{1}{4}, \frac{1}{4}, \frac{1}{4}\right)$,	2.01	

It is observed from the DOS plots that the Fermi level has not been crossed which confirms the semiconducting nature of the alloys. The high peak in the valence band for RbYSi alloy is obtained at −6 eV due to s states of Si while in the conduction band, the peaks are due to d states of Rb and Y atoms. Further, in the case of RbYGe, the peak in the valence band is obtained due to s states of Ge whereas peaks in the conduction band are obtained due to d states of Rb and Ge. The direct band gaps of 0.61 eV for RbYSi and 0.63 eV for RbYGe are obtained at X point as shown in Fig. 5a–b. These results revealed that the compounds have semiconducting nature.

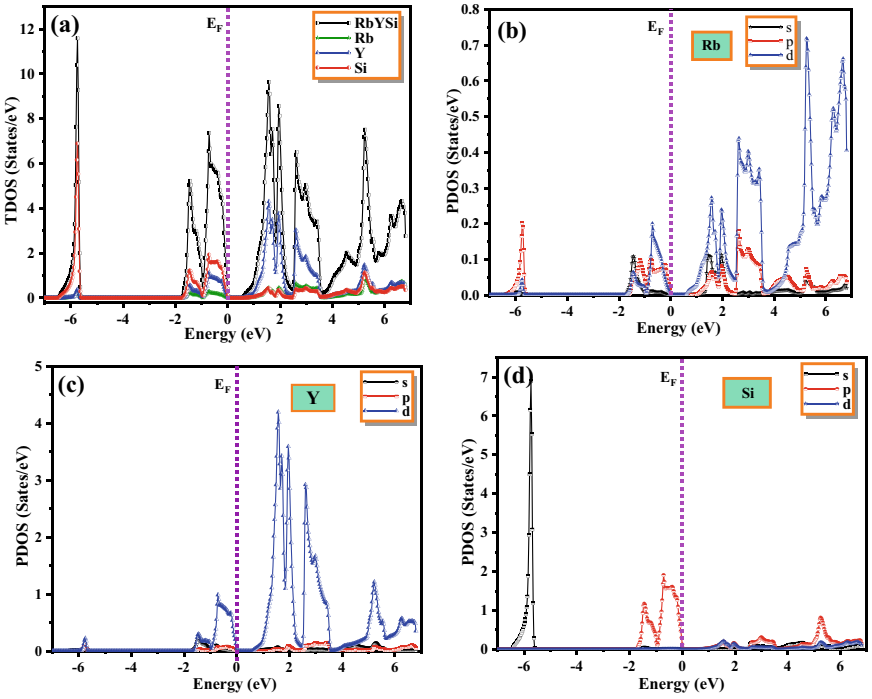

Fig. 3 **a–d** Total DOS of **a** RbYSi **b** RbYGe

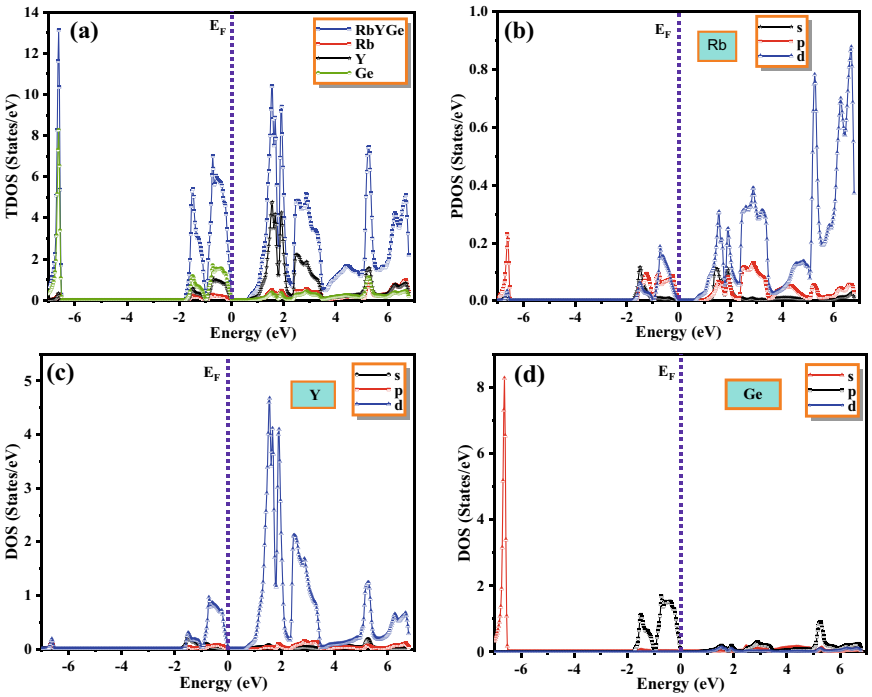

Fig. 4 **a**–**d** Partial DOS of **a** RbYSi **b** RbYGe

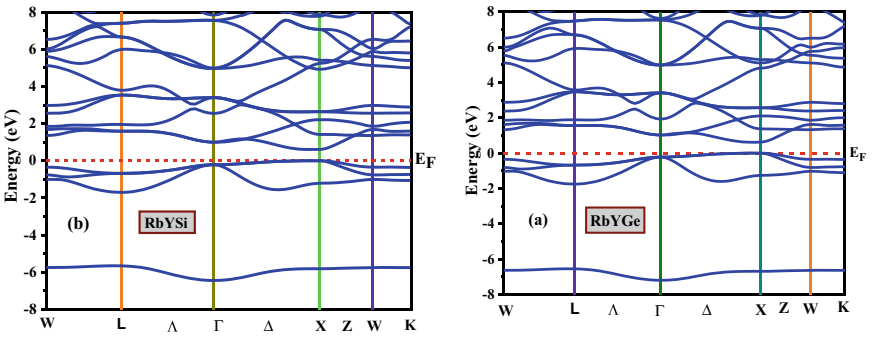

Fig. 5 **a**–**b** Band structure of **a** RbYSi **b** RbYGe

3.3 Elastic Properties

The elastic properties are examined in this section. We have investigated the yield strength, stress, shear forces, and structure stability using an elastic constant. These constants are the primary parameters to determine Young's modulus (Y), shear

modulus (G), ductility, and Poisson's ratio (η). To investigate the various mechanical properties, we just need to know the elastic constants C_{11}, C_{12}, and C_{44}. When a material is compressed then the volume of the material changes that can be measured with the help of the bulk modulus of elasticity whereas the shear modulus of elasticity takes into account the material's resistance to shear deformation. The VRH (Voigt, Reuss, and Hill) approach is used for the calculation of the modulus of elasticity.

3.3.1 Mechanical Stability

The most important elements in the manufacture of materials are elastic structures. The dynamical and mechanical stability of the materials is determined using elastic constants C_{11}, C_{12}, and C_{44}. The condition for mechanical stability is as follows [30]:

$$C_{11} > 0;\ C_{44} > 0;\ C_{11} - C_{12} > 0;\ C_{11} + 2C_{12} > 0;\ (C_{11} + 2C_{12}) > 0$$

3.3.2 Computation of Elastic Characteristics

The investigated compounds have satisfied the above conditions, therefore the alloys RbYX (X = Si, Ge) are mechanically stable. Tables 3 and 4 show the elastic results of the investigated materials.

The bulk modulus and shear modulus are determined using (VRH) approach [31]

$$B_V = \frac{1}{3}(C_{11} + 2C_{12}) = B_R$$

$$G_V = \frac{1}{5}(C_{11} - C_{12} + 3C_{44})$$

Table 3 Elastic constants (in GPa) C11, C12, C44 and bulk modulus B (GPa), shear modulus (GPa), B/G ratio of alloys

Alloy	C_{11}	C_{12}	C_{44}	B	G	B/G
RbYSi	58.12	18.23	24.79	31.52	22.72	1.40
RbYGe	53.36	16.42	23.64	28.73	21.39	1.34

Table 4 The calculated values of Poisson's ratio (η), Young's modulus (Y), Zener anisotropic index (A) and Kleinman parameter (ζ) of alloys

Compounds	η	Y	A	ζ
RbYSi	0.50	54.98	1.24	0.45
RbYGe	0.21	51.40	1.27	0.45

$$G_R = \frac{5C_{44}(C_{11} - C_{12})}{4C_{44} + 3(C_{11} - C_{12})}$$

The bulk and shear modulus are determined by taking the statistical mean (Hill approximation).

$$B = \left(\frac{B_V + B_R}{2}\right) \text{and } G = \left(\frac{G_V + G_R}{2}\right)$$

The high G values imply high resistance to the materials' plastic mechanical deformation, but high B values suggest lower compressibility of the materials. The brittleness and ductility nature of the materials can be determined using the B/G ratio. In the case of ductile materials, this ratio should be more than 1.75. But in the present work, the B/G ratio of 1.4 for RbYSi and 1.34 for RbYGe is obtained which indicates the brittle nature of the materials. Another important parameter is Poisson's ratio to study the mechanical properties. The materials exhibit covalent and metallic bonding for $0.1 < \eta < 0.33$ and incompressible nature for $\eta = 0.5$. In our work, the Poisson's ratio of 0.50 for RbYSi and 0.21 for RbYGe are obtained. On the basis of these results, the alloy RbYSi is perfectly incompressible. The Poisson ratio is determined by the following equation.

$$\eta = \frac{3B - Y}{6B}$$

The hardness and stiffness of the material can be determined using the Young's.modulus (Y) of elasticity which is given by

$$Y = \frac{9BG}{3B + G}$$

where B and G represent the bulk and shear modulus.

Young's modulus of 54.98 and 51.40 GPa for RbYSi and RbYGe are obtained. The stiffness order is RbYSi > RbYGe.

The Zener anisotropic factor (A) can be calculated as

$$A = \frac{2C_{44}}{C_{11} - C_{12}}$$

The Zener anisotropic factor (A) of the considered compounds is found to be more than unity, therefore the compounds RbYX (X = Si, Ge) show anisotropic behavior.

The bond bending and bond stretching are explained using the Kleinman parameter (ζ) which is given by the following equation [32].

$$\zeta = \frac{C_{11} + 8C_{12}}{7C_{11} + 2C_{12}}$$

The obtained value of ζ is 0.45 for both alloys which are toward zero and hence the bond bending dominates the bond stretching.

3.4 Optical Properties

Researchers are working very hard to develop novel, promising materials for thermoelectric and optoelectronic devices in order to overcome the problems with energy storage. Therefore, the optical properties of the alloys must be considered since different forms of radiation react with materials in various ways. All the optical properties of the alloys are determined by the crucial factor, called the dielectric function $\varepsilon(\omega)$. The dielectric function was utilized to analyze the optical characteristics of the alloys using the relation $\varepsilon(\omega) = \varepsilon_1(\omega) + i\varepsilon_2(\omega)$.

Figure 6a–b represents the real $\varepsilon_1(\omega)$ and imaginary part $\varepsilon_2(\omega)$ of the dielectric constant upto energy range of 12 eV. The highest peak of the real dielectric function $\varepsilon_1(\omega)$ is obtained in the infrared region. After this, the value of $\varepsilon_1(\omega)$ decreases and reaches the negative region due to the total reflection of the incident light. So the real part of the dielectric function determines the reflection of the incident light from the surface of the material. On the other hand, the highest peak of the imaginary part $\varepsilon_2(\omega)$ is observed in the visible region (VR) and then it decreases with increasing value of energy. This part is directly proportional to the energy band gap. It determines the absorbance of the photons. Because of the direct and narrow energy band gap, these materials can be used as potential candidates for photoelectronic energy applications.

The optical conductivity $\sigma(\omega)$ of 7250 and 7240 Ω^{-1} cm^{-1} for RbYSi and RbYGe alloys is obtained as shown in Fig. 6c. These values are obtained in the visible—region that makes the materials suitable candidates for photovoltaic applications.

The absorption coefficient I(ω) plays a significant role in optoelectronic energy applications. It determines the absorbance per unit thickness of the incident light. In our study, an absorption coefficient of more than 10^4 cm^{-1} is obtained. The various peaks are observed in the ultraviolet region as shown in Fig. 6 (d).

Fig. 7a–b represents the energy loss and reflectivity curves. The maximum e-loss of 4.76 for RbYSi and 5.22 for RbYGe is obtained in the UV region. The maximum reflectivity of 0.64 for RbYSi and 0.60 for RbYGe is obtained in the UV region. The reflectivity determines the opacity of the material [33]. The materials can be promising candidates for photovoltaic applications based on the obtained values of e-loss and reflectivity. The refractive index and the extinction coefficient curves are displayed in Fig. 7c–d. These two parameters also play a significant role in solar energy applications. The maximum refractive index (n) of 4.83 and 4.82 for RbYSi and RbYGe is obtained in the IR region. These values of refractive indices are nearly the same. The maximum extinction coefficient (K) of 3.41 and 3.37 is obtained in the infrared region and then it decreases with increasing energy values. The materials can be utilized as a promising candidate for optoelectronic as well as solar energy applications based on the above-examined optical properties.

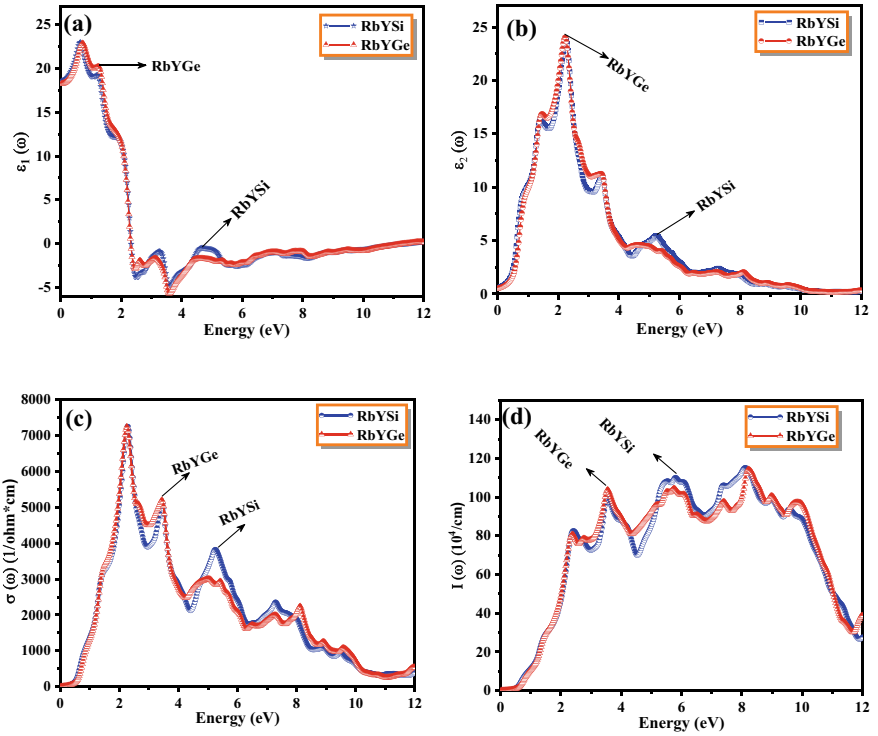

Fig. 6 **a**–**d** Calculated optical spectra of RbYX (X = Si, Ge) alloys with GGA approach **a** Real and **b** Imaginary part of dielectric function **c** Optical conductivity **d** Absorption coefficient

3.5 Thermoelectric Properties

Thermoelectric substances are able to convert unused heat energy into useful electric energy. This usage makes the materials more sustainable. The effectiveness of the materials can be determined with the help of the figure of merit $ZT = \frac{S^2\sigma T}{\kappa}$, here $S^2\sigma$ is the power factor, where S denotes the Seeback coefficient, σ is the electrical conductivity and T is the absolute temperature, κ is the thermal conductivity. The BolzTrap2 approach is used to calculate the transport properties of the materials. The electrical conductivity (σ/τ) increases with increasing temperature and attained the maximum value of 4.13×10^{19} Scm^{-1} s^{-1} for RbYSi and 3.96×10^{19} Scm^{-1} s^{-1} for RbYGe at 1100 K. Further, the power factor also increases as the temperature increases. The highest power factor of 1.71×10^{12} W/m K^2 s for RbYSi and 1.66×10^{12} W/m K^2 s for RbYGe at 1100 K is obtained. Figure 8a–d illustrates the variation of electrical conductivity, thermal conductivity, Seeback coefficient, and power factor with temperature.

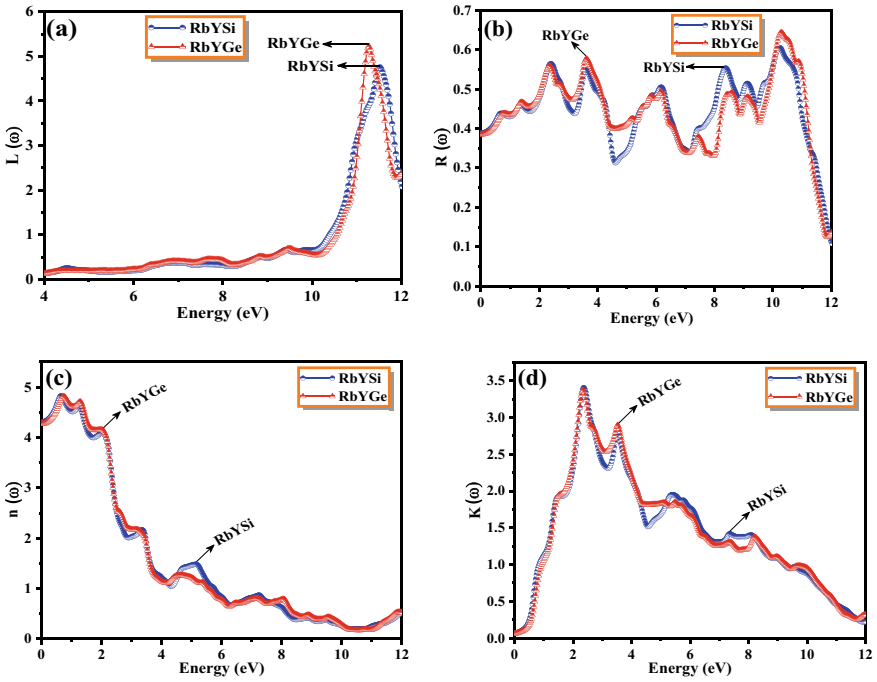

Fig. 7 **a**–**d** Calculated optical spectra of RbYX (X = Si, Ge) alloys with GGA **e** Electron e-loss function. **f** Reflectivity. **g** Refractive index **h** Extinction coefficient

Figures 9a–d and 10a–d show the variation of electrical conductivity, thermal conductivity, Seeback coefficient, and power factor with carrier concentration N(e/uc) of cubic RbYX (X = Si, Ge) at different temperatures. The-ve values of N (e/uc) indicate the n-type doping whereas the + ve values of N(e/uc) indicate the p-type doping.

4 Conclusions

In the present paper, the mechanical quantum model (DFT) is utilized to study the elastic, optical, and thermoelectric properties of RbYX (X = Si, Ge) compounds. The direct-band gap of 0.61 eV for RbYSi and 0.63 for RbYGe is obtained at point X which shows the semiconducting nature as tabulated in Table 2. The elastic properties are also studied which confirms the mechanical stability of the alloys. The various optical properties are also studied using the dielectric function. The low reflectivity and high absorption coefficient indicate that the materials can be used as suitable candidates for optoelectronics and solar energy applications. The transport properties are also investigated to check the thermoelectric performance of the materials.

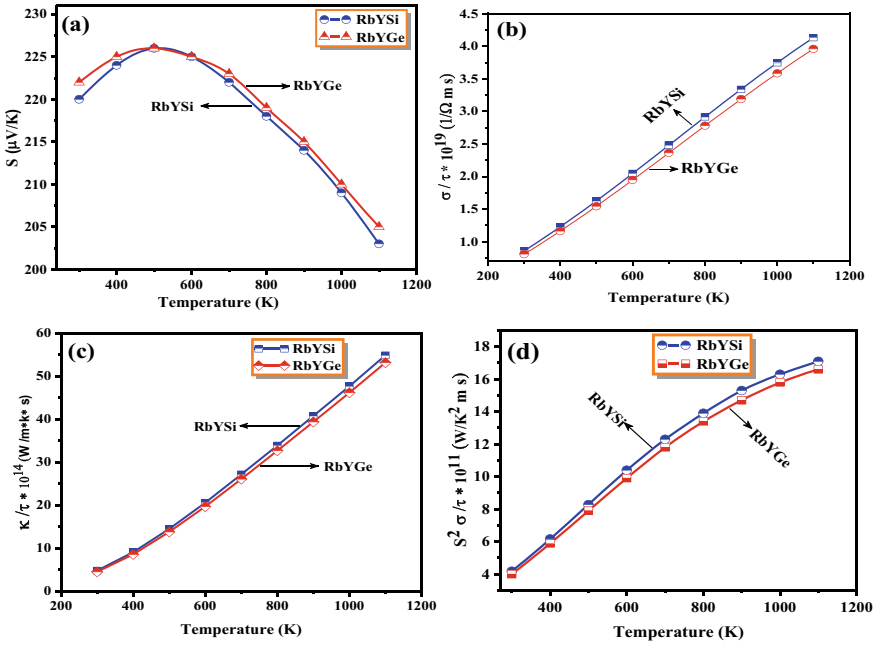

Fig. 8 **a**–**d** Calculated thermoelectric properties of RbYX (X = Si, Ge) alloys with GGA approach **a** Seebeck coefficient **b** Electrical Conductivity **c** Thermal conductivity **d** Power factor (PF)

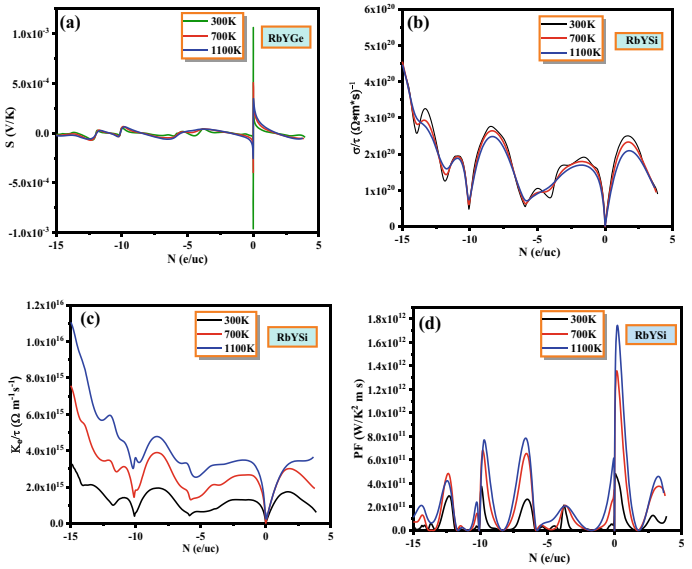

Fig. 9 **a**–**d** Calculated thermoelectric properties of RbYSi alloy versus carrier concentration N (e/uc) **a** Seebeck coefficient **b** Electrical Conductivity **c** Thermal conductivity **d** Power factor (PF)

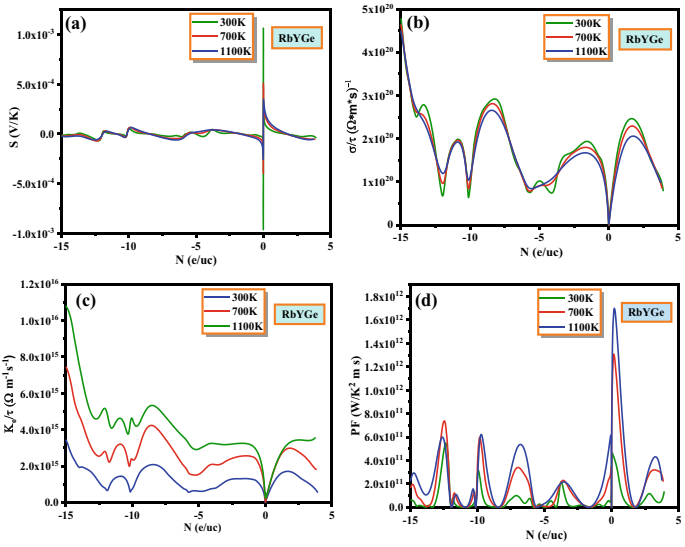

Fig. 10 **a–d** Calculated thermoelectric properties of RbYGe alloy versus carrier concentration N (e/uc) **a** Seebeck coefficient **b** Electrical Conductivity **c** Thermal conductivity **d** Power factor (PF)

The positive value of the Seeback coefficient indicates the p-type nature of the semiconductors. The electrical conductivity, as well as the power factor, increases with increasing temperature. The highest electrical conductivity of 4.13×10^{19} Scm^{-1} s^{-1} for RbYSi and 3.96×10^{19} Scm^{-1} s^{-1} for RbYGe is obtained at 1100 K. And the highest power factor of 1.71×10^{12} W/m K^2 s for RbYSi and 1.66×10^{12} W/m K^2 s for RbYGe is observed at 1100 K. The power factor (PF) decides the thermoelectric performance and effectiveness of the alloys. We conclude on the basis of these results that the alloys can be used as promising candidates for thermoelectric applications.

Acknowledgements We are extremely grateful to the Director.of the NIT, Kurukshetra (India) for his valuable support to carry out this research.

References

1. Sefir Y, Terkhi S, Zitouni Z, Siad AB, Seddik T, Benani MA, Lantri T, Bentata S (2021) Structural, electronic, magnetic and thermodynamic properties of the new multifunctional half-Heusler alloy CoTcSn: half-metallic and ferromagnetic behaviour. Pramana 95:1–12
2. Zhang C, Sun D, Vardeny ZV (2017) Multifunctional optoelectronic–spintronic device based on hybrid organometaltrihalide perovskites. Adv Electr Mater 3:1600426
3. Obeid MM, Jappor HR, Edrees SJ, Shukur MM, Khenata R, Mogulkoc Y (2019) The electronic, half-metallic, and magnetic properties of Ca1–xCrxS ternary alloys: insights from the first-principle calculations. J Mol Graph Model 89:22–32

4. Rani U, Soni Y, Kamlesh PK, Shukla A, Verma AS (2021) Fundamental theoretical design of Na-ion and K-ion based double antiperovskite X6SOA2 (X= Na, K; A= Cl, Br and I) halides: potential candidate for energy storage and harvester. Int J Energy Res 45:13442–13460
5. Snyder GJ, Toberer ES (2010) Complex thermoelectric materials. In: Materials for sustainable energy: a collection of peer-reviewed research and review articles from nature publishing group. World Scientific Publishing Co., pp 101–110
6. Khare IS, Szymanski NJ, Gall D, Irving RE (2020) Electronic, optical, and thermoelectric properties of sodium pnictogen chalcogenides: a first principles study. Comput Mater Sci 183:109818
7. Choudhary S, Shukla A, Chaudhary J, Verma AS (2020) Extensive investigation of structural, electronic, optical, and thermoelectric properties of hybrid perovskite ($CH_3NH_3PbBr_3$) with mechanical stability constants. Int J Energy Res 44:11614–11628
8. Hussain MI, Khalil RMA, Hussain F, Rana AM (2020) DFT-based insight into the magnetic and thermoelectric characteristics of $XTaO_3$ (X = Rb, Fr) ternary perovskite oxides for optoelectronic applications. Int J Energy Res 45:2753–2765
9. Lindorf M, Mazzio K, Pflaum J, Nielsch K, Brütting W, Albrecht M (2020) Organic based thermos electrics. J Mater Chem A 8:7495–7507
10. Chu J, Huang J, Liu R, Liao J, Xia X, Zhang Q, Wang C, Gu M, Bai S, Shi X, Chen L (2020) Electrode interface optimization advances conversion efficiency and stability of thermoelectric devices. Nat Commun 11:2723
11. Chopra U, Zeeshan M, Shambhawi S, Dhawan R, Singh HK, van den Brink J, Kandpal HC (2019) First–principles study of thermoelectric properties of Li–based Nowotony-Juza phases. J Phys Condens Matter 31:505504
12. Sofi SA, Gupta DC (2020) Systematic study of ferromagnetic phase stability of CobasedHeusler materials with high figure of merit: hunt for spintronics and thermoelectric applicability. AIP Adv 10:105330
13. Shastri SS, Pandey SK (2020) First-principles electronic structure, phonon properties, lattice thermal conductivity and prediction of figure of merit of FeVSbhalfHeusler. J Phys Condens Matter 33:085714
14. Mukhopadhyay A, Lakshminarasimhan N, Mohapatra N (2019) Electronic, thermal and magneto-transport properties of the half–Heusler. DyPdBi, Intermetallics 110:106473
15. Hammou M, Bendahma F, Mana M, Terkhi S, Benderdouche N, Aziz Z, Bouhafs B (2020) Thermoelectric and half-metallic behavior of the novel Heusler alloy RbCrC: ab-initio DFT study. Spin 10:2050029. https://doi.org/10.1142/S2010324720500290
16. Roy A, Bennett JW, Rabe KM, Vanderbilt D (2012) Half–heusler semiconductors as piezoelectrics. Phys Rev Lett 109:037602
17. Hussain A, Kashif M, Belabbas M, Noreen M, Janjua FR, Arbouche O (2020) First principle calculation of mechanical stability, opto-electronic and thermo-electric properties of TaIrGeSn ($0 \leq x \leq 1$) Half–Heusler alloy. Comput Condens Matter 25:00511
18. Chadov S, Qi X, Kübler J, Fecher GH, Felser C, Zhang SC (2010) Tunable multifunctional topological insulators in ternary Heusler compounds. Nat Mater 9:541–545
19. Kumar D, Chand P, Mohan L (2022) A DFT based analysis of LiYX (X = C, Ge, Si) alloys for energy applications. Mater Today: Proc 67:680−687
20. Liu J, Zhao Y, Dai Z, Ni J, Meng S (2020) Low thermal conductivity and good thermoelectric performance in mercury chalcogenides. Comput Mater Sci 185:109960
21. Zerrouki T, Rached H, Rached D, Caid M, Cheref O, Rabah M (2021) First-principles calculations to investigate structural stabilities, mechanical and optoelectronic properties of NbCoSn and NbFeSb half-Heusler compounds. Int J Quant Chem 121:26582
22. Mostari F, Rahman MA, Khatun R (2020) First principles study on the structural, elastic, electronic and optical properties of cubic 'half–Heusler' alloy RuVAs under pressure. Int J Math Math Sci 2:51–63
23. Sahni B, Vikram J, Kangsabanik A (2020) Alam, reliable prediction of new quantum materials for topological and renewable-energy applications: a high-throughput screening. J Phys Chem Lett 11:6364–6372

24. Ahmad M, Naeemullah GM, Khenata R, Bin Omran S, Bouhemadou A (2015) Structural, elastic, electronic, magnetic and optical properties of RbSrX (C, SI, Ge) half–Heusler compounds. J Mag Mag Mater 377:204–210
25. Kumar D, Chand P (2023) Enhanced optical and thermoelectric properties of Ti doped half–Heusler alloy NbRuP: a first principles study. Solid State Commun 115179:366–367
26. Blaha P, Schwarz K, Tran F, Laskowski R, Madsen GKH, Marks LD (2020) J Chem Phys 152:074101
27. Kohn W, Sham LJ (1965) Self-consistent equations including exchange and correlation effects. Phys Rev 140:A1133–A1138
28. Birch F (1947) Finite elastic strain of cubic crystals. Phys Rev 71:809–824
29. Toboła J, Pierre J (2000) Electronic phase diagram of the XTZ (X=Fe Co, Ni; T=Ti, V, Zr, Nb, Mn; Z=Sn, Sb) semi-Heusler compounds. J Alloys Comp 296:243–252
30. Born M, Huang K (1956) Dynamical theory of crystal lattices. Acta Cryst 9:837–838
31. Hill R (1952) The elastic behaviour of a crystalline aggregate. Proc Phys Soc Lond A 65:349
32. Kleinman L (1962) Deformation potentials in silicon. I. Uniaxial strain. Phys Rev 128:2614–2621
33. Kamlesh PK, Agrawal R, Rani U, Verma AS (2022) Comprehensive ab-initio calculations of AlNiX (X = P, As and Sb) half-Heusler compounds: Stabilities and applications as green energy resources. Mater Chem Phys 275:125233

Gap Solitons Supported by Cosine Apodized Optical Lattices in Centrosymmetric Photorefractive Crystals

Draupath Umesh, Ritesh Kumar Chourasia, and Aavishkar Katti

1 Introduction

The study of how spatial solitons can form from laser beams in photorefractive media has been a highly popular research area in recent years, with particular focus on how the diffraction broadening can be counteracted by the spatial self-focusing nonlinearity. When the media is exposed to a non-uniform light beam, it triggers the diffusion and drift of charge carriers that generate a space-charge field [1], creating an index waveguide to counteract diffraction broadening and self-trapping the light within the waveguide. The photorefractive effect is an appropriate tool for modeling soliton characteristics in saturable nonlinear periodic media. Even at low light intensities, these media can produce significant refractive index changes, providing a controlled and precise method for studying nonlinear optics. Photonic lattices can be easily imprinted and adjusted for periodicity during crystal growth, making them suitable for studying optical gap solitons and their linear stability in the band gaps of biased centrosymmetric uniform optical lattices in a systematic manner [2].

Our research explores the existence and properties of solitons formed in the forbidden regions (band gaps) of crystals, using a raised cosine apodized optical lattice. To achieve this, we utilized biased photorefractive crystals, which enabled us reversible optical induction in the photonic lattice by controlling the conditions under which the refractive index of the material changes in response to light. The lattice is apodized to reduce side lobes in the reflection spectrum by gradually reducing the

D. Umesh · A. Katti (✉)
Department of Physics, Dr. Vishwanath Karad MIT World Peace University, Pune, Maharashtra 411038, India
e-mail: aavishkarkatti89@gmail.com

R. K. Chourasia (✉)
Department of Physics, Samastipur College (A Constituent College of L.N.M.U., Darbhanga, 846004, Bihar, India), Samastipur, Bihar 848134, India
e-mail: riteshphyzics@gmail.com

S. B. Krupanidhi et al. (eds.), *Recent Advances in Functional Materials and Devices*, Springer Proceedings in Materials 37, https://doi.org/10.1007/978-981-99-6766-7_19

refractive index variation to zero at each end. Although apodized gratings are aperiodic structures and the transfer matrix method must be used to analyze their bandgap structure, we can approximately use the photonic band gap for the corresponding uniform photonic lattice.

We may analyze the uniform lattice to find out the photonic band gap using Bloch wave solutions. A uniform grating is generated using two ordinarily polarized laser beams inside the photorefractive crystal [3], which can be apodized by altering the mark-to-space ratio of the grating in a raised cosine manner. The effects of lattice periodicity on the band structure are also considered. By inducing periodicity optically, we can observe various types of lattice solitons, such as vortex and vector solitons, reduced symmetry solitons, nonlocal solitons, and solitons supported by Bessel photonic lattices to name a few [1, 3]. Grating filters fabricated using electron beam lithographic techniques can be used for practical realization of the apodization process [4]. Our findings are significant as they contribute to the understanding of solitons in centrosymmetric photorefractive media and provide insights for future experimental investigations. Here we have chosen the crystal to be KLTN as an example to illustrate our results.

2 Theoretical Model

In order to investigate centrosymmetric gap solitons in biased photo-refractive media, we utilize a highly intense optical beam propagating through a crystal imprinted with an apodized photonic lattice. This lattice is apodized through a raised cosine envelope along the x-axis, allowing the beam to diffract only in the x direction. This apodization technique shapes the reflectivity profile of the grating and tunes the spectral properties of the solitons. Assuming a linearly polarized incident optical beam along the x-direction, we can express the optical field in the medium as a gradually changing envelope function $E = \hat{x}A(x, z)\exp(ikz)$. Even though there is a dependence on the z-axis for the amplitude of the optical field, we can assume that most of the dependence is encapsulated by the phasor. Using this assumption, we can expand the perturbed extra-ordinary refractive index of the centrosymmetric media as $\left(n_e^{'}\right)^2 = n_e^2 - n_e^4 g_{eff}\varepsilon_0^2(\varepsilon_r - 1)^2 E_{SC}^2$, where the space charge field E_{sc} is generated by the diffusion and drift of the charge carriers when a photorefractive crystal is subjected to non-uniform incident light. Under moderate bias conditions, this field can be mathematically expressed in terms of the dark irradiance I_d and the intensity I, g_{eff} is the electro-optic coefficient exhibiting quadratic behavior, ε_0 is the permittivity of vacuum and ε_r is the relative dielectric constant of the media. Under the above-mentioned conditions, the Helmholtz equation gets modified into the paraxial equation for diffraction [5, 6],

$$iA_z + \frac{1}{2k}A_{xx} - \frac{k}{n_e}(\Delta n_{PR} + \Delta n_G)A = 0 \tag{1}$$

where Δn_G is the refractive index modulation caused by the photonic lattice, the subscripts on A signify the partial derivatives with respect to the variable given in the subscript and the number of subscripts signifies its order. Here A_{xx} and A_z signify the second and first order partial derivatives with respect to x and z respectively. $\Delta n_{PR} = -\frac{1}{2}n_e^3 g_{eff}\varepsilon_0^2(\varepsilon_r - 1)^2 E_{SC}^2$ is the refractive index variation of the photorefractive media. For convenience, we can convert Eq. (1) into dimensionless coordinates using $s = \frac{x}{x_0}$, $\xi = \frac{z}{kx_0^2}$ and $A = \left(2\eta_0 I_d \big/ n_e\right)^{1/2} q$ as follows,

$$iq_\xi + \frac{1}{2k}q_{ss} + pR(s)q - \frac{\beta q}{\left(1 + |q|^2\right)^2} = 0 \tag{2}$$

where x_0 is an arbitrary scaling length, k is a free space wave vector, and $\beta = (k_0 x_0)^2 n_e^4 g_{eff}\varepsilon_0^2(\varepsilon_r - 1)^2 E_0^2 \big/ 2$. Hence, the parameter β is a marker of the strength of the nonlinearity. Although it is not feasible to use the inverse scattering transform method to solve the nonlinear Eq. (2), it is still plausible to attain a spatially localized soliton solution for this equation. To achieve this, we assume that a shape-preserving solution can be expressed in a generic form as $q(s, \xi) = w(s, \xi)\exp(i\mu\xi)$, and then search for stationary soliton solutions that fall in the photonic band gap region by modifying Eq. (2) as follows:

$$\frac{1}{2}w_{ss} + pR(s)w - \frac{\beta w}{\left(1 + w^2\right)^2} - \mu w = 0 \tag{3}$$

Simplifying the expression further yields,

$$\frac{1}{2}w_{ss} + F(I)w - \mu w = 0 \tag{4}$$

where $F(I) = pR(s) - \frac{\beta}{(1+w^2)^2}$ dictates the total nonlinearity of the system and $I = (n_e/2\eta_o)|w|^2$ describes the intensity. In a uniform grating, the refractive index change is generally expressed in terms of a cosine variation as $R(s) = \cos\left(\frac{2\pi s}{T}\right)$. This periodicity in refractive index gives rise to forbidden energy ranges in the crystal. The width and position of the photonic band gaps in the dispersion curve of the lattice are dependent upon the scaled lattice depth and periodicity. For a cosine apodized grating, the refractive index change is expressed as,

$$R(s) = \cos\left(\frac{2\pi s}{T}\right)\cos^2\left(\frac{\pi s}{L}\right) \tag{5}$$

where L is the grating length. We plot the index variation of (5) in Fig. 1. Using (5), Eq. (3) gets modified to,

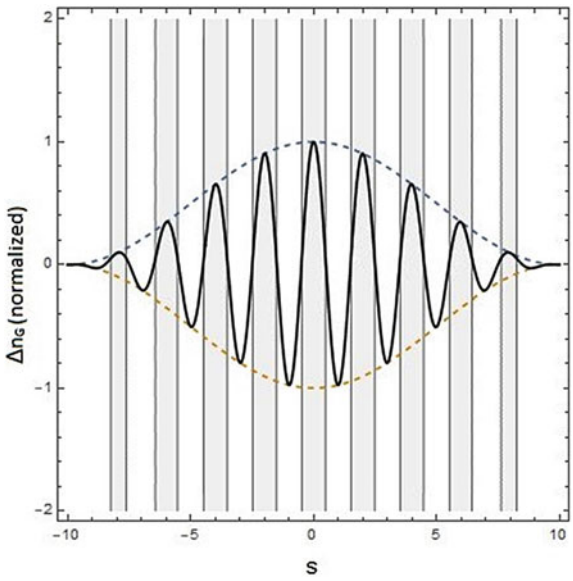

Fig. 1 Raised cosine apodized grating in a 1-dimensional photonic lattice

$$\frac{1}{2}w_{ss} + p\cos\left(\frac{2\pi s}{T}\right)\cos^2\left(\frac{\pi s}{L}\right)w - \frac{\beta w}{\left(1+w^2\right)^2} - \mu\omega = 0 \tag{6}$$

We should note here that an electromagnetic wave propagating in a periodic uniform photonic lattice is characterized by an allowed and forbidden frequency spectrum as predicted by the Floquet-Bloch theory. If we see the reflection or transmission spectrum, the uniform optical lattices show a typical peak or dip respectively along with side lobes at the adjacent wavelengths. Apodization is a process where the refractive index variation is gradually reduced to zero over a particular distance at each end. Apodization of the grating causes the side lobes in the reflection spectrum to be suppressed [7, 8]. But the Floquet-Bloch theory is not valid for finding the reflection coefficient or the bandgap structure of apodized gratings which are aperiodic and usually, the transfer matrix method is used. However, the apodization typically does not change the edges of band gap appreciably when compared to the uniform grating [8]. Hence, we again return to Eq. (3) which considers a uniform grating. Equation (3) admits Bloch wave solutions for all values of the wave vector that spans the forbidden band gap of the photonic lattice. Using the Floquet Bloch theory and the parameters for periodicity $T = 2$, scaled lattice depth $p = 5$, we substitute the Bloch wave function in (3) and solve the ensuing eigenvalue problem treating the nonlinearity as a perturbation. Hence, we have found the band structure of the uniform photonic lattice in Fig. 2. The first finite, second finite and semi-infinite band gaps lie between $-2.946 \leq \mu \leq 1.76$, $-6.41 \leq \mu \leq -4.52$ and $\mu > 1.908$ respectively.

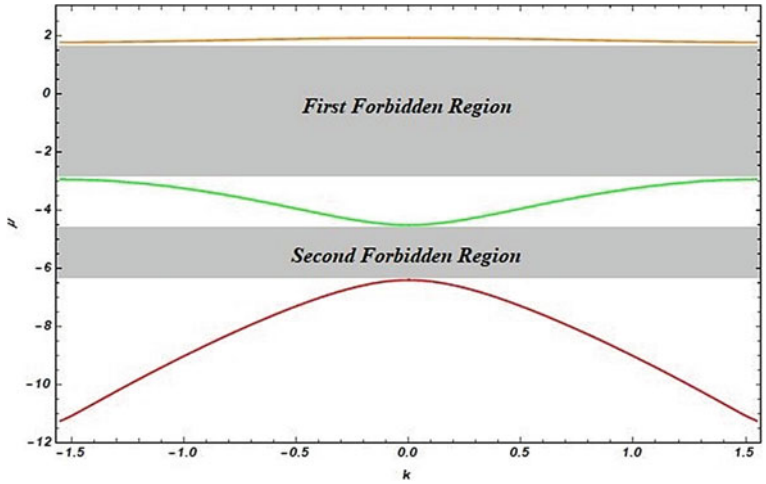

Fig. 2 Band structure for a uniform grating in a one-dimensional photonic lattice

3 Results and Discussion

3.1 Existence of Gap Solitons

In this section, we will elaborate on the existence and properties of various gap solitons that can be formed within the photonic bandgap of the photonic lattice. Basically, we solve Eq. (6) taking the value of μ to be within either the first finite band gap or the second finite band gap and searching for single peaked, double peaked or multi peaked solitons by imposing the requisite boundary conditions. For illustration of our results, we shall consider the KLTN crystal with the following parameters [1], $n_e = 2.2$, $g_{eff} = 0.12\ m^{-4}C^{-2}$, $\varepsilon_r = 8000$, $\lambda_0 = 515$ nm., $x_0 = 20\ \mu$m., $E_0 = 1100$ V/cm. With these parameters, $\beta \approx 5$. In the first and second finite bandgap, single and double peaked solitons where observed. Figure 3a–c depicts the formation of single peaked solitons in the high, medium, and low power regime $\mu = 1.16, -0.09$ and -2.74. Figure 4a–c shows double peaked solitons in the first forbidden band gap in the high, medium and low power regime for $\mu = 1, -0.19$ and -1 respectively. There is a concomitant existence of single peak and double peak solitons in the first forbidden band gap. At very low powers, we can see little bit of distortion in the soliton profiles for the single peaked soliton as seen in Fig. 3c. Figure 5a, b depict the existence of high and low power single-peaked solitons in second forbidden band gap for $\mu = -4.61$ and $\mu = -5.11$). Figure 6a, b depicts the formation of double peaked solitons with low and high powers respectively in the second finite band gap of the optical lattice when $\mu = 6.21$ and 4.76. It is very interesting that in the second band gap also, we can observe concomitant formation of single peaked and double peaked solitons.

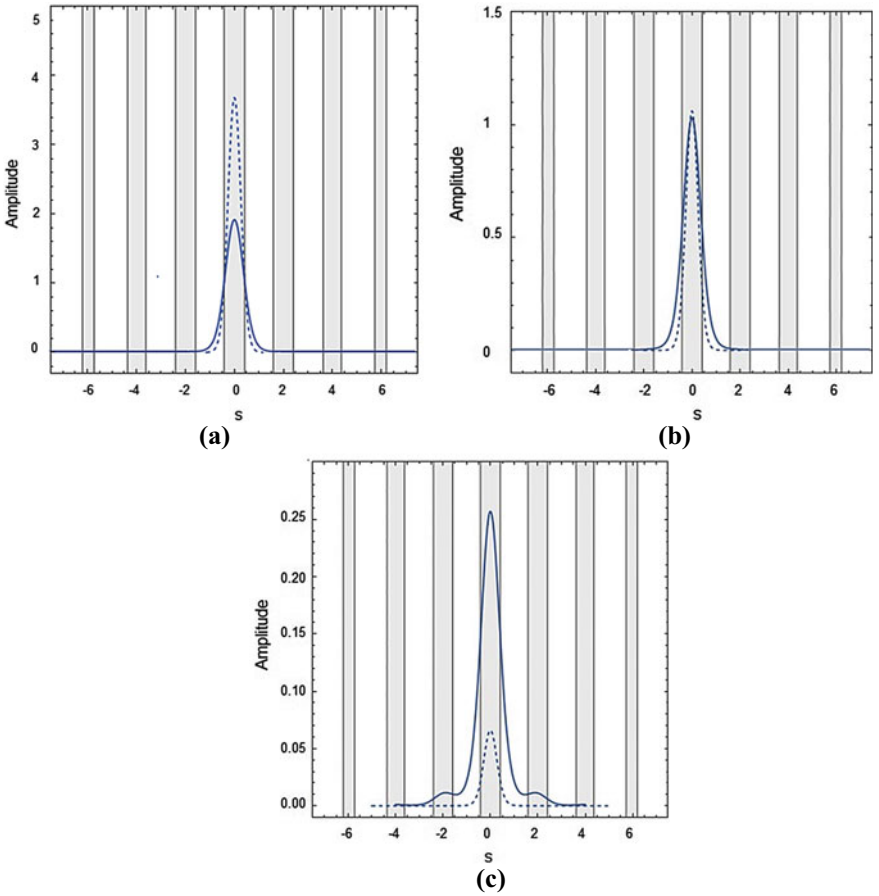

Fig. 3 Single peaked gap soliton spatial field profile (solid curve) and intensity profile (dashed curve) in the first finite band gap ($T = 2, p = 5, \beta = 5$) in **a** the high power regime; $\mu = 1.16$ **b** the moderate power regime $\mu = -0.09$ **c** the low power regime; $\mu = -2.74$

Figure 7a, b show the variation of single peaked soliton field and intensity throughout the first and second finite band gap. It is also reasonable now to see the changes in the self-trapping within the band gap. Hence, we shall plot the variation of the soliton width inside the photonic band gap. Figure 7c shows the trend of full width at half maxima (FWHM) of the single peaked solitons throughout the first band gap for the single peaked solitons. For single peaked solitons in the first finite band gap, the FWHM first decreases and then increases as we traverse throughout the band gap. It is observed that the FWHM of soliton keeps on increasing as the wave vector decreases until a particular point and from there onwards the FWHM also increases with respect to the increase in wave vector. This trend in FWHM can be explained by considering the frequency of the input pulse. As the wave vector is directly related to the frequency of the wave the FWHM of the soliton keeps on

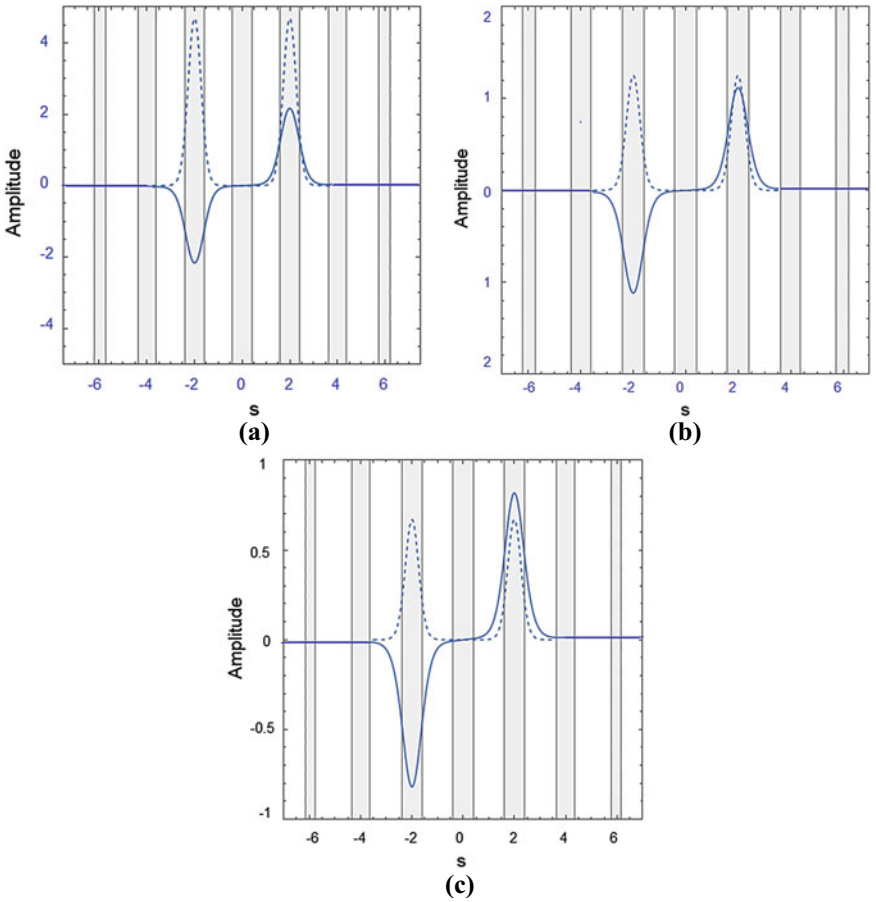

Fig. 4 Double peaked gap soliton spatial field profile (solid curve) and intensity profile (dashed curve) in the first finite band gap ($T = 2$, $p = 5$, $\beta = 5$) in **a** the high power regime; $\mu = 1$ **b** the moderate power regime; $\mu = -0.19$ **c** the low power regime; $\mu = -1$

increasing until a particular value. Beyond that value, the soliton starts to interact with the higher order modes of the grating thereby reducing the FWHM value.

3.2 Stability of Gap Solitons

When dealing with solitons in nonlinear media, it is widely recognized that they tend to preserve their shape. However, their stability cannot be guaranteed in case of non-integrability of the underlying modified Nonlinear Schrödinger (NLS) equation, for example in case of photorefractive nonlinear media. Therefore, it is crucial

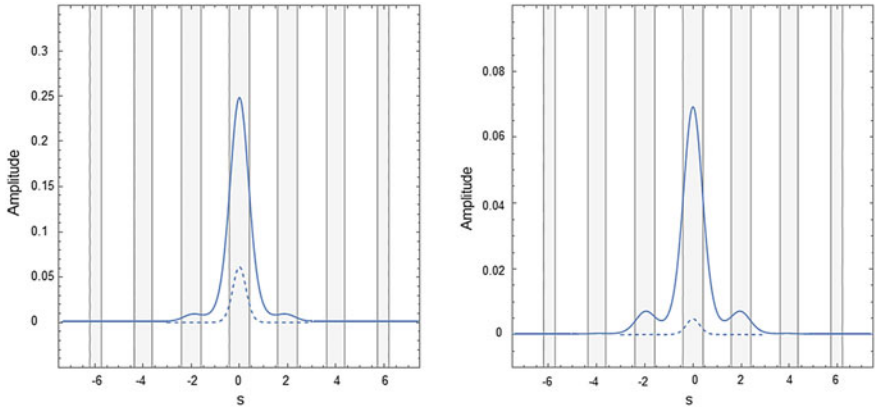

Fig. 5 Single peaked gap soliton spatial field profile (solid curve) and intensity profile (dashed curve) in the second finite band gap ($T = 2$, $p = 5$, $\beta = 5$) in **a** the high power regime; $\mu = -4.61$ **b** the low power regime; $\mu = -5.11$)

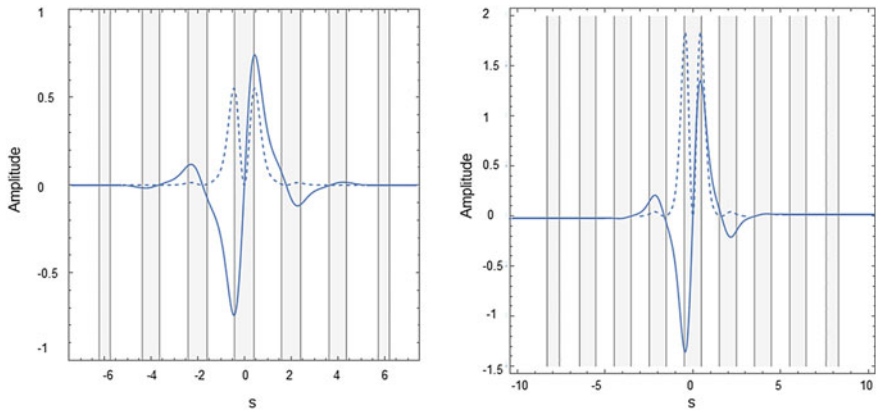

Fig. 6 Double peaked **g**ap soliton spatial field profile (solid curve) and intensity profile (dashed curve) in the second finite band gap ($T = 2$, $p = 5$, $\beta = 5$) in **a** the low power regime; $\mu = -6.21$ **b** the high power regime; $\mu = -4.76$

to perform linear stability analysis to determine whether the solitons are stable or weakly unstable against small perturbations, as only these types of solitons can be observed experimentally. Linear stability analysis involves examining small perturbations around the soliton solutions, which can be expressed as a linear superposition of eigenmodes. These eigenmodes fall into one of three categories when analyzed using this approach namely, neutrally stable internal modes whose eigenvalues tend

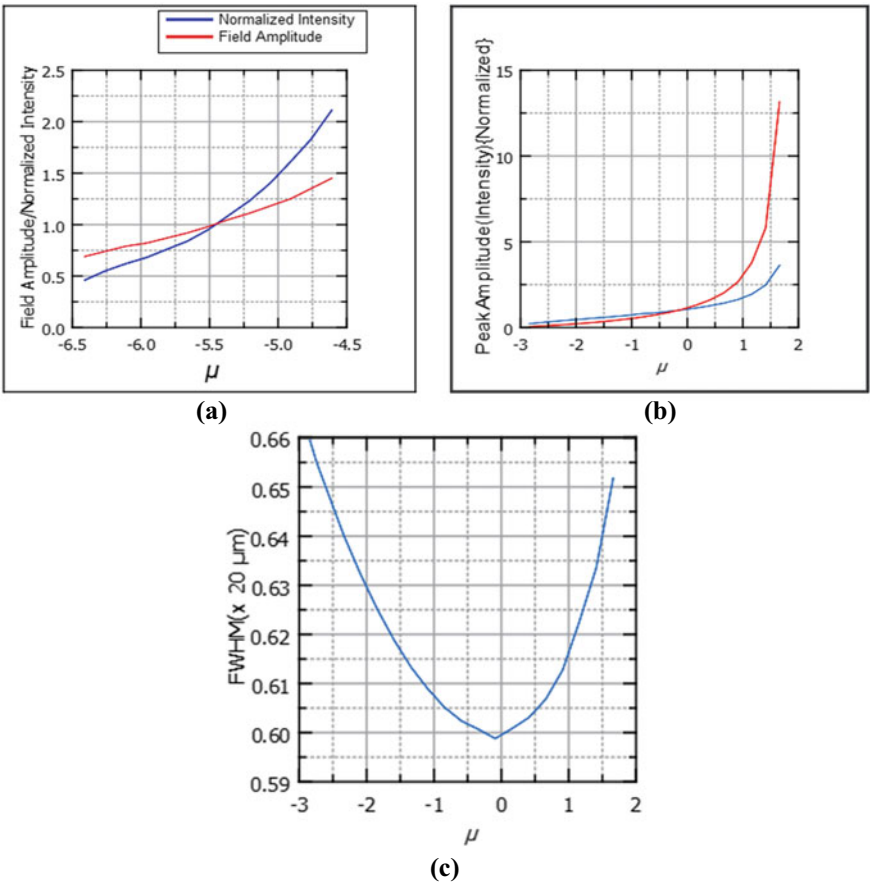

Fig. 7 **a** Amplitudes for field profile and normalized intensity profile of the single peaked solitons throughout the second finite bandgap. **b** Amplitudes for field profile and normalized intensity profile of the single peaked solitons throughout the first finite bandgap. **c** General trend of full width at half maximum values for single peaked solitons throughout the first finite bandgap

to be real, unstable modes whose eigenvalues tend to be imaginary, and oscillatory modes whose eigenvalues tend to be complex.

Linear stability analysis is a method used to develop necessary conditions for the stability of solitons. This analysis involves examining small perturbations around the soliton solution to a nonlinear partial differential equation, and analyzing the growth or decay of these perturbations using instability modes with imaginary eigenvalues. The Vakhitov-Kolokolov (VK) criterion is a well-known example of such an analysis. It states that a soliton is stable only if its power increases with an increase in the propagation constant, which is represented mathematically as $dP/d\mu > 0$. To further investigate the linear stability properties of solitons, perturbative methods can be used in subsequent analyses. This involves examining the effects of small

perturbations on the soliton solution, and analyzing how these perturbations affect the overall stability of the soliton.

In linear stability analysis, small perturbations around the soliton solutions are treated as normal modes of the linearized system around the soliton solution,

$$q(s,\mu) = \left\{w(s,\mu) + [u(s) - v(s)]e^{i\delta\xi} + [u*(s) + v*(s)]e^{i\delta\xi}\right\}e^{i\mu\xi} \tag{7}$$

where *u(s)* and *v(s)* describe small perturbations and the asterisk describes the complex conjugation. Now by substituting Eqs. (7) in (3) and linearizing it, *u(s)* and *v(s)* are found to satisfy the eigenvalue problem,

$$\begin{pmatrix} 0 & L_0 \\ L_1 & 0 \end{pmatrix}\begin{pmatrix} u \\ v \end{pmatrix} = \delta\begin{pmatrix} u \\ v \end{pmatrix} \tag{8}$$

Here L_0 and L_1 are the differential operators given by [9],

$$L_j = -\frac{1}{2}\frac{\partial^2}{\partial s^2} + \mu - U_j,\ (j = 0, 1) \tag{9}$$

where, $U_0 = F(I)$, $U_1 = F(I) - 2|w|^2\frac{dF}{d(w^2)}$ which yields

$$L_0 = -\frac{1}{2}\frac{\partial^2}{\partial s^2} - pR(s) + \frac{\beta}{\left(1+w^2\right)^2} + \mu \tag{10}$$

and

$$L_1 = -\frac{1}{2}\frac{\partial^2}{\partial s^2} - pR(s) + \frac{\beta\left(1-3w^2\right)}{\left(1+w^2\right)^3} + \mu \tag{11}$$

Now solving the eigenvalue problem is a tedious task, but it can be simplified and solved by reducing the problem comprising of two eigenvalue equations, into a problem consisting of single equation of the form,

$$L_0 L_1 u = \delta^2 u \tag{12}$$

This can be tackled numerically using the method of finite differences that was done by discretizing the continuous domain into a finite number of points and then approximating the derivatives of the solution around these points using central differences. By considering the perturbed soliton solutions using this method, we were able to characterize the linear stability of the solitons. The growth rate of perturbation terms in solitons can be complex and expressed as $\delta = \delta_r + i\delta_i$. If the perturbation term (δ) has a non-zero imaginary component ($\delta_i \neq 0$), the solitons become unstable and grow exponentially. On the other hand, if the perturbation term only

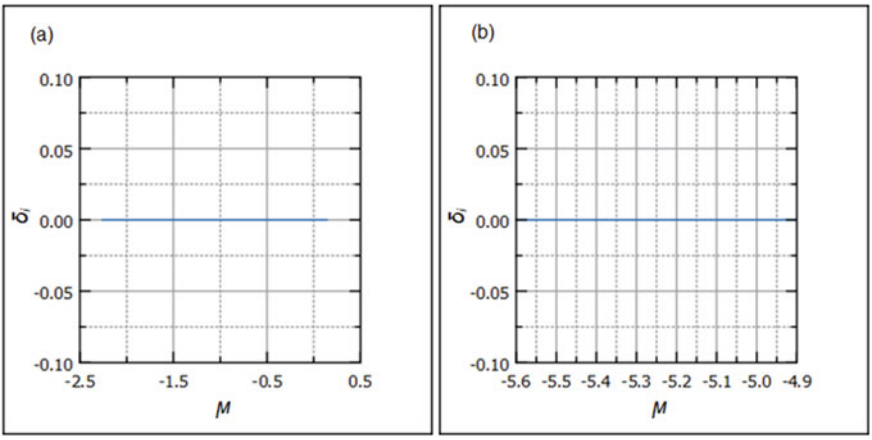

Fig. 8 Imaginary component of δ_i **a** throughout the first forbidden band gap **b** throughout the second forbidden band gap for single and double peaked solitons

has a real component ($\delta_i = 0$), it oscillates periodically between -1 and $+1$, which is known as a harmonic perturbation and indicates that the solitons are stable. Using the finite difference method, we have found that the perturbations of the single and double-peaked solitons in the first as well as the second band gap exhibited harmonic behavior. Hence, both the single peaked and double peaked solitons can be said to be stable throughout the first and second band gap, as depicted in Fig. 8a, b.

4 Conclusions

In this study, we have investigated the existence and characteristics of spatial optical gap solitons in photorefractive materials with a quadratic nonlinearity and a raised cosine apodized photonic lattice embedded within. The band structure of photonic lattice has been found using the Floquet-Bloch theory. The photorefractive nonlinearity allows for the formation of spatial solitons even within the photonic band gap. We have observed the existence of various types of soliton solutions, including single peaked and double peaked solitons, in each of the finite band gaps. Characteristics of these gap solitons like the intensity, field amplitude, and soliton width across the band gap have been investigated in detail. We have also investigated the stability of the solitons to perturbations across the entire band gap. Our findings indicate that the solitons formed in both the forbidden band gaps are stable.

Acknowledgements Aavishkar Katti would like to acknowledge financial assistance from Department of Science and Technology-Science and Engineering Research Board (DST-SERB), Govt. of India through the Core Research Grant awarded (File No. CRG/2021/004740)

References

1. Zhan K, Hou C (2012) Opt Commun 285:3649.https://doi.org/10.1016/j.optcom.2012.04.040
2. Christodoulides DN, Carvalho MI (1995) Bright, dark, and gray spatial soliton states in photorefractive media. J Opt Soc Am B 12:1628–1633. https://doi.org/10.1364/JOSAB.12.001628
3. Feischer JW, Segev M, Efremidis NK, Christodoulides DN (2003) Nature 422:147. https://doi.org/10.1038/nature01452
4. Millar P, Liu X, De La Rue R, Aitchison JS (1998) Fabrication of complex integrated waveguide filters using electron beam lithography. In: Conference on lasers and electro-optics-europe, technical digest series. Optica Publishing Group, paper CThK3. https://opg.optica.org/viewmedia.cfm?uri=CLEO_Europe-1998-CThK3&seq=0
5. Aavishkar Katti RA, Yadav (2021) Optical spatial solitons in photorefractive materials, progress in optical science and photonics (POSP), vol 14. ISBN 978-981-16-2549-7, https://doi.org/10.1007/978-981-16-2550-3
6. Zhan KY, Hou CF (2014) Lattice surface solitons in diffusive nonlinear media driven by the quadratic electro-optic effect. Opt Express 22:11646–11653. https://doi.org/10.1364/OE.22.011646
7. Sun N-H et al (2009) Numerical analysis of apodized fiber Bragg gratings using coupled mode theory. Prog Electromag Res 99:289–306. https://doi.org/10.1177/00368504221094173
8. Ashry I, Elrashidi A, Mahros A, Alhaddad M, Elleithy K (2014) Investigating the performance of apodized fiber Bragg gratings for sensing applications. In: Proceedings of the 2014 Zone 1 conference of the american society for engineering education, pp 1–5. https://doi.org/10.1109/ASEEZone1.2014.6820640
9. Kivshar YS, Agrawal GP (2003) Chapter 2—Spatial solitons. In: Kivshar Y, Agrawal GP (eds) Optical solitons. Academic, pp 31–62. ISBN 9780124105904, https://doi.org/10.1016/B978-012410590-4/500024

Characterization of Nanocrystalline ZnS Thin Film on *p*–Si by Chemical Bath Deposition Method

Ajeet Gupta, Arun Kumar, Mudit Prakash Srivastava, Vijay Singh Meena, Sandeep Kumar, and Devendra Kumar Rana

1 Introduction

In the last decade, zinc sulfide (ZnS) has attained much recognition among various functional materials mainly due to its wide band gap (3.4–3.9 eV). The superior chemical and physical properties of ZnS make it a suitable material for various applications such as piezoelectricity and luminescence. ZnS is a high refractive index, chemically stable, and non-toxic material [1]. Recently industries have shifted their attention to producing nanostructured semiconductors to portray the enhanced properties of the systems. In this regard, ZnS nanostructures have found many applications in the area of semiconductor device fabrication for instance solar cells, gas sensors, UV sensors, heterojunction diodes, photovoltaic cells, and LEDs, etc. [2]. An important aspect of the thin film preparation is the deposition technique that determines the device morphology and performance. In the literature, a number of methods such as Thermal evaporation [3], CVD (chemical-vapor deposition) [4], RF-sputtering [5],

D. K. Rana (✉)
Material Science Research Lab (Theory and Experiment), Department of Physics, ARSD College, University of Delhi, New Delhi 110021, India
e-mail: drana@arsd.du.ac.in

A. Gupta · M. P. Srivastava
Department of Physics, SRM Institute of Science and Technology, Delhi-NCR Campus, Modinagar, Ghaziabad 201204, India

A. Kumar
Department of Applied Physics, Amity Institute of Applied Science (AIAS), Amity University, Noida Campus, Sector 125, Noida, Uttar Pradesh 201313, India

V. S. Meena
Solid State Physics Laboratory, Lucknow Road, Timarpur, Delhi 110054, India

S. Kumar
Department of Physics, Bhaskaracharya College of Applied Sciences, University of Delhi, Delhi 110075, India

S. B. Krupanidhi et al. (eds.), *Recent Advances in Functional Materials and Devices*, Springer Proceedings in Materials 37, https://doi.org/10.1007/978-981-99-6766-7_20

spray pyrolysis [6], sol–gel [7], chemical bath deposition (CBD) [8], dip coating [9], spin coating [10], etc. have been employed to synthesize ZnS thin films. Each synthesis technique has its own pros and cons in terms of film thickness, growth orientation, crystal structure, surface morphology, and composition, which greatly affects physical and electronic properties of the deposited thin films. Thus, the method of deposition plays a critical role in specifying the device morphology and performance.

In the present study, the chemical bath deposition (CBD) method was utilized for depositing a ZnS thin film on a silicon substrate of thickness. CBD method is potentially a straightforward and cost-effective method to fabricate high-quality thin films. Likewise, the quality of the thin film depends on the substrate used in the deposition. In this report, a p-type silicon substrate is utilized for growing ZnS thin film. UV–Vis and X-ray diffraction (XRD) techniques were utilized to examine the optical properties and crystalline phase in as-fabricated zinc sulfide (ZnS) thin film. Also, I-V characteristic measurement was performed on the deposited film to investigate the electrical properties [11].

2 Materials and Method

In the present study, the zinc sulfide (ZnS) nanoscale film was grown on a *p*-type silicon substrate via CBD method. Zinc Chloride ($ZnCl_2$), Thiourea (CH_4N_2S), Ammonia (NH_3), and Hydrazine (N_2H_4) have been used as the starting materials for the ZnS thin film growth. The growth process holds three major steps including, the preparation of the substrate, preparation of precursor solution, and deposition of zinc sulfide (ZnS) on substrate. The silicon substrate was first thoroughly washed with de-ionized water and then washed with acetone. The Si substrate was then dried in air to achieve well-adherent and high-quality ZnS thin film. In addition, all apparatus such as thermometer, beaker, magnetic bead, and watch glasses, etc., used in the experiment were also washed thoroughly to avoid any contamination during the deposition process. The bath solution of zinc sulfide thin film consists of zinc chloride ($ZnCl_2$: 0.02 M) as a source of zinc and thiourea (CH_4N_2S: 0.02 M) as a source of sulfur. The ammonia (NH_3) was used to maintain the pH level of the solution, whereas hydrazine (N_2H_4) was used as a reaction reagent. In the first reaction step, zinc chloride ($ZnCl_2$) and hydrazine (N_2H_4) were taken into the reaction vessel and stirred well with the help of a magnetic stirrer for about 10 min to obtain a 250 ml bath solution. In the second step, ammonia (NH_3) was added to the bath solution under continuous stirring to obtain a clear solution. In the third step, thiourea was mixed into the bath solution and temperature of the solution was kept in 80–85 °C range [12]. The pH value of the solution is kept at ~12 throughout the deposition process. In the final step, the dried Si substrate was vertically dipped into the bath solution for depositing a nanoscale ZnS film. After a duration of 180 min, a uniform thin layer of zinc sulfide (ZnS) appears on the exterior face of the substrate. In order to remove the loosely adherent particles, the substrate was rinsed in the deionized

water. The as prepared substrate then given a heat treatment at 200 °C temperature for an hour to anneal the deposited film [13].

3 Results and Discussion:

3.1 Crystalline Phase Analysis

The crystal structure of as-fabricated nanoscale ZnS film was investigated using a Bruker D8 X-ray diffractometer within the criterion Cu K_α 1.5418 Å from 20 to 80° with the step of 0.02°. Figure 1 portrays an XRD pattern of as fabricated nanoscale ZnS film in the 2θ range of 20–80°. The XRD pattern clearly displays four Bragg peaks at the diffraction angles (2θ) of around 28.3, 47.5, 49.01 and 56.4°. The broad XRD peak at around 28.3° can be a result of the overlap of (111) and (002) peaks of cubic zincblende and wurtzite hexagonal phases, respectively. The XRD peaks at 47.5° and 56.4° may respectively be assigned to (220) and (311), crystal planes of a cubic zincblende structure as verified using JCPDS Card No: 05–0566. In contrast, the peak at 49.01° can be linked to (110) planes of wurtzite hexagonal ZnS phase (JCPDS file no. 75–1547). The lattice constants a and c of ZnS hexagonal phase are 3.72 and 6.16 Å, respectively, which are found in agreement with the previously reported values [14]. The calculated c/a ratio stands at 1.656, which is very close to the theoretical value. Moreover, the XRD peak at about 51.2° is most likely to be linked with (113) planes of Si substrate. XRD pattern confirms the polycrystalline character with formation of mixed phase (cubic zincblende and wurtzite hexagonal) in the prepared ZnS film [15].

Scherrer formula was explored to estimate the average size of crystallite in the nanoscale ZnS film via accounting for the full-width at half maximum (FWHM) of the sharpest (111) peak of XRD pattern using the equation:

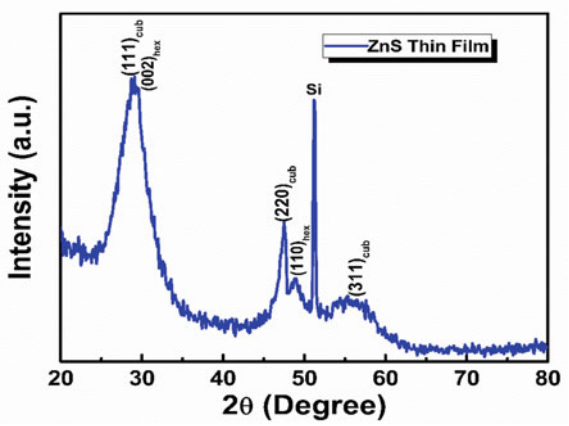

Fig. 1 The XRD patterns of as-fabricated ZnS thin film on *p*-type Si-substrate

$$D = \frac{k\lambda}{\beta cos\theta} \tag{1}$$

where β and θ are FWHM and Bragg angle of XRD peaks, respectively. k is a shape factor constant, which can be chosen as 0.9 in nanoscale films. λ (1.5406 Å) is wavelength of monochromatic incident X-rays. From Eq. 1, It is estimated that ZnS thin film has an average crystallite size (D) of 2.6 nm. Also, the calculated lattice constant ($a = 5.45$ Å) in the cubic phase of ZnS is found in close agreement with the reported literature [16, 17].

3.2 Optical Analysis

The optical properties and energy band gap (E_g) of as-fabricated zinc sulfide (ZnS) thin film on a glass slide were obtained using UV–Visible spectroscopy technique (UV spectrometer 3092 Lab India). The optical spectra in the absorption mode for the fabricated nanoscale ZnS film were examined in the wavelength range of about 300–800 nm. The as fabricated film shows an approximate 75% transparency in the entire visible range of the spectra. The results clearly indicate that as prepared films can be used in transparent and nearly-transparent devices [17]. The band gap (E_g) energy of the fabricated nanoscale ZnS film can be estimated using Tauc's formula given below,

$$\alpha hv = C\left(hv - E_g\right)^n \tag{2}$$

where *hv,* α, and E_g represent the photon energy, absorption-coefficient, and band gap energy of the nanoscale film, respectively. *C and n are* constants. For the direct band gap semiconductors, the value of "*n*" can be chosen as 1/2.

Figure 2 displays the variation of $(ahv)^2$ against the photon energy (hv). The inset curve in Fig. 2 shows the graph of absorbance *vs* wavelength (λ) of incident beam of photons. The effective optical band gap (E_g) of the as prepared ZnS thin film was calculated using Tauc plot analysis. As per the relation, the intercept of the extrapolated line onto the photon energy (hv) axis provides the estimation of the band gap. It can be noted that the as calculated band gap (3.8 eV) is slightly higher than the previously reported band gap (~3.6 eV) for ZnS thin film [1, 2]. A trivial rise in the band gap can be accredited to the possible quantum size effects in the nanoscale ZnS film. The direct energy band gap of the fabricated nanoscale ZnS film is at around 3.8 eV, which is equivalent to an absorption edge at about 328 nm. The results clearly show that as-fabricated ZnS thin film can be employed in the fabrication of excellent UV sensing devices in the future [18].

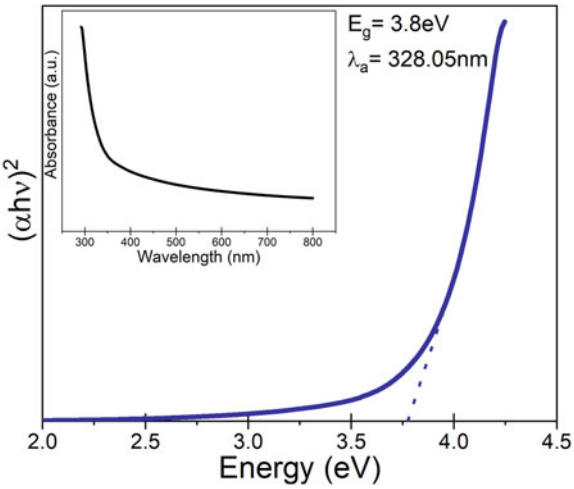

Fig. 2 The plot of $(ahv)^2$ vs photon energy (hv) (the inset shows the UV–Vis absorption spectra)

3.3 Electrical Analysis

The variation of the current against the voltage (I–V) on as fabricated nanoscale ZnS film was recorded by making a *n-ZnS/p-Si* heterojunction on a Keithley 6517 electrometer. The heterojunction was prepared by developing the silver connections on the annealed ZnS film on a Si substrate.

Figure 3 displays a I–V (current-voltage) analysis of the n–ZnS/p–Si heterojunction at room-temperature with a forward bias condition. The heterojunction of n–ZnS/p–Si portrays an almost exponential variation of the current against the forward applied voltage, which closely resembles the forward-biased rectifier diode characteristics in a voltage range of 0–10 V. From the I–V analysis on the deposited film, it can be said that as prepared n–ZnS/p–Si heterojunction can be employed in fabrication of variety of diodes and photoconductive devices [19].

4 Conclusions

In the present study, the thin film of zinc sulfide (ZnS) was fabricated successfully on a silicon substrate employing a very simple and effective chemical bath deposition (CBD) method. CBD method allows the deposition of a large area of thin film at low temperatures inexpensively, and conveniently. The structure of the fabricated thin film has been analyzed using XRD technique, which confirms the formation of mixed, cubic zincblende and wurtzite hexagonal, phases in the prepared ZnS thin film. The crystallite size in the thin film, estimated from the Scherrer formula, is found to be about 2.6 nm. The UV–Vis spectroscopy portrays the absorbance and transmittance properties of ZnS thin film. The energy band gap of about 3.8 eV

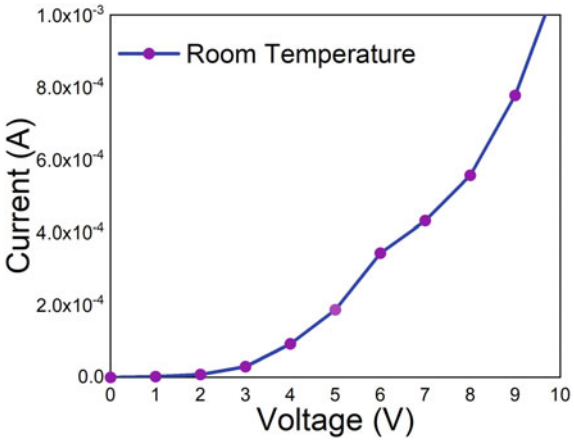

Fig. 3 The current–voltage (I–V) investigation of n–ZnS/p–Si heterojunction

was calculated in ZnS thin film using Tauc plot analysis. I–V characteristics of the deposited thin film show a diode-type behaviour. In today's semiconductor industry, ZnS is an extremely dominant and versatile material that can be used in a wide range of applications including UV light sensors, photodetector, solar photovoltaic cells, and semiconductor diodes, etc.

Acknowledgements It is our pleasure to thank Dr. Arvind Kumar for all his support and encouragement throughout the experiment. Our sincere gratitude goes to ARSD College, University of Delhi, New Delhi-110021, India which provided us with the thin film fabrication facilities that we needed for this study. This was made possible through the Material Science Research Lab (Theory and Experiment), Department of Physics, ARSD College. In addition, we appreciate the financial support provided by SRM Institute of Science and Technology, Delhi-NCR Campus, Modinagar, Ghaziabad, 201204.

References

1. Kumar A et al (2021) Highly responsive and low-cost ultraviolet sensor based on ZnS/p–Si heterojunction grown by chemical bath deposition. Sens Actuators, A Phys 331:112988. https://doi.org/10.1016/j.sna.2021.112988
2. Kaplan HK, Akay SK, Ahmetoglu M (2018) Photoelectrical properties of fabricated ZnS/Si heterojunction device using thermionic vacuum arc method. Superlattices Microstruct 120:402–409. https://doi.org/10.1016/j.spmi.2018.05.055
3. Alsultany FH, Hassan Z, Ahmed NM (2016) A high-sensitivity, fast-response, rapid-recovery UV photodetector fabricated based on catalyst-free growth of ZnO nanowire networks on glass substrate. Opt Mater (Amst) 60:30–37. https://doi.org/10.1016/j.optmat.2016.07.004
4. Ahmadi A, Shoushtari MZ, Farbod M (2019) Photoelectrochemical application of WS2 nanosheets prepared via a low-temperature CVD method. J Mater Sci Mater Electron 30(7):6342–6349. https://doi.org/10.1007/s10854-019-00936-7
5. Sreedhar M, Neelakanta Reddy I, Bera P, Shyju TS, Anandan C (2017) Studies of Cu-doped ZnS thin films prepared by sputtering technique. Surf Interface Anal 49(4):284–290. https://doi.org/10.1002/sia.6130
6. Ebrahimi S, Yarmand B, Naderi N (2019) Enhanced optoelectrical properties of Mn-doped ZnS films deposited by spray pyrolysis for ultraviolet detection applications. Thin Solid Films 676(February):31–41. https://doi.org/10.1016/j.tsf.2019.02.046
7. Tanaka K, Moritake N, Uchiki H (2007) Preparation of Cu_2 $ZnSnS_4$ thin films by sulfurizing sol-gel deposited precursors. Sol Energy Mater Sol Cells 91(13):1199–1201. https://doi.org/10.1016/j.solmat.2007.04.012
8. Kumar A et al (2023) Materials science in semiconductor processing fabrication of low-cost and fast-response visible photodetector based on ZnS : Mn/p–Si heterojunction. Mater Sci Semicond Process 155:107226. https://doi.org/10.1016/j.mssp.2022.107226
9. Sathishkumar M, Saroja M, Venkatachalam M (2018) Influence of (Cu, Al) doping concentration on the structural, optical and antimicrobial activity of ZnS thin films prepared by Sol-Gel dip coating techniques. Optik (Stuttg) 182:774–785. https://doi.org/10.1016/j.ijleo.2019.02.014
10. Sharma A, Sahoo P, Thangavel R (2018) A study on photoelectrochemical properties of ZnO@ZnS nanostructures synthesized via facile ion-exchange approach. AIP Conf Proc 1961. https://doi.org/10.1063/1.5035217
11. Kumar A et al (2022) Role of deposition parameters on the properties of the fabricated heterojunction ZnS/p–Si Schottky diode. Phys Scr 97(4):45819. https://doi.org/10.1088/1402-4896/ac6078
12. Kumar A, Pednekar D, Mukherjee S, Choubey RK (2020) Effect of deposition time and complexing agents on hierarchical nanoflake-structured CdS thin films. J Mater Sci Mater Electron 31(19):17055–17066. https://doi.org/10.1007/s10854-020-04263-0
13. Gupta S et al (2023) Temperature-dependent study of the fabricated ZnS/p–Si heterojunction. Phys B Condens Matter 657:414831. https://doi.org/10.1016/j.physb.2023.414831
14. Mahmood K et al (2015) Phase transformation from cubic ZnS to hexagonal ZnO by thermal annealing. J Semicond 36:033001. https://doi.org/10.1088/1674-4926/36/3/033001
15. Mohamed SH, El-Hagary M, Emam-Ismail M (2010) Thickness and annealing effects on the optoelectronic properties of ZnS films. J Phys D Appl Phys 43(7). https://doi.org/10.1088/0022-3727/43/7/075401
16. Zazueta-Raynaud A et al (2019) ZnS and ZnO nanocomposite for near white light tuning applications. In: 2019 symposium on design, test, integration and packaging of MEMS and MOEMS, DTIP, pp 1–3. https://doi.org/10.1109/DTIP.2019.8752671.
17. Lee GJ, Anandan S, Masten SJ, Wu JJ (2016) Photocatalytic hydrogen evolution from water splitting using Cu doped ZnS microspheres under visible light irradiation. Renew Energy 89:18–26. https://doi.org/10.1016/j.renene.2015.11.083
18. Xu X et al (2018) A real-time wearable UV-radiation monitor based on a high-performance p–CuZnS/n–TiO_2 photodetector. Adv Mater 30(43):1–8. https://doi.org/10.1002/adma.201803165

19. Das M, Sarmah S, Sarkar D (2019) Distinct and enhanced ultraviolet to visible ZnS-porous silicon (PS):p–Si hybrid metal-semiconductor-metal (MSM) photodetector. Mater Today Proc 46:6247–6252. https://doi.org/10.1016/j.matpr.2020.04.779

Investigation of Dielectric and Electrical Behaviour of $Y_2Ti_2O_7$ Pyrochlore

Saurabh Singh, Raghvendra Pandey, Gaurav Gautam, Anjani Kumar Singh, Bheeshma Pratap Singh, Asha Dhaiya, and Prabhakar Singh

1 Introduction

Yttrium titanate $Y_2Ti_2O_7$ (referred as YTO) is one of the pyrochlores, has prime importance due to its thermal stability, high refractive index value (~2.34), low phonon energy (~712 cm^{-1}), electrical and dielectric behaviour [1]. The total valence state in the metal cations of $A_2B_2O_7$ is + 14 which is balanced by O^{2-} anions with its 7 lattices [2]. The structure of the stable crystalline phases of $A_2B_2O_7$ is different and it depends on the ionic radii ratio, i.e. r_A/ r_B. If the value of ionic radius ratio is greater than 1.78, then the phase will be monoclinic layered perovskite belonging to P21 space group [3]. If the value of ionic radii ratio is in between 1.46 and 1.78, then the phase will be ordered pyrochlore belonging to Fd-3m space group [2]–[5]. However, in the case where the value of ionic radius ratio is less than 1.46, the phase

S. Singh (✉)
Department of Applied Sciences, Bharati Vidyapeeth's College of Engineering, GGSIP University Delhi, New Delhi 110063, India
e-mail: saurabh.singh@bharatividyapeeth.edu; saurabh.singhiitbhu@gmail.com

R. Pandey · A. K. Singh
Department of Physics, Atma Ram Sanatan Dharma College, University of Delhi, New Delhi 110021, India

G. Gautam
Department of Physics, Graphic Era Hill University, Dehradun 248001, India

B. P. Singh
Department of Physics, Gandhi Institute of Technology and Management, Deemed to Be University, Visakhapatnam, AP 530045, India

A. Dhaiya
Department of Physics, Ramjas College, University of Delhi, New Delhi 110007, India

P. Singh
Department of Physics, Indian Institute of Technology (Banaras Hindu University) Varanasi, Varanasi, UP 221005, India

S. B. Krupanidhi et al. (eds.), *Recent Advances in Functional Materials and Devices*, Springer Proceedings in Materials 37, https://doi.org/10.1007/978-981-99-6766-7_21

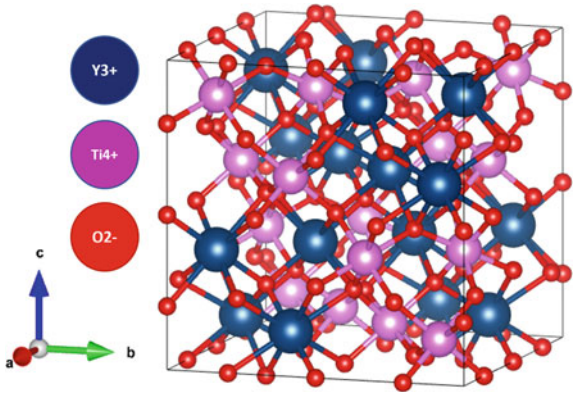

Fig. 1 Crystal strcture of $Y_2Ti_2O_7$ Pyrochlore

will be disordered defective fluorite belonging to Fd-3m space group. But, when the value of ionic radius ratio is near 1.17, the phase will be rare earth C-type having a structure similar to Y_2O_3 [4, 5]. The crystal structure of $Y_2Ti_2O_7$ pyrochlore is shown in Fig. 1.

The $Y_2Ti_2O_7$ pyrochlore is a single phase polycrystalline ceramic having dense and compact microstructure [6]. The conduction mechanism in $Y_2Ti_2O_7$ was investigated by impedance spectroscopy and exhibited the dielectric dispersion due to influence of low-frequency and assists in understanding conduction mechanism with oxygen ions. The conductivity of YTO depends on the temperature and follows Jonscher's power law [7]. This exhibits the strong dispersive nature at the lower temperature on the entire frequency range and the weak dispersive behaviour at high temperature in the high frequency range [7, 8]. At high temperature, the electrical conductivity rises due to relaxation phenomenon owing to the change of transformation by hopping with small-range ionic transportation [8]. However, the improvement in the elecrrical conductivity by temperature depicts the negative coefficient of resistance in YTO.

The electrical behaviour of the YTO pyrochlore ceramic is generally investigated by using electrical impedance spectroscopy in term of frequency at different temperature values. There are contribution of different relaxation (grains and its boundaries, and other like interface) in the impedance spectra used for electrical response of polycryatalline materials. There are four parameters to investigate the dielectric and electrical behaviour of materials. These are complex parameters, i.e. impedance (Z*), electric modulus (M*), admittance (Y*), and permittivity (ε*) [9]. These parameters are also correlated mutually as per the following equations:

$$Z^* = Z' - j\,Z'' = \frac{1}{j\omega C_o \epsilon^*},$$

$$M^* = M' + \,jM'' = \frac{1}{\epsilon^*},$$

$$Y^* = Y' + jY'' = j\omega C_o \epsilon^*,$$

$$\epsilon^* = \epsilon' - j\epsilon'',$$

$$D = tan\delta = \frac{\varepsilon''}{\varepsilon'} = \frac{M''}{M'} = \frac{Z'}{Z''} = \frac{Y'}{Y''}$$

where (Z′, M′, Y′, ε′) and (Z″, M″, Y″, ε″) are real parts and imaginary parts of the complex quantity, respectively. $\omega = 2\pi\nu$ is the angular frequency, C_o is the vacuum capacitance, defined mathematically as ε_o/k, where ε_o is called the permittivity of free space (i.e. 8.854×10^{-14} F/cm). The k is the ratio of l (thickness of th sample) and A (area of the sample).

Moreover, YTO pyrochlore has trivalent Y-site cations and tetravalent Ti-site cations. The intercalation of Y and Ti sites exhibits oxygen deficiencies and creates lattice distortions that can be used for different applications like IT-SOFC, oxygen sensors, photocatalysts, etc. Generally, YTO play a prime role for high oxygen vacancy concentration and interactions between phonon which exhibit low activation energy for diffusion [10]. Therefore, in the present work, the electrical properties are discussed on the basis of dielectric behaviour.

2 Experimental Procedure

The $Y_2Ti_2O_7$ pyrochlore was fabricated using the two oxide powders namely Y_2O_3 and TiO_2 in stoichometric ratio via solid state technique. These two powders were procured from Alpha Aessar having a purity of 99.9%. These oxide powders were taken in zirconia jar and mixed for 6 h in planetary ball mill using acetone medium at 150 rpm. After mixing, the powder was taken in alumina crucible and calcined for 12 h at 1300 °C under normal atmosphere and which was followed by furnace cooling [11]. The solution of polyvinyl alcohol solution (2%) was used to bind the powder and pellets were made at 75 kN load. The sintering was performed on the pallets at 1400 °C temperature in two sections. In the first section, the pellets were heated at temperature of 500 °C for 1 h using the 2 °C temperature per minute to remove the binder. While in the second section, the same pellets heated at 500 °C were heated at 1400 °C using the heating rate of 4 °C per minute followed by cooled in furnace [12]. The one or two pellets were converted into fine powder using crushing method and different charecterization was performed. The purity of the developed phases in the material was investigated via X-ray diffractometer at ambient temperature which was using the Cu-Kα radiation having the wavelength of 1.54 Å. The pellets sample were also made according to standard procedure for further charecterization. First, the pellet samples were polished via a different range of emery paper and also coated with the help of silver paint on both of the surfaces which were matured via heating

process conducted at 750 °C for 20 min [7, 12]. After that, these silver-coated pellets were tested by using Wayne Kerr (6500 P Series) LCR meter where the pellets were placed in between the two electrodes for the measurement of electric and dielectic properties under the 260–800 °C.

3 Results and Discussion

3.1 Electrical Properties

The conductivity spectra of YTO ceramic depending on frequency over the temperature from 400 °C to 800 °C represents the dispersion behaviour on both the frequency, i.e. low and high regime [7, 15].

The real portion of the total conductivity of YTO ceramic can be defined as:

$$\sigma' = \sigma_{dc} + \sigma_{ac} \tag{1}$$

where σ_{ac} is the ac conductivity and in general it can be represented by power law of Jonscher

$$\sigma_{ac}(\nu, T) = A\nu^n \tag{2}$$

where A, ν and n are the constant, frequency and the exponent factor. Generally, the value of n is less than 1. The above Eq. (1) can be written as below form:

$$\sigma' = \sigma_{dc}\left[1 + \left(\frac{\nu}{\nu_H}\right)^n\right] \tag{3}$$

$$\nu_H = \left(\frac{\sigma_{dc}}{A}\right)^{1/n} \tag{4}$$

ν_H is called the frequency of hopping, which emerges the dispersion in conductivity spectra [7, 13, 16].

The hopping frequency can be interpreted from the power law of Jonscher as defined in Eq. (3) while A is the function of site quantity and depends on the length of hopping for consecutive jumps of charge carriers [7, 17]. For YTO ceramic, the conductivity spectra obey the Jonscher power law at all measured temperatures as per Eq. 1. The dc conductivity does not depend on frequency as shown in Fig. 2 which indicates the long-term transportation of the ions. As a result of it, the successful jump between the two sites may be remarkable [18]. Frequency independent plateau region of this conductivity spectra occurs due to random motion of charge carriers however frequency dependent dispersive regime of the conductivity spectra arises due to correlated hopping motion of charge carriers. DC conductivity, hopping frequency

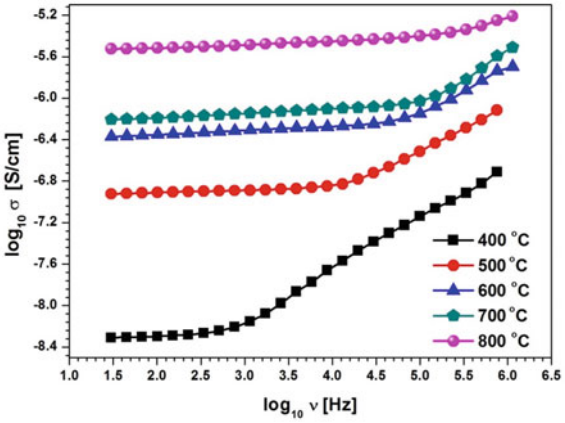

Fig. 2 Conductivity spectra as a function of frequency for YTO pyrochlore in 400 to 800 °C temperature range

and exponent factor for this conductivity spectra were calculated by Jonscher's power law fitting of the spectra.

Arrehinus plot was obtained from the DC conductivity values and from the single fitted line value of activation energy comes ~0.99 eV which shows the conduction is due to the continuous generation of charge carriers at elevated temperature. The DC electrical conductivity of YTO was observed ~10^{-5} S.cm^{-1} at 800 °C which shows its insulating properties although its conductivity can be improved with acceptor or donor doping metal ions at different sites. Figure 3 shows the Arrhenius plot obtained conductivity spectra along with linear fit.

In order to understand the electrical behaviour in the investigated pyrochlore, we have fitted the impedance spectra by semicircular equation using the method of non-linear fit [7]. Figure 4a–f shows the Cole–Cole plots of YTO at various temperatures viz. 300 to 800 °C at a step of 100 °C. These figures clearly reveal the occurrence of two relaxation activities which are due to grain and its boundary in

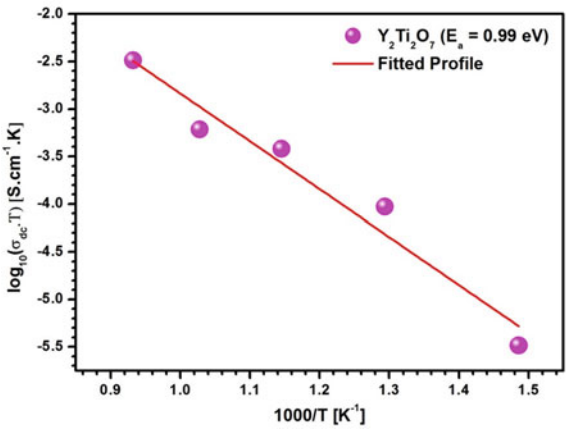

Fig. 3 Arrehnius plot for the dc conductivity spectra of $Y_2Ti_2O_7$ pyrochlore

high and low frequency regions, separately. However, the contribution by interface is not noticed clearly. When the temperature is less than 300 °C, a straight line is observed in the impedance spectra which clearly indicates the insulating behaviour of the present material. The semicircular arc is observed as a rise in temperature, i.e. greater than 300 °C which represents the grain contribution in electrical properties on both of the frequency (low and high) regions [13, 14]. These two semi-circular arcs are fitted using the Nyquist equation and non-linear least square technique. In high frequency region, the diameter value of the first semicircle gives the value of grain resistance represented by R_g while in low frequency region, the diameter value of second semicircle provides the value of grain boundary resistance represented by R_{gb} [14]. From the cole cole plot, it can be clealy seen that as the temperature rises the value of real resistance decreases and at 800 °C it was observed as minimum. The value of total conductivity can be calculated using these plots by utilizing the dimensional details of the YTO sample. These values are almost similar as obtained from the conductivity spectra of YTO. The increase in conductivity with the rise of temperature is mainly due to the increase of mobile charge carriers in the conduction process.

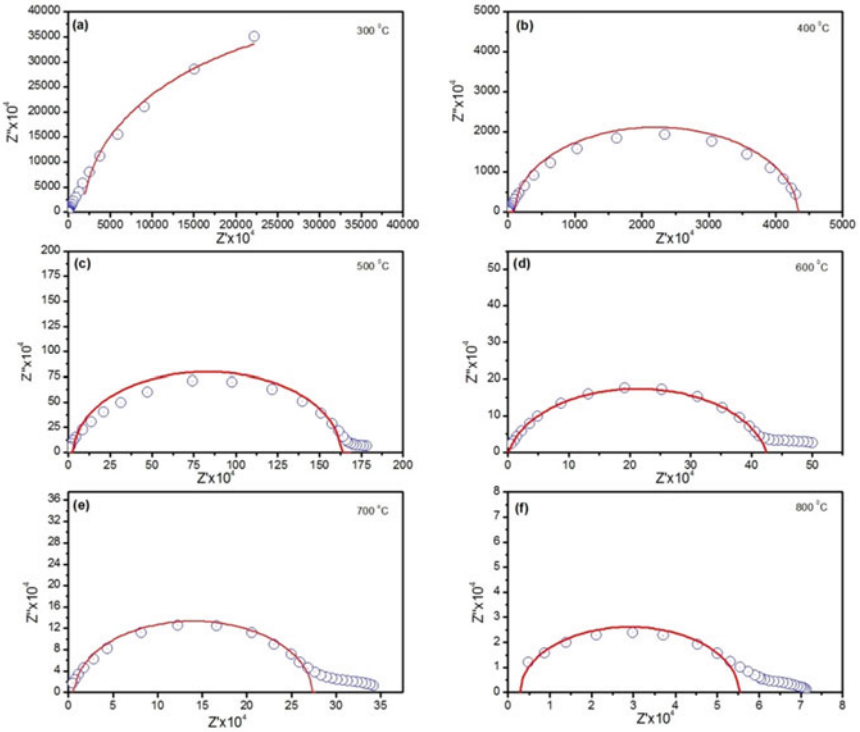

Fig. 4 The Cole-Cole plots of YTO pyrochlore at various temperatures

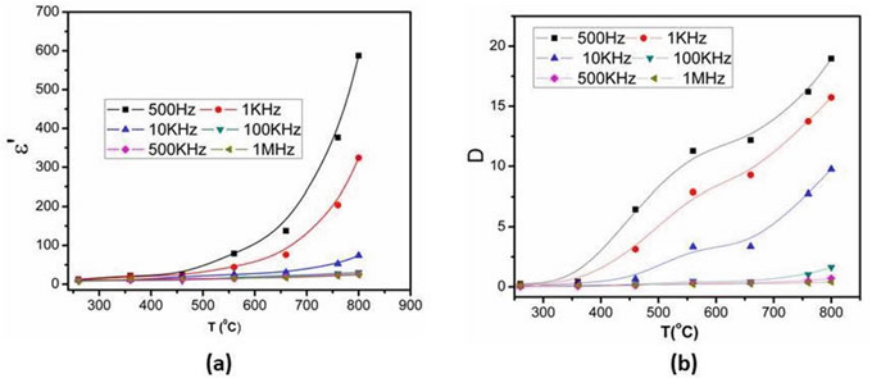

Fig. 5 The variation of **(a)** Real part of permittivity (ϵ') and **(b)** loss tangent (D) w.r.t. temperature at a few frequencies values

3.2 Dielectric Properties

Figure 5a, b reveals the variation of the real part of permittivity (ϵ') and loss tangent (D) in terms of temperature at a few frequencies. It is clearly observed the relaxation peak above 500 °C is found for all investigated frequencies in the plot between loss tangent and temperature as shown in Fig. 5b. This relaxation peak is moved to higher side of temperature on increasing frequency [17, 19]. However, this kind of relaxation peak is not observed in plot between permittivity and temperature as shown in Fig. 5a. The minute investigation of this plot indicates the movement of peaks to high temperature on rising frequency value [20].

Figure 6a, b also shows the ϵ' and D in terms of frequency for some temperature values. It is observed from Fig. 6a of permittivity versus frequency plot that the ϵ' decreases suddenly as increasing the frequency prior to 1 kHz and beyond that it decreases gradually with frequency followed by gaining the constant value [21]. However, the plot between tangent loss versus frequency shows the small relaxation between the frequencies 1 kHz and 100 kHz at all investigated temperatures (Fig. 6b). When the temperature is increased then the position of the peak related to this relaxation moves to the side of high frequency. The rapid increment in the values of permittivity and loss tangent at low frequencies and high temperature corresponds to space charge polarization in the system [22].

Figure 6a, c depicts the variation in dielectric constant (ε') and modulus (M'') with the variation of frequency between 50 Hz and 1 MHz at a few temperatures. The values of these dielectric parameters decrease as the value of frequency increases at all measured temperatures. It was observed that the real part of the permittivity versus frequency plot supports the decrement of ϵ' and suddenly increases with frequency upto 1 kHz and beyond that it decreases gradually with frequency as interpreted by Fig. 5a. This behaviour supports the polar nature in YTO ceramic [7]. In the low frequency region, the dispersion of M'' with frequency is more and it rises with an

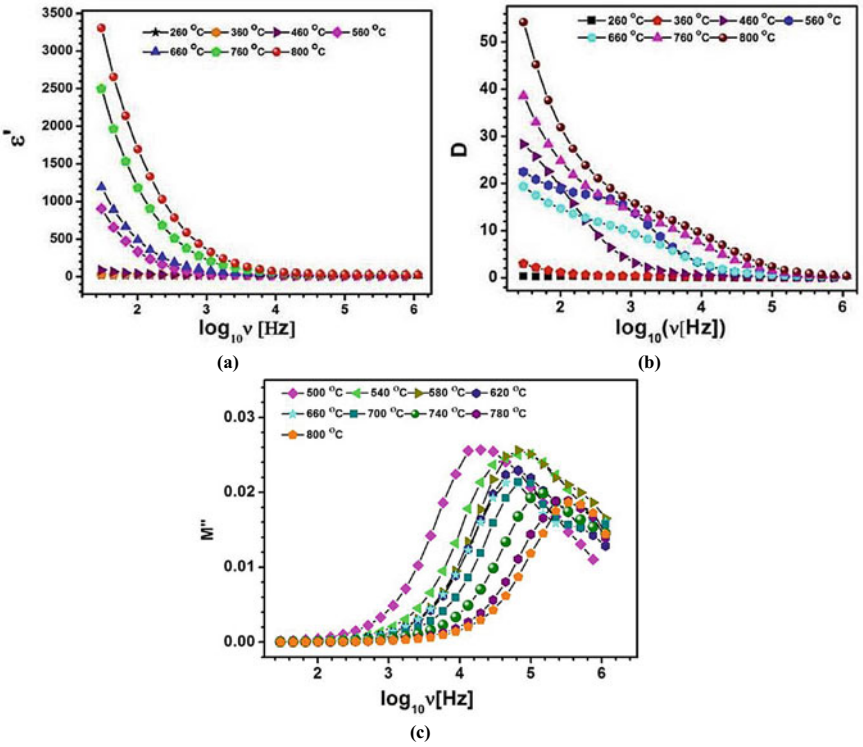

Fig. 6 **(a)** Dielectric constant (ϵ') **(b)** loss tangent (D) and **(c)** electric modulus (M") with the variation of frequency at different temperature values

increase in the temperature. The observed relaxation peaks in the Fig. 6 reflects the contribution of the orientational and space charge polarization process in the system.

The ε′ and D decline with increase in frequency for all investigated temperatures, which corresponds the polar nature of YTO pyrochlore ceramic. It is also observed that the ε' and D both rise with rise in temperature. The dispersion of dielectric constants at various frequency ranges is noticed and this behaviour rises with rise in temperature [23]. The oxygen ions are responsible for the polarization, which is called as space charge polarization. Figure 6c shows the variation of electric modulus (M″) versus $\log_{10}\nu$ at a few selected temperatures. It is observed that the value of electric modulus (M″) rises with increasing frequency and attains highest value followed by decrement. However, modulus peak decreases with the rise of temperature and shifted higher frequency side. This modulus relaxation was investigated between the temperature 500 °C and 800 °C. It is also observed from this figure that an asymmetric broadening and shifting occurs along the high frequency regime in M''_{max} with an increase in temperatures. As a result of this, the relaxation changes with varying time constants in YTO ceramic and having non-Debye type relaxation [24]. The occurrence of this peak in the value of M″ at ν_{max} represents the frequency resembles

to the transition from large to small hopping of ionic transport, which depicts the relaxation frequency of YTO pyrochlore ceramic [25, 26].

4 Conclusions

The pyrochlores ceramic $Y_2Ti_2O_7$ is successfully fabricated by solid state method. Electrical and dielectric properties were studied this single phase formed $Y_2Ti_2O_7$ pyrochlore. The impedance spectroscopic results show the non-debye response and activation energy values indicate conduction is due to the regulation of ionic transport. The grain and grain boundary characteristics contribution is also observed in the impedance curves. The AC conductivity depends on frequency and follows the Jonscher power law behaviour to describe the electrical properties. Electrical condctivity increases with rise of temperature due to generation of mobile charge carriers. Space charge polarization dominates at lower frequencies. YTO shows good dielectrc properties although the dielectric behaviour of YTO can be modified by altering the inherent disorder available in pyrochlores structure.

Acknowledgements One of the authors Saurabh Singh is thankful to Prof. P. Singh, Department of Physics, at Indian Institute of Technology (BHU), Varanasi for providing the experimental facilities to investigate the dielectric and electrical behaviour of YTO Pyrochlore ceramic with LCR meter.

References

1. Ting H-A, Chen Y-Y, Li Z-M, Hsieh Y-P, Chiu S-K, Ting C-C (Apr.2022) The Effect of Annealing on the Optoelectronic Properties and Energy State of Amorphous Pyrochlore Y2Ti2O7 Thin Layers by Sol-Gel Synthesis. Crystals 12(4):564
2. Subramanian MA, Aravamudan G, Subba Rao GV (1983) Oxide pyrochlores—A review. Prog Solid State Chem 15(2):55–143
3. Lang M et al (2010) Review of A2B2O7 pyrochlore response to irradiation and pressure. Nucl Instruments Methods Phys Res Sect B Beam Interact with Mater Atoms 268(19): 2951–2959
4. Zhang X et al (2017) Ni/Ln 2 Zr 2 O 7 (Ln = La, Pr, Sm and Y) catalysts for methane steam reforming: the effects of A site replacement. Catal Sci Technol 7(13):2729–2743
5. Xu J et al (Aug.2020) A2B2O7 pyrochlore compounds: A category of potential materials for clean energy and environment protection catalysis. J Rare Earths 38(8):840–849
6. Joseph D, Kaliyaperumal C, Mumoorthy S, Paramasivam T (Apr.2018) Dependence on temperature of the electrical properties of nanocrystalline Y2Ti2O7 ceramics. Ceram Int 44(5):5426–5432
7. Singh S, Jha PA, Varma S, Singh P (May2017) Large polaron hopping phenomenon in lanthanum doped strontium titanate. J Alloys Compd 704:707–716
8. Sharma SK et al (Dec.2020) Structural, dielectric and electrical properties of pyrochlore-type Gd2Zr2O7 ceramic. J Mater Sci Mater Electron 31(24):21959–21970
9. Sinclair DC, West AR (Oct.1989) Impedance and modulus spectroscopy of semiconducting BaTiO 3 showing positive temperature coefficient of resistance. J Appl Phys 66(8):3850–3856
10. Minervini L, Grimes RW, Sickafus KE (Dec.2004) Disorder in Pyrochlore Oxides. J Am Ceram Soc 83(8):1873–1878

11. Singh BP, Parchur AK, Singh RK, Ansari AA, Singh P, Rai SB (2013) Structural and up-conversion properties of Er3+ and Yb3+ co-doped Y2Ti2O7 phosphors. Phys Chem Chem Phys 15(10):3480
12. Singh S et al (Oct.2019) Suitability of Sm3+-Substituted SrTiO3 as Anode Materials for Solid Oxide Fuel Cells: A Correlation between Structural and Electrical Properties. Energies 12(21):4042
13. Kolekar YD, Sanchez L, Rubio EJ, Ramana CV (Apr.2014) Grain and grain boundary effects on the frequency and temperature dependent dielectric properties of cobalt ferrite–hafnium composites. Solid State Commun 184:34–39
14. Ali MA, Khan MNI, Chowdhury F-U-Z, Akhter S, Uddin MM (Sep.2015) Structural Properties, Impedance Spectroscopy and Dielectric Spin Relaxation of Ni-Zn Ferrite Synthesized by Double Sintering Technique. J Sci Res 7(3):65–75
15. Nealon TA (Dec.1987) Low-frequency dielectric responses in PMN-type ceramics. Ferroelectrics 76(1):377–382
16. Lin Y-H, Li M, Nan C-W, Li J, Wu J, He J (Jul.2006) Grain and grain boundary effects in high-permittivity dielectric NiO-based ceramics. Appl Phys Lett 89(3):032907
17. Dhahri A, Dhahri E, Hlil EK (2018) Electrical conductivity and dielectric behaviour of nanocrystalline La 0.6 Gd 0.1 Sr 0.3 Mn 0.75 Si 0.25 O 3. RSC Adv 8(17):9103–9111
18. Zhang Y, Wang M, Le Z, Huang G, Zou L, Chen Z (May2014) Preparation and characterization of pyrochlore oxide Y2Ti2O7 nanocrystals via gel-combustion route. Ceram Int 40(4):5223–5230
19. Ben Amor I, Ghallabi Z, Kaddami H, Raihane M, Arous M, Kallel A (2010) Experimental study of relaxation process in unidirectional (epoxy/palm tree fiber) composite. J Mol Liq 154(2–3):61–68
20. Huang S et al (Jul.2015) Effect of Al3+ substitution on the structural, magnetic, and electric properties in multiferroic Bi2Fe4O9 ceramics. J Solid State Chem 227:79–86
21. Maurya D, Kumar J, Shripal (2005) Dielectric-spectroscopic and a.c. conductivity studies on layered Na2-XKXTi3O7 (X=0.2, 0.3, 0.4) ceramics. J Phys Chem Solids 66(10):1614–1620
22. Barick BK, Mishra KK, Arora AK, Choudhary RNP, Pradhan DK (2011) Impedance and Raman spectroscopic studies of (Na 0.5 Bi 0.5)TiO 3. J Phys D Appl Phys 44(35):355402
23. Pandit P, Satapathy S, Gupta PK (Jul.2011) Effect of La substitution on conductivity and dielectric properties of Bi1−xLaxFeO3 ceramics: An impedance spectroscopy analysis. Phys B Condens Matter 406(13):2669–2677
24. Badali Y, Altındal Ş, Uslu İ (Jun.2018) Dielectric properties, electrical modulus and current transport mechanisms of Au/ZnO/n-Si structures. Prog. Nat. Sci. Mater. Int. 28(3):325–331
25. Ngai KL, Rendell RW (Apr.2000) Interpreting the real part of the dielectric permittivity contributed by mobile ions in ionically conducting materials. Phys Rev B 61(14):9393–9398
26. Mohapatra SR et al (Aug.2016) Effect of cobalt substitution on structural, impedance, ferroelectric and magnetic properties of multiferroic Bi2Fe4O9 ceramics. Ceram Int 42(10):12352–12360

Preparation and Structural Investigation of Olivine Structured $LiFePO_4$

Veronica Thongam, Hera Tarique, Radheshyam, and Raghvendra Pandey

1 Introduction

In order to achieve the goals of sustainability the advancement of rechargeable batteries is considered to be one of the great technical hurdles in today's world. Out of the various types of rechargeable batteries, one of the pivotal leaps is the development of lithium-ion batteries. It finds applications in various portable devices including mobile phones, tablets, laptops, etc., and also utilised in electric vehicles and grid applications. The dominance of lithium-ion batteries in the rechargeable battery market may be attributed to the fact that lithium metal possesses the lowest reduction potential in the electrochemical series and has small size and lower mass of the atoms and ions. Consequently, Li-ion batteries have high gravimetric/volumetric energy density as well as high-power density in comparison to other forms of rechargeable battery. The history of lithium-ion battery can be traced back to the determination of the electrode potential of lithium metal, which led to the search for a supper battery [1, 2]. The physical structure of lithium-ion battery comprises of an anode, a cathode, an electrolyte, and a porous separator with metal contacts connected to the anode and cathode for acting as charge collectors. A major advancement in the development of the research of cathode material came from the works of Goodenough et al. who worked on transitional metal oxide. All three of the leading

V. Thongam
Department of Physics, Amity Institute of Applied Sciences, Amity University, Noida 201303, India

H. Tarique
Department of Physics, Jamia Millia Islamia (Central University), New Delhi 110025, India

H. Tarique · R. Pandey (✉)
Department of Physics, ARSD College, University of Delhi, New Delhi 110021, India
e-mail: raghvendra@arsd.du.ac.in

Radheshyam
Department of Physics, Ramjas College, University of Delhi, New Delhi 110007, India

S. B. Krupanidhi et al. (eds.), *Recent Advances in Functional Materials and Devices*,
Springer Proceedings in Materials 37, https://doi.org/10.1007/978-981-99-6766-7_22

cathode oxide chemistries came into existence from the works of Goodenough and his team at University of Oxford and University of Texas [1]. This gave rise to the discovery of three types of lithium cathode oxide in the 1980s, with the support of three visiting scientists, Koichi Mizushima, Michel Thackeray and Arumugam Manthiram. They worked separately on three different oxide cathodes, Layered oxides, spinel and polyanion types [2]. Layered oxide, the first class of cathode oxide discovered was so called because its structure consists of alternating layers of metal oxide and lithium stalked together [3, 4]. The structure of layered lithium oxide cathode consists of hexagonal close-packed (HCP) layers of oxygen atoms with octahedral sites between them occupied by cobalt and lithium ions. It exhibits favourable structural attributes, with high electrical conductivity of lithium-ions. It also exhibits fast charging and discharging characteristics with impressive cycling life [2]. Of all the various types of layered metal oxides, the first cathode material to be investigated and used for commercial application in the early 1990s is the layered $LiCoO_2$ [5]. The crystal structure of $LiCoO_2$ is incredibly dependent on its stoichiometry. At perfect stoichiometry the lithium ions are evenly distributed between the cobalt ions in the octahedral sites. However, at low concentrations of Li, the lattice becomes distorted, and the lithium ions may occupy interstitial sites between the octahedral layers, resulting in lower stability and reduced performance [6]. $LiCoO_2$ has a theoretical capacity of 274 mAh/g, but its actual practical capacity is typically around 140–160 mAh/g, owing to the inherent structural instability at low lithium concentrations [6]. $LiCoO_2$ has good electrochemical performance due to its low resistance and high conductivity, which enables efficient electron transfer and ion diffusion. In 1991, Sony introduced the first commercially available lithium-ion battery using a $LiCoO_2$ cathode [5]. This led to the widespread adoption of lithium-ion batteries in portable electronic devices. However, $LiCoO_2$ is susceptible to structural degradation over time, which can lead to capacity fade and reduced performance. This degradation is mainly due to solid-electrolyte interphase (SEI) layer being formed on the surface of the cathode material, which can reduce the availability of lithium ions for transport and increase the resistance of the cathode [7]. To address these issues, researchers have explored modifications to the $LiCoO_2$ structure, such as doping with other elements or replacing cobalt with other transition metals [6]. Another popular type of layered oxide used for battery cathode is Lithium Nickel Cobalt Manganese Oxide ($LiNi_xMn_yCo_zO_2$) also known as NCM cathode. Depending on the concentration of nickel cobalt and manganese there are different types of NCM cathodes. An example is NCM111 which has an equal ratio of Ni, Co and Mn. They generally offer a better capacity retention and longer cycle life compared to $LiCoO_2$. They also have good thermostability and high energy density depending on the type used [8]. The second type of cathode discovered was $LiMn_2O_4$ [2]. Its structure possesses similarities to the structure of $LiMO_2$ layered structure. $LiMn_2O_4$ crystal structure is characterised by a face-centered cubic (FCC) lattice with metal cations occupying both tetrahedral and octahedral sites. The general formula for spinel compounds is LiM_2O_4, where M represents different transitional metals. In the case of $LiMn_2O_4$, M is manganese (Mn) [6]. In the spinel structure of $LiMn_2O_4$, the cations of lithium are found in the tetrahedral sites while those of manganese are found in the octahedral sites (Fig. 1).

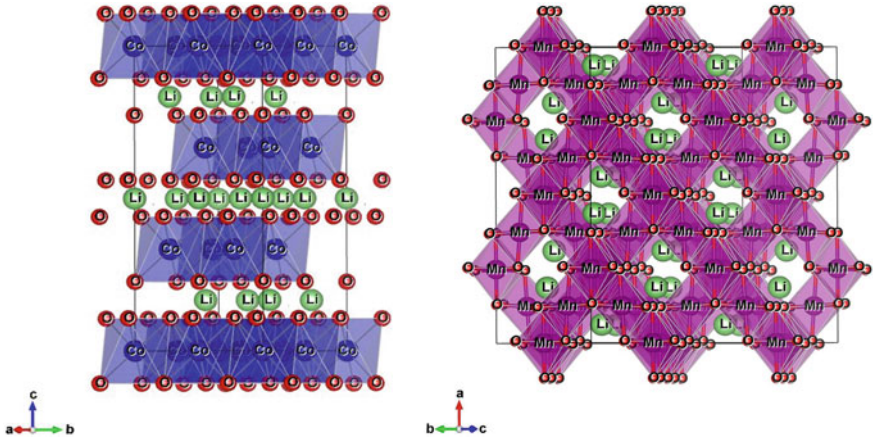

Fig. 1 Crystal structure of $LiCoO_2$ and $LiMn_2O_4$

The oxygen atoms are located at the center of both the tetrahedra and octahedra, forming a close-packed oxygen sublattice. The structure of $LiMn_2O_4$ is quite stable and provides a three-dimensional diffusion pathway for Lithium ions resulting in fast conductivity of lithium ions [6]. $LiMn_2O_4$ has good theoretical capacity (148 mAh/g) and is relatively low cost, making it an attractive alternative to $LiCoO_2$ [7]. However, $LiMn_2O_4$ faced significant fading of capacity owing to the dissolution of Mn^{2+} ion into the electrolyte and presence of new phases generated by micro strain arising from the cycling process. To combat these problems $LiMn_2O_4$ was doped with many dopants at the Mn sites [6].

The other significant type of cathode was polyanion type, out of which $LiFePO_4$ was found to be the most impressive. It was discovered in 1997 by Goodenough et al. [9] and significant improvements were made to find widespread application in battery materials of electric vehicles [10]. In the structure of $LiFePO_4$ iron and lithium ions each occupy one-eighth of the octahedral positions in the slightly deformed hexagonal closed packed oxygen anion arrays that make the structure of $LiFePO_4$ (Fig. 2). LiO_6 and FeO_6 are both found along the c axis and alternately in the b axis direction. The matching tetrahedral locations where the Li atoms are located are connected by PO_4 in the a–c planes. The diffusion of Lithium ions is limited to a unidirectional motion along the direction of the b axis [6, 11]. It possesses a theoretical value of specific capacity equivalent to 170 mAh/g with a practical value of 165 mAh/g. It has been observed that $LiFePO_4$ exhibits excellent cycle stability at low currents, which can be attributed to the similarity in structures between $LiFePO_4$ and $FePO_4$. The $LiFePO_4$ possesses a highly stable crystal structure even at high temperatures of up to 400 °C [10]. This contributes to the excellent cycle performance, is attributed to the fact that there is only a very small change in volume occurs during charge and discharge, an estimate of only 6% [6].

Therefore, seeing the widespread application of $LiFePO_4$ as battery material, it is worthy to study its physical, structural, spectroscopic and electrochemical properties.

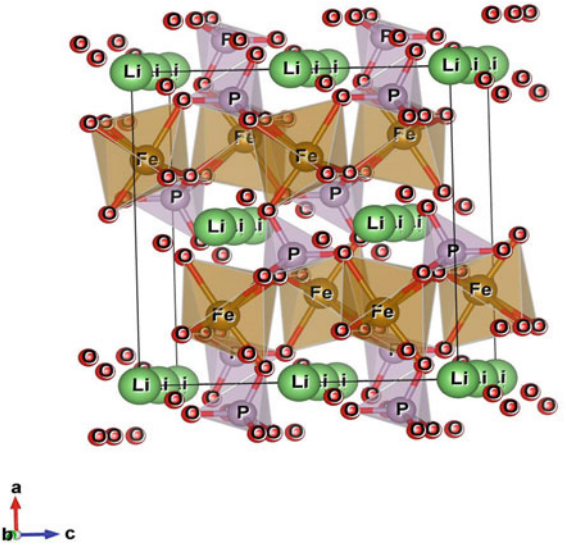

Fig. 2 Crystal structure of olivine $LiFePO_4$

2 Experimental Procedure

The solid-state synthesis route was adopted for the preparation of $LiFePO_4$. The used precursors were Li_2CO_2 (99.9%), $NH_4H_2PO_4$ (99.9%) and Fe_2O_2 (99.9%). The precise stoichiometric amounts of precursors were weighed out and ground together with acetone in an agate mortar pestle for two hours. This mixture was further processed using a planetary ball mill in acetone media within a zirconia jar at 25 rpm. The mixture is then dried to remove all residual acetone. The mixture was further calcined in a muffle furnace at a constant temperature 600 °C for three hours. Heating rate is carefully controlled at a steady rate of 5 °C per minute to ensure that the sample is evenly heated throughout the process. Once the three-hour calcination period is complete, the sample is then cooled down slowly at a constant rate of 5 °C per minute. This calcined sample is ground again and characterisations were performed.

The X-Ray diffraction of calcined powder sample of $LiFePO_4$ was carried out at room temperature. Cu-Kα source of radiation was used for XRD measurement. XRD data was recorded in the range of 15 to 60º with a step size of 0.026. After this FTIR spectroscopy measurement was carried out for $LiFePO_4$ for the range of 400–4000 cm^{-1} at room temperature. UV absorption spectra was also recorded for the $LiFePO_4$ samples. For SEM and EIS measurement sample powder was pelletised with the mixture of 4% PVA (Polyvinyl Alcohol) solution. Then pellets were subjected to sintering in a muffle furnace at temperature 800 °C. This sintering process promotes bonding and consolidation of the particles, resulting in densification of the pellet structure. During the sintering process, the heating and cooling rate of the furnace is carefully controlled at a steady pace of 5 °C per minute. The sample pellet was

coated with gold—palladium using Gold Sputter Coater model JEC300 and SEM–EDX was performed for that pellet sample. SEM micrographs were collected at room temperature. This technique is used for the examination of the surface morphology, microstructure, and elemental composition of the pellets. The sintered pellet is taken and coated with conducting film (silver) on both of its faces. This is then bound to the surface of the pellet by placing the muffle furnace for one hour at 500 °C, the heating and cooling rates are kept at a constant rate of 5 °C per min. Impedance Spectroscopy measurement was done using Nova control Impedance analyser at temperature range of –10 °C to 150 °C taking interval of 20 °C.

3 Results and Discussion

The XRD patterns of the material obtained by Bruker D8 Discover machine consist of Primary $LiFePO_4$ phase along with a few minor secondary phases (marked with *). The XRD pattern of $LiFePO_4$ is shown in Fig. 3. Powder XRD pattern was index using standard JCPDS data No. 83–2092 which corresponds to orthorhombic *Pnma* space group.

In this case, the X-ray pattern shows that the fabricated sample is crystalline in nature. There is presence of other phases along with primary phase indicates the presence of impurities in the sample. These impurities were identified as FeP and $FePO_4$, and may be appeared due to incomplete reactions or unfavourable condition during synthesis. Overall, the XRD pattern provides valuable information about the crystal structure, composition, and symmetry of the sample.

FTIR (Fourier-transform infrared spectroscopy) of the sample was obtained using Nicolet iS50 FTIR Tri-detector. The FTIR analysis of the sample revealed the presence of two absorption regions in the spectrum. These regions are associated with

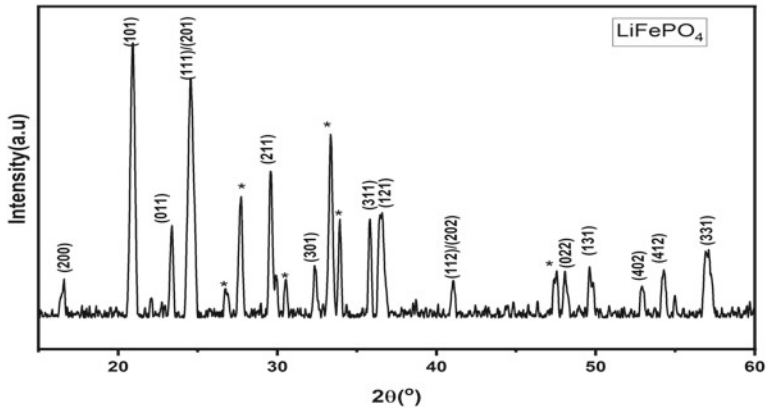

Fig. 3 XRD pattern of $LiFePO_4$

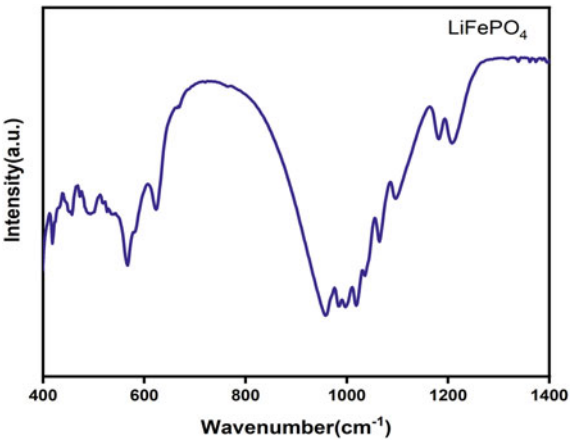

Fig. 4 FT-IR spectra of $LiFePO_4$

the vibrations of bonds of the phosphate ions present in the sample. Figure 4 shows the FTIR spectrum of $LiFePO_4$.

In the high wave number region, the vibrations observed are predominantly symmetrical and asymmetrical vibrations of the P-O bonds. The internal vibrations of the $\nu 3$ mode were observed at 1100 cm^{-1} and 1040 cm^{-1}, which correspond to the asymmetrical stretching of the P-O bonds in the phosphate ion. The $\nu 1$ mode was found at 960 cm^{-1} and corresponds to the symmetrical stretching of P-O bonds in the phosphate ion. In the low wavenumber region, symmetrical and asymmetrical bending of the P-O bonds were observed. The vibrational modes of $\nu 4$ were found at 500 cm^{-1} and 560 cm^{-1}, corresponding to the asymmetrical bending of P-O bonds in the phosphate ion. The $\nu 2$ modes were found at 420 cm^{-1} and 460 cm^{-1} and correspond to the symmetrical bending of P-O bonds in the phosphate ion [13]. Overall, the observed FTIR spectrum indicates that the sample contains phosphate ions and provides information about the vibrational modes associated with the P-O bonds. The specific positions and intensities of the peaks can provide insights into the sample composition and structure.

SEM micrograph of the $LiFePO_4$ surface obtained in the lab using JEOL JSM6610LV model reveals the phase crystal formation, characterised by polygonal-shaped grains with a porous nature (Fig. 5). The SEM micrograph revealed that the $LiFePO_4$ sample connected grains with porous spaces. The sample's grain size ranges from 0.75 μm to 6 μm, with the highest grain density, as determined by ImageJ software, with the highest grain density seen between 1–3 μm. The SEM image indicates that the $LiFePO_4$ exhibits a distinct and uniform grain structure throughout the surface. Some dots were seen the the SEM image may corresponds impurity phases.

Figure 6 shows the SEM—EDX scan of the $LiFePO_4$ pellet. The elementary analysis of the pellets of the sample using Energy-Dispersive X-ray (EDX) analysis on its surface revealed the presence of three elements: oxygen, phosphorus, and iron. However, the inability to detect Lithium is attributed to its low atomic number which

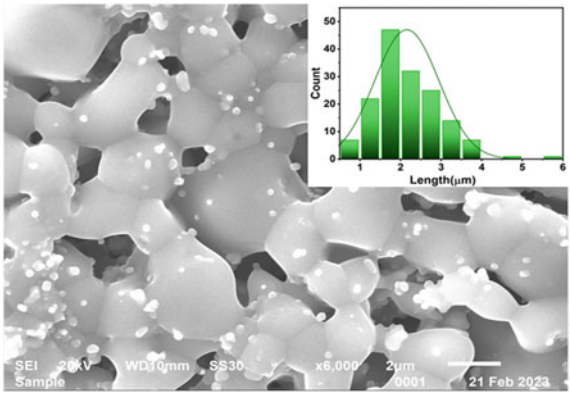

Fig. 5 SEM morphology of $LiFePO_4$ pellet

makes it difficult to detect using EDX analysis. Additionally, the position of lithium within the $LiFePO_4$ crystal structure may further hinder its detection as the lithium ions are located within the tunnels formed by $FePO_4$ tetrahedra, which can shield them from X-ray interactions and reduce their signal intensity in the analysis. The EDX results are shown in Table 1. Theoretical and observed values of elemental confinement were almost found comparable.

The UV spectra was plotted w.r.t. absorbance vs energy over the energy range 1.55–4.55 eV using double beam UV—Visible Spectroscopy in Fig. 7. Band gap of $LiFePO_4$ was also calculated using this absorption spectra. In the initial stage, 1.55–3.4 eV a constant value of absorbance was observed and after 3.4 eV steady increase in the absorbance was observed and after 3.65 eV there was an abrupt increase in the absorbance seen, this is where the absorbance edge present.

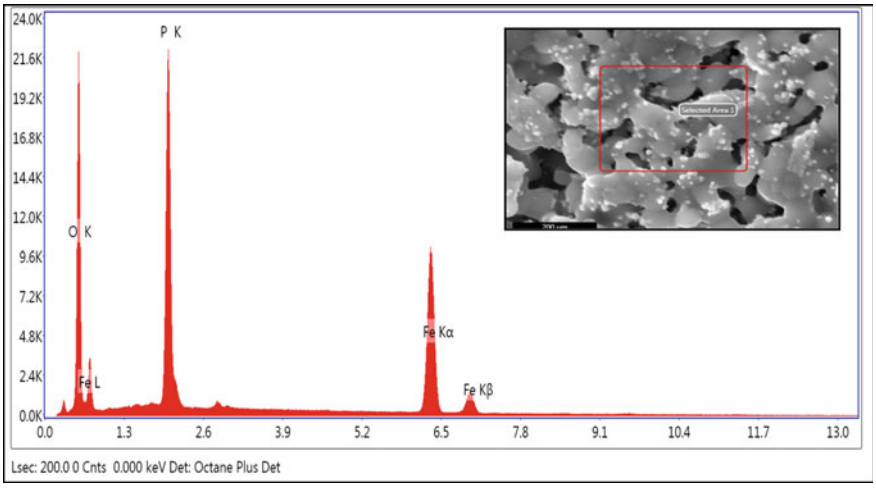

Fig. 6 EDX scan of surface of $LiFePO_4$ pellet

Table 1 The result of EDX data from surface of the $LiFePO_4$ pellet

Elements	Weight percentage	
	Theoretical	Observed
O	40.57	35.01
P	19.63	22.17
Fe	35.40	42.82
Li	4.40	nil

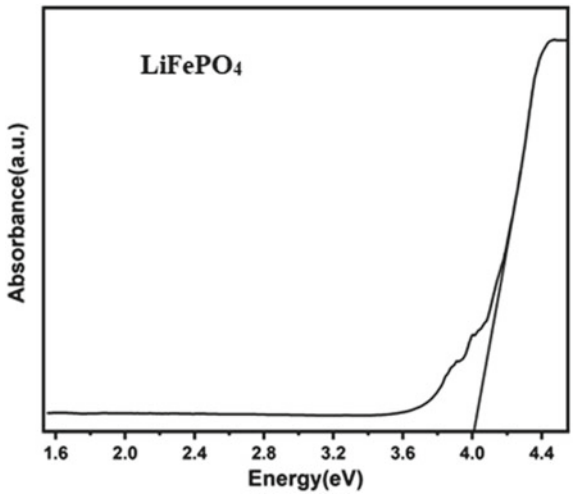

Fig. 7 Absorbance spectra (Tauc plot) of $LiFePO_4$

The abrupt increase in the compound indicates the presence of band gap and that the energy is approaching the threshold value of band gap, which is responsible for the absorbance of energy. By plotting the Tauc plot, the band gap was found to be ~ 4 eV which is consistent with previous experimental value [14, 15].

Impedance analysis was conducted on silver-coated sintered pellet of $LiFePO_4$ in the temperature range from -10°C to 150°C with the help of Novocontrol impedance analyser, at intervals of 20 °C (Fig. 8). From the Impedance Spectroscopy measurement, Cole–Cole Plots were drawn and it observed that two semicircles are present, one at high frequency region and another at mid-frequency region followed by a straight line in the low frequency region. The presence of two semicircles in the Cole–Cole Plot point towards the presence of two separate charge transfer mechanisms occurring in the $LiFePO_4$ pellet. Since the pellet is a polycrystalline material the two semicircles indicate different charge transfer mechanisms present in the crystal due to grain and grain boundary.

Cole—Cole indicates the variation of real vs imaginary impedance at various temperatures. Conductivity of the sample at various temperature was obtained from Arrhenius's plot as shown in Fig. 9. It was observed that as temperature increases the value of the conductivity was also increases this is due to generation of mobile

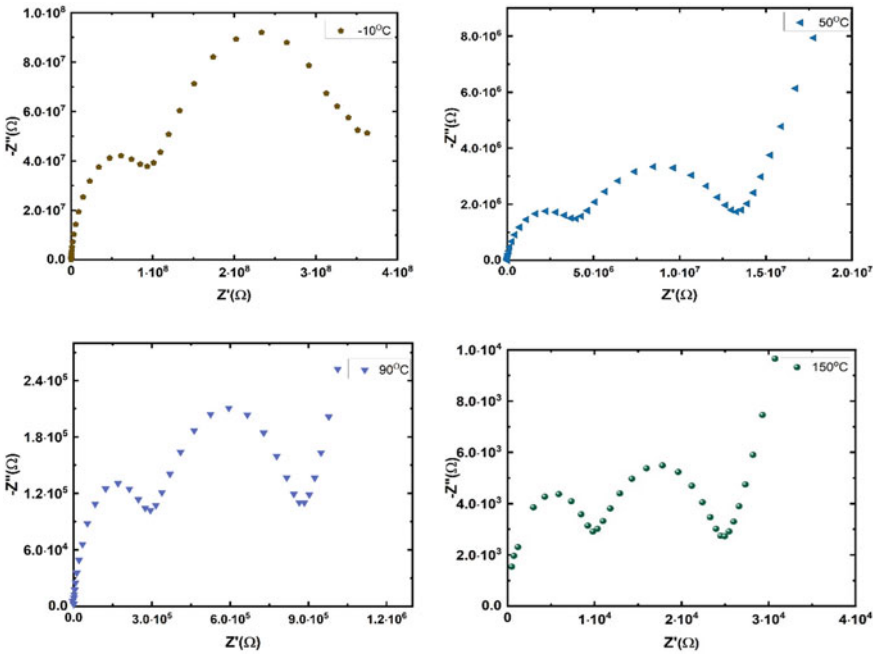

Fig. 8 Cole–Cole impedance plot of $LiFePO_4$ at −10 °C, 50 °C, 90 °C and 150 °C

charge carriers inside the system. The electrical conductivity was found to be around 10^{-5} to 10^{-6} S.cm^{-1} at 150 ºC.

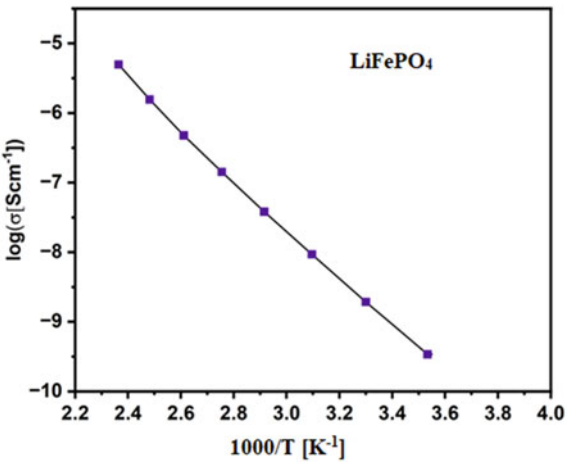

Fig. 9 Arrehnius plot for total conductivity of $LiFePO_4$

4 Conclusions

In conclusion, we have synthesised the $LiFePO_4$ sample using solid state synthesis method and further analyse it using X-Ray Diffraction, FT-IR Spectroscopy, UV and Scanning Electron Microscopy techniques. The SEM imaging of the pellet of $LiFePO_4$ indicates that polygonal crystal grains are formed, it gives information on the size of the grain and indicates the porous structure of the pellet of the compound. The FTIR spectroscopy provided data on the functional groups present in a phosphate group, aiding in the identification of molecular bonds and vibrations. The UV—Visible gives us insight on the energy band gap and EIS establishes the electrical properties of $LiFePO_4$ synthesised. These studies provided valuable insights on its structural and chemical properties. The use of these combined techniques has allowed for a comprehensive characterisation of the sample of $LiFePO_4$, providing a deeper understanding of its properties and behaviour. The results obtained from XRD, SEM, and FTIR analysis have contributed to the understanding of the compound's structure, morphology, and chemical composition, which are crucial aspects for further analysis of properties and development of modification of its properties, and exploration of its potential applications. EIS measurements give insight on the material's conductivity and electrochemical behaviour which is much required for its use as battery cathode material.

Acknowledgements Authors are thankful to USIC, DU for providing all the measurement facilities. Authors acknowledge the UGC-BSR for funding support.

References

1. Winter M, Barnett B, Xu K (2018) Before Li Ion Batteries. Chem Rev 118(23):11433–11456. https://doi.org/10.1021/acs.chemrev.8b00422
2. Whittingham MS (1976) Electrical energy storage and intercalation chemistry. Science (80) 192(4244):1126–1127 https://doi.org/10.1126/science.192.4244.1126.
3. Manthiram A (2020) A reflection on lithium-ion battery cathode chemistry. Nat Commun 11(1):1550. https://doi.org/10.1038/s41467-020-15355-0.
4. Mizushima K, Jones PC, Wiseman PJ, Goodenough JB (1980) LixCoO 2 (0<x-1): A new cathode material for batteries of high energy density. Mater Res Bull 15(6):783–789. https://doi.org/10.1016/0025-5408(80)90012-4
5. Goodenough JB (1971) Metallic oxides, Prog Solid State Chem 5(C): 145–399 https://doi.org/10.1016/0079-6786(71)90018-5.
6. Schipper F, Erickson EM, Erk C, Shin J-Y, Chesneau FF, Aurbach D (2017) Review—Recent Advances and Remaining Challenges for Lithium Ion Battery Cathodes. J Electrochem Soc 164(1):A6220–A6228. https://doi.org/10.1149/2.0351701jes
7. Xu B, Qian D, Wang Z, Meng YS (2012) Recent progress in cathode materials research for advanced lithium ion batteries. Mater. Sci. Eng. R Reports 73(5–6):51–65. https://doi.org/10.1016/j.mser.2012.05.003
8. Nitta N, Wu F, Lee JT, Yushin G (2015) Li-ion battery materials: Present and future. Mater Today 18(5):252–264. https://doi.org/10.1016/j.mattod.2014.10.040

9. Manthiram A (2017) An Outlook on Lithium Ion Battery Technology. ACS Cent Sci 3(10):1063–1069. https://doi.org/10.1021/acscentsci.7b00288
10. Padhi AK, Goodenough JB (1997) Phospho-Olivines as positive-electrode materials for rechargeable lithium batteries. J Electro chem Soc 144:1188–1194. https://doi.org/10.1149/1.1837571
11. Zhang WJ (2011) Structure and performance of LiFePO4 cathode materials: A review. J Power Sources 196(6):2962–2970. https://doi.org/10.1016/j.jpowsour.2010.11.113
12. Kulova TL, Fateev VN, Seregina EA, Grigoriev AS (2020) A brief review of post-lithium-ion batteries. Int J Electrochem Sci 15:7242–7259. https://doi.org/10.20964/2020.08.22
13. Burba CM, Frech R (2004) Raman and FTIR Spectroscopic Study of Li[sub x]FePO[sub 4] ($0 \leq x \leq 1$). J Electrochem Soc 151(7):A1032. https://doi.org/10.1149/1.1756885
14. Zhou F, Kang K, Maxisch T, Ceder G, Morgan D (2004) The electronic structure and band gap of LiFePO4 and LiMnPO 4. Solid State Commun 132(3–4):181–186. https://doi.org/10.1016/j.ssc.2004.07.055
15. Shi S et al (2003) Enhancement of electronic conductivity of LiFePO4 by Cr doping and its identification by first-principles calculations. Phys Rev B - Condens Matter Mater Phys 68(19): 1951081–1951085 https://doi.org/10.1103/PhysRevB.68.195108.

$Tm^{3+}/Dy^{3+}/Tb^{3+}$ Doped Barium Zinc Phosphate Glasses for Multicolor Emission

Kusum Rawat, Amit K. Vishwakarma, Kaushal Jha, and Vinita Tuli

1 Introduction

Solid-state lighting has received a great deal of attention from researchers in recent years. In particular, high-power phosphor-converted (PC) white light-emitting diodes (w-LEDs) are more popular than conventional lighting such as incandescent and fluorescent lamps due to their long life, low power consumption, energy saving, and environmental friendliness [1, 2]. The commercially available phosphor is a combination of InGaN-based LED chip and YAG:Ce^{3+} phosphor, however this has the disadvantage of low Color rendering index (CRI or Ra) value. The value of Ra is nearly 65, which results due to the lack of red component and the value is not acceptable for high quality lighting. To, achieve high Ra, multi-phosphor technique was employed with n-UV LED chip as the source for excitation, which significantly improved the CRI to 90. The InGaN LED chip has the input current falling in the range of 350–1000 mA, which [3] produces high heat flux and the junction temperature of the chip becomes in the range of 150–200 °C. This heat causes severe deterioration of the phosphor material, leading to thermal quenching and yellowing, and carbonization of the organic resin, leading to a decrease in the emission intensity of the phosphor, and a decrease in light transmittance. These effects reduce the luminous efficiency and chromaticity after long-term use, and shorten the life of PC-w LEDs. Therefore, thermal management is one of the most important issues for the fabrication of

K. Rawat
Department of Electronics, Deen Dayal Upadhyaya Gorakhpur University, Gorakhpur, India

A. K. Vishwakarma (✉) · V. Tuli
Department of Physics, Atma Ram Sanatan Dharma College, University of Delhi, New Delhi, India
e-mail: amitvishwakarma85@gmail.com

K. Jha (✉)
University Department of Electronic Science, B R A Bihar University, Muzaffarpur, India
e-mail: kaushaljha096@gmail.com

S. B. Krupanidhi et al. (eds.), *Recent Advances in Functional Materials and Devices*,
Springer Proceedings in Materials 37, https://doi.org/10.1007/978-981-99-6766-7_23

high-power w-LEDs. Glass is considered as the best alternative for this purpose, as it offers excellent thermal resistance, and plays the role of both luminescent converter and encapsulating material. Further, they do not exhibit light scattering loss, which is due to the refractive index mismatch between phosphor and organic resin in pc-w-LEDs. Therefore, luminescent glass is the best alternative and an excellent choice for fabrication of w-LEDs by combining with InGaN LED chip as compared with pc-w-LEDs.

Recently, efforts were made to achieve white light emission from different glasses doped with rare earths. Kesavulu et al [4] and Jha et al [5] reported white light emission from Dy^{3+} doped phosphate glasses. Lakshminarayana et al. reported white light emission from Tm^{3+}/Dy^{3+} co-doped germanate glasses [6] and Sm^{3+}/Tb^{3+} co-doped aluminosilcate glasses [7]. Yang et al. [8] and Zhang et al. [9] revealed white light emission from $Ce^{3+}/Tb^{3+}/Mn^{2+}$, while Zhong et al. [10] proposed the same from $Tm^{3+}/Tb^{3+}/Mn^{2+}$ co-doped glasses. However, there is no report in the literature on the photoluminescence study on $Tm^{3+}/Dy^{3+}/Tb^{3+}$ tri-doped system for the white light generation.

In this work, for the first time Tm^{3+}/Dy^{3+} co- and $Tm^{3+}/Dy^{3+}/Tb^{3+}$ single composition BZT glasses with tunable light emission was prepared through melt-quenching method. The energy transfer analysis and interaction for Tm^{3+}/Dy^{3+} co-doped BZT glasses is discussed in detail based on emission profile. The aim is to prepare BZT glasses for white light and multicolor emission under n-UV excitation.

2 Experimental Procedure

High purity Tm_2O_3, Dy_2O_3, and Tb_4O_7. used to make the glasses, along with analytical $NH_4H_2PO_4$, ZnO, TiO_2, and $BaCO_3$. The table contains information about the glass samples' chemical composition. Stoichiometrically measured chemicals were added to a mortar and pestle, and acetone was used as the mixing liquid. To create a uniform, transparent melt, the homogenized mixed ingredients were placed inside a muffle furnace and heated to 1150 °C for one hour. To lessen thermal and mechanical stress, the melt was removed and then placed onto a metal plate that had been heated to 400 °C for three hours. Using a Shimadzu RF-5301PC spectrofluorometer with a xenon flash lamp as the excitation source, data on photoluminescence (PL) emission and excitation were gathered. Using an Edinburgh FLS920 and a xenon flash lamp as the excitation source, lifetime decay measurements were examined.

3 Result and Discussion

3.1 *Photoluminescent Properties of Tm^{3+}/Dy^{3+} Co-Doped BZT Glasses*

The photoluminescence excitation (PLE) and emission spectra of Tm^{3+} and Dy^{3+} doped BZT glasses are illustrated in Fig. 1a, b, respectively. Figure 1a, represents the PLE spectrum that was attained by fixing emission at 575 nm, and the emission spectrum was recorded at an intense excitation wavelength of 362 nm. The excitation spectrum reveals emission peak centered at 350, 362, 384, 425, 452, and 473 nm arising from the ground level $^6H_{15/2}$ to different excited levels $^6P_{7/2}$, ($^4I_{11/2}$, $^6P_{5/2}$), ($^4F_{7/2}$, $^4I_{13/2}$), $^4G_{11/2}$, $^4I_{15/2}$, and $^4F_{9/2}$, respectively of Dy^{3+} ions. The emission spectra have two intense peaks at 482 and 575 nm attributed to the magnetic dipole ($^4F_{9/2}$ → $^6H_{15/2}$) and forced electric dipole ($^4F_{9/2}$ → $^6H_{13/2}$) transitions, respectively. In Fig. 1b, it can be observed that the excitation spectrum represents a sharp excitation peak centered at 358 nm attributed to the $^3H_6$ → $^1D_2$ transition of Tm^{3+} ion by monitoring emission at 452 nm [6, 11]. The emission spectrum represents a single peak at 452 nm assigned to the $^1D_2$ → $^3F_4$ transition, suggesting it as a suitable candidate for blue LEDs under n-UV excitation.

Figure 2a represents the spectral overlap of the emission peak of Tm^{3+} and excitation peak of Dy^{3+} in the co-doped BZT glasses. This spectral overlap indicates a possible transfer of energy from Tm^{3+} to Dy^{3+}. To study the energy transfer from Tm^{3+} to Dy^{3+} ions, a series of Tm^{3+}/Dy^{3+} co-doped glasses were prepared with

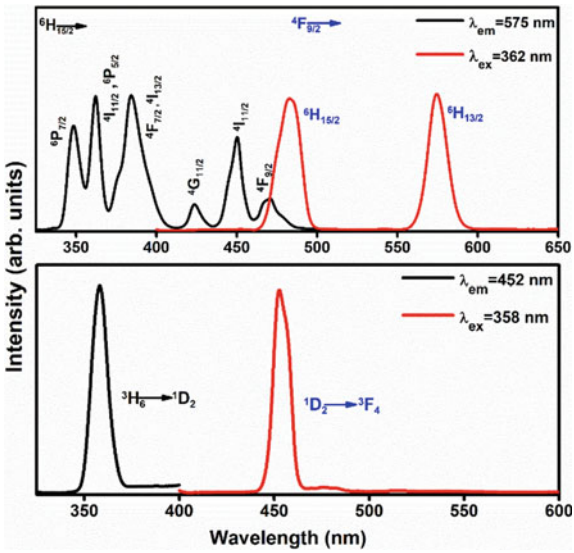

Fig. 1 **a** The excitation spectrum recorded at 575 nm emission and emission spectrum at 362 excitation for DY01 glass. **b** Excitation spectrum at 452 nm emission and emission spectrum at 358 excitation for TM01 glass

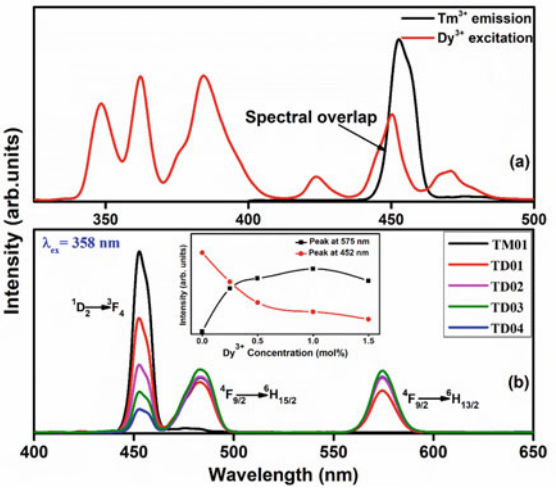

Fig. 2 **a** Spectral overlap of Tm^{3+} emission and Dy^{3+} excitation **b** emission spectra of TM01, TD01, TD02, TD03, and TD04 glass samples under 358 nm excitation (Inset: variation in the emission peaks at 575 and 452 nm under 358 nm excitation)

fixed Tm^{3+} and varying Dy^{3+} concentrations [12, 13]. Figure 2b represents the emission spectra for fixed Tm^{3+} (1.0 mol%) and varying Dy^{3+} (0.0, 0.25, 0.5, 1.0, and 2.0 mol%) concentrations under 358 nm excitation. The emission spectra represented peak at 452 nm attributed to the Tm^{3+}, while the peaks at 482 and 575 nm are due to Dy^{3+} as discussed earlier. With an increase in Dy^{3+} concentration, the emission intensity of the Dy^{3+} bands enhanced and that of Tm^{3+} decreases as represented in the inset of Fig. 2b, which indicates energy transfer from the Tm^{3+} to Dy^{3+} ions. Moreover, the intensity of Dy^{3+} bands increases upto 1 mol% and decreases thereafter as observed in the inset of Fig. 2b, which is due to the concentration quenching phenomenon [14]. The above-mentioned results indicate interaction and energy transfer among Tm^{3+} and Dy^{3+} ions.

The energy transfer between the rare earth ions may occur via exchange or multipolar interactions. To identify, the nature of the interaction between the sensitizer (Tm^{3+}) and the activator (Dy^{3+}), Dexter energy transfer formula, and Reisfeld's approximation, a relation can be deduced as [15]:

$$\frac{\eta_0}{\eta} \propto C^{n/3} \tag{1}$$

where η_0 and η are the quantum efficiencies of the sensitizer/donor (Tm^{3+}) in the absence and presence of the activator/acceptor (Dy^{3+}), C is the additive result of the mole percent of sensitizer (Dy^{3+}) and activator (Dy^{3+}), and n represents the nature of the interaction, that can be 3, 6, 8 and 10 corresponding to exchange, dipole—dipole, dipole-quadrupole and quadrupole—quadrupole interaction, respectively. The value of η_0/η can be approximately determined by the ratio of relative luminescence intensities as:

$$\frac{I_{so}}{I_s} \propto C^{n/3} \tag{2}$$

where I_{so} and I_s are the luminescence intensities of Tm^{3+} in the absence and presence of Dy^{3+}. Figure 3a–d represents the plot of I_{so}/I_s versus $C^{n/3}$ for different values of n = 3, 6, 8, and 10. The best linear fit value was obtained for n = 8, which indicates that the transfer of energy occurs as a result of dipole-quadrupole interaction among the Tm^{3+} and Dy^{3+}.

The lifetime decay curves were recorded by monitoring emission at 462 nm corresponding to $^1D_2 \rightarrow {}^3F_4$ transition of Tm^{3+} ions glass samples (TM01, TD01, TD02, TD03, and TD04) as presented in Fig. 4.

The decay curves were best fitted with the bi-exponential equation equation [16] as mentioned beneath:

$$I = I_0 + A_1 exp\left(-\frac{t}{\tau_1}\right) + A_2 exp\left(-\frac{t}{\tau_2}\right) \tag{3}$$

where I and I_0 are the luminescence intensities at time t and 0, τ_1 and τ_2 represent the fast and slow exponential components respectively; A_1 and A_2 denote the fitting

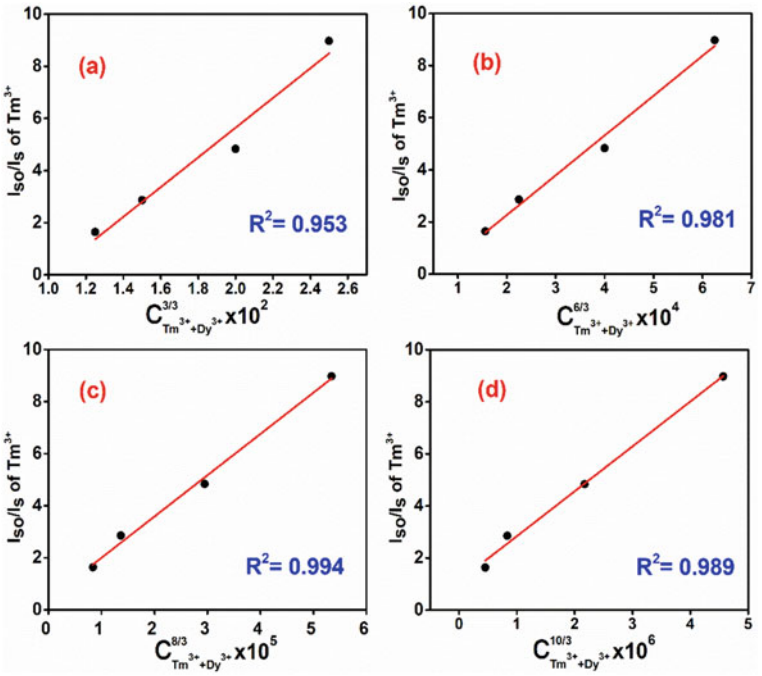

Fig. 3 The dependence of I_{s0}/I_s of Tm^{3+} versus $C_{Dy+Tm}{}^{3/3} \times 10^2$, $C_{Dy+Tm}{}^{6/3} \times 10^4$, $C_{Dy+Tm}{}^{8/3} \times 10^5$, and $C_{Dy+Eu}{}^{10/3} \times 10^6$ for the co-doped glasses under 358 nm excitation

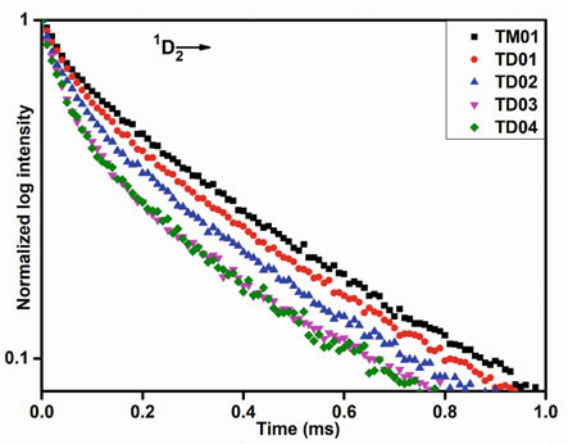

Fig. 4 Decay profiles of DY01, DE01, DE02, DE03, and DE04 glass samples for $^1D_2$ level under 358 nm excitation

constants, and t is the time. The value of the average lifetime for the bi-exponential equations is given by formulae [16]

$$\tau = \frac{A_1\tau_1^2 + A_2\tau_2^2}{A_1\tau_1 + A_2\tau_2} \tag{4}$$

The lifetime values using the above formulae for TM01, TD01, TD02, TD03, and TD04 were found to be 0.492, 0.461, 0.421, 0.401, and 0.388 ms (ms). It is evident that the average lifetime values decrease as we enhance the Dy^{3+} concentration, which strongly indicates energy transfer from Tm^{3+} to Dy^{3+}. The energy transfer efficiency (η_T) values from the Tm^{3+} to Dy^{3+} is evaluated by the formulae mentioned below [17]:

$$\eta_{T(Tb\rightarrow Sm)} = 1 - \left(\frac{\tau_d}{\tau_{d0}}\right) \tag{5}$$

where τ_{d0} and τ_d represents the average decay lifetime of the Tm^{3+} without and with the presence of Dy^{3+}, respectively. The energy transfer probability rate can be calculated in terms of lifetime with the equation mentioned below:

$$P_{T(Tb\rightarrow Sm)} = \frac{1}{\tau_d} - \frac{1}{\tau_{d0}} \tag{6}$$

The energy transfer efficiencies (η_T) and probability rates (P_T) values are presented in Tables 1 and 2. Figure 5 represents the plot for the variation in the average lifetime and energy transfer efficiency values with Dy^{3+} concentration in Tm^{3+}/Dy^{3+} co-doped BZT glasses. It was found that the value of η_T and P_T increases with enhancement in the acceptor concentration.

Table 1 The notations for the glass sample with different rare earth concentration is mentioned in the table

S. No	Glass samples = (40-x) ZnO-35P_2O_5-20BaO-5TiO_2-x(RE_2O_3/RE_4O_7)	Sample name
1	Dy_2O_3 = 1.0 mol %	DY01
2	Tm_2O_3 = 1.0 mol %	TM01
3	Tb_4O_7 = 1.0 mol%	TB01
4	Tm_2O_3 = 1.0 mol %, Dy_2O_3 = 0.25 mol %	TD01
5	Tm_2O_3 = 1.0 mol %, Dy_2O_3 = 0.50 mol %	TD02
6	Tm_2O_3 = 1.0 mol %, Dy_2O_3 = 1.0 mol %	TD03
7	Tm_2O_3 = 1.0 mol %, Dy_2O_3 = 2.0 mol %	TD04
8	Tm_2O_3 = 1.0 mol %, Dy_2O_3 = 0.25 mol %, Tb_4O_7 = 1.0 mol%	TDT01

Table 2 Average lifetime (τ_{avg}), Energy transfer efficiency (η_T), and Energy transfer probability rate (P_T) for glass samples under 358 nm excitation

S. No	Sample name	Average lifetime (τ) (ms)	Energy transfer efficiency (η_T) %	Energy transfer probability rate ($\times 10^3$ s − 1) (P_T)
1	TM01	0.492	–	–
2	TD01	0.461	0.063	0.1367
3	TD02	0.421	0.1443	0.3428
4	TD03	0.391	0.2053	0.5250
5	TD04	0.368	0.2520	0.6849

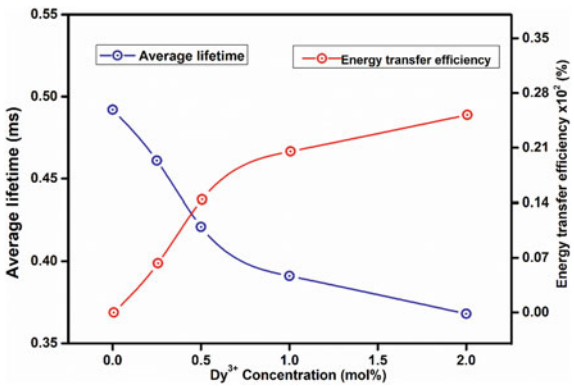

Fig. 5 Average lifetime and energy transfer efficiency variation with Dy^{3+} concentration in Tm^{3+}/Dy^{3+} co-doped BZT glass samples

3.2 *Photoluminescent Properties of $Tm^{3+}/Dy^{3+}/Tb^{3+}$ Co-Doped BZT Glasses*

The emission spectrum for TDT01 was recorded under n-UV excitation of 358 nm as represented in Fig. 6.

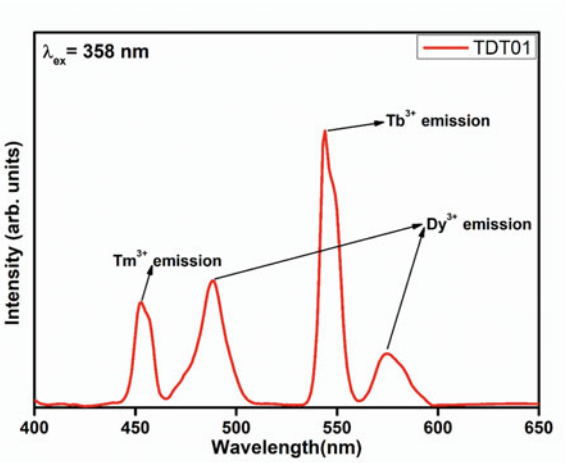

Fig. 6 The emission spectrum of TDT01 glass sample under 358 nm excitation

The emission spectrum reveals the bands related to Tm^{3+} centered 452 nm, while that of Dy^{3+} centered at 482 and 575 nm. In addition to this, an emission band at 575 nm is also observed. The emission band at 544 nm is due to $^5D_4 \rightarrow {}^7F_5$ transition of Tb^{3+} ion [18, 19]. The tri-doped glass sample TDT01 reveals emission bands due to all the three dopants. Based on the emission spectra obtained, the CIE chromaticity coordinates were evaluated which is shown in Fig. 7. The value of the CIE chromaticity coordinates for TM01, DY01, TB01, TD03, and TDT01 glass samples were (0.155, 0.057), (0.365, 0.381), (0.259, 0.590), (0.176, 0.136), and (0.551, 0.437), respectively. The variation in the emission color is all the way from blue to white to green to orange, this clearly indicates that by tuning the dopant concentration such variation in the emission color is achievable. Further, many emissions colors can be obtained by fine-tuning the dopant concentration in co-doped/tri-doped glass samples. All the above results clearly indicate that the above-mentioned glass is a suitable candidate for white light as well as multicolor emission under n-UV excitation.

4 Summary

In conclusion, Tm^{3+}/Dy^{3+} co-doped and $Tm^{3+}/Dy^{3+}/Tb^{3+}$ tri-doped ZBT glasses were successfully prepared by melt quenching technique. In the co-doped glasses, the emission bands of both Tm^{3+} and Dy^{3+} were observed. The emission intensity of Dy^{3+} enhance but Tm^{3+} falls with an increase in Dy^{3+} concentration, which indicates energy transfer among Tm^{3+} and Dy^{3+} under 358 nm excitation. The dipole-quadrupole interaction was found to be present among Tm^{3+} and Dy^{3+}, as confirmed

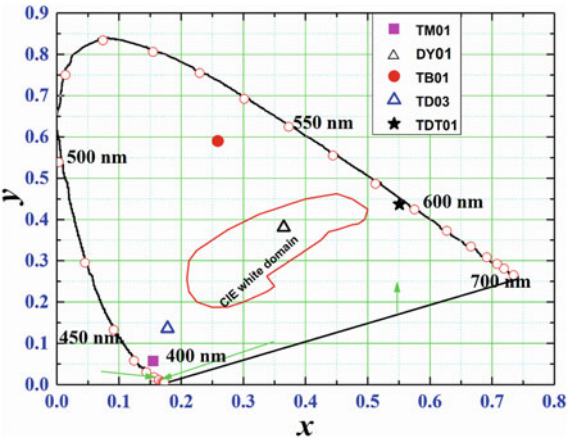

Fig. 7 CIE chromaticity coordinates for TM01, DY01, TB01, TD03, and TDT01 glass sample

by Dexter's energy transfer formula and Reisfeld's approximation. The decay analysis revealed important parameters such as average lifetime, energy transfer efficiency, and probability rate. $Tm^{3+}/Dy^{3+}/Tb^{3+}$ tri-doped glass sample revealed emission due to all three dopants under 358 nm excitation. The CIE chromaticity coordinates reveal that white as well as multicolor emission is achieved in the prepared glass samples. The above results indicate that these glasses will be a suitable candidate for light-emitting diodes under n-UV excitation. Also, there is much future research in the field on possibility of achieving the desired emission color by fine tuning in the dopant concentration. Research possibility is also there to achieve the desired emission color by variation in the excitation wavelength.

References

1. Jiao M et al (2013) Tunable Blue-Green-Emitting $Ba_3LaNa(PO_4)_3F:Eu^{2+}, Tb^{3+}$ Phosphor with Energy Transfer for Near-UV White LEDs. Inorg Chem 52:10340–10346
2. Masai H et al (2013) Narrow energy gap between triplet and singlet excited states of Sn^{2+} in borate glass. Sci Rep 3:3541
3. Liu XY et al (2016) Thermal quenching and energy transfer in novel Bi^{3+}/Mn^{2+} co-doped white-emitting borosilicate glasses for UV LEDs. J. Mater. Chem. C 4:2506–2512
4. Kesavulu CR et al (2017) Physical, vibrational, optical and luminescence investigations of Dy^{3+} -doped yttrium calcium silicoborate glasses for cool white LED applications. J Alloys Compd 726:1062–1071
5. Jha K, Jayasimhadri M (2016) Spectroscopic investigation on thermally stable Dy^{3+} doped zinc phosphate glasses for white light emitting diodes. J Alloys Compd 688:833–840
6. Lakshminarayana G, Yang H, Qiu J (2009) White light emission from Tm^{3+}/Dy^{3+} co-doped oxyfluoride germanate glasses under UV light excitation. J Solid State Chem 182:669–676
7. Lakshminarayana G et al (2009) White light emission from Sm^{3+}/Tb^{3+} codoped oxyfluoride aluminosilicate glasses under UV light excitation. J Phys D Appl Phys 42:015414
8. Yu Y et al (2011) Ce-Tb-Mn co-doped white light emitting glasses suitable for long-wavelength UV excitation. Opt Express 19:19473

9. Zhang X et al (2014) Highly Thermally Stable Single-Component White-Emitting Silicate Glass for Organic-Resin-Free White-Light-Emitting Diodes. ACS Appl Mater Interfaces 6:2709–2717
10. Zhong HJ et al (2015) Luminescence and energy transfer of tm/tb/mn tri-doped phosphate glass for white light-emitting diodes. J Mater Sci: Mater Electron 26:8130–8135
11. Wu L et al (2012) Luminescence and energy transfer of a color tunable phosphor: Dy^{3+}, Tm^{3+}, and Eu^{3+} coactivated $KSr_4(BO_3)_3$ for warm white UV LEDs. J Mater Chem 22:6463
12. Lakshminarayana G et al (2017) Optical absorption, luminescence, and energy transfer processes studies for Dy^{3+}/Tb^{3+}-codoped borate glasses for solid-state lighting applications. Opt Mater (Amst) 72:380–391
13. Xu W et al (2010) Photoluminescence Properties and Energy Transfer of Dy^{3+}-Eu^{3+} Codoped Phosphate Glasses. J Am Ceram Soc 93:3064–3067
14. Sun X-Y, Wu S, Liu X, Gao P, Huang S-M (2013) Intensive white light emission from Dy^{3+}-doped $Li_2B_4O_7$ glasses. J Non Cryst Solids 368:51–54
15. Li G et al (2011) Tunable luminescence of Ce^{3+}/Mn^{2+}-coactivated $Ca_2Gd_8(SiO_4)_6O_2$ through energy transfer and modulation of excitation: potential single-phase white/yellow-emitting phosphors. J Mater Chem 21:13334
16. Li K et al (2015) Host-Sensitized Luminescence Properties in $CaNb_2O_6$:Ln^{3+}(Ln^{3+}=Eu^{3+}/Tb^{3+}/Dy^{3+}/Sm^{3+}) Phosphors with Abundant Colors. Inorg Chem 54:323–333
17. Jha K, Vishwakarma AK, Jayasimhadri M, Haranath D (2017) Multicolor and white light emitting Tb^{3+}/Sm^{3+} co-doped zinc phosphate barium titanate glasses via energy transfer for optoelectronic device applications. J Alloys Compd 719:116–124
18. Rawat K, Vishwakarma AK, Jha K (2020) Thermally stable $Ca_2Ga_2SiO_7$:Tb^{3+} green emitting phosphor for tricolor w-LEDs application. Mater Res Bull 124:110750
19. Zhang X, Mo F, Wu ZC, Chen Y (2018) Achieving green–red-tunable emission through Tb^{3+}–Eu^{3+} energy transfer in $Sr_3Y_2(Si_3O_9)_2$: Tb^{3+}, Eu^{3+} phosphors. J Mater Sci 53:3613–3623

Structural and Optical Properties of Chalcogenide WS_2 Thin Film

Avneesh Kumar, Sandeep Kumar, Mudit Prakash Srivastava, Prachi Yadav, Surbhi, and Devendra Kumar Rana

1 Introduction

The transition metal dichalcogenide compounds are found very useful in a wide range of applications these days [1]. Among the known 2D transition metal dichalcogenides, the tungsten disulphide (WS_2) material possesses high electron mobility owing to the decreased effective mass of electrons in WS_2 [2]. WS_2 exhibits a layered structure. The molecules in the layers of WS_2 are held together by weak van der Waals interactions within each layer of WS_2, there are strong covalent bonds between tungsten and sulfur atoms. The covalent bonds hold the atoms together within each layer, forming a hexagonal lattice [3]. Due to low toxicity, WS_2 can be used safely in a variety of applications including optoelectronic and light-sensing devices [4]. Thin films of WS_2 possess a polycrystalline structure with a hexagonal phase. The WS_2 structure consists of three layers, with a tungsten (W) layer sandwiched between two Sulphur (S) layers. The widely studied transition metal

A. Kumar · M. P. Srivastava
Department of Physics, SRM Institute of Science and Technology, Delhi, NCR Campus Modinagar, Ghaziabad 221005, India

S. Kumar
Department of Physics, Bhaskaracharya College of Applied Sciences, University of Delhi, Delhi 110075, India

P. Yadav
Department of Physics, Kirori Mal College, University of Delhi, New Delhi 110007, India

Surbhi
Department of Applied Physics, Amity Institute of Applied Science (AIAS), Amity University, Noida Sector 125, Noida 201313, India

D. K. Rana (✉)
Material Science Research Lab (Theory and Experiment), Department of Physics, ARSD College, University of Delhi, New Delhi 110021, India
e-mail: drana@arsd.du.ac.in

S. B. Krupanidhi et al. (eds.), *Recent Advances in Functional Materials and Devices*, Springer Proceedings in Materials 37, https://doi.org/10.1007/978-981-99-6766-7_24

dichalcogenide WS_2 nano-thin films have been employed in a range of applications such as low-cost photovoltaics [3], solar cells [4], lubricants [5], and IR sensors [6].

In literature, a lot of techniques such as chemical vapor deposition [7], RF sputtering [8], evaporation [9], and chemical bath deposition [10] techniques have been employed to fabricate WS_2 2-D Nano thin films. Amongst, the chemical bath deposition (CBD) technique offers several advantages such as the processing, low cost, uniformity, large area, and low-temperature thin film deposition [10]. In this study, the CBD method was employed to deposit the tungsten disulfide (WS_2) thin film on a p-Si substrate. The low cost and easy processing of the fabricated WS_2 thin film are the significant features of this study.

2 Experimental Details

2.1 Starting Materials

1. Sodium tungstate (Na_2WO_4), Molar mass = 293.82 g/mol.
2. Thiourea (CH_4N_2S), Molar mass = 76.12 g/mol.
3. Liquid ammonia (NH_3), volume = 50 ml.

2.2 Synthesis of Thin Films

To fabricate the WS_2/p-Si interfacial structure, the WS_2 film was fabricated on a p-Si substrate. WS_2 thin film exhibits a n-type semiconducting characteristic and the deposition of WS_2 thin film on p-type silicon substrate leads to the formation of a heterojunction. First, the substrate was washed with the distilled (DI) water and then cleaned with acetone to remove any contamination from the Si substrate. The chemical bath deposition (CBD) method was employed to prepare the WS_2 thin film on p-Si substrates. For preparing the WS_2 thin film, 0.01 mol sodium tungstate (Na_2WO_4) solution was prepared in 50 ml DI water. 40 ml ammonia (NH_3) was mixed with 500 ml DI water and the resulting solution was then mixed with Na_2WO_4 solution. As the obtained solution was stirred for 30 min. 0.02 mol thiourea was added to the solution once sodium tungstate was fully dissolved in the ammonia solution. In addition, the ammonia solution was added dropwise to the prepared solution via a pipette at a temperature of about 80 °C–85 °C during the stirring. Finally, the cleaned and masked p-Si substrate was immersed into the final solution along an inclined plane for the deposition of WS_2 thin film. After a deposition time of 150 min, a uniform thin film of WS_2 appeared on the surface of the p-Si substrate. After deposition, the as-prepared thin films were heated at 250 °C in a furnace for about 60 min.

3 Results and Discussions

3.1 Structural Analysis

In order to examine the structural characteristics of the deposited WS_2 thin film, X-ray diffraction pattern was recorded. XRD pattern of the as-fabricated thin film of WS_2 is displayed in Fig. 1, which clearly reveals the existence of Bragg's diffraction peaks and shows the development of the WS_2 Nano thin layer on the p-Si substrate. XRD pattern of WS_2 thin film confirms the crystallization in hexagonal phase with $P6_3/mmc$ space group. As obtained XRD peaks (Fig. 1) are indexed to the planes of hexagonal phase (JCPDS card no. 08–0237). However, a low intensity XRD peak at ~45° can be attributed to (009) planes of rhombohedral phase (JCPDS card no. 35–0651). The XRD peak at ~51.2º can be assigned to (113) planes of the Si substrate. In addition, the XRD peaks at around 36.7 and 53.5 can be assigned to the impurity WO_2 phase. The lattice parameters (a and c) were also calculated from the XRD data using the standard hexagonal relation given below [11]:

$$\frac{1}{d^2_{(hkl)}} = \frac{4(h^2 + hk + k^2)}{3a^2} + \frac{l^2}{c^2} \tag{1}$$

where a and c refer to the lattice constants for the hexagonal structure and (hkl) are the standard Miller indices.

The lattice parameters a and c determined from the above Eq. (1) are 3.15 Å and 12.49 Å, respectively. As estimated lattice parameters are found according to the recorded literature values [12]. The crystallite size (D) of the deposited WS_2 thin film was estimated by applying the Debye-Scherrer formula as follows:

$$D = \frac{k\lambda}{\beta \cos\theta} \tag{2}$$

where k (=0.9) is the shape factor constant, and λ (=0.154) nm is the wavelength of the X-ray source. β is FWHM (full width at half maxima) and 'θ' represents Bragg's angle, and the crystallite size (D) of fabricated WS_2 thin film was estimated to be ~ 10 nm.

3.2 Optoelectrical Properties: UV-Vis Absorption Spectra

To study the optical response of the deposited WS_2/p-Si thin film structure, the absorption spectra have been recorded using ultraviolet-visible spectroscopy. Figure 2a shows the recorded absorption spectra of WS_2/p-Si thin film at room temperature for wavelengths between 300 and 800 nm, which displays the maximum

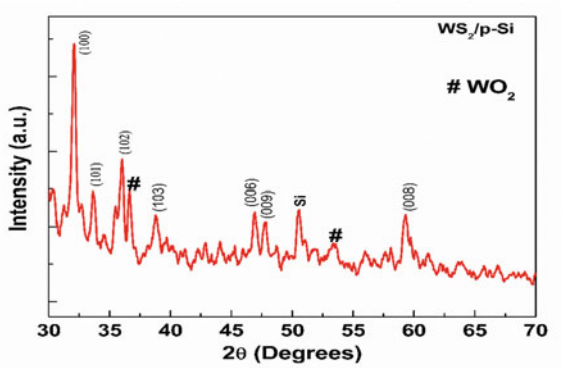

Fig. 1 X-Ray Diffraction characteristics of the fabricated WS_2/p-Si interfacial structure

absorption at ~305 nm in the ultraviolet region or near the visible region of the electromagnetic (EM) spectrum. The optical energy band gap (E_g) of WS_2/p-Si thin film was estimated through Tauc's expression as shown in Fig. 2b. Tauc's expression is given by [13]:

$$\alpha hv = C(hv - Eg)^n \tag{3}$$

where 'α' is absorption coefficient. 'h' refers to Planck's constant. 'v' refers to the frequency of photons. E_g is the band gap energy. C is an energy independent positive constant. The constant n can take the value of 2 or $\frac{1}{2}$ for the direct and indirect band gap semiconductors, respectively.

Figure 2b displays the variation of $(\alpha hv)^2$ *vs* the energy of photon (hv) for the direct band gap WS_2 semiconductor thin film. A direct energy band gap of approximately 2.50 eV was obtained for WS_2 thin film by taking an intercept of the extrapolated line

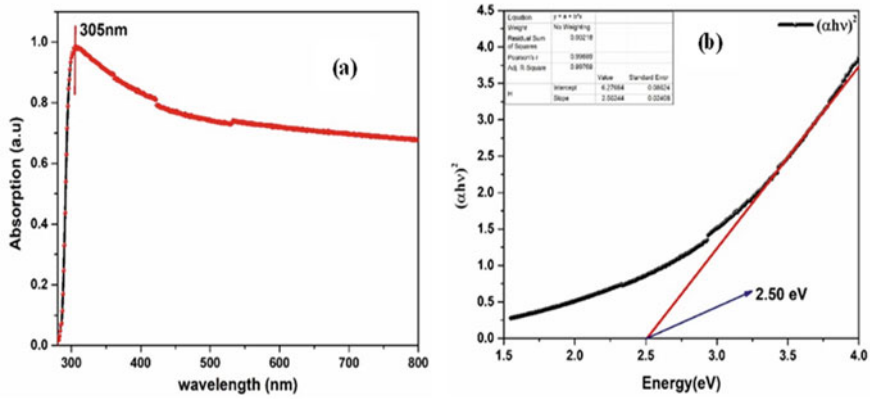

Fig. 2 **a** UV—Visible absorption spectra of WS_2/p-Si structure and, **b** Tauc's plot of WS_2/p-Si structure from UV—Vis spectra to estimate the band gap

on the energy of photon (hν) axis, as displayed in Fig. 2(b). The thin film deposited with WS_2 had a band gap energy slightly more extensive than that of bulk WS2 (2.10 eV) [14], which can be attributed to the quantum confinement effect of the charge carriers in the deposited thin film.

3.3 Electrical Properties: I-V Characteristics

To study the electrical response of the prepared WS_2 thin film, the I-V (current—voltage) characteristics were recorded under light and dark conditions. For I-V measurements, the thin film sample was first annealed and then top—bottom heterojunction contacts were deposited using the silver contact point. Under the visible light irradiation of 30 mW/cm^2 intensity, the current—voltage characteristics were recorded by sweeping the voltage from -9 V to + 9 V [15]. The measured current—voltage characteristics are displayed in above Fig. 3a, which illustrates the rectifier diode-like behaviour in the entire range of measurements [16].

A cycle type pattern can be seen in Fig. 3b due to a direct relationship between the intensity of light and the photocurrent. The photocurrent increases on increasing the intensity of light and vice-versa. In this experiment, when the light illumination level is set to a certain level, the photocurrent is stable, whereas the current drops rapidly under the condition of no light illumination. The variation of the photocurrent with the light intensity confirms an excellent reproducibility of the results. As can be seen from the results, the fabricated WS_2 thin film device demonstrates exceptional reproducible and stable on/off states under light/dark conditions [17, 18].

It is observed that under the light illumination, the current rapidly increases first and then saturates. In contrast, under dark conditions, the current decreases rapidly and returns to its core value. From the results, it can be seen that the response of the WS_2 thin nanolayer-based photoconductor is significantly fast as it switches very

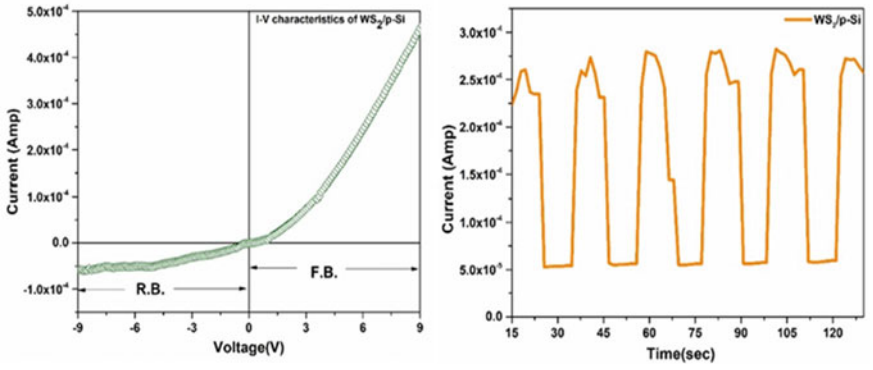

Fig. 3 **a** The I-V (current—voltage) characteristics and **b** the photoresponsivity at 30 mw/cm^2 illumination for the WS_2/p-Si structure

Table 1 A comparative study of the results of photodetection parameters against the reported literature

Parameter	Formula	Present work	Reference [19]	Reference [20]	Reference [21]
Response Current (A)	$\Delta I = I_{light} - I_{dark}$	2.19×10^{-4}	–	–	–
Sensitivity	$S = \frac{(I_{light} - I_{dark})}{I_{dark}}$	4.07	–	–	–
Response time (s)	$\tau_r = T_{90\%} - T_{10\%}$	1.1	2.1	11.6	1.03
Recovery time (s)	$\tau_d = T_{10\%} - T_{90\%}$	1.54	–	7.9	1.03
Responsivity (mA/W)	$R_s = \frac{\Delta I}{P}$	1.7×10^{-2}	4.4×10^{2}	4.04	4.2
Specific detectivity (Jones)	$D^* = R_s \left(\frac{A_0}{2eI_{dark}}\right)^{\frac{1}{2}}$.	2.56×10^{-2}	1.41×10^{10}	2.55×10^{9}	1.27×10^{10}

quickly between the on/off states. A comparison of the results of this study with that of recently published reports is shown in Table 1.

As can be seen from Table 1, the photo response current and responsivity of the WS_2 nanolayers were measured at 0.3 mA and 1.7×10^{-2} mA/W, respectively. The response time is the duration in which maximum photocurrent increases from 10 to 90%. The response time of the deposited WS_2 thin film is calculated to be ~1.1 s. A recovery time refers to the duration in which the photocurrent decreases from 90 to 10%. The calculated recovery time for the film is ~ 1.5 s. The other important parameters such as the responsivity and specific detectivity were also calculated and are listed in Table 1.

4 Conclusions

In the present study, WS_2/p-Si thin films were successfully formed via a CBD (chemical bath deposition) method. The result of XRD data confirms the formation of polycrystalline hexagonal phase in the deposited WS_2 thin film. An estimated ~ 10 nm crystallinity was found in the thin film of WS2. UV—Vis spectra show a maximum absorption in the UV region of EM spectrum. The direct semiconductor energy band gap (E_g) of deposited WS_2 thin film, estimated from Tauc's relation, was about 2.50 eV. The measured I-V characteristics of the WS_2/p-Si structure show a rectifier diode-like behavior. The photo response (I-V-T) measurements show an excellent response and recovery time. The results clearly indicate that as-deposited WS_2 thin film can be utilized in potential photodetector applications.

Acknowledgements We would like to thank Dr. Arvind Kumar for his encouragement and support during this experimental study. the Material Science Research Lab (Theory and Experiment), Department of Physics, ARSD College, University of Delhi, New Delhi -110021, India has been very helpful to us in providing the synthesis and characterization facilities. We are also grateful to SRM Institute of Science and Technology, Delhi-NCR Campus, Modinagar, Ghaziabad, 201204 for providing the financial support.

References

1. Hotovy I, Spiess L, Mikolasek M, Kostic I, Romanus H (2020) Structural and morphological evaluation of layered WS2 thin films. Vacuum 179:109570. https://doi.org/10.1016/j.vacuum.2020.109570
2. Shimakawa K (2020) Electrical transport properties. World Sci Ref Amorph Mater Struct Prop Model Main Appl 3(8): 177–202. https://doi.org/10.1142/9789811215575_0007
3. Hankare PP, Manikshete AH, Sathe DJ, Chate PA, Patil AA, Garadkar KM (2009) WS2 thin films: Opto-electronic characterization. J Alloys Compd 479(1–2):657–660. https://doi.org/10.1016/j.jallcom.2009.01.024
4. Ahmadi A, Shoushtari MZ, Farbod M (2019) Photoelectrochemical application of WS2 nanosheets prepared via a low-temperature CVD method. J Mater Sci Mater Electron 30(7):6342–6349. https://doi.org/10.1007/s10854-019-00936-7
5. Rapoport L, Moshkovich A, Perfilyev V, Tenne R (2007) On the efficacy of IF-WS 2 nanoparticles as solid lubricant: The effect of the loading scheme. Tribol Lett 28(1):81–87. https://doi.org/10.1007/s11249-007-9250-9
6. Kumar A, Pednekar D, Mukherjee S, Choubey RK (2020) Effect of deposition time and complexing agents on hierarchical nanoflake-structured CdS thin films. J Mater Sci Mater Electron 31(19):17055–17066. https://doi.org/10.1007/s10854-020-04263-0
7. Gutiérrez HR et al (2013) Extraordinary room-temperature photoluminescence in triangular WS 2 monolayers. Nano Lett 13(8):3447–3454. https://doi.org/10.1021/nl3026357
8. Nair PK et al (1998) Semiconductor thin films by chemical bath deposition for solar energy related applications. Sol Energy Mater Sol Cells 52(3–4):313–344. https://doi.org/10.1016/S0927-0248(97)00237-7
9. Kumar A et al (2021) "Highly responsive and low-cost ultraviolet sensor based on ZnS/p-Si heterojunction grown by chemical bath deposition", *Sensors Actuators*. A Phys 331:112988. https://doi.org/10.1016/j.sna.2021.112988
10. Gupta S et al (2023) Temperature-dependent study of the fabricated ZnS/p-Si heterojunction. Phys B Condens Matter 657: 414831. https://doi.org/10.1016/j.physb.2023.414831.
11. Cong C, Shang J, Wang Y, Yu T (2018) Optical Properties of 2D Semiconductor WS2. Adv. Opt. Mater. 6(1):1–15. https://doi.org/10.1002/adom.201700767
12. Kumar A et al (2022) Role of deposition parameters on the properties of the fabricated heterojunction ZnS/p-Si Schottky diode. Phys Scr 97(4):45819. https://doi.org/10.1088/1402-4896/ac6078
13. Patel KJ, Desai MS, Panchal CJ (2011) Properties of RF magnetron sputtered indium tin oxide thin films on externally unheated glass substrate. J Mater Sci Mater Electron 22(8):959–965. https://doi.org/10.1007/s10854-010-0243-3
14. Guan Y, Yao H, Zhan H, Wang H, Zhou Y, Kang J (2021) Optoelectronic properties and strain regulation of the 2D WS2/ZnO van der Waals heterostructure. RSC Adv 11(23):14085–14092. https://doi.org/10.1039/d1ra01877a
15. Kumar A et al (2021) ZnS microspheres-based photoconductor for UV light-sensing applications. Chem Phys Lett 763:138162. https://doi.org/10.1016/j.cplett.2020.138162

16. Huang R, Yu M, Yang Q, Zhang L, Wu Y, Cheng Q (2020) "Numerical simulation for optimization of an ultra-thin n-type WS2/p-type c-Si heterojunction solar cells". Comput Mater Sci 178: 109600 doi:https://doi.org/10.1016/j.commatsci.2020.109600.
17. Kumar A et al (2022) Materials Science in Semiconductor Processing Fabrication of low-cost and fast-response visible photodetector based on ZnS : Mn/p-Si heterojunction. Mater Sci Semicond Process 155: 107226. https://doi.org/10.1016/j.mssp.2022.107226.
18. Kumar A, Mukherjee S, Sahare S, Choubey RK (2021) Influence of deposition time on the properties of ZnS/p-Si heterostructures". Mater Sci Semicond Process 122: 105471. https://doi.org/10.1016/j.mssp.2020.105471
19. Pataniya PM, Sumesh CK (2020) WS2Nanosheet/Graphene Heterostructures for Paper-Based Flexible Photodetectors. ACS Appl Nano Mater 3(7):6935–6944. https://doi.org/10.1021/acsanm.0c01276
20. Li J, Han J, Li H, Fan X, Huang K (2020) Large-area, flexible broadband photodetector based on WS2 nanosheets films. Mater Sci Semicond Process 107: 104804. https://doi.org/10.1016/j.mssp.2019.104804.
21. Aggarwal P et al (2022) Centimeter-Scale Synthesis of Monolayer WS_2 Using Single-Zone Atmospheric-Pressure Chemical Vapor Deposition: a Detailed Study of Parametric Dependence, Growth Mechanism, and Photodetector Properties. Cryst. Growth Des 22(5):3206–3217

Investigating Efficiency of Glucose-Derived Graphene Quantum Dots in Photocatalysis

Anshu Gangwar and Mohan Singh Mehata

1 Introduction

Graphene is a distinctive manifestation of carbon possessing an innovative structural configuration, initially unveiled in 2004. It is an unprecedented two-dimensional material that comprises densely packed carbon atoms in a flat sheet exhibiting a hexagonal lattice pattern [1]. It offers unique physicochemical qualities such as an expansive surface area, outstanding biological compatibility, great mechanical strength, excellent thermal conductivity, and quick electron movement, making it adaptable to different applications [2]. Electronics, composites, energy, telecommunications, sensors and imaging, and biomedical technologies are the most potential application fields. Although graphene has various uses, it cannot be employed in many of them owing to the lack of energy gap in graphene, low water dispersivity, and low spectrum absorption [3, 4]. The enriching of chemical functional groups to the surface of graphene through functionalization can lead to a modification in graphene's thermal and electrical conductivity, and allows for the processing of monolayers in a solution, without clustering. Graphene comes in many different forms, including graphene oxide (GO), graphene nanoplatelets (GNPs), graphene nanoribbons (GNRs), reduced graphene oxide (rGO), and graphene quantum dots (GQDs) [5]. Functionalizing GO with groups like carbonyl, hydroxyl, and epoxy can increase its hydrophilicity, making it a better choice for solvent-based samples than pristine graphene [6].

Among these graphene derivatives, GQDs are zero-dimensional nanoparticles, that exhibit graphene properties as well as unique quantum size confinement phenomena and edge effects [7, 8]. The structure of GQDs is composed of one

A. Gangwar · M. S. Mehata (✉)
Laser-Spectroscopy Laboratory, Department of Applied Physics, Delhi Technological University, Bawana Road, Delhi 110042, India
e-mail: msmehata@dtu.ac.in

S. B. Krupanidhi et al. (eds.), *Recent Advances in Functional Materials and Devices*, Springer Proceedings in Materials 37, https://doi.org/10.1007/978-981-99-6766-7_25

or a few layers of graphene. The majority of GQDs are round or elliptical in structure [9]. Because of their quantum-size impact, they are unique and diverse. Solar cells, biosensors, light-emitting diodes, and photodetectors are just a few of the applications. The size-dependent opening of the bandgap is a crucial factor that distinguishes GQDs from graphene, setting clear boundaries between the two materials [4, 10]. Graphene quantum dots display exceptional features in a variety of disciplines. They are excellent for fluorescence sensing, photodegradation of dyes, and bioimaging applications due to their exceptional optical capabilities [11].

Recent studies show that graphene dots have up-conversion photoluminescence features that contribute to the increased photocatalytic activity. Up-conversion is just the absorption of multiple low-energy photons as a result of which a single high-energy photon is emitted [12–14]. The process typically involves a sequential absorption of photons, each promoting an electron to a higher energy state within the material. These absorbed photons can be of lower energy, such as in the near-infrared range, and are combined to provide the energy necessary for the electron to transition to a higher energy level. The excited electron then undergoes relaxation processes within the excited states, such as vibrational relaxation, and eventually reaches a higher energy state. From where, the electron can emit a photon of higher energy, corresponding to the up-converted emission.

GQDs absorb visible light, resulting in the creation of photo-excited electrons and holes. The photogenerated electrons from GQDs were subsequently received by other nanoparticles, aiding the charge carrier separation process. The displaced charged carriers subsequently produced highly reactive radicals, which caused dye photodegradation [15]. In addition to GO, graphene quantum dots are also attractive due to their excellent water solubility and chemical robustness, which make them non-toxic and biocompatible. They may also be mixed with other substances to create GQDs-based nanomaterials to establish collaborative effects to promote catalytic interactions with target analytes in many contexts. Also, GQDs-based nanocomposites have several uses in electrochemical sensors [16].

In the field of nanoscience, diverse physical and chemical traits of nanomaterials are often examined via construction approaches. Depending on the starting material, GQDs preparation techniques developed in the past few years are separated into two groups, namely top-down and bottom-up methodologies [17]. The top-down methodology for synthesizing graphene quantum dots involves the exfoliation and cutting of carbon precursors using chemical, thermal, or physical techniques to achieve the desired size and morphology. This involves the hydrothermal process, chemical oxidation method, chemical vapor deposition, electrochemical oxidation method, pulsed laser ablation technique, ultrasonic aided method, and also a combination of these [18]. To break apart graphene sheets, powerful reducing or oxidizing agents act as "scissors" to make GQDs. Despite this, these methods are commonly characterized as requiring harmful chemicals and considerable purification. A top-down method, hydrothermal, is essentially a solution reaction-based strategy that is often adopted for synthesizing quantum dots. The process of crystal growth is conducted utilizing an autoclave system, which is a steel pressure vessel. The synthesis of nanomaterials can occur over a broad range of temperatures, from ambient conditions to extremely

elevated temperatures [19]. It also relies on the aqueous solution's solubility in hot water, at higher temperatures. The process of hydrothermal synthesis offers significant advantages over other methods. It can generate nanomaterials that may be unstable at high temperatures and can produce nanomaterials possessing high vapor pressures while minimizing material loss [20]. The composition of nanomaterials created by hydrothermal synthesis may be carefully adjusted.

In comparison, the bottom-up technique employs chemical or physical interactions at the nano to construct small units into bigger structures. A variety of bottom-up strategies for generating nanoparticles have been explored. Carbonization, microwave irradiation, and electron beam irradiation are some of the technologies available [18]. This has fewer defects and the advantage of tunable size and shape. Because top-down synthesis processes include machine cost complexity, surface imperfections, contamination, cost and complexity of clean rooms, material damage, and heat dissipation. Bottom-up procedures are becoming an increasingly significant addition to top-down strategies. Carbonization, a bottom-up strategy, is significant in the production of graphene quantum dots since it is an ecologically benign and simple procedure. It is a process in which solid materials with increasing carbon content are created from organic material, typically through pyrolysis. It enables fine control of shape and size [21, 22]. Generally, for the production of GQDs, the reaction temperature required for carbonizing glucose is higher than the glycosidation temperature (160–180 °C) [23].

Here, we present an economical synthesis technique to produce water-soluble graphene quantum dots at room temperature, which utilizes glucose as the starting material and involves carbonization with the aid of ammonia as a catalytic reagent. The formation of as-synthesized GQDs is investigated through various characterizations. Also, they demonstrated excellent fluorescence properties.

2 Experimental Section

2.1 Materials

D-(+)-Glucose (99.5%) was procured from Sigma-Aldrich. Ammonia solution (NH_4OH) 25% and sodium hydroxide (NaOH) pellets (97%) were acquired from Rankem. The materials used throughout the experiment were conventional and used without additional purification. Throughout the experiments, ultrapure water was employed as a solvent, which had a resistivity of 18.2 MΩ-cm.

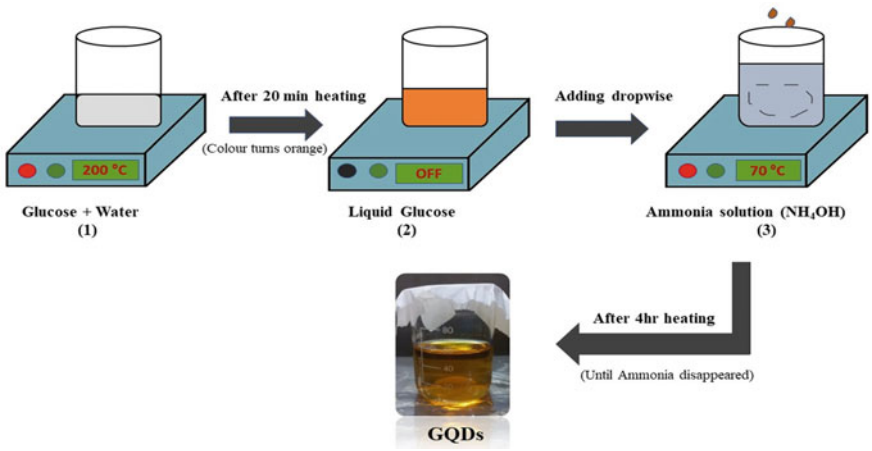

Fig. 1 A schematic representation of carbonization for producing graphene quantum dots

2.2 Synthesis of Graphene Quantum Dots (GQDs)

Initially, 2 g of glucose was heated in a beaker on a hot plate at 200 °C. After 4–5 min of heating, the powdered glucose turned into liquid form. The liquid was then heated for another 15 min and thus the color was altered from colorless to yellow-brownish. Further, prepared a 12% ammonia solution in 100 mL of ultrapure water. Successively, added the yellow-brownish solution, drop by drop, to the prepared ammonia solution with rapid stirring. The final solution was subjected to thermal treatment at 70 °C for 4 h until the solution had adjusted to pH 7 and the ammonia odor had evaporated. Figure 1 represents the process of synthesizing graphene quantum dots. In carbonization, ammonia dehydrates the glucose molecules in an aqueous solution. During the generation of GQDs, glucose molecules hydrogen atoms communicate through the hydroxyl groups of a neighboring glucose monohydrate. Due to the generation of water molecules, carbon atoms create covalent bonds with one another, which results in the creation of graphene quantum dots [15].

2.3 Preparation of Samples for Photocatalysis

A stock solution of 50 μM concentration of rhodamine dye was prepared by adding 1.1 mg of the dye to 50 mL of deionized water (formula: C_{28} $H_{31}ClN_2O_3$; Molar mass: 479.02 g/mol). The solution was further diluted to a concentration of 10 μM, and stirred for 30 min to validate the thorough mixing of the dye. Subsequently, the dye solution was transferred to a pair of quartz cells, with one cell being subjected to UV light and the other exposed to visible light.

2.4 Characterization Techniques

The UV-Vis absorption spectra of the samples were acquired using a Perkin Elmer Lambda 750 UV/Vis/NIR spectrometer. The measurement of the photoluminescence (PL) and PL-excitation spectra was conducted using a spectrofluorometer (Horiba Jobin Yvon, Fluorolog-3), which was fitted with a 450 W xenon lamp and a photomultiplier tube. The Perkin Elmer Spectrum Two FTIR spectrometer was employed to record the FTIR spectrum. HRTEM images were obtained by operating a TALOS HRTEM at 20 kV.

3 Results and Discussion

3.1 UV-Vis Absorption Spectra

The UV-Vis absorption spectrum of as-prepared GQDs within the range 200–600 nm shows two peaks (as shown in Fig. 2). The observed transitions correspond to electronic transitions from the π-orbitals to π*-orbitals and from non-bonding electron pairs to π*-orbitals. Note that the precursor used does not display any significant absorption. The first maximum at 232 nm (not shown) is related to the electronic transition of C=C through the π-π* pathway in the sp^2 region, while another peak is noticed at around 280 nm, which corresponds to the n-π* transition of C=O in sp^3 hybrid regions that rises due to the existence of oxygen-inclusive heteroatoms in the graphene quantum dot structure [24–26]. These are the main peaks that characterize pure GQDs. No additional peaks are observed up to the 600 nm wavelength. Both the heating time and heating temperature significantly affect the size or growth of quantum dots. Heating increases the temperature of the reaction mixture, leading to higher thermal energy. This increased thermal energy overcomes activation barriers, enhancing the nucleation process, which is the initial formation of quantum dots from precursor molecules. After nucleation, quantum dots continue to grow with the addition of precursor molecules to the existing nanocrystals. The growth process is influenced by both thermodynamics and kinetics. Higher heating temperatures accelerate the diffusion of precursor molecules, increasing the rate of material deposition onto the quantum dot surfaces. This rapid deposition can result in faster growth and larger quantum dots [27–29]. The band gap is a significant property of a material that directly influences its electronic and optical characteristics, including its absorption and emission properties [27]. Therefore, it can be computed based on the absorption parameters by drawing a tangent on the Kubelka–Munk (K-M) function $(\alpha h\upsilon)^2$ against photon energy ($h\upsilon$) plot, commonly termed as the Tauc plot, as illustrated in Fig. 2 (inset), where α represents the coefficient of optical absorption, υ is the frequency of light, h refers to the Planck's constant (value equals to 6.626×10^{34} J.s) [27, 30]. The value of the optical band gap (Eg) was determined to be 3.81 eV from Tauc's plot, which is consistent with the reported values (as shown

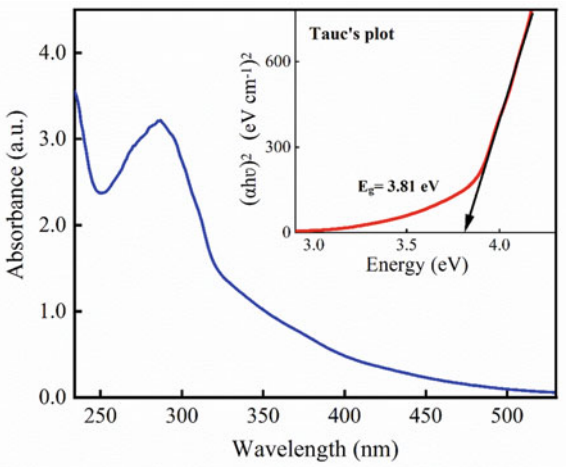

Fig. 2 The absorption spectrum of GQDs along with the 'Tauc's plot' analysis (inset)

in the inset of Fig. 2) [30]. While graphene possesses a bandgap of zero, GQDs have a discernible bandgap. GQDs vary in size and surface condition, and hence in the size of the band gap. As a result, bandgap varies according to size, surface, and edge type [25, 31]. According to theoretical calculations, the bandgap of pure GQDs can differ from 0 to 5 eV [25, 32].

3.2 Photoluminescence of GQDs

Photoluminescence (PL) arises due to the recombination of electron holes in sp^2 clusters, which function as emission centers. As a result, the intensity of PL is directly proportional to the concentration of sp^2. Therefore, an increase in sp^2 concentration leads to an increase in PL intensity. The PL and PL-excitation spectra are demonstrated in Fig. 3a, b. The excitation wavelengths for GQDs varied between 350 and 450 nm. Upon excitation with a 300 nm wavelength, a broad PL peak around 350 nm is observed (as shown in Fig. 3a). The observed phenomenon of a shift toward longer wavelengths in the PL peaks and a reduction in the intensity as the excitation increases, is common in carbon-based fluorescent materials, as presented in the visual in Fig. 3a. Hence, this shows the phenomenon of "excitation-dependent PL," which is caused by the existence of various dimensions of GQDs. The blue and green emission of GQDs indicates that GQDs have at least a minimum of two distinct emitting states [24]. The PL wavelength of quantum dots varies with particle size, with larger particles emitting light at longer wavelengths. In this case, strong blue PL is detected in GQDs subjected to irradiation by a 305 nm UV light, as depicted in the inset of Fig. 4.

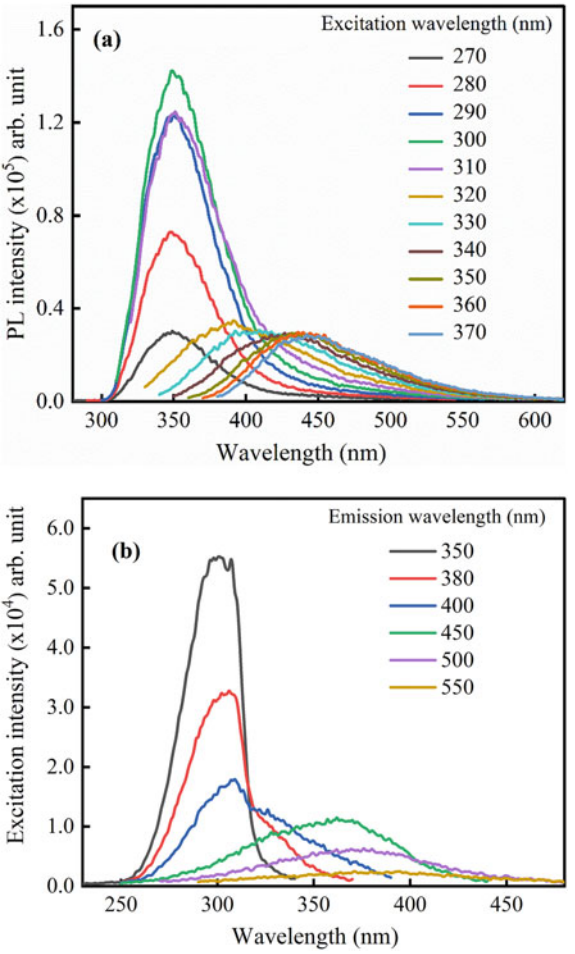

Fig. 3 Photoluminescence spectra of GQDs acquired at various excitation wavelengths (**a**) and PL-excitation spectra at different PL wavelengths (**b**)

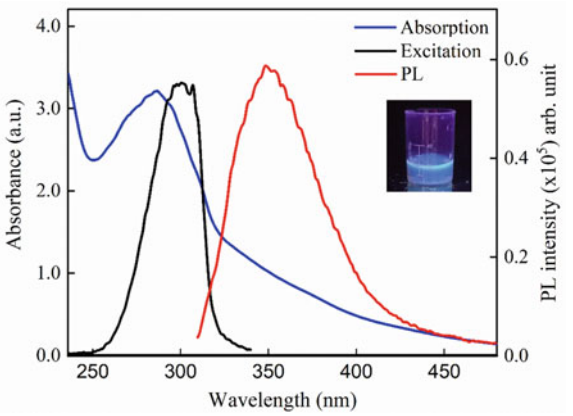

Fig. 4 Absorption, PL and PL-excitation spectra of GQDs. The inset shows a photograph of GQDs under UV irradiation

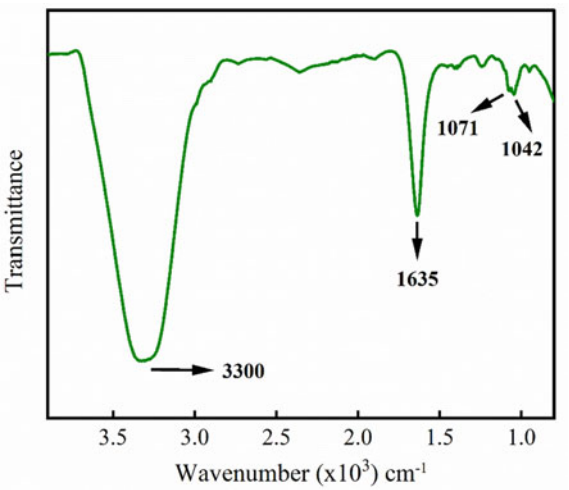

Fig. 5 FTIR spectrum of GQDs in water

3.3 FTIR Analysis

Fourier Transform analysis is performed to identify and quantify chemical compounds in a sample by measuring the absorption or transmission of infrared radiation. Figure 5 displays the FTIR spectrum of GQDs, which confirms the existence of diverse chemical moieties. The broad peak at 3300 cm^{-1} is common to all samples that use water as a solvent and represents the vibrational stretching of the O-H bond. The C=C vibrational stretching mode, which is the fundamental constituent of GQDs is ascribed to the 1635 cm^{-1} spectral feature. The peaks at 1042 cm^{-1} and 1071 cm^{-1} demonstrate the existence of C-O-H functional groups [29].

3.4 HRTEM Analysis

The investigation involved using electron microscopy techniques to analyze the morphology and distribution of the nano-sized graphene particles. Figure 6 shows the HRTEM images at two different magnifications along with the particle size analysis of GQDs. Figure 6a, b show the magnification of as-synthesized GQDs at 50 nm and 10 nm, showing the approximate spherical formations of GQDs. Figure 6c represents the range of particle sizes, the average particle size to be 24 nm. In the case of graphene quantum dots, due to their charged nature, they tend to accumulate or aggregate together. The existence of lattice fringes is evidence of the particle's crystallinity, which is visible under certain conditions when the particles are examined with high-resolution imaging techniques.

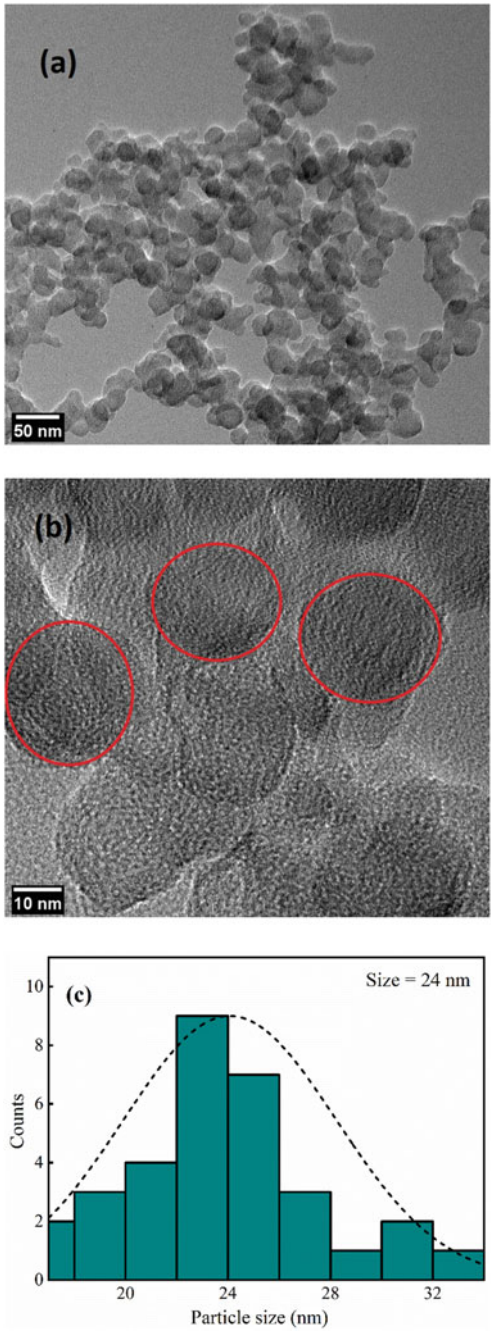

Fig. 6 HRTEM images of GQDs at magnifications of 50 nm (**a**) and 10 nm (**b**) along with particle size distribution (**c**)

4 Photocatalytic Breakdown of Rhodamine B Dye

The efficiency of GQDs in photocatalytic activity was analyzed for the disintegration of rhodamine B, an organic dye, under the influence of $NaBH_4$ as a reductant. To study the degradation percentage of rhodamine B dye, 0.2 mL of GQDs was added as a photocatalyst, and 5 mg of $NaBH_4$ was added as a reducing agent. The solution was exposed to UV and visible light, and after each exposure, the dye concentration was evaluated by measuring absorption spectra. Rhodamine B is a pink cationic dye with an absorption band at 554 nm associated with the $n \rightarrow \pi^*$ transition of C=N and C=O groups [33]. Figure 7 illustrates the absorption spectra of rhodamine B dye upon exposure to UV and visible light at different times. The dye exhibited degradation, transitioning from a pink color to a colorless state within a brief period of 16 min (as shown in the inset of Fig. 7). Figure 7a, b compare the degradation of rhodamine B dye through UV irradiation in the presence and absence of photocatalyst (GQDs). When both GQDs and $NaBH_4$ were added, the peak intensity gradually decreased with increased exposure time. The intensity reduction was observed for 16 min, and no further changes in color were noticed thereafter. Similarly, $NaBH_4$ alone exhibited the same mechanism but at a slower rate than the combined effect of GQDs and $NaBH_4$. The presence of GQDs + $NaBH_4$ resulted in the quenching of the absorption band of rhodamine B dye, achieving 86% degradation in about 16 min [34, 35]. However, in the absence of GQDs, only 30% degradation was observed, highlighting the significant contribution of GQDs in enhancing the rate of degradation [36, 37]. Furthermore, as shown in Fig. 7c, the visible-light-induced degradation of rhodamine B in the presence of GQDs with $NaBH_4$ was observed to be relatively slow, with the absorption intensity of dye gradually decreasing and reaching 51% degradation in the same time frame. Thus, the degradation rate of the dye under visible light was relatively slower and required more time compared to its degradation under UV irradiation. The results indicate that the synthesized GQDs possess the ability to degrade organic dyes and pollutants, highlighting the importance of further research in this area [38].

To determine the extent of degradation of rhodamine B dye, the percentage degradation R can be calculated using the formula,

$$\mathrm{R} = \left(\frac{A0 - At}{A0}\right) \times 100 \tag{1}$$

Here, the dye's absorbance was recorded at a wavelength of 554 nm at two different times, with A_0 representing the absorbance at the start of the reaction and A_t representing the absorbance after a specific time interval t, respectively [37, 39, 40]. The degradation kinetics of the dye were analyzed using a pseudo-first-order chemical reaction model to obtain a rate constant (k) using the equation $\ln(A_t/A_0) = -kt$, where A_o and A represent the initial and subsequent absorbance values of the dye at 554 nm, respectively [41, 42]. This assumes that the solvent concentration is greater than the dye concentration. The results showed a direct correlation between $\ln(A_t/A_0)$ and radiation exposure time, indicating that the photodegradation reaction adhered

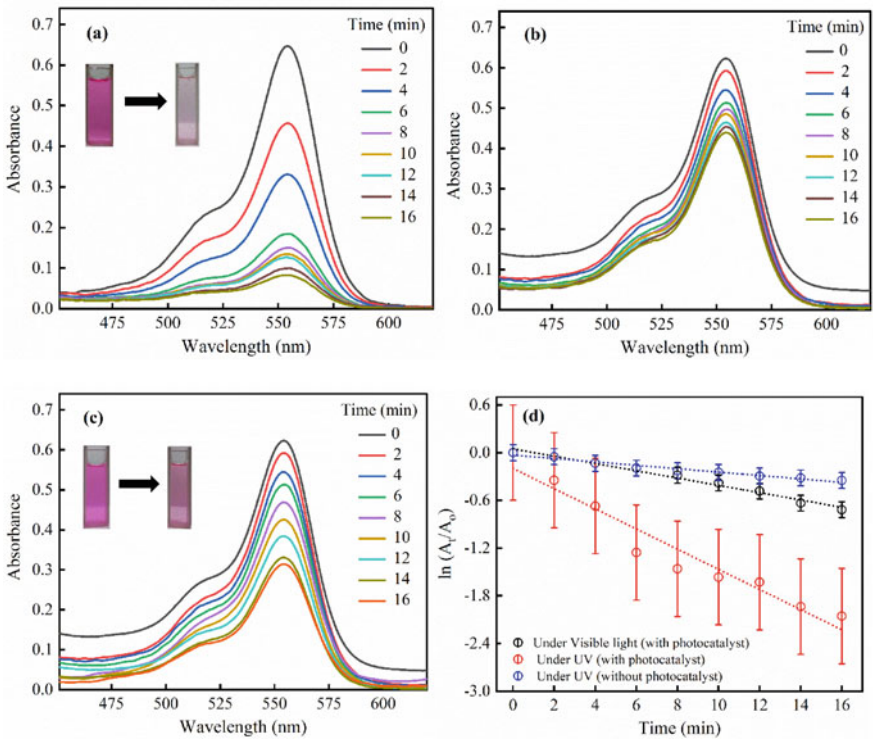

Fig. 7 Absorption spectra of rhodamine B with $NaBH_4$ under UV light with (**a**) and without (**b**) photocatalyst, as well as under visible light with photocatalyst (**c**), and a plot of $\ln(A_t/A_0)$ vs. reaction time (**d**)

to kinetics that was pseudo-first-order in nature [38, 43]. Figure 7d illustrates the rate constant (k) values for rhodamine B dye under UV and visible-light irradiation. The GQD + $NaBH_4$ system exhibited a rate constant of 0.126 min^{-1}, whereas $NaBH_4$ alone resulted in a reaction kinetic constant of 0.021 min^{-1} under UV irradiation. Conversely, the rate constant for GQD + $NaBH_4$ was 0.045 min^{-1} when treated with visible light.

5 Degradation Mechanism

The photodegradation of rhodamine B by GQDs in the presence of $NaBH_4$ occurs through a combination of photocatalytic and reduction processes. When exposed to light, GQDs generate reactive oxygen species (ROS), which are powerful oxidizing agents. These ROS can directly degrade rhodamine B by attacking its chromophore, causing it to break down into smaller, less toxic fragments [44]. In addition, $NaBH_4$

acts as a reducing agent, which can facilitate the degradation process by donating electrons to rhodamine B, making it more susceptible to oxidation by the ROS generated by GQDs [32]. The presence of both $NaBH_4$ and GQDs together advances the efficiency of the photodegradation process by increasing the rate of electron transfer between the two components [45]. The adherence of rhodamine B on GQDs surface also increases the concentration of the dye in the proximity of the ROS generated by GQDs, further promoting its degradation [36, 46]. Overall, the mechanism of photodegradation of rhodamine B by GQD in the presence of $NaBH_4$ involves a combination of photocatalysis and reduction, where GQDs generate ROS under light irradiation and $NaBH_4$ acts as a reducing agent to facilitate the degradation process.

6 Conclusion

In conclusion, the fabrication of graphene quantum dots utilizing glucose as a precursor through the carbonization method was successfully achieved. With a particle size of 24 nm, the GQDs displayed a spherical morphology. The GQDs exhibited strong blue emission under irradiation by UV lamp at 305 nm, exhibiting broad PL at 350 nm upon excitation at 300 nm. This revealed the excitation-dependent PL activity of GQDs. The absorption spectrum indicated the characteristic peak of GQDs with a bandgap energy of 3.81 eV, confirmed by the $n \rightarrow \pi^*$ transition peak of the C=O group at 280 nm. FTIR analysis further validated the existence of relevant functional substituents bonded to the surface of GQDs. Photocatalytic experiments demonstrated that GQDs acted as an excellent photocatalyst in the availability of $NaBH_4$, possessing a fast reaction rate of 0.126 min^{-1} under UV light, leading to the degradation of RhB dye by 86%. In contrast, only 30% of the dye was degraded without the photocatalyst. Under visible light, the presence of both $NaBH_4$ and GQDs resulted in the degradation of 50% of the dye. Thus, the combination of photocatalytic and chemical reduction processes can lead to the efficient degradation of RhB dye. These findings highlight the potential of GQDs as promising candidates for environmental remediation applications.

Acknowledgements The author Ms. Anshu Gangwar expresses gratitude to Mr. Vinay K. Yadav and other lab scholars for their constant support and valuable motivation throughout this study.

Declaration of Competing Interest In the paper presented, the authors declare that they have no known financial interests or personal relationships that could be perceived as competing and potentially influencing the reported work.

References

1. Choi W, Lahiri I, Seelaboyina R, Kang YS (2010) Synthesis of graphene and its applications: a review. Crit Rev Solid State Mater Sci 35:52

2. Shehab M, Ebrahim S, Soliman M (2017) Graphene quantum dots prepared from glucose as optical sensor for glucose. J Lumin 184:110
3. Ghaffarkhah A, Hosseini E, Kamkar M, Sehat AA, Dordanihaghighi S, Allahbakhsh A, Kuur C, Arjmand M (2022) Synthesis, applications, and prospects of graphene quantum dots: a comprehensive review. Small 18:2102683
4. Yan Y, Gong J, Chen J, Zeng Z, Huang W, Pu K, Liu J, Chen P (2019) Recent advances on graphene quantum dots: from chemistry and physics to applications. Adv Mater 31:1808283
5. Tiwari SK, Sahoo S, Wang N, Huczko A (2020) Graphene research and their outputs: status and prospect. J. Sci. Adv. Mater. Devices 5:10
6. de M Rocha AP, Alayo MI, da Silva DM (2022) Synthesis of nitrogen-doped graphene quantum dots from sucrose carbonization. Appl Sci 12:8686
7. Yan X, Cui X, Li B, Li L (2010) Large, solution-processable graphene quantum dots as light absorbers for photovoltaics. Nano Lett 10:1869
8. Pan D, Zhang J, Li Z, Wu M (2010) Hydrothermal route for cutting graphene sheets into blue-luminescent graphene quantum dots. Adv Mater 22:734
9. Wang Z, Hu T, Liang R, Wei M (2020) Application of zero-dimensional nanomaterials in biosensing. Front Chem 8:320
10. Yan Y, Chen J, Li N, Tian J, Li K, Jiang J, Liu J, Tian Q, Chen P (2018) Systematic bandgap engineering of graphene quantum dots and applications for photocatalytic water splitting and CO_2 reduction. ACS Nano 12:3523
11. Biswas MC, Islam MT, Nandy PK, Hossain MM (2021) Graphene quantum dots (GQDs) for bioimaging and drug delivery applications: a review. ACS Mater. Lett. 3:889
12. Feizpoor S, Habibi-Yangjeh A, Seifzadeh D, Ghosh S (2020) Combining carbon dots and $Ag_6Si_2O_7$ nanoparticles with TiO_2: visible-light-driven photocatalysts with efficient performance for removal of pollutants. Sep Purif Technol 248:116928
13. Li H, He X, Kang Z, Huang H, Liu Y, Liu J, Lian S, Tsang CHA, Yang X, Lee S-T (2010) Water-soluble fluorescent carbon quantum dots and photocatalyst design. Angew Chem Int Ed 49:4430
14. Zhang H, Zhao L, Geng F, Guo L-H, Wan B, Yang Y (2016) Carbon dots decorated graphitic carbon nitride as an efficient metal-free photocatalyst for phenol degradation. Appl Catal B Environ 180:656
15. Akbar K, Moretti E, Vomiero A (2021) Carbon dots for photocatalytic degradation of aqueous pollutants: recent advancements. Adv. Opt. Mater. 9:2100532
16. Facure MHM, Schneider R, Lima JBS, Mercante LA, Correa DS (2021) Graphene quantum dots-based nanocomposites applied in electrochemical sensors: a recent survey. Electrochem 2:490
17. Tian P, Tang L, Teng KS, Lau SP (2018) Graphene quantum dots from chemistry to applications. Mater. Today Chem. 10:221
18. Zhao C et al (2020) Synthesis of graphene quantum dots and their applications in drug delivery. J. Nanobiotechnology 18:142
19. Gan YX, Jayatissa AH, Yu Z, Chen X, Li M (2020) Hydrothermal synthesis of nanomaterials. J Nanomater 2020:1
20. Zheng B, Chen Y, Li P, Wang Z, Cao B, Qi F, Liu J, Qiu Z, Zhang W (2017) Ultrafast ammonia-driven microwave-assisted synthesis of nitrogen-doped graphene quantum dots and their optical properties. Nanophotonics 6:259
21. Ge S, He J, Ma C, Liu J, Xi F, Dong X (2019) One-step synthesis of boron-doped graphene quantum dots for fluorescent sensors and biosensor. Talanta 199:581
22. Ratre P, Jain B, Kumari R, Thareja S, Tiwari R, Srivastava RK, Goryacheva IY, Mishra PK (2022) Bioanalytical applications of graphene quantum dots for circulating cell-free nucleic acids: a review. ACS Omega 7:39586
23. Hou X, Li Y, Zhao C (2016) Microwave-assisted synthesis of nitrogen-doped multi-layer graphene quantum dots with oxygen-rich functional groups. Aust J Chem 69:357
24. Mehata MS, Biswas S (2021) Synthesis of fluorescent graphene quantum dots from graphene oxide and their application in fabrication of GQDs@AgNPs nanohybrids and sensing of H_2O_2. Ceram Int 47:19063

25. Biswal R, Khan B, Singh MK (2022) Synthesis, optical, dielectric, and magneto-dielectric properties of graphene quantum dots (GQDs). J Mater Res 37:3459
26. Tang L, Ji R, Li X, Teng KS, Lau SP (2013) Size-dependent structural and optical characteristics of glucose-derived graphene quantum dots. Part Part Syst Charact 30:523
27. Mi W, Tian J, Tian W, Dai J, Wang X, Liu X (2012) Temperature dependent synthesis and optical properties of CdSe quantum dots. Ceram Int 38:5575
28. Ye R et al (2015) Bandgap engineering of coal-derived graphene quantum dots. ACS Appl Mater Interfaces 7:7041
29. Tang L et al (2012) Deep ultraviolet photoluminescence of water-soluble self-passivated graphene quantum dots. ACS Nano 6:5102
30. Bhatnagar D, Singh S, Yadav S, Kumar A, Kaur I (2017) Experimental and theoretical investigation of relative optical band gaps in graphene generations. Mater Res Express 4:015101
31. Zhu S, Shao J, Song Y, Zhao X, Du J, Wang L, Wang H, Zhang K, Zhang J, Yang B (2015) Investigating the surface state of graphene quantum dots. Nanoscale 7:7927
32. Li L, Wu G, Yang G, Peng J, Zhao J, Zhu J-J (2013) Focusing on luminescent graphene quantum dots: current status and future perspectives. Nanoscale 5:4015
33. Singh MK, Mehata MS (2019) Phase-dependent optical and photocatalytic performance of synthesized titanium dioxide (TiO_2) nanoparticles. Optik 193:163011
34. Teymourinia H, Salavati-Niasari M, Amiri O, Safardoust-Hojaghan H (2017) Synthesis of graphene quantum dots from corn powder and their application in reduce charge recombination and increase free charge carriers. J Mol Liq 242:447
35. Amakali T, Živković A, Warwick MEA, Jones DR, Dunnill CW, Daniel LS, Uahengo V, Mitchell CE, Dzade NY, de Leeuw NH (2022) Photocatalytic degradation of rhodamine B dye and hydrogen evolution by hydrothermally synthesized $NaBH_4$-spiked ZnS nanostructures. Front Chem 10:835832
36. Mehata MS (2021) Green route synthesis of silver nanoparticles using plants/ginger extracts with enhanced surface plasmon resonance and degradation of textile dye. Mater Sci Eng B 273:115418
37. Bhatt N, Mehata MS (2023) A sustainable approach to develop gold nanoparticles with Kalanchoe Fedtschenkoi and their interaction with protein and dye: sensing and catalytic probe. Plasmonics
38. Mandal P, Nath KK, Saha M (2021) Efficient blue luminescent graphene quantum dots and their photocatalytic ability under visible light. Biointerface Res Appl Chem 11:8171
39. Abbas Alshamsi H, Abbas Al Bedairy M, Hussein Alwan S (2021) Visible light assisted photocatalytic degradation of rhodamine B dye on CdSe-ZnO nanocomposite: characterization and kinetic studies. IOP Conf Ser Earth Environ Sci 722:012005
40. Phuruangrat A, Keereesaensuk P-O, Karthik K, Dumrongrojthanath P, Ekthammathat N, Thongtem S, Thongtem T (2020) Synthesis and characterization Ag nanoparticles supported on Bi_2WO_6 nanoplates for enhanced visible-light-driven photocatalytic degradation of rhodamine B. J Inorg Organomet Polym Mater 30:1033
41. Singh MK, Mehata MS (2020) Enhanced photoinduced catalytic activity of transition metal ions incorporated TiO_2 nanoparticles for degradation of organic dye: absorption and photoluminescence spectroscopy. Opt Mater 109:110309
42. Roushani M, Mavaei M, Rajabi HR (2015) Graphene quantum dots as novel and green nanomaterials for the visible-light-driven photocatalytic degradation of cationic dye. J. Mol. Catal. Chem. 409:102
43. Jeyapragasam T, Kannan RS (2016) Microwave assisted green synthesis of silver nanorods as catalysts for rhodamine B degradation. Russ J Phys Chem A 90:1334
44. Ibarbia A, Grande HJ, Ruiz V (2020) On the factors behind the photocatalytic activity of graphene quantum dots for organic dye degradation. Part Part Syst Charact 37:2000061
45. Shukla S, Aryan AM, Mehata MS (2022) Catalytic activity of silver nanoparticles synthesized using crinum asiaticum (Sudarshan) leaf extract. Mater Today Proc 56:3714
46. Aryan R, Mehata MS (2021) Green synthesis of silver nanoparticles using Kalanchoe Pinnata leaves (life plant) and their antibacterial and photocatalytic activities. Chem Phys Lett 778:138760

Structural, Electrical and Hydroelectric Cell Investigation in Environment Friendly LSMO:BT Composite

Chitralekha, S. Shankar, and Aman Pal Singh

1 Introduction

Perovskite manganites $R_{1-x}A_xMnO_3$ (R, i.e. La and rare earths and A, i.e., Sr) exhibit intricate connections among spin, lattice degrees of freedom, charge and orbital; leading to novel physical phenomena like the giant magnetic entropy effect, the metal to insulator transition, separation of electronic phase, the ordering of charges or orbitals and their phase formation in structural phases [1, 2]. Magnetic nanoparticle systems have received a lot of attention recently as a result of their remarkable physical properties and industrial applications such as magnetic recording media, magnetic sensors for making permanent magnets, ferrofluids, magnetic refrigeration, in medical zone as enhancement in magnetic resonance imaging (MRI), magnetically guided drug delivery, and hyperthermia [3].

The most thoroughly researched titanate is barium titanate ($BaTiO_3$), which is regarded as the model for ferroelectric materials devoid of lead [4]. According to reports, $BaTiO_3$ has a reported Curie point of 120 °C at ambient temperature and also it crystallises into a cubic structure; at lower temperatures, it forms a structure of tetragonal perovskite [5, 6]. The ionic displacement of the Ti ions in relation to the oxygen ions results in the formation of a tetragonal structure [7]. $BaTiO_3$ has a band gap of 3.2 eV and a polarisation of 26 C/cm^2 at ambient temperature [8]. It has been noted that $BaTiO_3$ loses its ferroelectricity in particles smaller than 120 nm [9]. However, in BT, the characteristic rises to a maximum value for a certain grain size

Chitralekha · S. Shankar (✉)
Functional Materials Research Laboratory, Department of Physics, ARSD College, University of Delhi, Delhi 110021, India
e-mail: sssubramaniam@arsd.du.ac.in

Chitralekha · A. P. Singh (✉)
Department of Physics, Multanimal Modi College, Ch. Charan Singh University, Meerut, U.P, India
e-mail: dramanpal.singh23@gmail.com

S. B. Krupanidhi et al. (eds.), *Recent Advances in Functional Materials and Devices*, Springer Proceedings in Materials 37, https://doi.org/10.1007/978-981-99-6766-7_26

near the nanoscale scale before falling. $BaTiO_3$ was the first commercial ferroelectric and piezoelectric material. In general, as size decreases, the ferroelectric property which is governed by the dielectric constant also increases [10]. It has been employed as a dielectric in multilayer ceramic capacitors for more than 70 years, making it the most frequently used functional ceramic in the electronic industry. The simplicity with which its qualities can be used has greatly influenced barium titanate's economic success [11].

In the current work, focus was on observing hydroelectric cells performance as they are purely eco-friendly and don't produce such byproducts that are unsuitable for human health. Oxygen deficiency and the creation of porosity in managanite and metal oxides have played a crucial and remarkable role in the dissociation of water molecules to cause energy by hydroelectric cell (HEC) [12]. We have used a multiferroic compound to limit the oxygen deficiency present in the chemical to cause water molecules to dissociate, resulting in the generation of HEC [12]. To address the same problems, LSMO-BT and their composite were created at low temperatures and water molecule dissociation was analyzed for producing energy using HEC based on composite.

In this study, technique namely, solid state synthesis was opted to create perovskite $La_{0.67}Sr_{0.33}MnO_3$ and $BaTiO_3$ particles in different ratio. The effects of room temperature on the structural and electrical properties were thoroughly studied and assessed. For each material, hydroelectric cells were designed, and their performance in the dry, sprinkled water, and wet states was evaluated. These cells electrodes were made using zinc plate on one side and coated with silver pattern on another side and joining both ends with thin wires. Thereafter, their performance was recorded.

The high temperature treated powder and pellets were opted for attaining the XRD patterns, FTIR spectra and dielectric measurements. The Fourier transform infrared spectroscopy (FT-IR) spectroscopy were made using Bruker FT-IR instrument operating in the wavenumber range of $400\,cm^{-1}$–$1000\,cm^{-1}$. The high temperature treated round pellets were layered with silver paste on parallel surface for observing dielectric properties by using setup of Waynekerr 6500 P high frequency LCR meter over the frequency between 20 Hz and 5 MHz at ambient temperature. The hydroelectric cell performance at dry and wet conditions was performed.

2 Experimental Details

The (1-x)LSMO: xBT binary composites (x = 0, 0.5 and 1) were prepared via solid-state reaction method. Initial ingredients of chemicals of Lanthanum Oxide (La_2O_3), Strontium carbonate ($SrCO_3$), manganese dioxide (MnO_2) were used for preparation of LSMO. Barium carbonate ($BaCO_3$) and Titanium Dioxide (TiO_2) were used to prepare barium titanate ($BaTiO_3$). All chemicals were used in stoichiometric ratio. The starting oxides i.e., LSMO and BT were grinded individually for 6 h. The grinded powders of LSMO and $BaTiO_3$ were calcined in muffle furnace at different temperatures at 900 °C and 1000 °C respectively. To prepare the selected 0.5LSMO:0.5BT

composite, stoichiometric grinding of the calcined powder was performed. For each sample, pellets were formed using ground powder. These pellets were created by combining powders with a polyvinyl alcohol binder and strongly pressing the mixture into cylinder-shaped pellets with a 10 mm diameter and a 1 mm thickness. Each sample's pellets and residual powder were sintered at 1050 °C for 5 h. Later, hydroelectric cells were made using zinc plates and silver paste to create hydroelectric cell, and their responses were determined. The sintered composites were given the name 0.5LSMO:0.5BT.

3 Results and Discussion

3.1 XRD Analysis

The XRD pattern attained for LSMO-BT and its composite at room temperature is shown in Fig. 1. The pure LSMO sample exhibits single phase and crystallises in the rhombohedral single perovskite structure having Pnma space group. The XRD pattern for BT shows the pure phase formation of $BaTiO_3$ barium titanate and contains tetragonal-$BaTiO_3$ easily identifiable by the peak splitting near 46 °C [13]. LSMO:BT composite show dual nature reflecting the LSMO and BT dominating peaks. This demonstrates that the LSMO and BT phases coexist in composite sample without any discernible interphase diffusion. However, merging and broadening of peaks were observed in all composite indicating the formation of composite. The Debye Scherrer Eq. (1) is used to understand the effects of BT addition in LSMO and is given by:

$$D = k\lambda \, \beta \cos \theta \tag{1}$$

where k = 0.9, λ is the wavelength of X-rays, β is full width at half maximum (FWHM) of the diffraction peak, θ is angle of diffraction. The crystallite size obtained for each sample is shown in Table 1. LSMO exhibits smaller crystallite size than BT and their composite shows intermediate crystallite size.

3.2 FT-IR Analysis

Figure 2 shows the room temperature FT-IR spectra of LSMO, BT and composite over wave number 400cm^{-1}–1200 cm^{-1}. For LSMO, band in the range of 500cm^{-1}–560 cm^{-1} correspond to asymmetric stretching vibration. For the pure BT, two major absorption peaks at 453 cm^{-1} and 490 cm^{-1} correspond to Ti–O bending and stretching normal vibrations, respectively. The metal-oxygen stretching vibrations at the B-site are often associated with bands between 500 cm^{-1} and 750 cm^{-1}. The

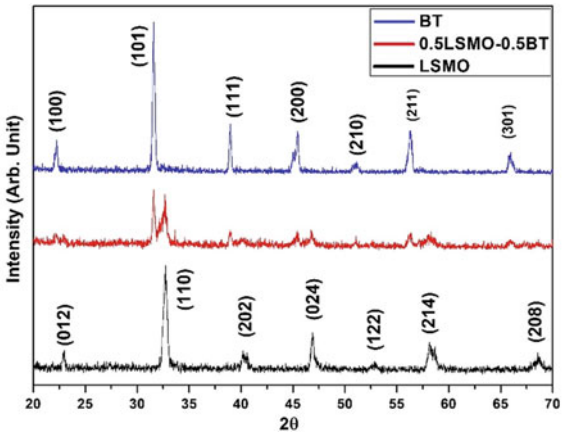

Fig. 1 XRD pattern of LSMO-BT series

Table 1 Crystallite size of LSMO:BT series using Debye- Scherrer formula

Material	Crystallite size (nm)
BT	35.33
LSMO	15.16
0.5LSMO-0.5BT	24.52

O-H stretching vibration in moist state is attributed to the distinctive absorption band near 3600 cm^{-1}, which indicates the presence of moisture in both the BT and the composite [14].

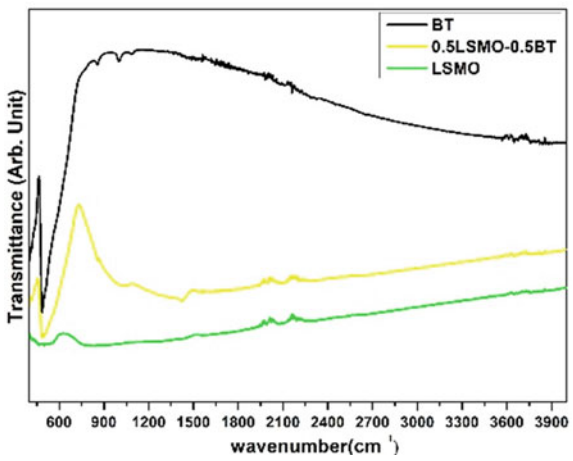

Fig. 2 FTIR spectra of LSMO-BT series

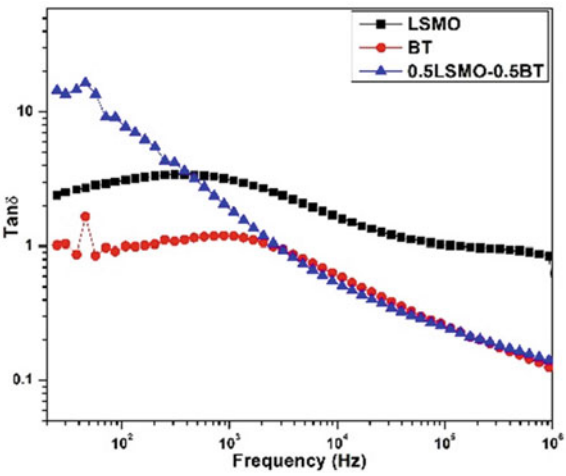

Fig. 3 Dielectric Loss (Tan δ) versus frequency varation for LSMO-BT series

3.3 Dielectric Loss Versus Frequency Analysis

Figure 3 shows dielectric loss over frequency at ambient temperature. BT shows minimal loss due to its ability to have great dielectric properties. The presence of impurity causes the dielectric loss in LSMO. At higher frequency region, the dielectric loss for each material is very less. For composite, the value of tan δ is higher is observed in lower frequency region.

3.4 Nyquist Plot

The Nyquist plot of LSMO-BT series at ambient temperature is shown in Fig. 4. BT exhibits maximum semicircle and LSMO exhibits minimum semicircle. Both materials exhibit more than one arcs and indicate the presence of grain and grain boundaries. The composites' impedance value rises as BT suggests their nature is highly resistant. The net impedance of composite increases as BT content in the material increases. The composite exhibits a single semicircular arc beginning at the origin. Pure BT indicates a highly resistant character by increasing the impedance value in the composites.

3.5 Hydroelectric Cell Performance

Hydroelectric Cells (HECs) of LSMO:BT series were tested for functionality, and their behaviour in three different states, i.e. dry, with a few drops of water applied,

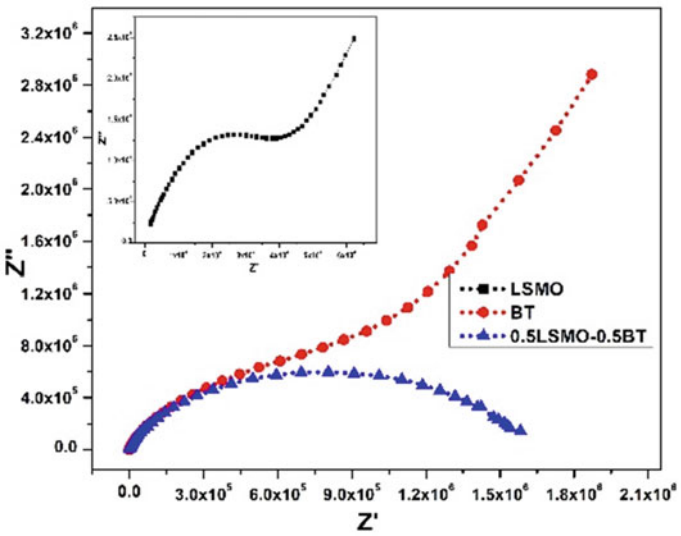

Fig. 4 Nyquist plot for LSMO:BT series

and submerged in water was examined. The corresponding current noted is shown in Table 2.

There was no current sensed in the dry state. Each hydroelectric cell showed some current in mA when few drops of water were sprayed on it. LSMO, BT and 0.5LSMO-0.5BT composite show current values of 2.1 mA, 0.2 mA, and 0.15 mA, respectively, when exposed to water drops. When HECs were completely submerged in water, all the samples functioned admirably. The BT HEC produced a current of 0.305 mA, however the LSMO performed better than the BT HEC by producing a current of 4.51 mA when submerged in water, since more water molecule dissociation occurred in HECs [15]. The production of current in the cell is begun due to redox reactions between the two electrodes. Due to the presence of a greater amount of oxygen vacancies in LSMO than BT, the HEC of the former has been improved [16]. 0.5LSMO-0.5BT composite displays a current value of 2.29 mA. When submerged fully in water, the composite 0.5LSMO-0.5BT functioned effectively, demonstrating as BT concentration in LSMO increases, so does the wet state current values in the HEC.

Table 2 HEC performance in dry, sprinkled water and wet state for LSMO:BT series

Material	Dry state (mA)	Water sprinkled state (mA)	Wet state (mA)
BT	0	0.2	0.305
LSMO	0	2.1	4.51
0.5LSMO-0.5BT	0	0.15	2.29

4 Conclusion

In summary, composites of (1 - x)LSMO-(x)BT (x = 0, 0.5 and 1). The structural analysis made using XRD and FT-IR spectra revealed the occurrence of both LSMO and BT phases and revealed the composite formation. The frequency variation of dielectric properties follows Maxwell-Wagner polarization and improved diffusive type relaxor behavior in the composites. Impedance measurements revealed non-Debye type thermal dependent relaxation mechanism in LSMO:BT composites. Hydroelectric cells (HECs) of LSMO:BT composites with few drops of water sprinkled and in wet states displayed ionic diffusion and stable as well as improved performance with increasing content of LSMO. These results show improved structural, dielectric, impedance and enhanced HEC performance of LSMO:BT composites and demonstrate potential use in magnetoelectric and hydroelectric cell application.

References

1. Shlapa Y, Solopan S, Belous A, Tovstolytkin A (2018) Effect of synthesis method of La1—xSrxMnO$_3$ manganite nanoparticles on their properties. Nanoscale Res Lett 13:13. https://doi.org/10.1186/s11671-017-2431-z
2. Shinde KP, Thorat ND, Pawar SS, Pawar SH (2012) Combustion synthesis and characterization of perovskite La0.9Sr0.1MnO$_3$. Mater Chem Phys 134:881–885. https://doi.org/10.1016/j.matchemphys.2012.03.085
3. Rostamnejadi A, Salamati H, Kameli P (2012) Magnetic properties of interacting La0.67Sr0.33MnO$_3$ nanoparticles. J Supercond Nov Magn 25:1123–1132. https://doi.org/10.1007/s10948-011-1378-z
4. Kambale KR, Kulkarni AR, Venkataramani N (2014) Synthesis of barium titanate powder using nano sized titania. Int J Innov Res Sci Eng Technol (An ISO Certif Organ 3297). www.ijirset.com
5. Shankar S, Thakur OP, Jayasimhadri M (2021) Strong enhancement in structural, dielectric, impedance and magnetoelectric properties of NdMnO$_3$-BaTiO$_3$ multiferroic composites. Mater Chem Phys 270:124856. https://doi.org/10.1016/j.matchemphys.2021.124856
6. Bae H, Lee KT (2019) Effect of tetragonal to cubic phase transition on the upconversion luminescence properties of A/B site erbium-doped perovskite BaTiO$_3$. RSC Adv 9:2451–2457. https://doi.org/10.1039/c8ra09783f
7. Petrović MMV, Bobić JD, Ramoška T, Banys J, Stojanović BD (2011) Electrical properties of lanthanum doped barium titanate ceramics. Mater Charact 62:1000–1006. https://doi.org/10.1016/j.matchar.2011.07.013
8. Verma KC, Singh D, Kumar S, Kotnala RK (2017) Multiferroic effects in MFe$_2$O$_4$/BaTiO$_3$(M = Mn Co, Ni, Zn) nanocomposites. J Alloys Compd 709:344–355. https://doi.org/10.1016/j.jallcom.2017.03.145
9. Padalia D, Bisht G, Johri UC, Asokan K (2013) Fabrication and characterization of cerium doped barium titanate/PMMA nanocomposites. Solid State Sci 19:122–129. https://doi.org/10.1016/j.solidstatesciences.2013.02.002
10. Rached A, Wederni MA, Khirouni K, Alaya S, Martín-Palma RJ, Dhahri J (2021) Structural, optical and electrical properties of barium titanate. Mater Chem Phys 267:124600. https://doi.org/10.1016/j.matchemphys.2021.124600
11. Stojanovic BD, Simoes AZ, Paiva-Santos CO, Jovalekic C, Mitic VV, Varela JA (2005) Mechanochemical synthesis of barium titanate. J Eur Ceram Soc 25:1985–1989. https://doi.org/10.1016/j.jeurceramsoc.2005.03.003

12. Shah J, Verma KC, Agarwal A, Kotnala RK (2020) Novel application of multiferroic compound for green electricity generation fabricated as hydroelectric cell. Mater Chem Phys 239:122068. https://doi.org/10.1016/j.matchemphys.2019.122068
13. Belous A, V'yunov O, Kovalenko L, Makovec D (2005) Redox processes in highly yttrium-doped barium titanate. J Solid State Chem 178:1367–1375. https://doi.org/10.1016/j.jssc.2005.01.014
14. Shankar S, Kumar M, Tuli V, Thakur OP, Jayasimhadri M (2018) Energy storage and magnetoelectric coupling in ferroelectric–ferrite composites. J Mater Sci Mater Electron 29:18352–18357. https://doi.org/10.1007/s10854-018-9949-4
15. Pratibha K, Chitralekha, Kaur H, Shankar S, Gaurav S, Dwivedi Y (2023) Influence of annealing temperature on structural, optical and electrical properties of zinc silicate (Zn_2SiO_4) nanophosphors. Phys B Condens Matter 658:414836. https://doi.org/10.1016/j.physb.2023.414836
16. Chitralekha I, Maurya T, Gupta S, Shankar S, Gaurav V, Tuli J, Shah RK (2022) Kotnala, dielectric and impedance studies of binary ZnO–CuO nanocomposites for hydroelectric cell application. Mater Chem Phys 291:126690. https://doi.org/10.1016/j.matchemphys.2022.126690

Origin of Gap Solitons in Gaussian Apodized Centro-Symmetrical Non-linear KLTN Lattices

Draupath Umesh, Ritesh Kumar Chourasia, Aavishkar Katti, and Bajrang Lal Prashant

1 Introduction

Spatial soliton formation from a laser beam in a photorefractive media due to the counteraction of diffraction broadening of the beam by the spatial self-focusing nonlinearity of that media has been widely studied in past few years. Illuminating the media with a nonuniform light beam induces the diffusion and drift of charge carriers which in turn generates a space-charge field which in turn acts as an index waveguide by counteracting the diffraction broadening thereby self-trapping the light inside the waveguide. The photorefractive effect is a phenomenon that is not affected by the absolute intensity of light, making it a suitable tool for modeling systems that display characteristics of solitons in saturable nonlinear periodic media. These media are capable of producing significant changes in refractive index even at low light intensities. As a result, they offer a promising avenue for studying nonlinear optics in a controlled and precise manner. The periodicity in the photonic lattices can be easily imprinted and tuned as we desire during the time of crystal growth itself. An organized investigation has been conducted on the presence and features of optical gap solitons, including their linear stability, in the band gaps of biased centrosymmetric uniform optical lattice [1]. This study provides valuable insights

D. Umesh · A. Katti (✉)
Department of Physics, Dr. Vishwanath Karad MIT World Peace University, Pune, Maharashtra 411038, India
e-mail: aavishkarkatti89@gmail.com

R. K. Chourasia (✉)
Department of Physics, Samastipur College (A Constituent Unit of L.N.M.U., Darbhanga, 846004, Bihar, India), Samastipur, Bihar 848134, India
e-mail: riteshphyzics@gmail.com

B. L. Prashant
Department of Physics, ARSD College, University of Delhi, New Delhi 110021, India

S. B. Krupanidhi et al. (eds.), *Recent Advances in Functional Materials and Devices*, Springer Proceedings in Materials 37, https://doi.org/10.1007/978-981-99-6766-7_27

into the behavior of light waves in such structures and can inform the development of novel optical devices based on optical lattice [2].

In uniform photonic lattices, the allowed and forbidden frequency spectra of electromagnetic waves are determined by the Floquet Bloch theory, resulting in a peak in the reflection spectrum with side lobes at adjacent wavelengths.

In this study, a Gaussian apodized optical lattice was employed to examine the characteristics and existence of solitons formed in the band gaps of the crystal. The use of this lattice is advantageous because it reduces the side lobes in the reflection spectrum by gradually decreasing the refractive index variation to zero at each end. This approach enables a more precise and controlled study of the properties and behavior of solitons in the band gaps of the crystal [3, 4]. However, apodized gratings are aperiodic structures, and thus the Floquet-Bloch theory cannot be used to analyze the reflection coefficient or bandgap structure. Instead, the transfer matrix method must be used. Despite this, apodization does not significantly alter the edges of the bandgap compared to uniform gratings also the uniform photonic lattice, plays a major role in determining the properties of the light beam, disregarding any nonlinearity [4]. Under this assumption, the band structure of apodized photonic lattice can be approximately found by using Bloch wave solutions in case of the corresponding uniform optical lattice. Also, we have considered a different lattice periodicity from the previously mentioned work [1]. The effect of this parameter change on the band structure has been taken into consideration. We are specifically interested in biased photorefractive crystals because it gives us the monopoly to control the conditions under which the refractive index of the photorefractive material changes in response to light, enabling it to allow the changes in refractive index induced by light to be reversible (reversible optical induction) in the photonic lattice. This property makes biasing the photorefractive media to be one of the efficient methods for creating a reconfigurable (whose structure, parameters, or properties can be modified or reprogrammed) periodic lattice. The standard method for optically inducing periodicity in optical lattices is by interfering with two ordinarily polarized laser beams inside the photorefractive crystal [5]. This generates a uniform grating which can then be apodized by altering the mark-to-space ratio of the grating in a Gaussian manner. Now one way to practically realize this apodization process is by using grating filters that can be fabricated by electron beam lithographic techniques [6].

In addition to gap solitons, one can even observe various kinds of lattice solitons by using optically induced photonic lattices. A few examples of lattice solitons that falls under the category of screening nonlinearity include vortex solitons [7], dipole-like vector solitons [8], reduced symmetry solitons [9], solitons with nonlocal characteristics [10], as well as those supported by Bessel photonic lattices [11], etc. Both theoretical and experimental investigations are being conducted on lattice solitons, including those observed in non-centrosymmetric photorefractive and centrosymmetric photorefractive media in which the Pockels effect (linear electro-optic effect) and the Kerr effect (quadratic electro-optic effect) induces refractive index variation. But here we will be discussing about gap solitons as they find applications in all-optical signal processing, information storage, and slow light systems. Our findings in this work are significant as they contribute to the understanding of solitons in

centrosymmetric photorefractive media and provide insights for future experimental investigations. Here we have chosen the crystal to be KLTN as an example to illustrate our results. This approach offers a promising avenue for understanding the behavior of solitons in these materials and building innovative optical devices based on their unique properties.

2 Theoretical Model

In order to investigate the formation of centrosymmetric photorefractive solitons in the photonic band gap of a biased optical lattice, consider a high-intensity optical beam propagating through a crystal imprinted with a photonic lattice modulated by a Gaussian envelope function along the x axis. Also, the wave is only permitted to diffract in the x direction. This apodization technique was employed to shape the reflectivity profile of the grating and adjust the spectral properties of the solitons. It is important to remember that an electromagnetic wave propagating in a periodic uniform photonic lattice will have a permitted and forbidden frequency spectrum as predicted by the Floquet-Bloch theory. The uniform optical lattices will exhibit a characteristic peak or dip, respectively, along with side lobes at the nearby wavelengths, depending on whether we are looking at the reflection or transmission spectrum. Apodization is a process where the refractive index variation is eventually decreased to zero over a particular distance at each end. Additionally, the side lobes in the reflection spectrum are suppressed as a result of apodization of the grating [7, 8]. However, because apodized gratings are aperiodic, the Floquet-Bloch theory is invalid when determining the reflection coefficient or bandgap structure. Instead, the transfer matrix approach is typically employed. When compared to a uniform grating, the apodization often has little impact on the band gap's edges [8]. As a result, we go back to Eq. (3), which takes a uniform grating into account. For any value of the wave vector that spans the band gap of the photonic lattice, Eq. (3) admits Bloch wave solutions. We substitute the Bloch wave function in (3) using the Floquet Bloch theory and the parameters for periodicity T = 2.5, scaled lattice depth p = 5, and then solve the following eigenvalue problem using periodic boundary condition while treating the nonlinearity as a perturbation. As a result, Fig. 2 shows the band structure of the uniform photonic lattice. Assuming a plane wave dependence on the incident optical beam, which is linearly polarized along x-axis and biased field applied in the same direction, the optical field in the medium is expressed as a slowly varying Gaussian envelope function in z given by $\vec{E} = \hat{x}A(x, z)\exp[ikz]$. Now the perturbed extra-ordinary refractive index of the centrosymmetric media can be expanded as $(n_e')^2 = (n_e)^2 - n_e^4 g_{eff}\epsilon_0^2(\epsilon_r - 1)^2 \mathrm{E}_{sc}^2$. In a medium with inhomogeneous incident light, the interplay between the diffusion and drift of charge carriers induces a space charge field represented by E_{SC}. Under moderate bias conditions, this field can be expressed in terms of the dark irradiance I_d and the intensity I. The parameter g_{eff} is associated with the Kerr nonlinearity, whereas ε_0 and ε_r represent the vacuum permittivity and the relative dielectric constant of the medium, respectively. Under

the above-mentioned conditions, the Helmholtz equation will get modified into the paraxial equation for diffraction. The refractive index variation in the photorefractive medium is denoted by Δn_{PR} and is expressed as $\Delta n_{PR} = -\frac{1}{2} n_e^3 g_{eff} \epsilon_0^2 (\epsilon_r - 1)^2 E_{sc}^2$. Now the generalized paraxial equation for diffraction in a one-dimensional photonic lattice is modified to include the refractive index change induced by the photonic lattice Δn_G [12], and is expressed as:

$$i\frac{\partial A}{\partial z} + \frac{1}{2k}\frac{\partial^2 A}{\partial x^2} - \frac{k}{n_e}(\Delta n_{PR} + \Delta n_G)A = 0 \tag{1}$$

For convenience we can convert Eq. (1) into dimensionless coordinates using $s = \frac{x}{x_0}$, $\xi = \frac{z}{k x_0^2}$ and $A = \left(\frac{2\eta_0 I_d}{n_e}\right)^{1/2} q$ as follows

$$i\frac{\partial q}{\partial \xi} + \frac{1}{2}\frac{\partial^2 q}{\partial s^2} + pR(s)q - \frac{\beta q}{(1+|q|^2)^2} = 0 \tag{2}$$

Here the parameter β quantifies the influence of the drift nonlinearity and can be modified by varying the external voltage bias, the scaled lattice depth p, and the lattice pattern function $R(s)$ which is determined by the modulation period T.

However, employing the commonly used method to solve integrable nonlinear equations like inverse scattering transform method is beyond reach for integrating the equation given in (2), it is still possible to find spatially localized soliton solutions for this equation. In order to do so, we assume that a shape-preserving solution takes on a generic form $q(s, \xi) = w(s, \xi)\exp(i\mu\xi)$ we can then search for the stationary soliton solutions that can be described by the propagation constant μ and falls under the photonic band gap area by modifying Eq. (2) as

$$\frac{1}{2}\frac{\partial^2 w}{\partial s^2} + pR(s)w - \frac{\beta w}{(1+w^2)^2} - \mu w = 0 \tag{3}$$

Simplifying the expression further yields

$$\frac{1}{2}\frac{\partial^2 w}{\partial s^2} + F(I)w = \mu w \tag{4}$$

where $F(I) = pR(s) - \frac{\beta}{(1+w^2)^2}$ dictates the nonlinearity of the system and I describes the intensity. In a uniform grating, the refractive index change is generally expressed in terms of a cosinusoidal variation as $R(s) = \cos\left(\frac{2\pi s}{T}\right)$. This periodicity in refractive index give rise to band gaps in the crystal. Now Fig. 1 depicts the variation of refractive index in the photonic lattice after apodization.

For a Gaussian apodized photonic lattice, the refractive index change is expressed as

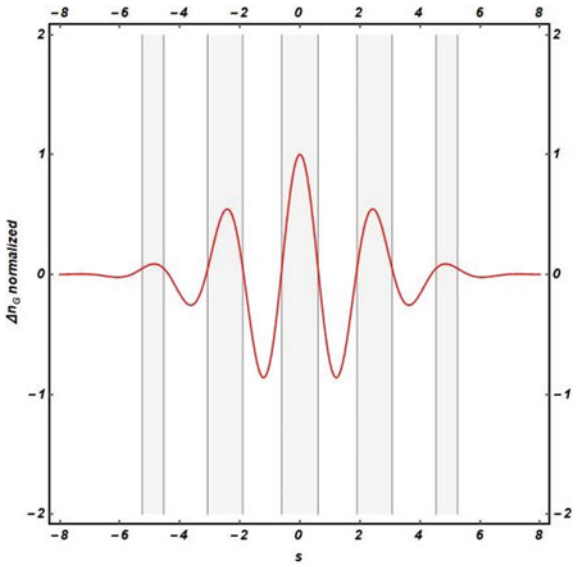

Fig. 1 Gaussian apodized grating in a 1-dimensional photonic lattice for $a = 0.5$, $b = 1$ and $L = 2.236$

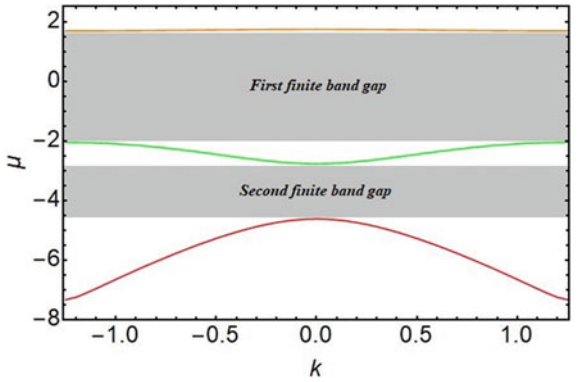

Fig. 2 Band structure for a uniform 1-dimensional photonic lattice obtained by Floquet-Bloch theory

$$R(s) = \cos\left(\frac{2\pi s}{T}\right) b \exp\left[\frac{-as^2}{L^2}\right] \tag{5}$$

where L is the grating length. We can tailor the band gaps and change the bands of the photonic lattice to suit our needs by modifying the lattice parameters. It is observed that the positions and structures of the Bloch bands are significantly affected by altering the parameters p and T. Now (3) gets modified to

$$\frac{1}{2}\frac{\partial^2 w}{\partial s^2} + pb\cos\left(\frac{2\pi s}{T}\right)\exp\left[\frac{-as^2}{L^2}\right]w - \frac{\beta w}{(1+w^2)^2} - \mu w = 0 \tag{6}$$

Note that Eq. (6) does not admit Bloch wave solutions for all values of the propagation constant that spans the band gaps of the photonic lattice. In Fig. 2, we have plotted the band gap for the uniform 1-D photonic lattice that lies between $-2.04 \leq \mu \leq 1.67$ for first finite band gap, $-4.612 \leq \mu \leq -2.799$ for second finite band gap, and $\mu > 1.725$ for semi-infinite band gap.

3 Results and Discussions

3.1 Existence of Gap Solitons

In this section, we will elaborate on the existence and properties of various gap solitons that can be formed within the photonic bandgap of the photonic lattice induced in KLTN crystal. For illustration of our results, we shall take the following parameters [1], $n_e = 2.2$, $g_{eff} = 0.12\,\mathrm{m}^{-4}\mathrm{C}^{-2}$, $\varepsilon_r = 8000$, $\lambda_0 = 515\,\mathrm{nm}$, $x_0 = 20.9\,\mu\mathrm{m}$, $E_0 = 1100\,\mathrm{V/cm}$. With these parameters, β will approximately take the value of 5.5. Solving Eq. (6), we see that in the first band gap single, double, and multi peaked solitons were observed whereas in second band gap only single and double peaked solitons where observed. In this section, we will also elaborate on the existence and properties of various gap solitons that can be formed in the band gaps of the photonic lattice. Figure 3a–c depicts the formation of low, moderate, and high power single peaked solitons respectively in the first finite band gap of the photonic lattice ($\mu = -1.1, 0.25$ and 1.4). Now by tweaking the base parameter for the periodicity of the lattice a little bit from T=2.5 to T=1.5, we were able to obtain the double peaked and multipeaked solitons in the first finite band gap which is shown in Fig. 4 b and c (μ=−1 and μ=−4.05). The photonic band structure gets modified as in Fig. 4(a). Figure 5a–c depicts the formation of single peaked solitons with low, moderate and high power respectively in the second finite band gap of the photonic lattice ($\mu = 3.102, -2.97$ and -2.8) and Fig. 6 depicts the existence of double-peaked solitons in second finite band gap ($\mu = -4.05$).

3.2 Stability of Gap Solitons

Solitons in photorefractive media with Kerr electro-optic effect exhibit remarkable shape preservation, but their stability cannot be assured due to the non-integrability of the underlying nonlinear Schrödinger equation. Thus, to detect these solitons experimentally, it is essential to conduct a linear stability analysis of their dynamics against small perturbations. This is because experimental observation of solitons is limited to stable ones. The small perturbations around the soliton solutions can be represented as a linear combination of eigenmodes. The stability of these soliton

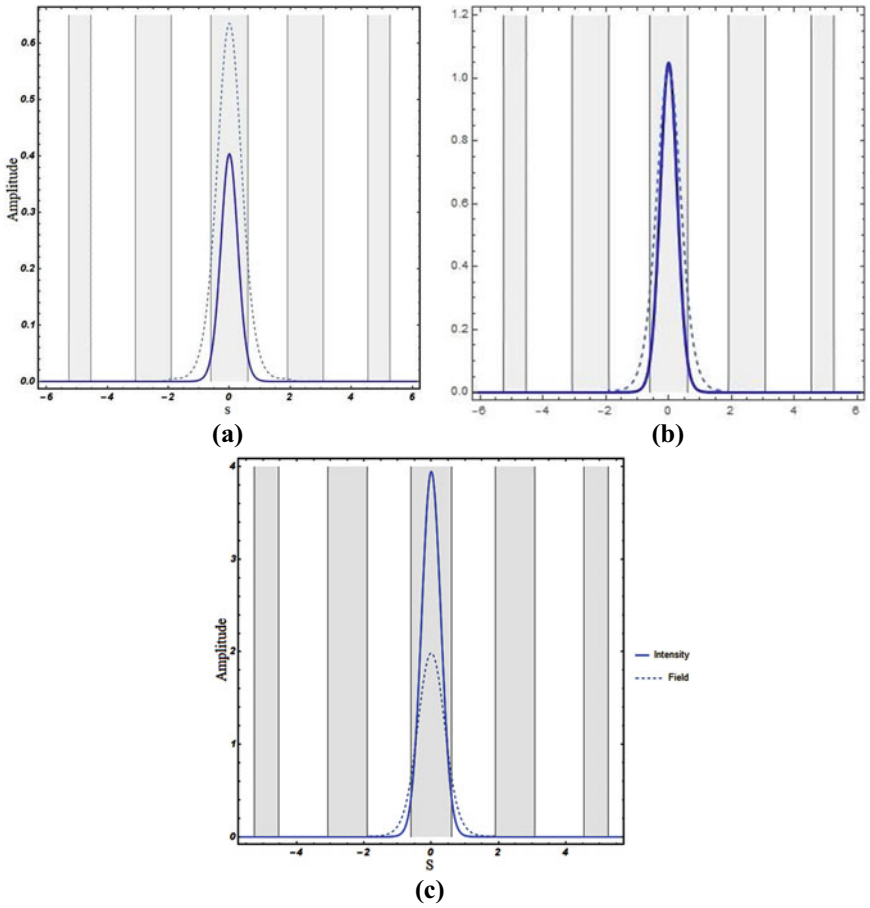

Fig. 3 Single peaked **g**ap soliton spatial field profile (dashed curve) and intensity profile (solid curve) in the first finite band gap $-2.04 \leq \mu \leq 1.67$. **a** Low power regime; ($\mu = -1.1$). **b** Moderate power regime; ($\mu = 0.25$). **c** High power regime ($\mu = 1.7$)

solutions is generally analyzed using linear stability analysis. Based on this approach, the discrete eigenmodes can be classified into one of three categories.

(a) Neutrally stable internal modes whose eigenvalues tend to be real.
(b) Instability modes whose eigenvalues tend to be imaginary.
(c) Oscillatory modes whose eigenvalues tend to be complex.

By linear stability analysis, one can develop a necessary condition for soliton stability that is based on the analysis of the growth or decay of small perturbations around the soliton solution to a nonlinear partial differential equation using the instability modes with imaginary eigenvalues. The Vakhitov-Kolokolov (VK) criterion is frequently utilized to examine the stability of solitons in Kerr media, where a soliton is stable

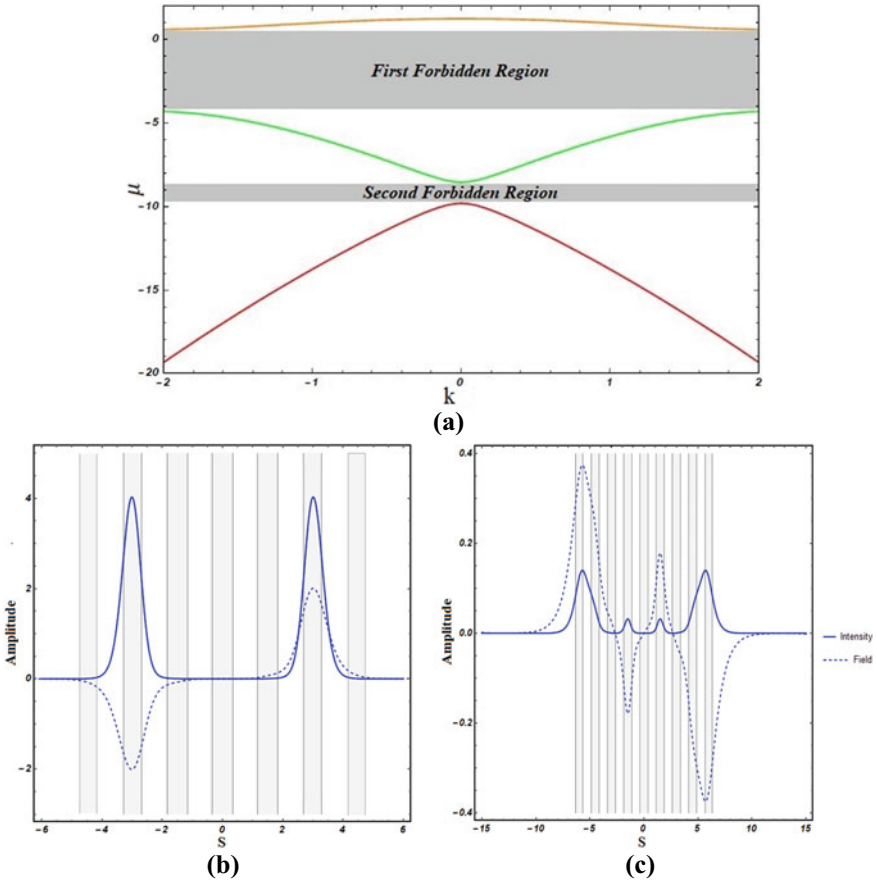

Fig. 4 **a** Modified band structure for lower lattice periodicity $T = 1.5$, i.e.: $(-4.12 \leq \mu \leq 0.26) \rightarrow$ **first band gap** and $(-9.56 \leq \mu \leq -8.65) \rightarrow$ **second band gap**. **b** Intensity (solid curve) and field (dashed curve) profile of double humped soliton in the first finite band gap of the photonic lattice ($\mu = -1$). **c** Intensity (solid curve) and field (dashed curve) profile of multi humped soliton in the first finite band gap of the photonic lattice ($\mu = -4.05$)

if its power grows with an increase in the propagation constant, i.e., $\frac{dP}{d\mu} > 0$. In the following section, we utilize a perturbation approach to investigate the linear stability characteristics of these solitons in greater depth.

3.3 Linear Stability Analysis

In linear stability analysis, small perturbations around the soliton solutions are treated as normal modes of the linearized system around the soliton solution.

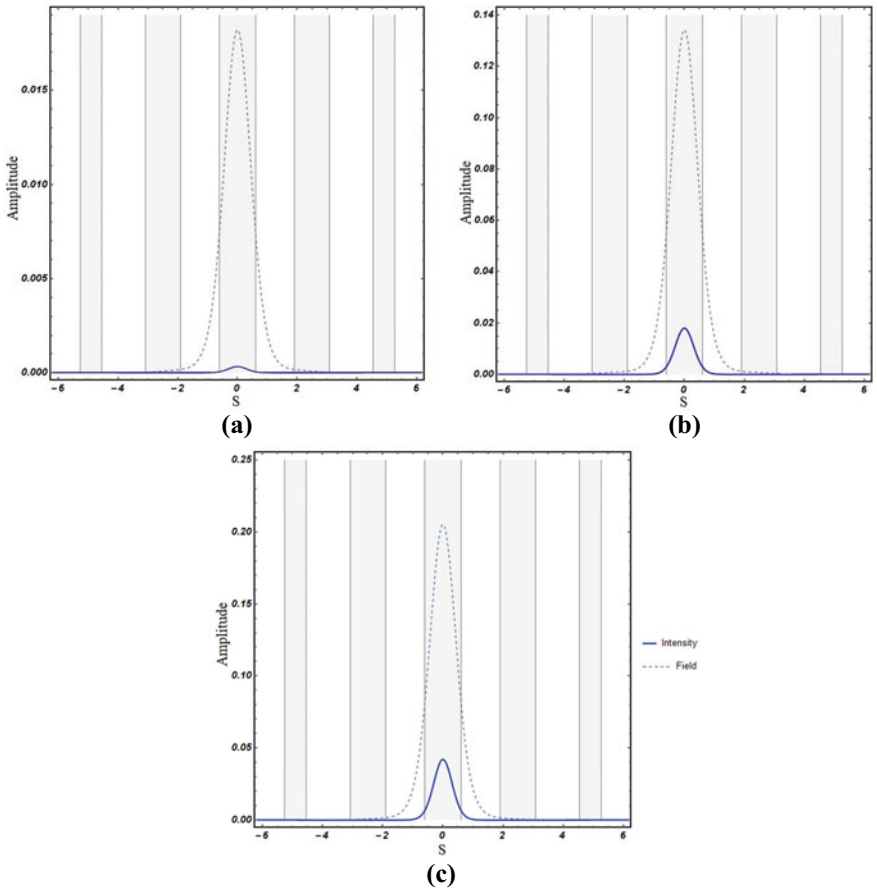

Fig. 5 Single peaked gap soliton spatial field profile (dashed curve) and intensity profile (solid curve) in the second finite band gap $-4.612 \leq \mu \leq -2.799$. **a** Low power regime; ($\mu = -3.102$). **b** Moderate power regime ($\mu = -2.97$). **c** High power regime; ($\mu = -2.8$)

$$q(s,\mu) = \left\{w(s,\mu) + [u(s) - v(s)]e^{i\delta\xi} + [u*(s) + v*(s)]e^{i\delta\xi}\right\}e^{i\mu\xi} \tag{7}$$

where u(s) and v(s) describe small perturbations and the asterisk describes the complex conjugation. Now By substituting Eq. (7) in Eq. (3) and linearizing it, u(s) and v(s) are found out to be satisfying an eigen value problem

$$\begin{pmatrix} 0 & L_0 \\ L_1 & 0 \end{pmatrix}\begin{pmatrix} u \\ v \end{pmatrix} = \delta\begin{pmatrix} u \\ v \end{pmatrix} \tag{8}$$

Here L_0 and L_1 are the differential operators given by L_j [13].

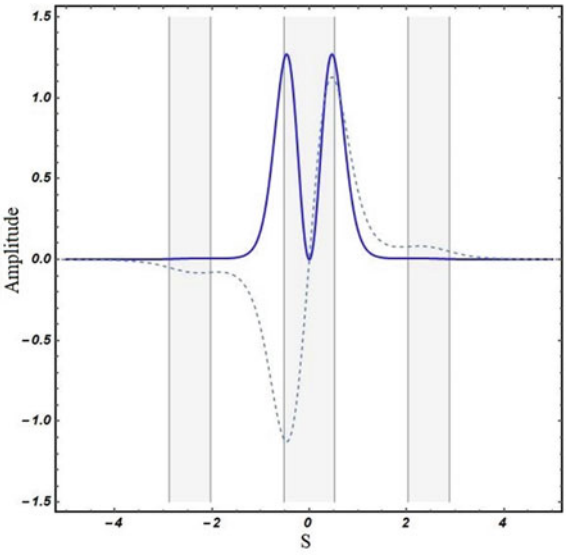

Fig. 6 Double peaked gap soliton spatial field profile (dashed curve) and intensity profile (solid curve) in the second finite band gap ($-4.612 \leq \mu \leq -2.799$) of the photonic lattice

$$L_j = -\frac{1}{2}\frac{\partial^2}{\partial s^2} + \mu - U_j,\ (j = 0, 1) \tag{9}$$

U_j is each term of Tylor expansion of the functions of s through the intensity and$U_0 = F(I)$, $U_1 = F(I) + 2|w|^2 \frac{\partial F}{\partial (w^2)}$ which yields,

$$L_0 = -\frac{1}{2}\frac{\partial^2}{\partial s^2} - pR(s) + \frac{\beta}{\left(1 + w^2\right)^2} + \mu \tag{10}$$

and

$$L_1 = -\frac{1}{2}\frac{\partial^2}{\partial s^2} - pR(s) + \frac{\beta\left(1 - 3w^2\right)}{\left(1 + w^2\right)^3} + \mu \tag{11}$$

Now solving the eigen value problem is a tedious task, but it can be simplified and solved by reducing the problem comprising of two eigenvalue equations, into a problem consisting of single equation of the form

$$L_0 L_1 u = \delta^2 u \tag{12}$$

This can be tackled numerically using the method of finite differences that was done by discretizing the continuous domain into a finite number of points and then approximating the derivatives of the solution around these points using central differences. By considering the perturbed soliton solutions using this method, we can characterize the linear stability of the solitons.

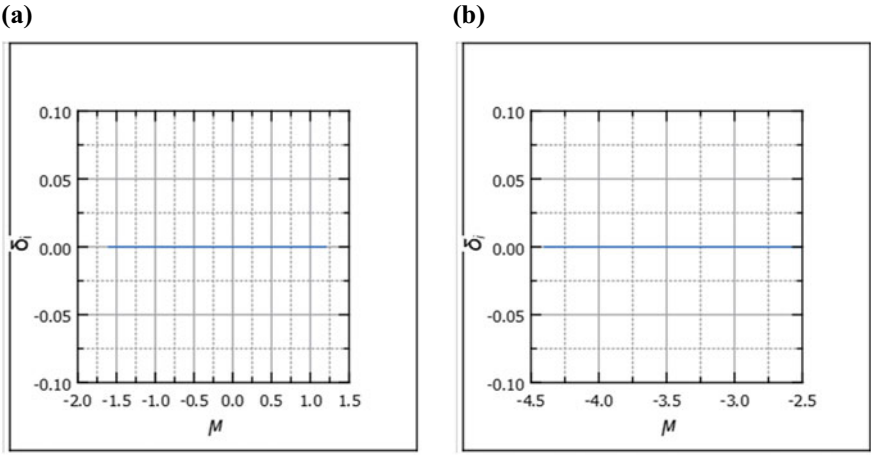

Fig. 7 **a** Imaginary component of instability growth rate versus wave vector for gap solitons formed inside the first band gap. **b** Imaginary component of instability growth rate versus the wave vector for gap solitons formed inside the second band gap

The aforementioned perturbation terms can grow in a complex rate given by $\delta = \delta_r + i\delta_i$. If the perturbation term δ where to have complex part ($\delta_i \neq 0$) then it would be growing exponentially which means the solitons are unstable, whereas if the perturbation term δ where to have only real part ($\delta_i = 0$) then it would be oscillating periodically between (-1 and $+1$) which is considered as a harmonic perturbation, that means the solitons are stable. Figure 7 depicts the imaginary part of the perturbation growth rate for all the solitons in both the bandgaps. By the finite difference method, we were able to find out that the perturbation introduced to the single, double, and multi-humped solitons of the first band gap as well as the single and double-humped solitons formed in second band gap showed the harmonic behavior that is the imaginary part of the perturbation was found out to be zero for all the three solitons throughout the band gap and hence making them stable throughout the band gap.

4 Conclusion

In this study, we have discovered the formation of optical spatial gap solitons in photorefractive media with a quadratic nonlinearity and a Gaussian apodized photonic lattice embedded within it. Using the Floquet Bloch theory, we determined the photonic lattice band structure. The photorefractive nonlinearity allowed for the formation of solitons within the photonic band gap. We derived soliton solutions for both band gaps using the paraxial Helmholtz equation and observed various types of soliton solutions, including single hump, double hump, and multi-hump solitons,

in each band gap. We also investigated the stability of the solitons to small perturbations across the entire band gap. Our findings indicate that the solitons formed in both band gaps exhibit complete stability to small perturbations.

Acknowledgements Aavishkar Katti would like to acknowledge financial assistance from DST-SERB, Govt of India through the Core Research Grant (CRG/2021/004740)

References

1. Zhan K, Hou C (2012) Opt Commun 285:3649. https://doi.org/10.1016/j.optcom.2012.04.040
2. Christodoulides DN, Carvalho MI (1995) Bright, dark, and gray spatial soliton states in photorefractive media. J Opt Soc Am B 12:1628–1633. https://doi.org/10.1364/JOSAB.12.001628
3. Sun N-H et al (2009) Numerical analysis of apodized fiber Bragg gratings using coupled mode theory. Prog Electromagn Res 99:289–306. https://doi.org/10.1177/00368504221094173
4. Ashry AE, Mahros A, Alhaddad M, Elleithy K (2014) Investigating the performance of apodized fiber Bragg gratings for sensing applications. In: Proceedings of the 2014 zone 1 conference of the American society for engineering education, pp 1–5. https://doi.org/10.1109/ASEEZone1.2014.6820640
5. Feischer JW, Segev M, Efremidis NK, Christodoulides DN (2003) Nature 422. https://doi.org/10.1038/nature01452
6. Millar P, Liu X, De La Rue R, Aitchison JS (1998) Fabrication of complex integrated waveguide filters using electron beam lithography. In: Conference on lasers and electro-optics-Europe, technical digest series, Optica Publishing Group. https://opg.optica.org/viewmedia.cfm?uri=CLEO_Europe-1998-CThK3&seq=0
7. Neshev D, Alexander TJ, Ostrovskaya EA, Kivshar YS, Martin H, Makasyuk I, Chen Z (2004) Phys Rev Lett 92:123903. https://doi.org/10.1364/OL.31.000607
8. Chen Z, Martin H, Eugenieva ED, Xu J, Bezryadina A (2004) Phys Rev Lett 92:143902. https://doi.org/10.1364/OL.29.001656
9. Fischer R, Trager D, Neshev DN, Sukhorukov AA, Krolikowski W, Denz C, Kivshar YS (2006) Phys Rev Lett 96:023905
10. Xu Z, Kartashov YV, Torner L (2006) Opt Lett 31:2027
11. Ruelas A, Lopez-Aguayo S, Gutierrez-Vega JC (2010) Phys Rev A 82:063808
12. Zhan KY, Hou CF (2014) Lattice surface solitons in diffusive nonlinear media driven by the quadratic electro-optic effect. Opt Express 22:11646–11653. https://doi.org/10.1364/OE.22.011646
13. Kivshar YS, Agrawal GP, Agrawal GP (eds) (2003) Spatial solitons. Academic Press, pp 31–62. ISBN 9780124105904. https://doi.org/10.1016/B978-012410590-4/50002-4. https://doi.org/10.1016/B978-012410590-4/50002-4